UNIVERSITÀ DEGLI STUDI DI ROMA TRE

SCUOLA DOTTORALE IN

GEOLOGIA DELL'AMBIENTE E DELLE RISORSE

(SDIGAR)

Ciclo XXVI

THE EVOLUTION OF TURRIALBA VOLCANO PLUMBING SYSTEM

(COSTA RICA)

Andrea Di Piazza

A.A. 2012/2013

Tutors: Dott.ssa Claudia Romano   Coordinatore: Prof. Claudio Faccenna

        Prof. Franco Barberi

Co-Tutor: Dott. Gianfilippo De Astis

"The future belongs to those who believe in the beauty of their dreams"

Eleanor Roosvelt

Content

1. *Introduction*

Turrialba volcano is situated on the southern tip of the 1000km-long volcanic chain that develops from Mexico to Costa Rica. It represents the second highest volcano after nearby Irazú and is upwind of the Central Valley of Costa Rica, which includes the city of San José (2 million inhabitants) and the metropolitan area around it. This volcano drew the attention of the Scientific Community after the 1996, when seismic swarms and the progressive enhancement of the gas emissions at crater fumaroles, seemed to be the precursors of a possible imminent eruption. This unrest phase, characterized by very high temperatures of gas emissions, strong degassing, microseismicity, and phreatic explosions, is still ongoing although till now no eruptions has occurred. An eruption of Turrialba could severely hamper the economy of Costa Rica, due to the geographical location of the volcano with respect to many important human activities (cities, industries, etc…).

The most recent eruption at Turrialba occurred between 1864 and 1866, and consisted of Strombolian to Vulcanian activity (Reagan et al., 2006), that produced ash-fall on the Central Valley up to the Pacific coast of Costa Rica. After this eruption, the volcano entered a quiescence period, characterized by low temperature fumarolic activity (Soto 1988; Tassi et al., 2004; Vaselli et al., 2010) that lasted ~150 years. Since 1996, an increase in seismicity and the progressive appearance of magmatic gas species (e.g. CO_2, SO_2 and H_2S; Vaselli et al., 2010) in the fumaroles was registered. On January 2010, the opening of a vent (65 x 20 m across) due to a phreatic explosion (OVSICORI-UNA, 2010, 2011) produced an ash and lithic fall-out to the southwest, that reached the cities of San José, Cartago and Tres Ríos. Other phreatic explosive events occurred in 2011, 2012 and more recently in May 2013 (OVSICORI-UNA, 2011, 2012, 2013). Nowadays, high temperature gases continue to escape from the phreatic vents opened in the last years and the possibility of a magmatic eruption still persists.

This unrest phase prompted an increasing number of investigations on the volcano, in particular geochemical (Tassi et al., 2004; Hilton et al., 2010; Vaselli et al., 2010; Campion et al., 2012) and geophysical studies (Martini et al., 2010; Eyre et al., 2013), all aimed at evaluating the state of activity of the volcano. Compared to the several studies on the fumarolic system, the geology and the plumbing system of the volcano are not well known. Soto (1988) was the first describing the geology of Turrialba volcano, the petrography and whole rock geochemistry of its products, and mapped the geology and the tectonic features of the edifice. Reagan et al. (2006) dated via [14]C

many charcoal fragments found on paleosoils, and described at least 20 eruptive units on the top of the volcano. More recently, Ruiz et al. (in press) dated via $^{40}Ar/^{39}Ar$ eight lava flow units erupted in the last 250ka, and partly modified the volcano stratigraphy of Reagan et al (2006).

This thesis combines whole rock, gases and fluid inclusions geochemistry to better constrain the magmatic source feeding the plumbing system of the volcano and to evaluate the state of activity at the date of sampling. Textural analysis of selected eruptive products were performed, in order to investigate different eruptive behaviors. Uniaxial press measurements were also performed on andesite samples from the most explosive eruption of the last 10ka, to constraint the rheology of these magmas. Combination of textural analyses and rheological measurements gives us additional constraints on the expected eruptive behaviour of Turrialba volcano in the event of a renewal of magmatic activity.

Thesis structure and summary of contents

Chapter 2: This chapter contains a description of the regional and local tectonic setting and presents review of the geological knowledge on Turrialba volcano. Fifteen rock samples were collected in the March 2011 survey, all related to the last 10ka activity of the volcano; samples were used for major and trace elements geochemical analyses and to perform noble gas geochemistry on olivine and pyroxenes crystals (Chapter 4). Whole rock geochemistry will be discussed in this chapter. Samples belong to the calc-alkaline series and cover the entire compositional range of Turrialba volcano, from basalts/basaltic-andesites to dacites.

Chapter 3: In this chapter, the results of the fluid geochemistry investigation performed during the March 2011 survey are presented. A brief overview on previous works on the gas discharge system is given at the beginning of the chapter. Then results the CO_2 soil degassing prospection are presented; soil flux data were collected by accumulation chamber method, and 973 measurements with a spacing of 30m and over a surface of 0.807 km^2 were carried out. Values of the CO_2 soil flux display a wide variation, ranging between 0.4 to 52090 gm^{-2}d^{-1}. Along with the gas flux survey, temperature measurements at a soil depth of 10 cm were also carried out, giving temperature anomalies up to 85°C. The CO_2 soil flux profiles were performed at "Falla Ariete", a peripheral fault with respect to the top of the volcano, where fumaroles appeared in 2007. Here the highest peak in flux anomaly gave a value of 5375 gm^{-2}d^{-1}, whereas soil temperatures measured ranged from 9.2°C to 73.7°C. At that time, 229 measurements of soil gas concentrations were performed in the summit crater area with the aim of mapping the soil concentration of He, H_2 and CO_2 Finally,

the chemical composition was analyzed of 10 fumaroles distributed between the West and Central Crater. These measurements were useful to constraint the state of activity of the volcano at the time of the investigation, and to complete the temporal data series available of the geochemistry of Turrialba gas discharge system.

Chapter 4: This chapter presents the results of a noble gas geochemical study of fumarolic gas discharge and of fluid inclusions hosted in olivine of Turrialba rocks. Main aim of this study is to give new insights on the magmatic source, particularly on the presently degassing magma involved in the ongoing unrest phase. The ^{3}He/^{4}He ratio of fluid inclusions from the most mafic eruptive products (SiO_2=52.5wt% and MgO=6wt%) varies from 7.86 to 8.07 Ra, while that from andesite lavas varies from 7.03 to 7.18 Ra. In order to evaluate the extent of crustal contamination, Sr and Nd isotope analyses were performed on selected samples. This helped to constrain the geochemistry of the local mantle source. The comparison of He-isotopic compositions of fluid inclusions with that of fumaroles shed new light on the composition of magma degassing at present day and on the ongoing unrest at Turrialba volcano. The fumaroles collected in 2007-2011 show an helium isotope composition of 7.50-7.96 Ra, which is well in the range of that measured in fluid inclusions from the more mafic recently erupted rocks. On the basis of this findings, we suggest that the magma involved in the ongoing unrest phase and feeding the crater fumaroles has a geochemical affinity with the most basic basaltic-andesitic magmas analyzed in this study. In addition, monitoring of He isotope composition of fumarolic gas in the last years at Turrialba volcano, displays a progressive increase of ^{3}He/^{4}He ratios, which could be related to the simultaneous unrest testified by the increased seismic activity. We infer that this variation is likely related to a refill of the plumbing system by a ^{3}He-rich magma, which should be very primitive and rising directly from the mantle.

Chapter 5: Noble gas geochemistry data presented in Chapter 4 indicate that magma involved in the ongoing unrest phase may have the same composition of that erupted during the last phase of activity. For this reason, basaltic-andesitic samples of the 1864-66 eruption and of the most explosive eruption of the last 10ka (1.9ka andesitic eruption) were chosen for textural analysis. Detailed stratigraphic studies and sampling of both eruptions were performed in 2011 and 2012. For the 1.9ka eruption, it was possible to study proximal, intermediate and distal outcrops, whilst for the 1864-1866 eruption, only one key outcrop was chosen. Textural analysis of vesicles and crystals were performed on selected samples, on the basis of their density and vesicularity. This study permits to understand the eruptive style of this two eretions and to classify them on the basis of their textural parameters.

Chapter 6: This chapter presents a study of high-temperature, uniaxial deformation experiments of natural, partially crystallized magma from Turrialba volcano (1.9ka) andesitic eruption. The experiments were performed using a high-temperature uniaxial Geocomp LoadTrac II press at dry atmospheric conditions and under controlled deformation rates. Each experiments involved deforming cores of natural (i.e. crystal- and vesicle-bearing) scoriaceous sample, at various step temperatures (790 – 870°C) and variable strain rates (from 10^{-5} to 10^{-3} s^{-1}). Objective of this study is to evaluate the multiphase rheology of these samples, and thus the effect of vesicles and crystals on the viscosity of the magma; in addition, it is useful for a general understanding of the full complexities governing the dynamics of magma transport in natural systems. Combination of textural analyses and rheological measurements were also performed to give additional constraints on the expected eruptive behaviour of Turrialba volcano in the event of a renewal of magmatic activity.

2. Turrialba volcano

The unrest phase that affected Turrialba volcano since 1996 drew the attention of the Scientific Community on this previously poorly known volcano. Understanding the volcanological and petrological evolution of Turrialba is an important step to better evaluate its potential hazard and delineate possible hazard mitigation plans. This chapter contains a brief introduction on the geological and tectonic context in which this volcano lies, and an overview of the geochemistry of Turrialba rocks younger than 10-ka with the contribution of new data coming from this study. Samples were collected during a field trip performed in March 2011. Results were merged with other studies in order to complete the dataset available and to assess the evolution of magmas feeding the plumbing system of the volcano.

2.1 Geodynamical background

2.1.1 Regional setting

Costa Rica is situated to the north-east of the Middle American Trench (MAT), which marks the subduction of the Cocos Plate underneath the Caribbean Plate and Panama Microplate, running from southern Mexico to Panama (deMets et al., 1994). The Cocos plate is being subducted at a rate of 8.5–9.0 cm y^{-1} towards N32E (Protti et al., 1996) and this process is responsible for contemporaneous superimposed compressive, wrench and extensive fault patterns in Central Costa Rica. The convergence rate between the Cocos and Caribbean plates increases to the south-east from 60 mm/yr to ~90 mm/yr off southern Costa Rica (deMets, 2001). Moving along the southern sector of the MAT, the N-S oriented Panama Fracture Zone separate the Cocos and Nazca plates, whose edges in the Pacific Ocean correspond to the W-E oriented boundary of the Cocos-Nazca Spreading Center Plates (*Fig. 2.1a*). Offshore, before the MAT, the Cocos Plate is morphologically subdivided in three sectors (*Fig. 2.1*; von Huene et al., 2000): a) the first northernmost sector is a smooth segment of oceanic crust formed 20-25 Ma ago at the East-Pacific-Rise and Cocos-Nazca Spreading Center; b) the second sector is characterized by 15-20 Ma oceanic crust covered by seamounts (seamounts domain or seamount province); c) the third sector is the aseismic Cocos Ridge that consists of 2-km-thick low density volcanic layers (Bently, 1974), which make this crust sector more buoyant than the adjacent Early to Middle Miocene oceanic crust (Hey, 1977; Meschede et al., 1978). This geodynamically peculiar subdivision is due to the interaction of the

Cocos-Nazca Spreading Center with the Galapagos hotspot (Barckhausen et al., 2001), which created multiple inactive volcanic ridges, almost perpendicular to the trench and as high as 2000 m above sea bottom (Cocos ridge, Coiba ridge, Malpelo Ridge, etc.). The subduction of Nazca Plate underneath Panama, Colombia and Ecuador is nearly perpendicular to the Middle and South American Trench (*Fig.2.1a*).
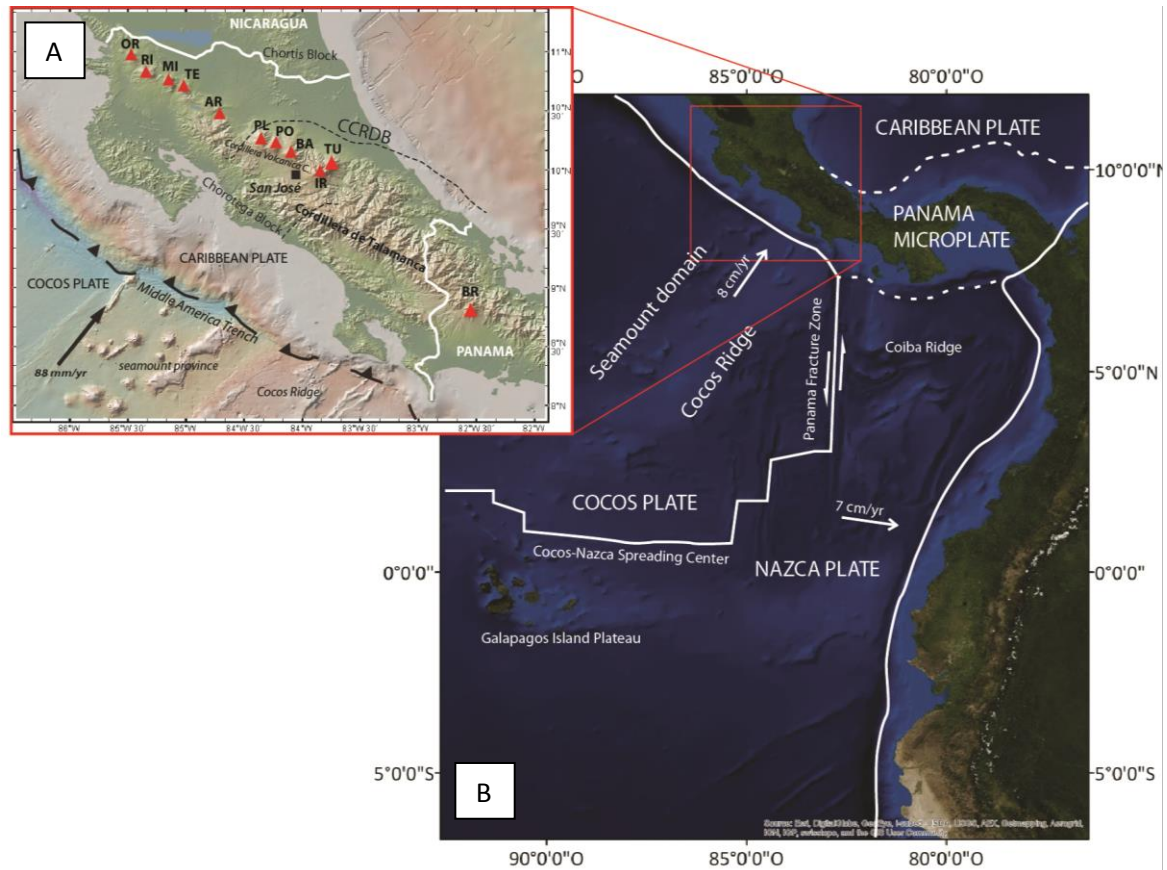
Fig. 2.1 – A) Location of Costa Rica in the geodynamic setting of Central America (base map is a satellite image; coordinates are in WGS84). B) Regional map of Costa Rica showing the locations of the major volcanoes which are identified with the following labels: TU, Turrialba; IR, Irazu; BA, Barva; PO, Poás; PL, Platanar; AR, Arenal; TE, Tenorio; MI, Miravalles; RI, Rincon de la Vieja; OR, Orosì; BR, Barù (base map from *www.geomapapp.org/*).

Southern Costa Rica and Panama are located on the Panama Microplate (Adamek et al., 1988), where the underthrusting of the Caribbean Plate beneath the Panama Block occurred between 69 and 52 Ma, along its northern boundary (Adamek et al, 1998; Camacho et al., 2010). Central Costa Rica is characterized by the presence of a diffuse fault system named Central Costa Rica Deformed Belt (CCRDB) that represents also the northwestern boundary of the Panama Microplate (Marshall

et al., 2000, Montero, 2001; Lewis et al., 2008). There is a large consensus that the CCRDB is a system of NW dextral and NE sinistral shears, reconstructed as an arcuate zone of diffuse strain, able to define the tectonic features of the central Costa Rica as early modeled by Alvarado Villalón (1984). Costa Rican volcanoes are the southern tail of the Quaternary volcanic front of Central America (CAVF), which extends over a length of about 1000 km from central Mexico to Central Costa Rica and comprises about 40 active or dormant volcanoes. This makes this boundary one of the volcanically most active convergent plate margin on Earth (Carr and Stoiber, 1990; de Boer et al., 1995). A volcanic gap of about 180 km in this arc extends between the active Irazú-Turrialba volcanic complex, in Central Costa Rica, and the historically active Barú complex in Panama(*Fig. 2.1a*). The temporal evolution of this volcanic arc is not well constrained. In Costa Rica there is an evidence of old arc volcanism in the sedimentary record since the Albian (Calvo and Bolz, 1994). The oldest volcanic rocks are those of the Sarapiquí Arc (22.2 – 11.4 Ma) (Gazel et al., 2005), located behind the present volcanic front of Central Costa Rica. A temporal gap in volcanism is recorded between 14 and 11 Ma, possibly due to the collision of older Galapagos hotspot tracks with the Caribbean Plate (Hoernle et al., 2008). Whereas arc magmatism is continuous in northern and central Costa Rica, there are no calc-alkaline arc rocks younger than 8Ma in the Cordillera de Talamanca (Alvarado et al., 1992; de Boer et al., 1995), in the southernmost part of Costa Rica (*Fig. 2.1a*).

This lack of younger arc products defines the magmatic gap in that part of the region. Apparently since 8Ma, the Cocos Ridge collided with Central America, causing uplift and the formation of the Cordillera de Talamanca between 4.5 and 3.5Ma (Krawinkel et al., 2000; Meschede et al., 1998). Alkaline backarc magmatic activity also occurred about this time (Abratis & Worner, 2001). Extrusive and intrusive rocks older than 8Ma in the Cordillera de Talamanca are mostly calc-alkaline in composition, followed in volume by older tholeiitic arc rocks (Abratis & Worner, 2001). Minor centers of alkali volcanic and intrusive rocks occur scattered in the Costa Rica backarc and in one location at the forearc region (5.8 Ma to Holocene; Abratis & Worner, 2001).

The Costa Rican volcanoes are built on the Chortis Block in the north and the Chorotega Block in central and southern Costa Rica (Escalante, 1990; Linkimer et al., 2010); the boundary between these blocks is still matter of debate. In south-central Costa Rica, the Moho of the overriding plate is found at an average depth of 35 km, and toward the Talamanca Mountain Range it reaches a depth up to 50 km (Dzierma et al., 2010). Some authors (Carr 1984; Donnelly et al. 1990) consider this relatively young and thick continental crust of southern Central America less radiogenic, if compared to the crust of other continental margins. Lavas from CAVF in southeast Guatemala, El

Salvador, Nicaragua and northern Costa Rica are basically representative of subalkaline to calc-alkaline basalts and andesites, which do not show obvious isotopic evidence of crustal assimilation (Patino et al., 2000). Volcanic rocks from central-eastern Costa Rica and Panama are basically calc-alkaline but one of the most striking feature of this region is the presence of andesites, dacites and rhyolites with geochemical signatures indicative of partial melting of the subducted slab. Although volumetrically minor, these rocks with slab-melt geochemistries are called adakites elsewhere (Defant and Drummond, 1990; Defant et al., 1992) and are usually associated to young, relatively hot, buoyant oceanic (lithospheric) slab. Small bodies of adakite lavas and dikes occur in the Talamanca range in southern Costa Rica (Drummond et al., 1995) and are dated between 1.9 and 3.5 Ma (Abratis and Wörner, 2001) or even occur above the (subducting) Cocos Ridge. By contrast, literature does not report adakite rocks along the CAVF. Currently, a wide variety of genetic processes (and arc settings) is invoked for the genesis of these rocks and therefore the term adakite should be used with extreme caution (Castillo, 2012).

Despite a rather homogeneous major elements composition – suites can be referred to CA and HKCA suites - one of the fascinating characteristics of the whole Central America magmatism is the pronounced regional variation along the arc of several geochemical ratios that are able to give insights about slab signals. Most of the authors (see Saginor et al., 2013 and references therein) agree that the geochemical features recorded along of the CAVF reveal changes in the mantle and crust, changes in the strength of the slab signal and changes in the type of slab signal, primarily the extent of the hemipelagic sediment component. The subducted sediment component appears to be dominant beneath Nicaragua, but on the other hand Guatemala and Central Costa Rica are characterized by an enriched OIB-type component (Eiler et al., 2005; Hoernle et al., 2008). Actually, the sediment cover of the Cocos Plate appears to be entirely subducted along most of its margin. Feigenson and Carr (1993) proposed two mantle reservoirs for Central America volcanism: 1) an analogous of Depleted Mantle, similar to source of mid-ocean ridge basalts (MORB); 2) veins of enriched mantle into the DM source. Melting of this veined mantle source and its interaction with the subduction component produced magmas with a typical arc signature (Carr et al., 2003; Feigenson et al., 2004).

In Central Costa Rica lavas display an anomalous Galapagos-OIB signature (Reagan and Gill, 1989; Herrstrom et al., 2005; Feigenson et al., 2004). Many models have been proposed to constrain the presence of OIB-signature in Costa Rican magmas. Abratis and Wörner (2001) suggested the presence of a slab window in the subducting Cocos Plate, allowing Galapagos asthenosphere to rise through the window into the mantle wedge below southern Costa Rica and Panama. Feigenson et al. (2004) suggested that the OIB signature is the result of melting Galapagos-modified mantle below

central Costa Rica and Panama. Goss and Kay (2006) invoked the incorporation of fore-arc oceanic complexes into the mantle wedge. More recently Benjamin et al. (2007), Hoernle et al. (2008) and Gazel et al. (2009), suggested the geochemical influence of the subduction of Galapagos hot spot tracks beneath central Costa Rica. The volcanic rocks from the seamounts range in composition from tholeiitic to alkalic, but most of them are alkalic.

2.1.2. *Local setting: the Turrialba volcanic system.*

Turrialba massif is located in a complex tectonic zone, where the Central Costa Rica Deforming Belt meets that of North Panama (Montero, 2003). Together with the Platanar, Poás, Barva and Irazù, the Turrialba volcano forms the Cordillera Central, a large massif of overlapping lava flows and pyroclastic rocks. The main volcano-tectonic structures of Turrialba volcano are oriented NE-SW. The summit of the volcano is characterized by a scissor-shape depression, interpreted either as a collapse caldera (Alvarado, 1984; Paniagua, 1984), a tectonic caldera related to a slope failure (Soto, 1988) or a glacial circus (Reagan et al., 2006). The top of the volcano shows a 1 km-long depression, with steep inner walls (50-70°) and three nested NE-SW oriented main craters inside. The summit depression is cut by at least three main normal fault systems (*Fig. 2.3*), described by Soto (1988) and named Ariete, Elia, and Guácimo.
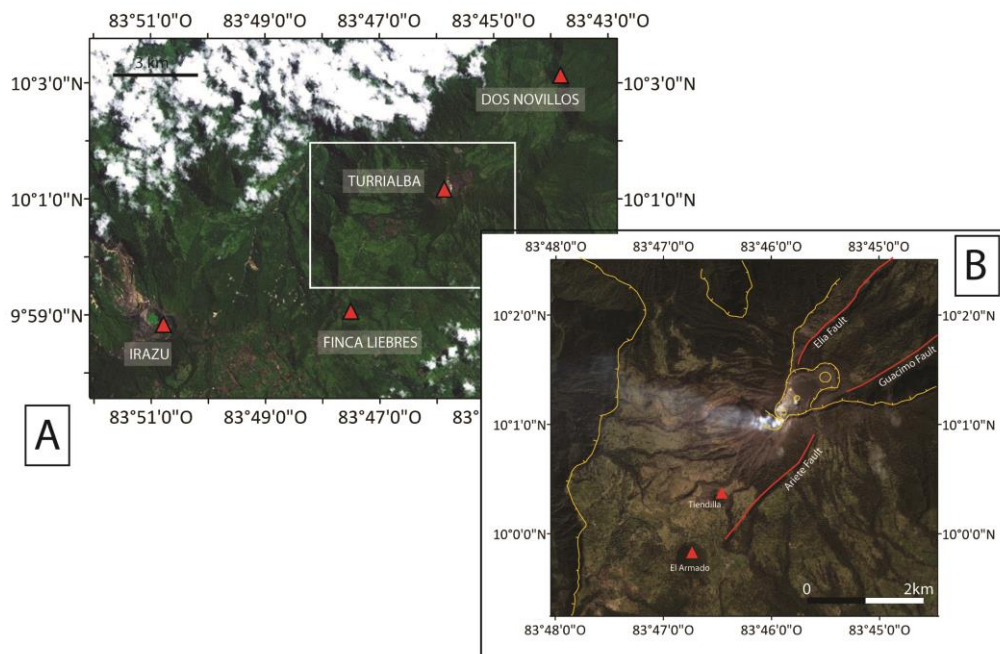
Fig. 2.3 – A) Location of Turrialba volcano and its surroundings. Red triangles are other volcanic edifices near Turrialba. B) Volcano-tectonic sketch map of Turrialba volcano. Red line are faults, red triangle are satellite pyroclastic cones; yellow lines are morphological scarps.

Ariete Fault cuts the entire southeastern flank of the volcano, running near to two satellite pyroclastic cones: Tiendilla (70 m high and 3.6×10^6 m^3 in volume) and El Armado (120 m high and 1.8×10^7 m^3 in volume), both coherently oriented along the main regional tectonic direction. El Armado pyroclastic cone has been dated 61.0 ± 6 ka (^{40}Ar/^{36}Ar method; Ruiz-Cabillo et al., 2010). On the same NE-SW tectonic system, other two volcanic edifices now inactive occur: Dos Novillos volcano and Finca Liebres, respectively (*Fig. 2.3a*). The first is located ~7 km NE of Turrialba summit and is a partially eroded and dissected volcanic apparatus, with an age of 100-200 ka, which is cut by a WNW tectonic structure that interrupts the Turrialba fault system. Finca Liebres is an eroded volcanic structure located ~5 km SW of Turrialba edifice and its most recent eruption has been dated 250ka (Ruiz-Cabillo et al., 2010).

The regional NE-SW oriented structure is responsible for the position of Turrialba volcano and related volcano-tectonic structures. Van Andel (1971) and Stoiber & Carr (1974) proposed that the very prominent N60E alignment Irazú – Turrialba could be related to tectonic structures created by the right lateral shear, striking N30E and reflecting a difference in subduction velocity between western and eastern Costa Rica. Seismicity extending from the surface to Moho depth (Dzierma et al., 2010), P-wave velocities and velocity ratios between P-waves and S-waves (vp/vs) imaged by tomography (Dinc, 2008), indicate that the total crust may be disrupted in this region. Güendel and Protti (1998) observed that at around lat. 83°55'W, where Turrialba and Irazú volcanoes lie, the region is characterized by a sudden arrest of the seismic activity to the south, in coincidence with the termination of the volcanic activity. They explain this with the subduction to the south of a younger crust (15Ma), which is characterized by a thermal structure that allows a more plastic behavior respect to the northern slab. These authors identify here a N30°E strike-slip tectonic regional boundary crossing the tectonic trough of the Central Valley of Costa Rica and connecting the North Panama Deformed Belt (NPDB) to the Middle American Trench. They describe this as a narrow and almost linear structure, due to the propagation of the NPDB. Fernández-Arce (2009) observed that the dominant trend of faulting, in this sector of Costa Rica, is northwest. So neither the set of sub-parallel strike-slip faults which comprises the transcurrent fault zone trending NE-SW proposed by Fan et al. (1993) nor the linear shear zone of Güendel and Protti (1998) are supported by the faulting of this area. The author suggests that the tectonic boundary previously proposed is not evident and it cannot be inferred from the observed surface faults and earthquake activity.

However, the region where Turrialba volcano lies is characterized by a high seismicity due to the presence of numerous active fault systems. The most important faults are Atirro, Juan Vinas, Tucurrique (NW-SE), Turrialba, Aquiares, Pejibaye (NE-SW, normal fault), Chirripó (NE-SW,

inactive) and the systems related to the North Panama Deformed Belt. The latter was responsible for the occurrence of violent earthquakes in 1822, 1916 and 1991 (Alvarado, 2002). The Turrialba region was always interested by microseismicity, in particular between the zone of Tucurrique and rio Chirripó (Barquero et al., 1993), and also major earthquakes occurred here, e.g. the April 1991 M_L 7.7 event and the magnitude 7.0 event of 19 November 1948 (Boschini, 1989) represent two of the highest magnitude events recorded in historical times.

2.2 **Volcanological evolution of Turrialba volcano**

Previous studies of Turrialba volcano were carried out by Soto (1988), Reagan et al. (2006) and more recently by Ruiz et al. (2010).

Soto (1988) produced the first geological map of the summit cone of Turrialba, identifying Finca Liebres (~7 km SW to the summit of the volcano) and other lavas outcropping on the eastern flank of the volcano as its oldest products. He recognized 15 eruptive units produced by the activity of the present cone. All the analyzed samples are medium to high-K calc-alkaline basaltic-andesites to dacites, with a typical mineral assemblage made of abundant plagioclase, clino- and orthopyroxenes and olivine.

Reagan et al. (2006) focused on the most recent activity of the volcano, identifying at least 8 "eruptive units" in the last 10 ka and some older units, distinguished on the basis of a significant erosional period occurred between 50 and 9 ka. The most recent products, dated by radiocarbon measurements of charcoal fragments in paleosoils and fall out deposits, range in age between 9300 y BP and 644 AD. The authors recognized products related to two younger eruptions: the former occurred during an unidentified time-span after 644 AD, and the latter in the period 1864-1866 AD. All the eruptive products of Turrialba volcano belong to the calc-alkaline series and are basaltic-andesitic to dacitic in composition. A general decrease in silica content and a contemporaneous increase in explosivity, was observed with time. Effusive activity was mainly concentrated in the first phase of the last 10ka activity, then Strombolian to Vulcanian eruptions occurred, fed by basaltic to andesitic magmas, with the exception of a Plinian andesite eruption occurred at 1.9 ka. Average repose time between major eruptive units is in the order of 600 – 800 years.

Ruiz et al. (2010) distinguished three main phases of construction of the Turrialba volcano edifice: Proto-Turrialba (~1Ma – 600 ka), Paleo-Turrialba (~600 – 250 ka) and Neo-Turrialba (< 250 ka). They obtained ^{40}Ar/^{39}Ar geochronological data on lava flows emitted between 251±4ka and 3±3ka.

According to the age obtained and the areal distribution of the products, the most important constructive period of the massif was during the Neo-Turrialba stage which has passed through two important constructing episodes, around 100-60ka and 10ka – present (Ruiz et al., 2010).

2.2.1 Chronicles of the 1864-1866 AD eruption

The most recent eruptive magmatic activity which occurred at Turrialba volcano was well described by the work of González-Viquez (1910), in a study which gathers all eyewitness accounts and which is briefly summarized below. Prior to the eruption, Turrialba was characterized by a fumarolic activity which at least since 1723 A.D. On 26 February 1864, an expedition reached the summit of the volcano and found a 100 m-deep crater, with more than 100 fumaroles feeding a 200m-high gas plume. All the vegetation seemed to have been burned by acid rains. On 17 August 1864 an ash fall was registered in San José and in the Central Cordillera; this represented the first phase of the eruptive activity. Ash fell again on the Central Valley of Costa Rica throughout 16-21 September. At the end of September 1864, a new expedition reached the Turrialba summit and its components described a single vent discharging gas into the atmosphere, producing a loud noise and creating a dark plume ~400m high. Large ejected blocks were noticed on the summit area, and the vegetation appeared destroyed for many kilometers to the north-west and west of the volcano. Ash fell on San José till the end of 1864 (von Seebach, 1865). On 8 March 1865, a third expedition reached the summit of the volcano: they described the widening of the West crater, characterized by a funnel shape. Between January and February 1866, the largest eruptive events of this eruption occurred. Ash fell in the Central Valley of Costa Rica for four days in January and three days in February. Ash reached Puntarenas, located 125km W of the volcano. Phreatic explosions occurred at the end of the eruption. Merging stratigraphic data with the chronicles published in González-Viquez (1910), Reagan et al. (2006) interpreted this eruption as a series of phreatic explosions and phreatomagmatic events producing eruptive columns with ash and lapilli rains, in the summit region and downwind to the west and with the deposition of pyroclastic surges only in the summit.

2.2.2 The present unrest phase (1996 – 2013)

After the 1864-1866 eruption, no volcanic magmatic activity has been recorded. A few strong fumarolic emissions were reported in local newspapers during the year 1920 and in 1950-60 (Tassi et al., 2004b). In 1996, a progressive increase in seismic activity and in the fumarolic emission from the summit craters interrupted this period of quiescence. The outlet temperature of crater fumaroles was buffered at T= 95°C (approximately the water boiling temperature at 3000m) because of the abundant rainfall feeding the shallow aquifer (Martini et al., 2010). This stage continued until the

year 2001, when a further increase in fumarolic activity and in the concentration of magmatic gases (i.e. SO_2, HCl and HF) was observed (Tassi et al., 2004; Vaselli et al., 2010). No significant variation in fumarolic output temperature was measured. In June 2005, new fumaroles with outlet temperatures of ~90°C appeared along Ariete Fault (Martini et al., 2010; Vaselli et al., 2010). During spring and summer 2007, two important seismic swarms were recorded. In July, the maximum seismic activity to date, with 2000 event/day, for several days, was recorded (Martini et al., 2010). At the same time, the widening of the fumarolic field was accompanied by a strong increase in fumarolic emissions, forming a plume that rose 2km in the atmosphere (OVSICORI-UNA, 2007). In 2008, fumarolic temperatures at the bottom of the West Crater increased from 88 to >270°C and SO_2 flux increased by three order of magnitude (from 1 t/d in 2002 to >1000 t/d in 2008; OVSICORI-UNA, 2008). The interaction of acid gases with steam produced acid rains, mainly in the west sector of the volcano, that burned the vegetation and strongly affected settlements and infrastructures downwind to the plume (OVSICORI-UNA, 2007, 2008; Martini et al., 2010). On 5 January 2010, a phreatic explosion occurred at the West Crater with the emission of ashes that reached a distance of 35 km WSW from the vent (OVSICORI-UNA, 2010). The explosion created a 55x20m vent in the western rim of the West Crater that emitted steam and gas with an output temperature of ~600°C (OVSICORI-UNA, 2010). In the spring of 2011, a new vent opened on the north side of the bottom of the West Crater (OVSICORI-UNA, 2012), and the temperature of the emitted gas reached more than 610°C. Phreatic explosions from a new vent produced, at the beginning of January 2012, two small ash emissions (on 12th and 18th) for several hours. Gas temperature from the new vent was in the range of 700-765°C, and at the end of 2012 it reached a value of 805°C (OVSICORI-UNA, 2013). On 21 May 2013 another intense gas discharge episode occurred from both 2010 and 2012 vents, followed by a peak in seismic activity reached in July (>600 events/day; OVSICORI-UNA, 2013). Since August 2013 a decrease in seismicity and gas temperature from the 2012 vent was registered (from ~800°C to ~600°C; OVSICORI-UNA, 2013).

2.3 **Field sampling**

Rock samples were collected during in March 2011. In total, 45 rock samples were collected from units belonging to the last 10ka activity, following the stratigraphic description of Reagan et al. (2006). 21 of these samples were chemically analyzed for major and trace elements. Particular attention was given to olivine-bearing rocks in order to select samples suitable for noble gas analyses in fluid inclusions hosted in crystals (see Chapter 3). In some key outcrops detailed

stratigraphic sections were described. Samples were collected in the summit area and also on the flanks of the volcano: *Fig. 2.5* shows the location of sampling sites on the volcano; *Table 2.1* shows samples characteristics and coordinates.
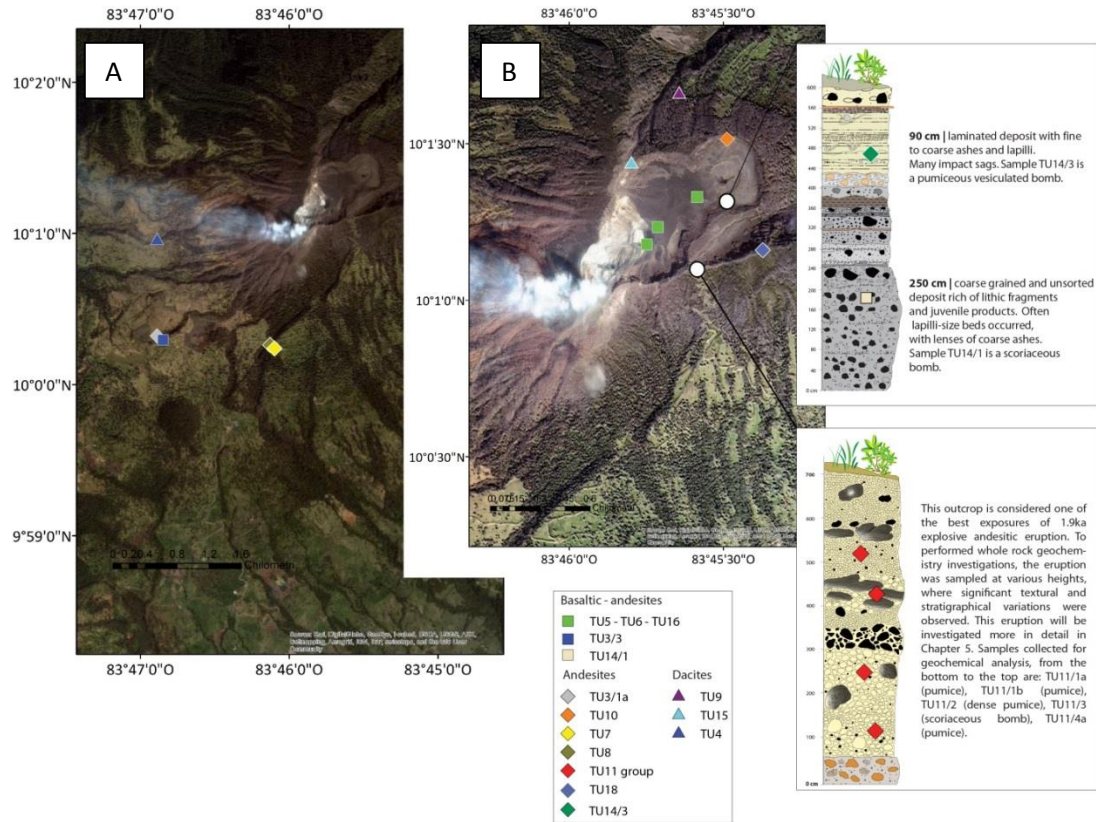
Fig. 2.5 – Location map of samples collected in 2011 at Turrialba volcano. Eruptive products were sampled on the flanks of the volcano (A) and at its summit area (B). The insets on the right are two of the studied stratigraphic sequences.

In the Crater Terrace sector, samples belonging to the last eruptive phase of 1864-66 A.D. were collected (TU5 – TU6 – TU16). They are dense (TU16) or scoriaceous (TU5-TU6) bombs emitted in the Vulcanian stage of the eruption, some with breadcrust morphology. They display porphyritic texture with phenocrysts of plagioclase, clinopyroxene and olivine. The key outctrop representative of this eruption was identified in the Cerro San Carlos sector; a stratigraphic study and a textural characterization of product related to this outcrop will be presented in Chapter 5. Xenoliths were observed in some samples. Also in this sector, between Central and NE Crater, dense bombs and ashes that should be related to historical activity (i.e. Unit 3 and 2, of Reagan et al., 2006) were also collected.

14

At the edge of the craters terrace, in the NE rim sector, three different lava flows were sampled (TU9 – TU10 – TU15). Sample TU9 belongs to a porphyritic lava flow sampled along the path descending toward NE from the top of the volcano; it contains phenocrysts of plagioclase clino- and orthopyroxenes with rare olivine. Sample TU10 was collected on the edge of the NE crater rim; at is porphyritic with plagioclase as the dominant phenocryst and could belong to the ~9 ka effusive activity described by Reagan et al. (2006). The last sample collected in this area, TU15, comes from a plug of lava showing a fluidal texture and a high density of xenoliths.

In the Radio Station sector, at the end of the road climbing up to the top of Turrialba volcano, we sampled and investigated in detail the deposits of the only Plinian eruption recently occurred at Turrialba, dated 1.9 ka. A detailed stratigraphic section describing the depositional succession of the eruption is reported in Chapter 5. This is considered one of the best exposure of the deposits of this eruption and displays an alternation of layers made of clasts with different density: from pumice to scoriaceous bombs and/or dense juvenile blocks.

Tab. 2.1 – Location and description of the collected Turrialba rocks

Sample	Sector	Coordinates	Altitude	Typology	Description	Age	Eruptive Unit
TU5	Crater Terrace	N10°01.191′ W083°45.732′	3175 m	Spatter scoria	Vesiculated and scoriaceous bomb, porphyric.	1864-66 A.D.	1864-66 A.D.
TU6	Crater Terrace	N10°01.192′ W083°45.674′	3174 m	Bomb	~150cm diameter, porphyric breadcrust bomb with xenoliths.	1864-66 A.D.	1864-66 A.D.
TU16	Crater Terrace	N10°01.517′ W083°45.577′	3198 m	Bomb	Porphyric dense bomb	1864-66 A.D.	1864-66 A.D.
TU14/1	Crater Terrace	N10°01.279′ W083°45.442′	3226 m	Bomb	Scoriaceous bomb with phenocrysts of plg	1.4ka	3[1] ?
TU14/3	Crater Terrace	N10°01.279′ W083°45.442′	3331 m	Bomb	Pomiceous bomb, highly vesiculated with dominant plg phenocrysts	< 1.4ka	2[1] ?
TU9	Rim NE	N10°01.589′ W083°45.654′	3106 m	Lava	Aletered porphyric lava flow with plg + cpx and rare olivines.	~9.3ka	8b[1] ?
TU10	Rim NE	N10°01.461′ W083°45.391′	3183 m	Lava	Porphyric lava with mm-size plg crystals	9 - 9.3ka	8a[1] ?
TU15	Rim NE	N10°01.517′ W083°45.483′	3210 m	Lava	Slightly altered vertical lava plug with many xenoliths	?	?
TU11 group	Radio Station	N10°01.084′ W083°45.572′	3282 m	Pumices / Bombs	cm-size creamy pumices and m-size scoriaceous bombs	1.9ka	4[1]
TU18	Radio Station	N10°01.124′ W083°45.467′	3320 m	Lava	Massive porphyric lava flow with plg and cpx	9 - 50ka	9[1]
TU3/1	Finca Retiro	N10°00.742′ W083°47.034′	2665 m	Lava	massive lava flow with autobreccia at top, mm-size plg and cpx	~10ka	?
TU3/3	Finca Retiro	N10°00.742′ W083°47.034′	2665 m	Scoriae	Black to red scoriae with dmed 1cm and Dmax 5 cm	3 - 10ka	?
TU4	Finca Retiro	-	-	Lava	Massive porphyric lava flow with plg phenocrysts and olivines	3±3ka[2]	La Picada
TU7	Ariete Fault	N10°00.282′ W083°46.106′	2800 m	Lava	Massive porphyric lava flow with cm-size plg crystals and ol	3 - 10ka	?
TU8	Ariete Fault	N10°00.326′ W083°46.139′	2787 m	Lava	Porphyric lava flow slightly vesiculated with plg, cpx and ol crystals	3 - 10ka	?

(1) Eruptive Units and age by Reagan et al. (2006)
(2) Age determined with $^{40}Ar/^{39}Ar$ dating by Ruiz et al. (in press)

Samples have porphyritic structure with abundant plagioclase and clinopyroxene. In the same sector a massive porphyritic lava flow was also sampled (TU 18).

Near the Ariete Fault watershed, two massive lava flows were also sampled (samples TU7 and TU8). They have a porphyritic structure with plagioclase as the dominant phenocryst phase, clinopyroxene and rare olivine. TU7 lava flow is N160° oriented, dipping toward WSW with an

angle of ~5-10°. The lava shows at least three different flow units, with a scoriaceous surface at the top of the deposit. Lava flow TU8, dipping toward N, is massive and shows slight vesiculation.

In Finca Retiro sector, along the western flank of the volcano (*Fig. 2.5*), a pyroclastic succession and a lava flow were sampled. A stratigraphic section (TU3) was measured and sampled along this very well preserved outcrop cut by the road. This succession of volcanic products overlays a porphyritic lava flow (TU3/1), containing phenocrysts of plagioclase and showing an irregular autobreccia at the top. The lava flow is covered by 10-30 cm of grey to blue thin ash beds mm- to cm-thick and interpreted as pyroclastic surge deposits. This unit is overlapped by a ~150 cm-thick sequence of alternating black to red scoriae, yellow pumices and varicolored ashes among which it is easy to recognize a layer of black and reddish scoriae with a $D_{med} = 1$ cm and $D_{MAX} = 4 - 5$ cm, highly vesiculated, with phenocrysts of olivine. The succession continues with an alternation of ash layers and thick carbon rich paleosoils up to the products of the 1.9 ka eruption.

2.4 **Whole rock geochemistry: results**

2.4.1 Analytical methods

Major and trace-element analyses have been performed on whole rock at Activation Laboratories Ltd. (Actlabs - Canada) using ICP-MS technical procedures (www.actlabs.com): molten rock samples were diluted and analyzed by Perkin Elmer Sciex ELAN 6000, 6100 or 9000 ICP/MS. Three blanks and five controls (three before sample group and two after) were analyzed per group of samples. Instrument were recalibrated every 40 samples. The analytical uncertainty varies between 0.001 and 0.01% for major and trace elements. Chemical analyses on minerals were performed at High Pressure and High Temperature Laboratory of Istituto Nazionale di Geofisica e Vulcanologia (INGV), Sezione di Roma-1, by using an Electronic Probe Micro Analysis (EPMA) Jeol-JXA8200 combined with EDS-WDS (five spectrometers with twelve crystals). For glasses, a slightly defocused electronic beam with a size of 1μm was used with a counting time of 5 sec on background and 15 sec on peak. For crystals, the beam size was 5μm with a counting time of 20 and 10 s on peaks and background, respectively.

Sr and Nd isotope analyses were performed on powdered whole rock at the Department of Earth Science of the University of Florence, following the methodology described in Avanzinelli et al. (2005). Samples were prepared dissolving the powder in successive HNO_3-HF and HCl 6N treatments. Sr and Nd isotopes were analyzed by Thermal Ionization Mass Spectrometry (TIMS)

with a Triton-Ti® as spectrometer equipped (Thermo Finnigan). Typical within-run precision (2σ) for Sr and Nd was ±0.000005 for both isotopes. Analyses of standard SRM987 for Sr-isotope measurements give a mean value of $^{87}Sr/^{86}Sr$ = 0.710248, with 2σ = ±0.000015. For Nd-isotopic ratio were used NiFi standard, that produced a mean value of $^{143}Nd/^{144}Nd$ = 0.511467, with 2σ = ±0.000008.

2.4.2 Nomenclature and classification

The volcanic rocks of Turrialba form a straight calc-alkaline suite in the AFM triangular diagram of Irvine & Baragar (1971; *Fig. 2.6a*). Only one sample (TU3/3) shows a marked increase in FeO$_{tot}$/MgO, falling in the limit between calc-alkaline and tholeitic field. We observed however that the TU3/3 sample displays an high degree of alteration, with the highest L.O.I. value (4.27 wt %; see *Tab. 2.2*) and we attribute its offset position to its high degree of alteration. In order to avoid possible errors in the classification and geochemical trends, samples with L.O.I. > 2.5 wt% (including therefore sample TU3/3) were discarded. The enrichment in potassium shown by the most evolved samples, places part of Turrialba magmatic series into the high-K calc-akaline field. On the basis of SiO$_2$ and alkali contents, these rocks show an evolution from basaltic-andesite to dacite, with a small compositional gap between 60 to 63 wt % of SiO$_2$ (*Fig. 2.6b*).
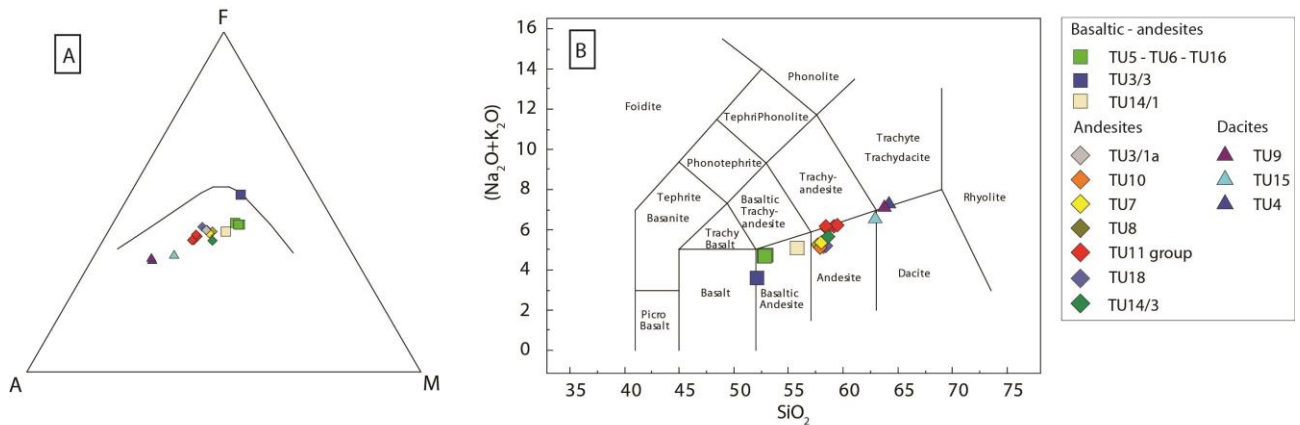
Fig. 2.6 – A) AFM classification diagram (after Irvine and Baragar, 1971) and B) Total Alkali versus Silica classification diagram (after Le Bas, 1986) for the analyzed Turrialba rocks.

2.4.3 Petrography and Mineral chemistry

The petrography of Turrialba rocks was described by Soto (1988) and Reagan et al. (2006) but no detailed investigation on mineral chemistry of the rocks was ever published. Here for the first time, together with a petrographic characterization of the volcanic series, we present and discuss results of chemical analyses performed on minerals from selected samples. Representative microprobe analyses of the selected crystals are contained in *Appendix 1*. In *Fig. 2.7* the textural characteristics of some selected samples representative of the magmatic series are illustrated. Classification of the analyzed minerals is shown in *Fig. 2.8*.
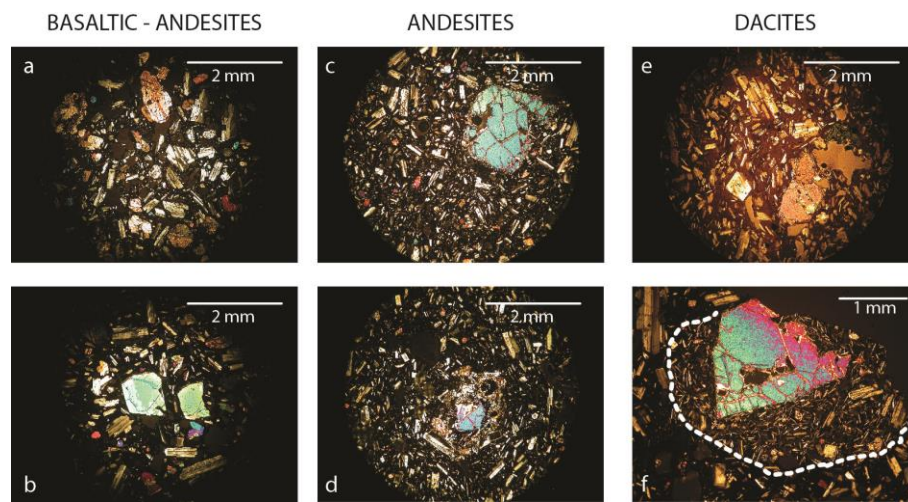
Fig. 2.7 – Microphotographs of some selected samples: a) TU5 basaltic-andesite; b) TU16, basaltic-andesite; c) TU7, andesite; d) TU8, andesite; e) TU4, dacite; f) TU15, dacite (the dotted white line indicates a mafic enclave with olivine).

Basaltic-andesites: black scoriae and bombs display vesicular to massive porphyritic structures (*Fig. 2.7a,b*), with plagioclase (>20 vol %), clinopyroxene (10 – 15 vol %), olivine (5-10 vol. %) and magnetite as the main mineral phases and a microcrystalline groundmass. Plagioclase crystals display a broad range in anorthite contents (An47 to An70) (*Fig. 2.8*). Clinopyroxenes are augitic and have an homogeneous composition (*Fig. 2.8*). Olivine composition ranges from Fo70 to Fo84, the higher Fo contents being found in the cores of large crystals of scoria samples that display normal zoning, with more fayalitic rims (Fo 70 – 73; *Fig. 2.8*).

Residual glasses from scoriae and bombs range from trachy-andesite to rhyolite in composition, with the more evolved compositions pertaining to the more crystalline volcanic bombs.
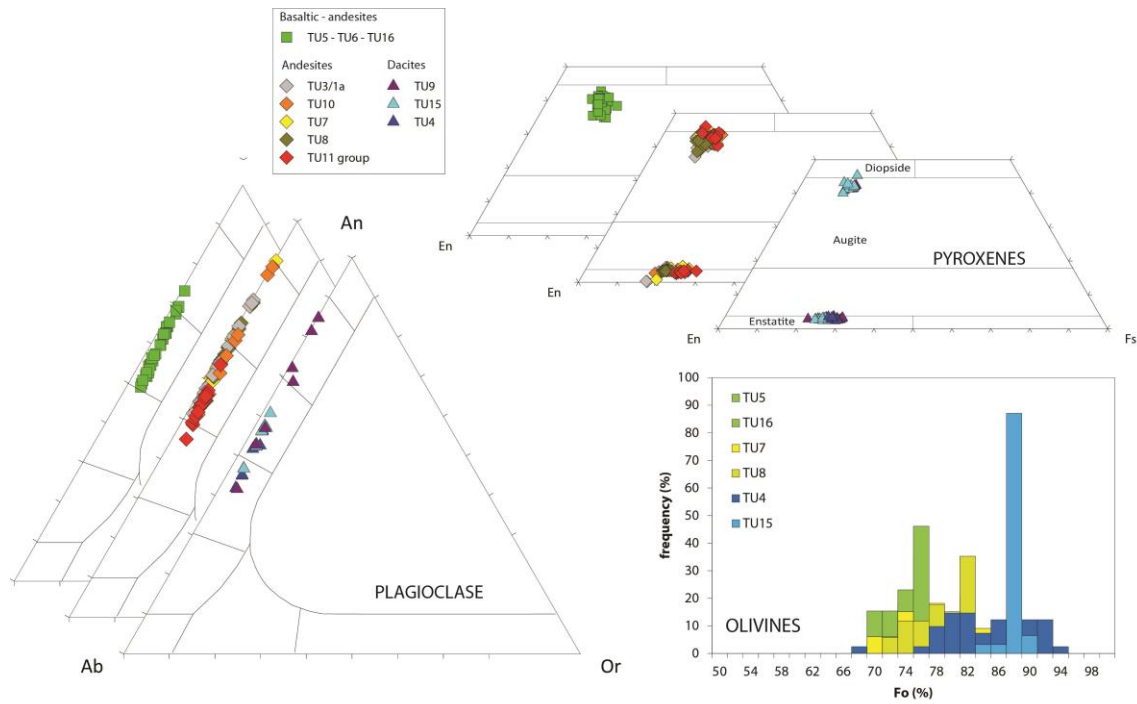
Fig. 2.8 - Classification diagrams of the main mineralogical phases found in Turrialba rocks: clockwise, pyroxenes ternary diagram; olivine forsteritic mole percentage (Mg/[Mg + Fe], expressed as Fo%) and frequency of single crystals analyzed; plagioclase ternary diagram.

Andesites: the analyzed samples are strongly porphyritic (up to 50 vol. %) massive lavas, and pumices with crystallinity of 25 - 30 vol % (*Fig. 2.7c,d*). Phenocrysts of plagioclase are always ehuedral and display a wide An content, ranging from anorthitic to andesine composition. All the analyzed phenocrysts display a strong chemical zonation with calcium-rich cores (An71 – An90) and less anorthitic rims (An59 – An48; *Fig. 2.8*). In samples TU7 and TU8 only few crystals show reverse zoning with sodic-rich cores (An51 – An61; *Fig. 2.8*) and more anorthitic rims (An67 – An74; *Fig. 2.8*). In contrast, microphenocrysts and microlites display more homogeneous anorthite contents between An53 and An64. Andesite samples contain both clinopyroxenes and orthopyroxenes in different amounts. Euhedral phenocrysts of clinopyroxenes (cpx) are diopsidic to augitic in composition (Wo_{39-44} En_{43-50} Fs_{8-13}; *Fig. 2.8*); cpx occurs also as microlites in the groundmass. Orthopyroxenes are less frequent as phenocrysts and are present essentially as microphenocrysts or microlites. Their average composition is En= 71 – 82% (*Fig. 2.8*), and they occur also in glomerophyric aggregates in association with clinopyroxenes and olivine. Some samples contain olivine crystals (in particular TU7 and TU8), with fractures and altered rims, sometimes with orthopyroxene crowns. Phenocrysts show normal zoning with Fo80-81 cores and Fo77-61 rims (*Fig. 2.8*); the smallest crystals show compositions ranging between Fo81 and Fo68.

In TU10 rare crystals of olivine Fo79 were found; they displayed skeletal shape and highly altered rim. Abundant magnetite occurs also as phenocryst, while apatite and ilmenite are found as inclusions within other crystal phases in certain andesites. Residual glass of andesites samples are dacitic to rhyolitic in composition.

Dacites: these lava samples are highly porphyritic (40-50 vol. %) with microcrystalline to cryptocrystalline groundmass (*Fig. 2.7e,f*). At times fluidal textures are observed and some analyzed samples contain xenoliths. Plagioclase is the dominant phase, with ehuedral crystals some of which displaying dense sieved textures. Phenocrysts are generally An60 – An46 in composition, but the sample TU9 contains also crystals with stronger normal zoning (cores An84 – An72; rims An 52 – An39; *Fig. 2.8*). Both clino- and orthopyroxene are found: crystals are generally ehuedral and in some sample they form glomerophyric aggregates. Clinopyroxene phenocrysts are augitic to diopsidic in composition (Wo_{40-45} En_{41-47} Fs_{10-13}; *Fig. 2.8*), while orthopyroxenes display an enstatitic content between 66 and 75%. TU4 dacite displays olivine xeno-phenocrysts >1 mm-size. The crystals present altered rims sometimes with orthopyroxene crowns and wide range of Fo in their cores (Fo94 – Fo76; *Fig. 2.8*). Sample TU15 is characterized by mafic enclaves with mm-size phenocrysts of olivine, commonly fractured and with Mg-rich cores (Fo90 – Fo82). The composition of these olivines is very rich in Mg with a narrow variation in forsterite as displayed in *Fig. 2.8*. The groundmass is cryptocrystalline and made of abundant plagioclase, clinopyroxenes and olivines.

2.4.4 Major and trace elements chemistry

18 samples of lavas, bombs and pumices erupted in the last 10 ka of activity, forming a compositional range from basaltic-andesite through andesite to dacite, have been analyzed for major and trace elements;the results are reported in *Table 2.2*. The analytical uncertainty varies between 0.001 and 0.01% respectively for major and trace elements.

Binary Harker variation diagrams of major elements show negative trends for TiO_2, Al_2O_3, Fe_2O_3, MnO, MgO, CaO and P_2O_5 and positive trends for Na_2O and K_2O (*Fig. 2.9*). Trends are always linear except for slight variations in and K_2O where andesites TU7, TU8, TU18 and TU3/1 appear slightly depleted if compared to other samples with similar silica content. The andesites TU7, TU8, TU18 and TU3/1 also appear to have a higher alumina content with respect to the other Turrialba andesites. The implication for this anomalous behavior will be discuss in *paragraph 2.5.3*. Basalts display a high content in Al_2O_3 (16 – 18 wt %), a typical feature of volcanic arc magmas already reported by previous studies (e.g. high-alumina basalts by Kuno, 1960; Crawford et al., 1987).

Tab. 2.2 – Whole rock analyses of major and trace elements of Turrialba volcanic rocks.

Age		1864-66	1864-66	1864-66	14ka	< 14ka	~9.3ka	9 - 9.3ka	?	19ka	19ka	19ka	19ka	9 - 50ka	~10ka	3 - 10ka	3±3ka [2]	3 - 10ka	3 - 10ka
Sample		TU5	TU6	TU16	TU14/1	TU14/3	TU9	TU10	TU15	TU11/1A	TU11/2	TU11/3	TU11/4A	TU18	TU3/1A	TU3/3	TU 4	TU7/2B	TU8
SiO_2	%	53.20	52.97	53.07	55.37	58.49	64.15	57.79	62.76	58.55	59.28	57.89	58.15	58.68	57.95	50.06	64.22	57.15	57.86
Al_2O_3	%	17.31	17.21	17.24	16.87	16.08	16.89	17.61	16.29	16.77	16.56	16.45	16.59	18.18	17.85	18.03	16.04	17.48	17.76
$Fe_2O_3(T)$	%	8.26	8.34	8.26	7.21	6.62	4.71	6.74	5.04	6.18	6.19	6.50	6.64	6.55	6.39	9.11	4.73	6.74	6.52
MnO	%	0.13	0.14	0.14	0.12	0.11	0.09	0.12	0.09	0.11	0.11	0.11	0.12	0.11	0.10	0.13	0.09	0.10	0.10
MgO	%	5.83	6.17	6.09	5.20	4.84	2.07	3.89	2.90	3.63	3.59	3.82	3.74	3.53	3.78	4.92	2.18	4.31	4.13
CaO	%	9.39	9.43	9.35	8.17	6.82	4.57	7.24	5.15	6.49	6.54	6.86	6.83	7.17	7.39	8.47	4.51	7.31	6.99
Na_2O	%	3.27	3.21	3.26	3.42	3.58	4.05	3.13	3.83	3.73	3.77	3.66	3.74	3.59	3.92	2.63	4.00	3.82	3.93
K_2O	%	1.47	1.44	1.43	1.60	2.17	3.15	2.10	2.76	2.35	2.38	2.31	2.35	1.62	1.18	0.80	3.35	1.38	1.40
TiO_2	%	1.04	1.05	1.04	0.91	0.85	0.64	0.77	0.62	0.84	0.85	0.91	0.91	0.71	0.71	1.50	0.65	0.84	0.83
P_2O_5	%	0.39	0.35	0.35	0.30	0.29	0.21	0.24	0.22	0.30	0.31	0.33	0.35	0.25	0.25	0.27	0.22	0.25	0.25
Total	%	100.6	100.8	100	99.16	100.2	100.5	99.62	100.6	99.59	99.95	99.26	100.1	100.7	99.88	100.2	100.5	99.37	100.5
LOI	%	0.26	-0.05	-0.20	0.00	0.35	0.00	0.00	0.89	0.64	0.37	0.40	0.69	0.26	0.36	4.27	0.51	0.00	0.76
Sc	ppm	26	27	27	22	18	9	17	11	17	17	18	18	14	15	30	10	18	17
Be	ppm	1	1	1	1	1	2	2	2	2	1	1	2	< 1	< 1	1	2	3	1
V	ppm	229	231	230	203	171	99	173	117	162	165	175	180	160	168	195	101	181	177
Ba	ppm	667	654	650	669	846	1117	805	993	904	921	890	901	692	681	474	1221	767	785
Sr	ppm	802	794	825	854	738	716	1014	729	740	743	790	743	1072	1000	848	610	926	902
Y	ppm	23	17	18	15	15	19	15	15	17	18	18	19	11	10	21	19	16	11
Zr	ppm	149	143	141	137	184	236	155	207	202	205	198	201	93	89	139	273	111	102
Cr	ppm	120	140	140	110	140	20	40	70	60	60	60	60	< 20	50	90	40	60	50
Co	ppm	28	30	30	26	23	12	22	15	19	19	20	20	20	21	31	14	24	24
Ni	ppm	50	60	50	50	70	< 20	40	30	30	30	30	30	40	50	< 20	50	40	40
Cu	ppm	70	100	100	70	90	50	80	60	80	80	80	70	50	100	120	50	110	70
Zn	ppm	60	80	80	80	70	60	70	60	70	60	70	60	60	70	80	60	70	60
Ga	ppm	17	18	18	18	18	18	19	17	18	18	18	17	20	19	20	17	18	18
Ge	ppm	1	2	2	2	2	2	1	2	1	2	2	2	1	1	2	2	1	1
Rb	ppm	27	28	29	33	48	72	41	64	53	56	52	48	27	19	20	82	26	26
Nb	ppm	13	13	14	13	17	18	11	16	18	20	20	18	6	6	19	23	9	8
Ag	ppm	0.8	0.8	0.9	0.8	1.2	1.6	0.8	1.3	1.1	1.4	1.2	1.2	0.6	0.6	0.9	1.8	0.6	0.5
La	ppm	32	32.9	32.8	29.7	36.7	45.9	30.1	37.5	40.3	40.9	42.3	38.6	15.6	20.1	26.5	50.7	27.6	23
Ce	ppm	62.6	67.1	66.1	58	68.8	83.4	58.2	68.6	75.4	76.8	79.9	72.9	31.3	37.9	54.4	91.1	52.7	43.6
Pr	ppm	7.62	7.78	7.9	6.83	7.73	8.93	6.68	7.39	8.43	8.74	9.02	8.13	4.03	4.52	7.02	9.86	6.23	5.15
Nd	ppm	29.6	31.6	30.9	25.9	28.6	31.1	25.1	26.3	31	31.4	33	30.8	15.9	17.4	28.6	33.5	23.8	20.5
Sm	ppm	5.6	6	5.8	4.8	5.1	5.2	4.8	4.4	5.5	5.5	5.9	5.3	3.3	3.3	6.2	5.9	4.3	3.9
Eu	ppm	1.56	1.67	1.6	1.27	1.28	1.21	1.29	1.08	1.42	1.39	1.51	1.32	1.06	0.97	1.76	1.34	1.18	1.17
Gd	ppm	4.4	4.9	4.5	3.6	3.6	3.9	3.7	3.3	4	4.2	4.4	4	2.8	2.4	5	4.4	3.6	3
Tb	ppm	0.6	0.7	0.6	0.5	0.5	0.6	0.5	0.5	0.6	0.6	0.6	0.6	0.4	0.3	0.7	0.6	0.5	0.4
Dy	ppm	3.3	3.8	3.5	2.8	3	3.2	2.8	2.7	3.3	3.4	3.3	3.2	2.2	1.7	4	3.4	3	2.3
Ho	ppm	0.6	0.7	0.7	0.6	0.6	0.6	0.5	0.5	0.6	0.6	0.6	0.6	0.4	0.3	0.8	0.7	0.6	0.4
Er	ppm	1.8	2	1.8	1.5	1.6	1.8	1.4	1.5	1.7	1.8	1.8	1.7	1.1	0.9	2	1.9	1.6	1.1
Tm	ppm	0.25	0.28	0.26	0.21	0.23	0.27	0.22	0.22	0.26	0.25	0.26	0.25	0.16	0.13	0.27	0.29	0.22	0.16
Yb	ppm	1.6	1.9	1.7	1.4	1.6	1.8	1.4	1.6	1.8	1.7	1.8	1.6	1	0.9	1.7	2	1.4	1
Lu	ppm	0.25	0.3	0.28	0.23	0.27	0.31	0.22	0.28	0.33	0.29	0.31	0.28	0.17	0.14	0.26	0.32	0.21	0.17
Hf	ppm	3	3.2	3.1	3	4	4.8	3.5	4.6	4.2	4.4	4.4	3.9	2.3	2	3.1	5.6	2.4	2.3
Ta	ppm	0.7	0.7	0.7	0.7	1	1.2	0.6	0.9	1.1	1.1	1.2	1	0.3	0.3	1.1	1.4	0.5	0.4
W	ppm	7	7	8	7	6	8	6	7	7	6	5	10	8	5	5	21	15	16
Pb	ppm	< 5	< 5	< 5	5	6	10	7	8	7	5	7	6	6	< 5	< 5	9	5	< 5
Th	ppm	5.3	5.1	5.3	6.6	9.2	15.5	9	12.8	10.1	10.2	9.9	9.4	3.1	2.3	3.6	15.9	4.1	3.1
U	ppm	1.8	2	1.8	2	3.1	4.7	2.6	4	3.3	3.5	3.3	3.1	1.3	0.9	1.1	5.4	1.3	1.2
$^{87}Sr/^{86}Sr$		0.703663	0.703678	0.703666					0.703593								0.703654	0.703621	0.703612
2 s.e.		±0.000005	±0.000005	±0.000005					±0.000006								±0.000005	±0.000005	±0.000005
$^{143}Nd/^{144}Nd$		0.512963	0.512960	0.512963					0.512967								0.512966	-	0.512968
2 s.e.		±0.000011	±0.000006	±0.000005					±0.000005								±0.000005	±0.000005	±0.000006

The progressive decrease of Fe_2O_3, MgO, CaO and MnO, from basalt-andesitic to dacitic samples is due to the crystallization of olivine and pyroxenes (clino- and ortho-). Plagioclase crystallization results in a decrease of Al_2O_3 with magma evolution, while the observed decrease in P_2O_5 is due to apatite crystallization. Magnetite and Ilmenite crystallization contributes to the decrease respectively of Fe_2O_3 and TiO_2 content from mafic to felsic eruptive products.

Trace elements variation diagrams display larger variations, and different trends can be envisaged (*Fig. 2.10*). In particular HFSE elements (Zr and Hf, and to a lesser extent Nb) display smooth positive correlation trend if plotted against SiO_2, except for a specific group of andesitic samples (TU7, TU8, TU10/1, TU3/1a, TU18) that fall systematically outside these trends due to the lower HFSE contents. Same behavior can be observed also for Y, although in this case the scattering complicates the interpretation of the data. LILE elemenst (Rb, Ba and Cs or Pb, not shown) are characterized by steeper positive correlation, while Sr display a quite linear negative correlation, if we exclude the group of andesitic samples with higher Sr contents.
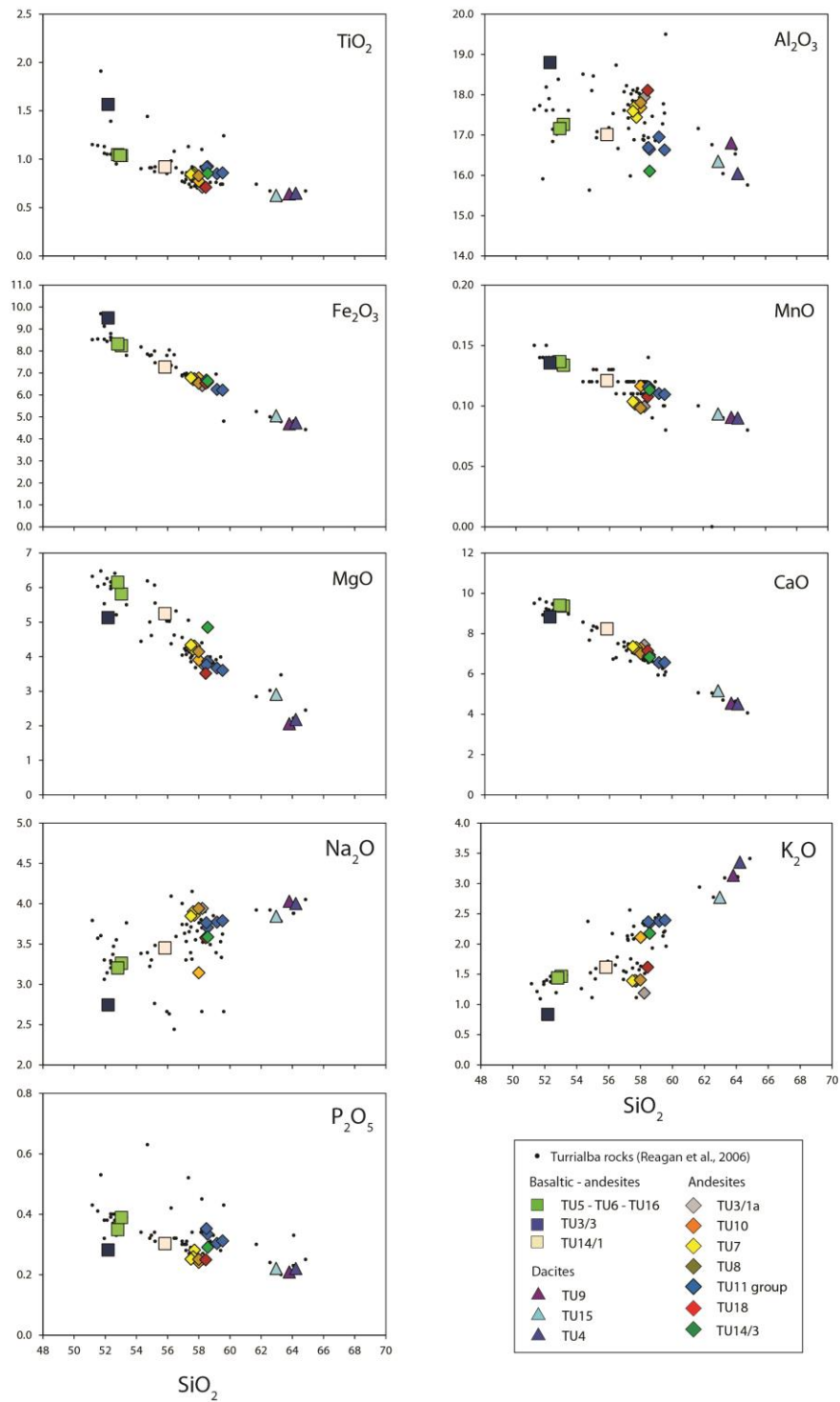
Fig. 2.9 – Major elements variation diagrams for Turrialba rock samples. Data are expressed in wt. % and are plotted on water-free basis.

In general, all LILE and HFSE elements investigated behave as incompatible elements, with the exception of Sr, substituting for Ca in plagioclases. The linear correlation among all samples suggest their cogenetic origin. The small group of andesite (TU7, TU8, TU10/1, TU3/1a, TU18), present clearly different values of trace elements, in particular they are depleted in all HFSE elements and in Rb and Th, but enriched in Ba and Sr, suggesting a different origin for this groups of samples. It must be noted that xenocrysts and enclaves of different origin may alter the overall composition of the rock. Xenocrysts of olivine and clinopyroxenes have been observed only for dacitic samples, however, and the trends that we observe in *Fig. 2.10* are not substantially modified by the presence of these cumulates. The peculiar trace elements content of the group of andesites reported above must therefore have another explanation.
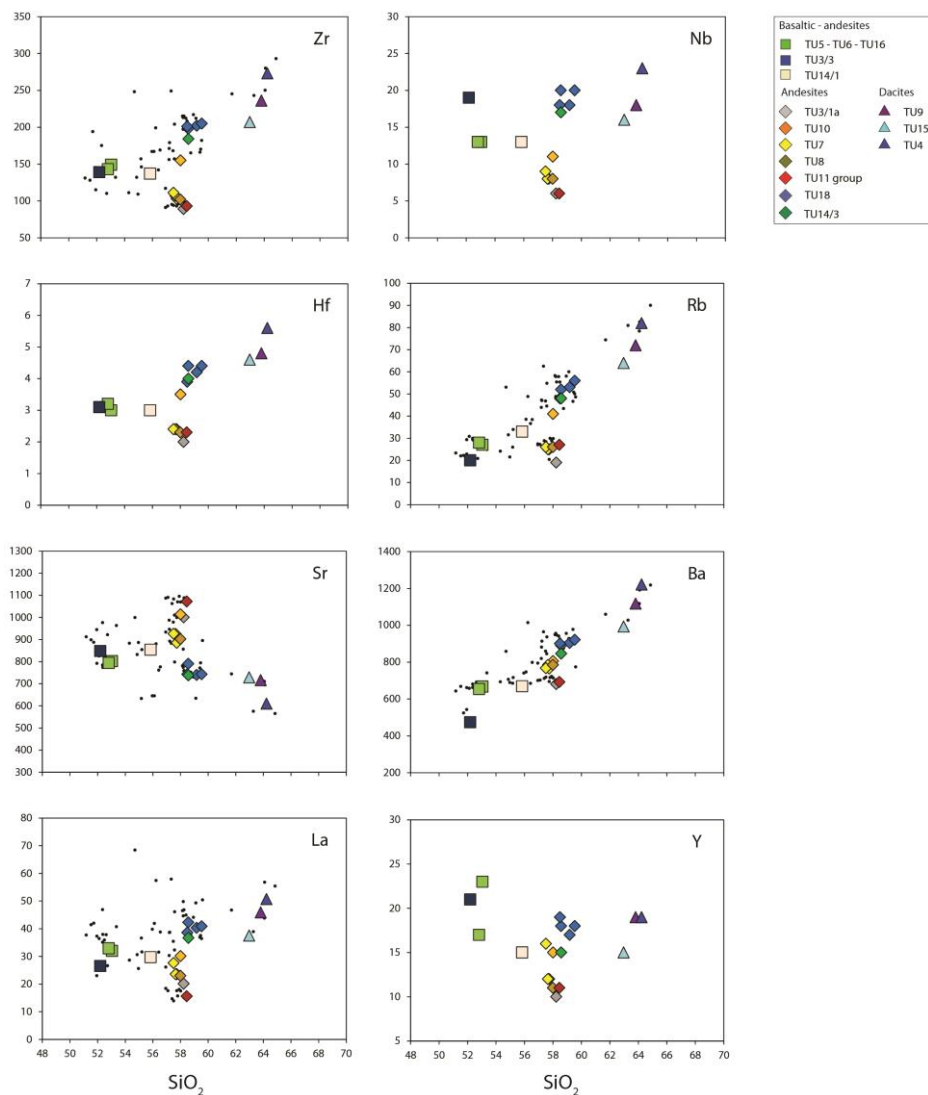

Fig. 2.10 – Trace elements variation diagrams for Turrialba rock samples. Data are expressed in ppm.

Mantle normalized (Sun and McDonough, 1989) incompatible trace element patterns of a representative suite of samples of Turrialba rocks are presented in *Fig. 2.11*. In the diagram, the elements are reported with degree of incompatibility increasing from right to left. The diagram shows a behavior typical of subduction-related magmas (e.g. Aeolian Island, see the inset in *Fig. 2.11*), as testified by the high concentrations of large-ion lithophile elements (LILE: i.e., Rb, Ba and K), Th and U, light rare-earth elements (LREE), and Sr relative to HFSE, such as Nb, Ta, and Ti, and heavy rare-earth elements (HREE) with significant Nb, Ta and Ti negative anomalies and positive anomaly in K.

A moderate fractionation between the basaltic-andesites and dacites can be observed in the spider diagram with a slight enrichment in Rb, Th, Ba and U, that could be ascribed to a progressive evolution from mafic magmas to dacitic by fractional crystallization. In the diagram, the average composition of basalts from mid ocean ridge (MORB) and ocean island basalts (OIB) (Sun & McDonough, 1989) are also reported for comparison.
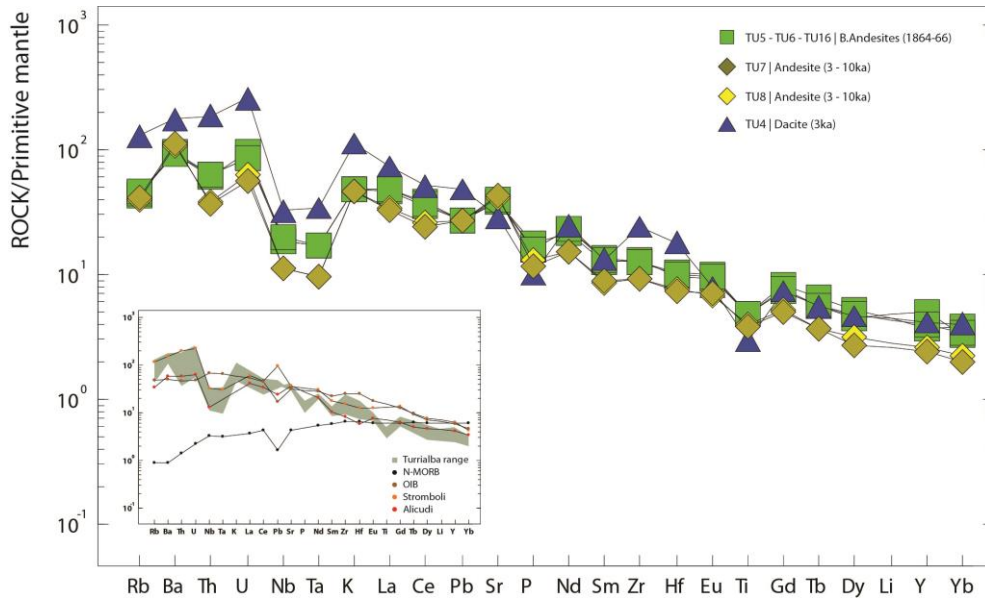

Fig. 2.11 – Mantle normalized trace elements patterns for Turrialba rocks. OIB and N-MORB average compositions and normalization values are from Sun and McDonough (1989). The inset shows the comparison between the Turrialba trace elements range (gray shaded), OIB and N-MORB magmas and two volcanic arc rocks: Alicudi and Stromboli. This two volcanoes represent respectively the most primitive and the most contaminated magma of the same volcanic arc system (data from Francalanci et al., 1993). Normalization factors and data for OIB and N-MORB magmas from Sun and McDonough (1989).

As it can be observed from *Fig. 2.11*, the overall trace elements pattern indicates a more complex source for these magmas, with a clear contribution of a OIB component; for example, ratios

between HFS elements in the most mafic samples (e.g. Zr/Nb = 10.0 – 11.4; Nb/Ti = 0.0020 – 0.0022) are more similar to those of OIBs (Zr/Nb = 5.9 – 14.5; Nb/Ti = 0.0011 – 0.0027; Frei and Clague, 1983; Chey and Frey, 1985) than to normal MORBs (Zr/Nb = 27; Nb/Ti = 0.00033; Sun, 1980), as observed also by Reagan and Gill (1989).

Chondrite-normalized (Sun & McDonough, 1989; *Fig. 2.12*) REE patterns show similar trend for all the samples studied, with fractionation of light LREE (La$_n$/Sm$_n$= 3.6 – 5.4) and nearly horizontal HREE, suggesting the absence of garnet at source. The LREE enrichment is between 40 - 100 in Turrialba basaltic-andesites and is in agreement with enrichment values observed for subduction-related magmas. The insets (*Fig. 2.12*) show the comparison between the patterns of Turrialba trace elements range (gray shaded), OIB and N-MORB magmas and two volcanic arc rocks: Alicudi and Stromboli (Italy). These two volcanoes represent respectively the most primitive and the most contaminated term of Aeolian volcanic arc (data from Francalanci et al., 1993). As we expect, Turrialba trace elements display many common features with an OIB source, showing similar characteristics with the Aeolian arc magmatism (e.g. Alicudi and Stromboli).
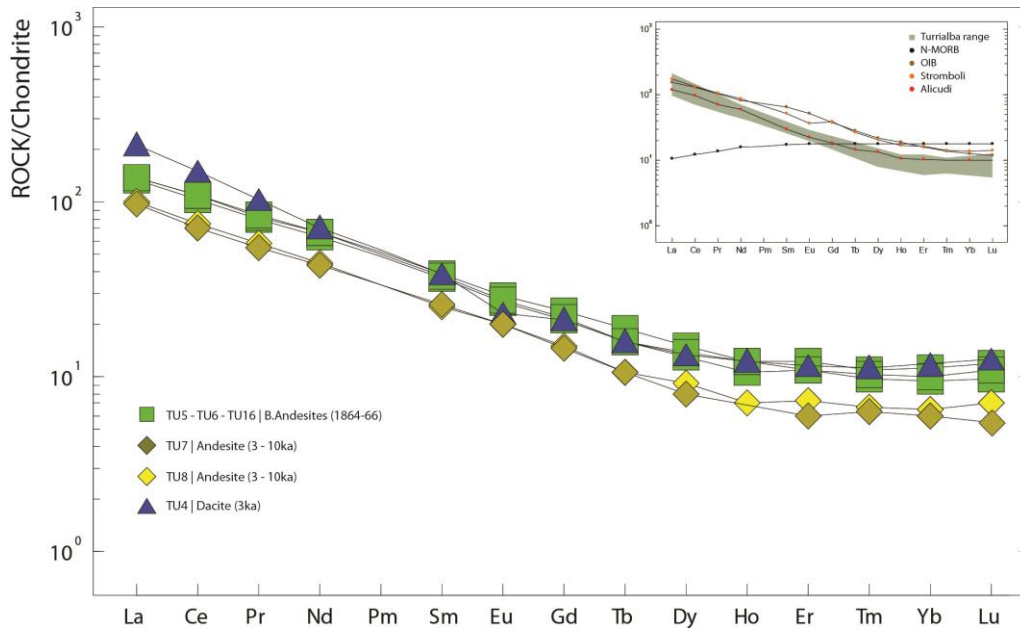

Fig. 2.12 – Chondrite-normalized REE patterns for the selected Turrialba samples, showing the typical trend of a subduction-related volcanic series. Normalization factors and data for OIB and N-MORB magmas from Sun and McDonough (1989). For inset details see *Fig. 2.11*.

2.4.5 Sr and Nd isotope geochemistry

Sr and Nd isotopic ratios have been measured on some selected Turrialba rocks at the University of Florence and are presented in *Tab. 2.2*. $^{87}Sr/^{86}Sr$ ratios show slight variations, ranging from 0.703593 to 0.703678. The Nd isotope ratios ($^{143}Nd/^{144}Nd$) display also minor variations, ranging between 0.512960 and 0.512968. Basaltic-andesites (TU5 – TU6 – TU16) and dacite (TU4) samples have slightly higher $^{87}Sr/^{86}Sr$ values (0.703678 - 0.703654), with respect to the andesite samples (TU7 – TU8 (0.703593 – 0.703621) (*Fig. 2.13a*). In other words, the highest values of radiogenic Sr have been found in the most mafic samples among the analyzed rocks, whereas high-K andesites products show lower Sr ratio. In the context of the Costa Rica volcanoes, Turrialba rocks have a poorly radiogenic isotopic signature (*Fig. 2.13a*), forming the less radiogenic end-member of an unusual positive trend between Sr and Nd isotope composition in Central America (Feigenson & Carr, 1986). The Central America volcanic arc displays a relatively small variation in Sr and Nd isotope composition respect to other volcanic arcs of the world (*Fig. 2.13b*), such as Banda volcanic arc or Aeolian Island arc where wide Sr and Nd isotopic variations has been observed.
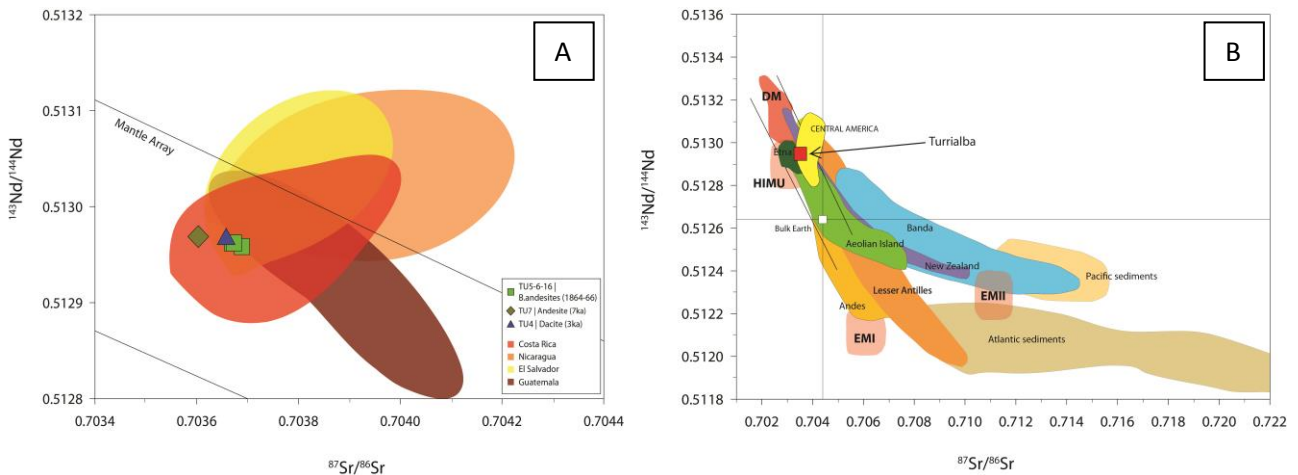
Fig. 2.13 – a) Variation diagram of $^{87}Sr/^{86}Sr$ isotope ratio against $^{143}Nd/^{144}Nd$ for Central America Volcanic Belt. Data from Costa Rica, Nicaragua, El Salvador and Guatemala are from Geochemical Database by Carr et al., available online at http://www.rci.rutgers.edu/~carr/ (DOI: 10.1594/IEDA/100263). b) Nd-Sr variation in some volcanic arc of the world, after Wilson (1989), Arculus and Powell (1986), Gill (1981), and McCulloch et al. (1994). Pacific sediments data are from Hauff et al., 2003; Atlantic sediments data are from White et al. (1985). DM, HIMU, EMI and EMII values are from Lustrino & Dalli (2005).

2.5 **Turrialba volcano in the geochemical framework of the volcanic front of Central America.**

As already observed in previous studies (e.g. Carr et al., 1990; Herrstrom et al., 1995; Patino et al., 2000), magma geochemistry of the Costa Rica subduction-related volcanoes is unusual both with respect to other volcanoes of the Central American Volcanic Front (CAVF) and to the compositional spectrum of the volcanic arcs magmatism on Earth. Magmas from the CAVF define regional and sometimes local geochemical trends, which reflect the variable influence of multiple mantle sources. The magmatic features vary from continental arc type, in Guatemala, to oceanic ones, in Nicaragua, and this suggests the influence of crustal contamination. The geochemical characteristics vary also along the volcanic front (e.g. Carr et al., 2003; Feigenson et al., 2004). Numerous mafic volcanics are found belonging to back-arc domains, unaffected by subduction-related fluids (e.g. Patino et al., 2000) and adakite magmatism can occurs in the southernmost termination of the arc. Regional variations are most clearly seen in element ratios that are nearly constant through the Cocos Plate sediment stratigraphy (Patino et al., 2000), suggesting that regional variations of these elements could be related to differences in intensity of the flux of the subducting slab. Isotopic data of Sr, Nd and Pb clearly reveal the influence of mixing trends between less and more radiogenic magmatic sources and crustal end-members. Turrialba volcano is located in this complex geological setting, lying in a key sector where significant geochemical and geodynamic variations occurred.

2.5.1 Bulk rock geochemistry insights: trace elements variations along the arc.

It has been observed that CAVF shows systematic variations in many geochemical tracers, which allow comparison with regions of high slab signal, to nearby regions of low slab signal (Carr et al., 1990; Morris et al., 1990; Leeman et al., 1994). For the study of the trace element variations along the arc, we selected the most mafic eruptive products of the arc ($SiO_2 < 54$ wt %; $MgO > 4$ wt %) from the "RU_CAGeochem" database (a free online database and sample repository for Central American volcanic rocks by Rutgers University). Ba/La ratio is appropriate for reviewing the regional variation in slab signal. The high Ba/La values observed in some regions along the CAVF are not surprising because the subducted sediments are highly enriched in Ba (Plank and Langimur, 1993; Patino et al., 2000). If plotted against latitude, the Ba/La ratio shows an asymmetrical chevron pattern (*Fig.2.15a*), with a peak in the contribution of sediment to the slab flux positioned in the central portion of the CAVF, in Nicaragua. By contrast, it falls nearly to the global minimum toward northwest and especially the southeast, in the terminal sector of the volcanic front that includes Turrialba. Indeed, Turrialba volcanic rocks display some of the lowest Ba/La ratios of the

entire CAVF, suggesting a light or negligible effect of fluids coming from sediments of the subducted slab, with values overlapping those from Galapagos OIB or Pacific MORB.

The concrete possibility of subduction of enriched-Ba sediments suggests that changes in the Ba/La ratio could be carried by the amount of subducted sediments. However, the regional variation is primarily driven by La (Carr et al., 2007). In *Fig. 2.15b* the La/Yb values with latitudes is shown; this variation suggests the different nature of the mantle source beneath different sectors of the volcanic chain. The mantle source seems to be strongly influenced by a MORB-like signature for volcanoes of Guatemala, El Salvador and northern Nicaragua, whereas an enriched mantle source (OIB-like signature) is dominant in the southernmost termination of the volcanic arc (part of Nicaragua and the entire Costa Rica). In particular Costa Rican volcanics display the most enriched characteristics, on the basis of their La/Yb ratio, of the entire volcanic arc.

Turrialba mafic volcanics are well in the range of the increase in La/Yb from the northern part of the arc, moving to the south, with values ranging between 17.3 and 20.0. La/Yb ratio indicates that more enriched sources are present beneath Costa Rica and Guatemala.
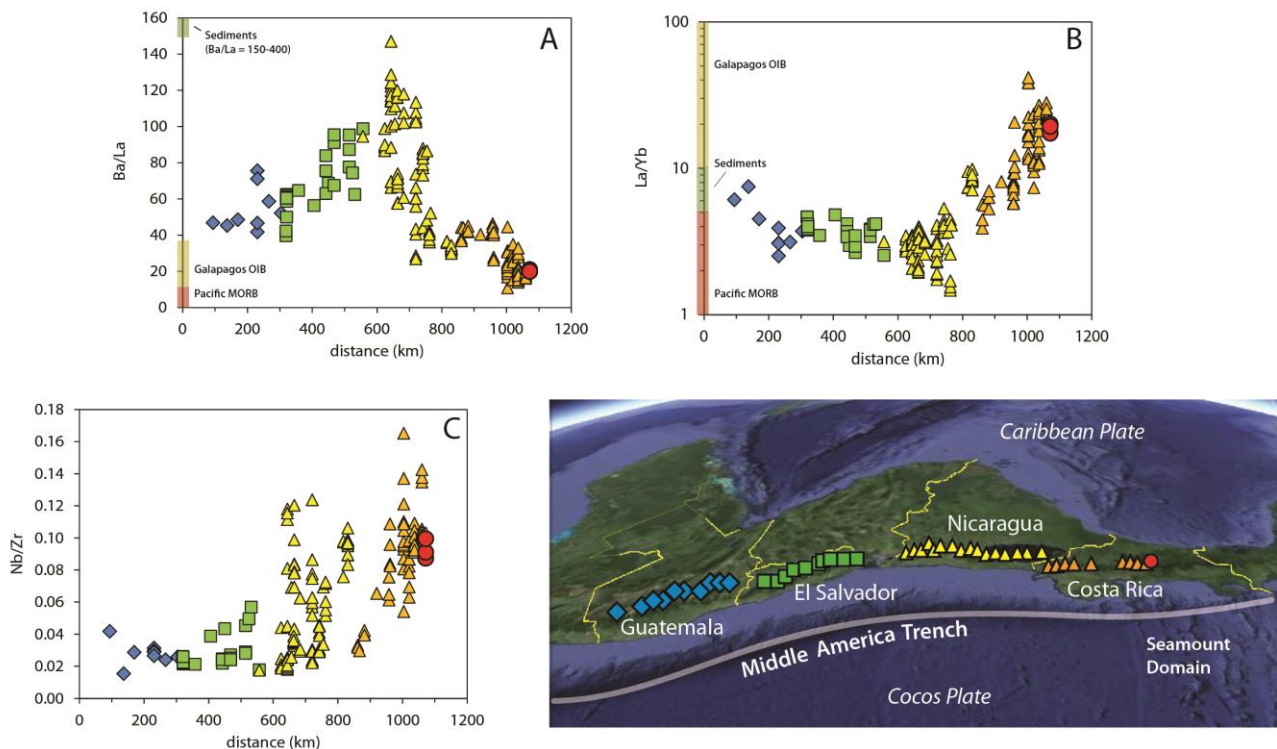
Fig. 2.15 – Ba/La (A), La/Yb (B) and Nb/Zr (C) ratios variation along-strike of the Central American arc (measured as distance from Mexico-Guatemala boarder). The range of subducting sediments, Pacific MORB, and Galapagos hot spot lavas are plotted in the y axis for comparison. Data for the volcanic front are from "RU_CAGeochem, a database and sample repository for Central American volcanic rocks at Rutgers University"; Pacific MORB and Galapagos hot spot data are from Georoc database (http://georoc.mpch-mainz.gwdg.de); subducting sediments data are from Patino et al., 2000. Only samples with $SiO_2 < 54$ wt. % and MgO > 4wt. % are plotted. Full red dots are Turrialba samples.

In general the concentrations of many trace elements in Turrialba rocks are higher than those from the CAVF or other arcs worldwide. The Nb/Zr ratio (*Fig. 2.15c*), for example, is a good parameter to characterize the original enrichment or depletion of the mantle sources because it is largely unaffected by the addition of mobile elements to the source from slab dehydration and the produced magma are insensitive to partial melting processes. The observed rough increase in Nb/Zr from Guatemala to Costa Rica (*Fig 2.15c*), suggests an enrichment of the mantle source underneath the southeastern termination of the arc, where Turrialba volcano is situated. In addition, chondrite normalized La/Sm ratio could be used as an enrichment index (Elliott, 2003). Sediment addition to the mantle wedge, for example, should increase the incompatible elements content and also cause light rare earth enrichment (i.e. an increase in La/Sm) in the arc lava source. Only a very small amount of sediment can result in a most extreme enrichment of the mantle wedge. Thus La/Sm should act as a useful tracer of the source composition of mafic arc front lavas and of possible sediment contribution to the mantle source. La/Sm is also possibly affected by different degrees of melting, although for the large degrees of melting proposed for arc front lavas (Plank and Langmuir, 1988) this should not be significant. *Figure 2.16* shows Ba/Th versus La/Sm for magmas from central America. This diagram is particularly useful in that it discriminates between the mantle source and the sediment contribution to the magmatic source. The high La/Sm ratio coupled with low Ba/Th ratio (high values are indicative of a sediment component added to the mantle source) is indicative of a enriched OIB type mantle source with no or minimum contribution from subducted sediments.
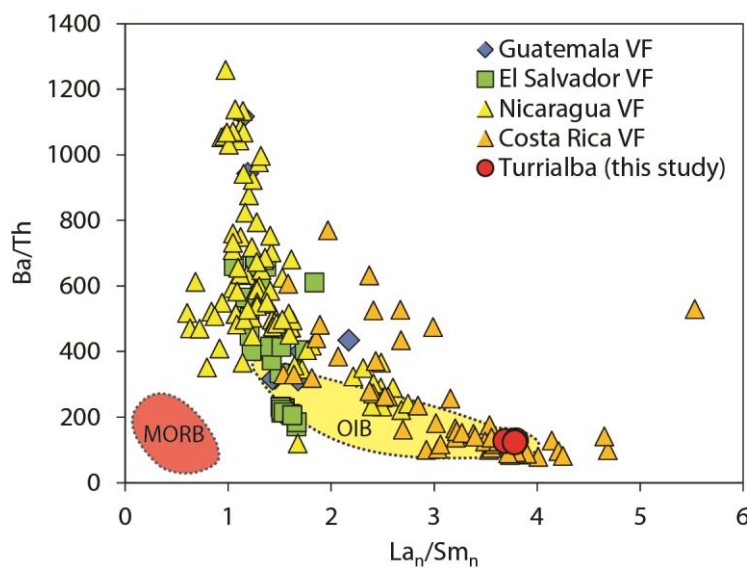

Fig. 2.16– La/Sm (normalized to primitive mantle in Sun and McDonough, 1989) versus Ba/Th of the CAVF rocks. Data of Turrialba (in red) are from this study, others are from "RU_CAGeochem, a database and sample repository for Central American volcanic rocks at Rutgers University".

This would be another important constraint on the presence of an OIB-like magmatic source beneath the two volcanoes.

The high concentrations of trace elements and the OIB-type signature of Central Costa Rica volcanoes have been interpreted by many authors (e.g. Carr et al., 1990; Herrostrom et al., 1995; Feigenson et al., 2004) as due to melting of an enriched mantle source with inputs from the subducting plate. In particular Carr et al. (1990) observed that the main constituent of mantle source should be a Depleted Mantle (DM) with small amounts of Enriched Mantle (EM). Nearly all calc-alkaline volcanic front samples could derive from a mixing between these two mantle sources. In this view the Enriched Mantle (EM) melts are generated by decompression of asthenosphere as it is drawn in and up toward the wedge corner. Reagan and Gill (1989), Carr et al. (1990) and Patino et al. (2000) agreed that enriched mantle mostly controls the abundance of most trace elements, with a relative influence of the slab flux. Other hypothesis relative to a minor slab flux beneath Costa Rica compared to Nicaragua, invoked a hotter slab in Costa Rica (Leeman et al., 1994), a greater degree of hydratation of the Nicaragua slab (Abers et al., 2003; Eiler et al., 2005) or loss of material from the slab during subduction beneath Costa Rica (Morris et al., 2002). More recent studies, involving isotope geochemistry and geodynamic studies shed new lights onto the complex framework of CAVF.

2.5.2 Isotope geochemistry evidences

The rocks from CAVF display several distinct isotopic reservoirs. When plotted in a $^{87}Sr/^{86}Sr$ versus $^{143}Nd/^{144}Nd$ correlation diagram (*Fig. 2.17*), data define two arrays: a) the first displays the classic negative slope of the MORB-OIB mantle trend and is prevalently composed of samples belonging to the volcanic back-arc (especially Honduras and Guatemala) plus those from Guatemala from the volcanic front; b) the second array has a unusual positive slope distribution and is made up primarily of volcanic front rocks. At one end of the second array there are the central sectors of the volcanic front (Nicaragua and El Salvador). These sectors display the highest $^{87}Sr/^{86}Sr$ ratios, as the result of incorporation of sediment-derived fluid in the source region (or bulk mixing with sediment), which has both high $^{87}Sr/^{86}Sr$ (0.7090) and high Sr (1200 ppm in the sediment) (Feigenson et al., 2004). At the same time they have Nd isotopic ratio similar to MORB. Mixing a small amount of sediment-derived fluids with solid Depleted Mantle (DM) creates a horizontal array of increasing $^{87}Sr/^{86}Sr$ and very minor changes in $^{143}Nd/^{144}Nd$. The first trend is explained simply by a mixing of a depleted-MORB mantle signature as indicated by the isotopic composition of lavas from behind the volcanic front (BVF) in Guatemala and Honduras, with a more enriched OIB source as testified by the Guatemala VF signature (*Fig. 2.17*).
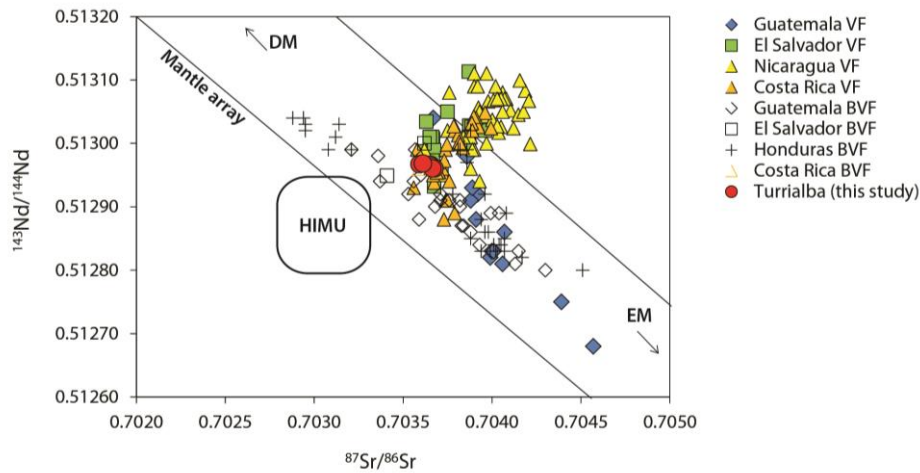
Fig. 2.17 – Sr and Nd isotope plot for Central American volcanics. VF = volcanic front; BVF = Back Volcanic Front. Data of Turrialba (in red) are from this study, others are from "RU_CAGeochem, a database and sample repository for Central American volcanic rocks at Rutgers University".

Guatemala volcanoes, at the northernmost termination of the VF, display a strong variation in Nd isotopic ratio, but at the same time define a negative slope trend. Costa Rican rocks fall entirely in the mantle array region, displaying a slight variation in both Sr and Nd isotopes. Turrialba samples can be considered as the less radiogenic rocks of the entire CAVF. Lavas from behind the volcanic front (BVF), especially from Honduras and Guatemala, display a clear negative slope mantle trend between a Depleted Mantle and an OIB-like mantle (Enriched Mantle – EM) end members. These samples plot along a mixing lines between mantle wedge components (ranging from DM to EM) and metamorphic (or granitic) basement (Feigenson et al., 2004).

A distinct Enriched Mantle source is present beneath Central America, with an isotopic composition similar to central Costa Rican lavas (Carr et al., 1990), as inferred by the intersection of the mantle array with the isotopic trend of the volcanic front lavas. This is confirmed by trace element patterns of Turrialba volcano that, as observed in the previous paragraph, display an OIB-like signature. To better constraint this mantle source, additional radiogenic isotope ratios (i.e. Lead isotopes) can be used. Hoernle et al. (2008) observed that moving along the volcanic front from central Costa Rica to northwestern Nicaragua, Nd isotope ratios increase and Pb isotope ratios decrease continuously (*Fig. 2.18*). The highest Pb isotope ratios in the arc rocks occur in the areas situated above the subducting Galapagos hotspot track. This domain is constituted by a seamounts chain that is known as "Seamount Province", having distinctly higher $^{208}Pb/^{204}Pb$ and lower $^{143}Nd/^{144}Nd$ for a given $^{206}Pb/^{204}Pb$ isotope ratio compared with the Cocos and Coiba Ridges. To explain the variation in Pb and Nd isotope ratios from Nicaragua to Panama, Hoernle et al. (2008) invoke three end members.

The northwestern Nicaraguan end member, with unradiogenic Pb and radiogenic Nd, reflects addition to the depleted mantle wedge of a slab fluid that contains Pb primarily from the subducting crust. The southern Costa Rica – Panama end member, with radiogenic Pb but intermediate $^{208}Pb/^{204}Pb$ and $^{143}Nd/^{144}Nd$ could be derived from the subducting Cocos – Coiba ridges and or the eroded basement (CLIP, Caribbean Large Igneous Province). The only source with the appropriate Pb (radiogenic Pb and high $^{208}Pb/^{204}Pb$) and Nd isotopic composition to derive the central Costa Rica end member is the Seamount Province, comprised between the Fisher and Quepos Ridge (von Huene et al., 2000; Carr et al., 2003), subducting beneath central Costa Rica. This seamount chain belongs to the Galapagos hotspot track and is constituted by cones, volcanoclastic aprons with extra thickness of igneous crust (von Huene et al., 2000) and constitute a large additional mass which would contribute a relevant chemical flux once subducted. This material is more enriched in many trace elements than the pelagic sediments that are subducted elsewhere along Central American trench. If the Galapagos seamount slab component has melt like properties, it could transport rare-earth elements (e.g. La, Nd) and HFS elements, consistent with the increase in Ba/La and decrease in La/Yb observed from Costa Rica to Nicaragua.

In this view, the transition from a dominantly fluid-like slab component beneath Nicaragua to melt-like slab components in Costa Rica and Panama, may be related to the influx of hot mantle through a slab window between central Costa Rica and Panama (Abratis and Worner, 2001).
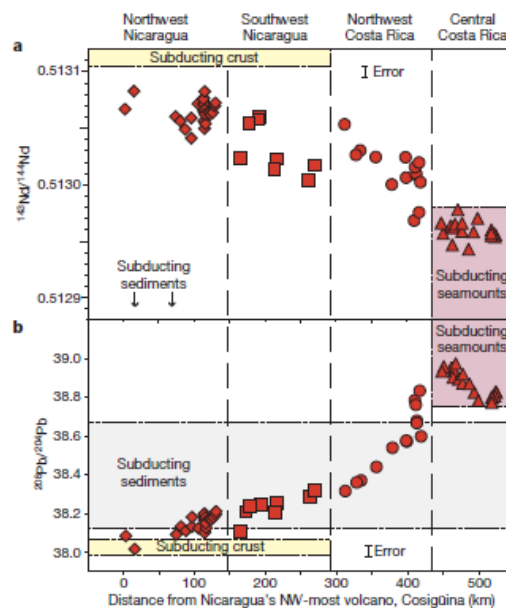

Fig. 2.18 – Nd and Pb isotopic composition variations along the volcanic front from Costa Rica to northwest Nicaragua (from Hoernle et al., 2008)

As inferred by trace elements geochemistry (e.g. trace element patterns in *Fig. 2.11*, Nb/Zr, La/Sm, Ba/Th ratios), the magmatic source of Turrialba has an OIB-like signature and the effect of the subducted sediments is negligible (e.g. Ba/La). The presence of an Enriched Mantle source beneath the southernmost termination of the Costa Rica volcanic front, is confirmed by the intersection of the mantle array with the Sr and Nd isotopic trend of the volcanic front lavas. The main enrichment source for the mantle in the Central Costa Rica sector derives from the subduction of the Seamount Province, comprised between the Fisher and Quepos Ridge (von Huene et al., 2000; Carr et al., 2003). This seamount chain belongs to the Galapagos hotspot track and is constituted by volcanoclastic products with extra thickness of igneous crust (von Huene et al., 2000) and constitute a large additional mass which would contribute a relevant chemical flux once subducted.

2.5.3 The occurrence of andesites with primitive geochemical characteristics

As observed from the major and trace element patterns, there is a group of andesites that deviates from the main evolutional trend. This difference is more appreciable in trace element variations, respect to major elements, where a constant depletion in HFSE (Nb, Zr, Hf) elements and in Rb (*Fig. 2.10*) and Th (not shown) is observed. Furthermore, these samples (TU3/1 – TU7 – TU8 – TU10/1 – TU18) are characterized by a significant enrichment in Sr and relatively low amount of Y (10 – 16 ppm), features that would indicate an adakite-like affinity for these andesites (Castillo, 2012), as observed in *Table 2.3* and *Fig. 2.19*.

Tab. 2.3 – Geochemical features of adakite magma (Castillo, 2012) versus the composition of Turrialba adakite-like andesites (this study).

| Geochemical features of adakite magma: comparison with andesites of Turrialba volcano								
Adakite characteristics		TU 3/1A	TU 7/1	TU 7/2A	TU 7/2B	TU 8	TU 10A	TU18
High SiO_2	≥ 56 wt. %	58.23	57.73	57.65	57.51	58.00	58.01	58.45
High Al_2O_3	≥ 15 wt. %	17.94	17.44	17.72	17.59	17.80	17.68	18.11
Low MgO	< 3 wt. %	-	-	-	-	-	-	-
High MgO	> 3 wt. %	3.80	4.31	4.21	4.34	4.14	3.90	3.52
High Na_2O	> ~ 3 wt. %	3.94	3.85	3.90	3.84	3.94	3.14	3.58
High Sr	> ~ 300 ppm	1000	885	925	926	902	1014	1072
Low Y	< ~ 10 ppm	10	12	12	16	11	15	11
High Sr/Y	> ~ 20	100	74	77	58	82	68	97
Low Yb	< ~ 1 ppm	0.9	1.1	1.1	1.4	1	1.4	1
High La/Yb	> ~ 20	22	21	21	20	23	22	16
Low HFSE's	Nb or Ta	✓	✓	✓	✓	✓	✓	✓
Low $^{87}Sr/^{86}Sr$	< 0.704	-	-	0.7036	-	0.7036	-	-
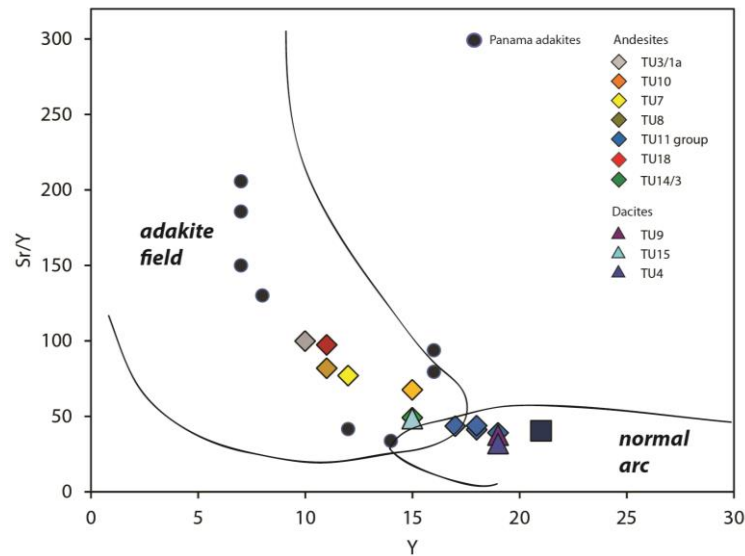
Fig. 2.19 – Plot of Sr/Y vs. Y (ppm) (modified after Drummond and Defant, 1990 and Castillo, 2012) typically used to distinguish adakites from normal arc andesites or more evolved compositions. Panama adakites composition are from Defant et al., 1992.

The term "adakite" was first introduced by Defant and Drummond (1990) and refer to intermediate to high silica ($\geq$ 56 wt %) Cenozoic arc igneous rocks, proposed to be direct melts of young ($\leq$ 25Ma) subducted oceanic basalt; they named the rocks after the magnesian andesites with similar trace element composition from Adak Island in the Aleutinians (Kay, 1978). These andesites are rather primitive, having relatively high MgO (5 wt. %) and Ni (150 ppm) contents and distinctively low FeO*/MgO ratios (<1.2), but at the same time they have much higher Sr contents and La/Yb ratios than typical convergent margin lavas. Kay (1978) proposed that these andesites may have formed as small degree hydrous melts generated through partial melting of the basaltic portion of the subducted Pacific plate that equilibrated with mantle peridotite. The results of combined partial melting models for basaltic crust and two-dimensional thermal models of subduction zones indeed allow young and, thus, still hot lithosphere to melt (e.g. Furukawa and Tatsumi, 1999; Peacock et al., 1994). Partial melting of subducted basalt, metamorphosed to amphibolite or eclogite facies rock at subduction zone, generates geochemical characteristics in the resultant magmas similar to those of the aforementioned magnesian andesites from Adak Island in the Aleutinians (Kay, 1978).

The adakite rock suite covers an array of compositions ranging from that of primary magmas (basalts - basaltic-andesites) derived from young subducted basalt to the composition of magnesian andesitic magma generated through equilibration of such a primary magmas with peridotite in the mantle wedge (Defant and Drummond, 1990). Adakites vary widely in major element contents and

petrographic characteristics (e.g. Drummond and Defant, 1990) and are very similar to other arc igneous rocks in terms of bulk rock composition. But they differ in trace elements geochemistry with respect to normal mantle wedge derived arc magma. In particular Defant and Drummond (1990) highlighted the high Sr/Y and La/Yb, but low Y and Yb of both the Cenozoic silicic arc and Adak magnesian andesitic rock groups compared to normal arc magmas. Since the early works on Adakitic magmas, claims of adakite occurrences have been made in many localities around the world and in a wide range of arc tectonic settings. Many authors would agree that the ideal condition for the formation of these magmas is an abnormal heating of the subducting lithosphere that allows even old or cold oceanic crust to melt. For example adakites were reported to have been formed from subducted oceanic basalts irrespective of age during subduction initiation or termination (Sajona et al., 1993; 1996), and arc collision (e.g. Sajona et al., 1996), in highly oblique subduction (Yogodzinski et al., 1995), or due to the breaking of the slab leading the opening of astenospheric (slab) windows (e.g. Calmus et al., 2003; Thorkelson and Breitsprecher, 2005; Yogodzinski et al., 2001), slab detachment following arc collision (e.g. Gao et al., 2007), and ridge subduction (Kay et al., 1993; Guivel et al., 2003). In spite of the many geodynamical settings in which adakite magmas were found, the chemical characteristics of adakite has been ascribed to the role of mantle peridotite in the melting of subducted basalt. Yogodzinski and Kelemen (1998) have shown that the adakite trace element signature (high Sr and Nd/Yb) is associated with the equilibration of slab melts with mantle peridotite. They propose that primitive magnesian andesites and dacites are parental to evolved adakites worldwide through extensive melt-mantle interaction at low pressure, just beneath the base of the arc crust.

As previously observed on the basis of their geochemical features, a suite of andesite rocks from Turrialba display adakite-like composition, either for major and trace element contents (*Tab. 2.3*). The low HFSE's as observed in many arc lavas, could suggest the presence of Ti-phase in the source. The very high Sr contents (885 − 1072 ppm) and, thus, the Sr/Y ratio (57 − 100), are well in the range of those of adakitic rocks (*Fig. 2.19*). Shallow level processes, including fractional crystallization, cannot produce these distinctive high, adakite-like Sr/Y and La/Yb (16 − 23), and low Y; the latter, along with Yb values, are in the range or slightly higher than values attended for adakite magma. All these features would suggest the presence of garnet at source, but this is in contrast with the REE pattern that displays an horizontal trend of the heavy-REE (*Fig. 2.12*). The Nd and Sr isotopic ratios of adakite and adakitic rocks are less susceptible to contamination by normal arc rocks or overlying crust, as these typically have lower Sr and Nd contents than adakites. So adakites should have low $^{87}Sr/^{86}Sr$ and high $^{143}Nd/^{144}Nd$ ratios, reflecting those of geochemically depleted oceanic basalt. Effectively data of isotopic Sr and Nd of two Turrialba adakite-like

andesites (TU7 and TU8), display respectively the lowest and the highest isotopic ratios of the suite of rocks analyzed (*Fig. 2.13*; data in *Tab. 2.2*).

Trace elements pattern suggest that the adakite-like magmas are presumably not co-magmatic with the Turrialba most primitive magmas. The latter are formed from an enriched mantle source, related to the subduction of the Galapagos hotspot track in this sector of the volcanic arc. To explain the presence of adakitic magmatism in this sector of the arc, we must consider the location of Turrialba volcano, that is followed to the south by a volcanic gap of ~180km. Turrialba volcano is located in a peculiar sector of the Central America volcanic belt, where the seamount domain of the Galapagos hotspot track is followed to the south by the Cocos Ridge domain (*Fig 2.20*). The collision between the Cocos Ridge and trench, shallow subduction, caused the end of volcanism in the southern sector of Costa Rica, and the relative slab window formation may have caused uplift of the Cordillera de Talamanca due the combination of tectonic and thermal processes (Abratis & Worner, 2001). The mantle flow could have entered through the slab window into the Caribbean realm, as testified by the eruption of alkali basaltic rocks (5.8 Ma) with OIB-like signature. The eruption of adakitic magmas occurred immediately after the opening of the slab window (Abratis & Worner, 2001). These volcanics are related to the upwelling and partially melting of asthenosphere in the slab window that may have indeed triggered a small amount of partial melting of the young and still relative hot and, thus, dry oceanic crust (Castillo, 2012); the subducted Cocos Ridge would have been too old (15 Ma) and too fast (7-9 cm/yr) to melt (Peacock et al., 1994) in a simple subduction context.

In this framework, the magmatic source of Turrialba volcano could be affected by the melting of portions of the Cocos Ridge, due to the proximity of Turrialba to the boundary between the Seamount Domain and the Ridge (*Fig. 2.20*). For this reason the magmatic source, that is dominated by the OIB-like signature due to the subduction of Galapagos Seamount, registers the presence of adakite-like magmas due to the melting of segments of the Cocos Ridge. Alternatively, the opening of the slab window, and the resulting increase of temperature of the asthenosphere, could have produced the melt of the very base of the Chortega Block, namely the Costa Rica sector. The base of this block is constituted by ~20km of Caribbean Large Igneous Province (CLIP) crust that formed during Late Cretaceous hot spot volcanism (Sinton et al., 2008) and that is essentially made of basaltic rocks and mafic granulites.
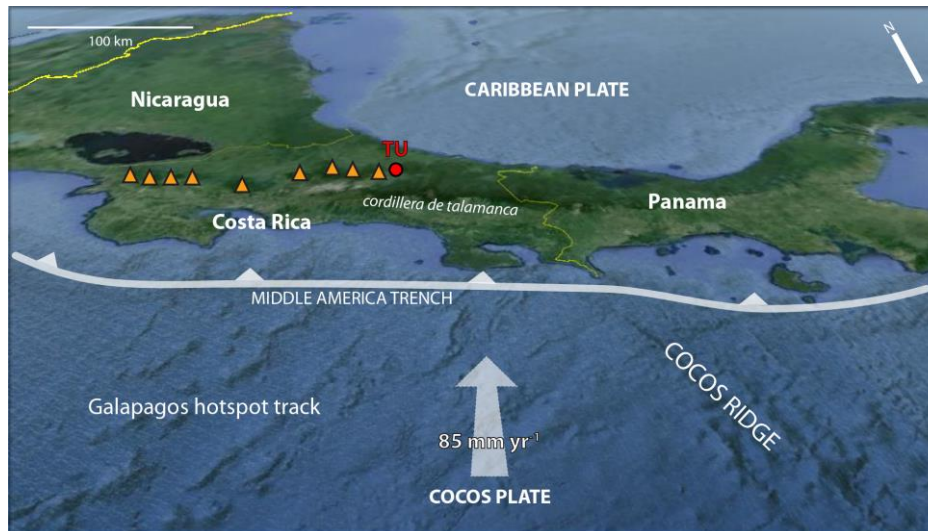
Fig. 2.20 – Regional map of Costa Rica, Turrialba volcano is indicated with the red dot, orange triangles are the other Costa Rican volcanoes.

In any case the occurrence of adakite magmatism in Panama (de Boer et al., 1991; Drummond et al., 1995) is a confirmation of the slab window theory, because such products of slab melting occur where spreading ridges are subducted (e.g. Kay er al., 1993; Stern and Kilian, 1996), along with the absence of shallow seismicity in the southern Costa Rica sector (Protti et al., 1995). Abratis & Worner (2001) agree that the astenospheric upwelling through the slab window by decompression of this Pacific mantle, should have induced partial melting and OIB-type magmatism.

As we will discuss in the next Chapter, the existence of a slab window could also explain the high ^{3}He/^{4}He ratios measured at the fumarolic gas discharge of Turrialba volcano that are the highest values of the entire Central America (is ~8 times the atmospheric ratio, Ra) (Shaw et al., 2003; Hilton et al., 2010).

3. *Mantle source feeding the plumbing system of Turrialba volcano: insights from noble gas geochemistry*

Noble gases are excellent tracers of mantle processes and their study, in both fumarolic gases and fluid inclusions hosted in crystals of erupted rocks, can be useful to unveil the features of the mantle sources beneath volcanic areas (e.g. Ozima and Podosek, 1983; Hilton et al., 1993; Marty et al., 1994; Martelli et al., 2004; Shaw et al., 2006; Nuccio et al., 2008; Correale et al., 2012, 2014). In particular He and Ar are highly sensitive to processes such as crustal contamination or degassing, that can occur during magma uprising toward the Earth surface. For this reason it is interesting to evaluate their relationship with other markers of crustal derivation such as mineral chemistry (Gasparon et al., 1994; Hilton et al., 1995; Shaw et al., 2006) or Sr-Nd isotopes (Condomines et al., 1983; Graham et al., 1990; Hilton et al., 1993, 1995; Van Soest et al., 2002; Martelli et al., 2004; Correale et al., 2014). Furthermore, helium may plays a critical role in the prediction of volcanic events (e.g. Sano et al., 1984) and merging data from both fumarolic gases and fluid inclusions hosted in crystals of eruptive products can give indication on the composition of the magma degassing and feeding the fumarolic emissions (Padrón et al., 2013). This in turn may have important implications on the style of the expected eruption and related hazard, particularly in the densely populated areas.

Turrialba volcano is upwind of the Central Valley of Costa Rica, which includes the Capital city of San José with its wide metropolitan area, and after almost 150 years of quiescence it is now showing signs of potential reawakening.

As we have seen from previous chapters, since 1996, the degassing from the summit craters has become more intense with the extension of the fumarolic field, the opening of new fractures and the occurrence of phreatic explosions (2010-2013) (Tassi et al., 2004; Vaselli et al., 2010; Martini et al., 2010; OVSICORI 2010, 2011, 2012, 2013). In this chapter new data on the chemical and isotopic composition of fluid inclusions hosted in mafic minerals separated from the Turrialba rocks are presented and compared to the chemical and isotopic composition of fumarolic emissions (*Chapter 4*). Main aim of this study is to give new insights on the magmatic source, i.e. the characteristics of magma degassing at present day and involved in the ongoing unrest phase.

3.1 Noble gas geochemistry background

Noble gases are excellent tracers of mantle processes. They occupy the last column of the periodic table, forming a single chemical family, and they are inert with respect to chemical reactions. Each noble gas element has both non radiogenic and radiogenic isotopes, which provide extremely useful time constraints on mantle processes. Because of their inert chemical nature, they tend to accumulate in atmosphere, and are unique indicators of the history of mantle degassing.

Helium isotope measurements in fluid inclusions hosted in crystals of magmatic rocks, provide some basic information on the magma source. There are two naturally occurring isotopes of helium: ^{3}He, considered "primordial Helium" and ^{4}He, the radiogenic one; the former is much less abundant than the latter. Nearly the entire abundance of terrestrial ^{4}He has been produced as α-particles from the radioactive decay of ^{238}U, ^{235}U and ^{232}Th over geological time, while nearly all the ^{3}He is primordial (Graham 2002). Because helium undergoes gravitational escape and has an atmospheric residence time of 1 to 10 million years, it is not recycled by plate tectonics to the inner of the Earth and this makes the Helium isotope ratio (^{3}He/^{4}He) unique among isotopic tracers of mantle sources involved in volcanism (Lupton 1983). Present day mantle contains both primordial and radiogenic helium isotopes but in different proportions depending on the geological context. The difference in ^{3}He/^{4}He ratio commonly observed between MORBs and OIBs has been accepted as evidence of two different mantle source regions (*Fig. 3.1a*), on the basis of a statistical comparison between datasets of the two end members (Anderson 2000a,b; 2001). The range in MORB is usually assumed to be 7 to 9 Ra (e.g. *Fig. 3.1b*; Kurz et al., 1982b; Graham 2002; where Ra is the He isotopic ratio in air), even though more recent studies have documented slightly larger variability within normal MORB from different ocean basins (e.g. Mahoney et al., 1989; Graham et al., 2001; Georgen et al., 2003). MORB He-isotopic values are relatively homogenous compared to OIB magmas, which display the highest magmatic ^{3}He/^{4}He ratios in Iceland and Hawaii, where they extend to values above 30 Ra (e.g. Kurz et al., 1983; Kurz et al. 1985; Barford et al., 1999; Breddam & Kurz 2001).

Neon (Ne) has three stable isotopes ^{20}Ne, ^{21}Ne and ^{22}Ne, and the isotopic composition of neon changes mainly through the so-called Wetherill reactions (e.g. Ballentine and Burnard, 2002; Ozima and Podosek, 2002). Mantle is characterized by elevated ratios of ^{20}Ne/^{22}Ne and ^{21}Ne/^{22}Ne compared to the atmosphere. The different correlations between ^{20}Ne/^{22}Ne and ^{21}Ne/^{22}Ne in magmatic sources is related to an ubiquitous presence of an atmospheric component (Porcelli and Ballentine, 2002). How and when this contamination by air occurs is still a matter of debate. Authors propose that it takes place during magma ascent and eruption (e.g. Farely and Poreda, 1993) or that it was introduced in the source by ancient subduction (e.g. Sarda et al., 2000), or that

the contamination occurs during sample preparation (e.g. Ballentine and Barfod, 2000). In general MORBs and OIBs display variations in Ne-isotope ratios and this results from differences in the dilution by primordial Ne of the nucleogenic ^{21}Ne that is produced in their mantle source (Graham 2002).
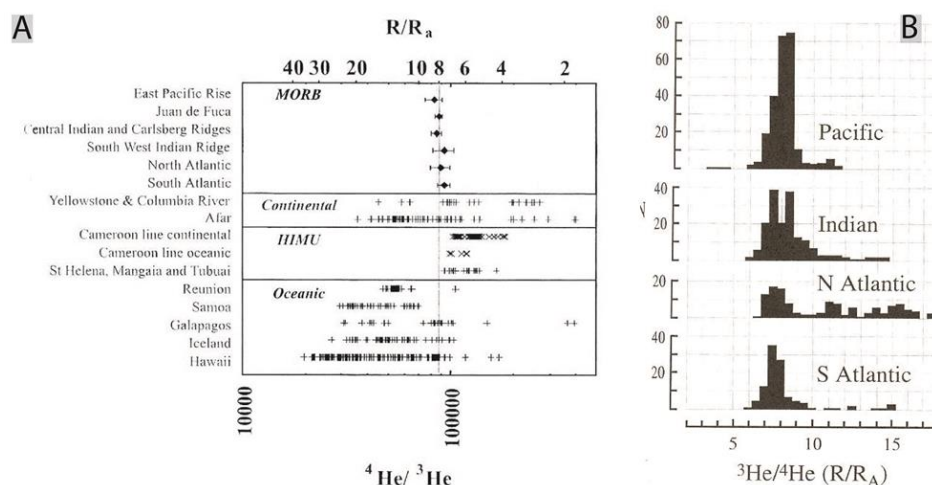
Fig. 3.1 – A) Comparison of He isotope ratios from selected MORBs, OIBs, and continental hotspots (after Barford, 1999). B) Histograms of MORB ^{3}He/^{4}He by ocean basins (from Graham, 2002).

Unlike He, which is lost from the atmosphere, argon (Ar) has accumulated over Earth history (Graham 2002). This noble gas has three isotopes ^{36}Ar, ^{38}Ar and ^{40}Ar. The two light isotope are not produced in significant quantities in the mantle, whereas ^{40}Ar is the end product of the branched decay of ^{40}K (Ozima and Podosek, 2002). The primordial ^{40}Ar/^{36}Ar ratio is extremely low, so the amount of ^{40}Ar initially present in the Earth can be reasonably taken as zero (Graham 2002). The ^{40}Ar isotope is almost entirely produced in the mantle, with subsequent degassing and accumulative storage in the atmosphere (Allègre et al., 1996; Ozima and Podosek, 2002). Transportation of ^{40}Ar from mantle to the atmosphere involves volcanic degassing and hydrothermal circulation through the crust. There are strong similarities between the systematics of ^{40}Ar/^{36}Ar and ^{3}He/^{4}He isotopic ratios that make them a useful pair for studies of mantle degassing (Farley and Craig 1994). Relatively high ^{40}Ar/^{36}Ar and low ^{3}He/^{4}He ratios occur in "degassed" mantle magma (e.g. MORB), while the opposite is observed in "undegassed mantle" materials (e.g. OIB) (Graham 2002). However the atmosphere is extremely poor in helium relative to the heavier rare gases, so the air addition to a mantle sample has an insignificant effect on ^{3}He/^{4}He but drastically alters ^{40}Ar/^{36}Ar. With the exception of cases in which the air contamination derives by assimilation of crust or by a near-atmospheric Ar isotope composition of the magmatic source, most authors agree that much of

the contamination occurs through the annealing of microfractures, following air entrapment that occurs either during sample collecting or preparation in the laboratory.

Mantle derived noble gases can be found in volcanic gas emissions (e.g. fumaroles), ground water samples, ultramafic xenoliths and phenocrysts or xenocrysts within lavas and eruptive products. In this study we will focus our attention on noble gases, and helium particularly, in fumarolic gas discharge and in fluid inclusions hosted in olivine and pyroxene crystals of eruptive rocks. Gases and fluids from fumaroles or degassing systems, give access to helium isotopic composition of magmatic source of active volcanoes through hydrothermal alteration of bedrock and/or gas-water interactions in deep aquifers. Olivine and pyroxenes phenocrysts of eruptive products contain fluid and melt inclusions that can potentially preserve mantle noble gases (Craig and Lupton, 1976; Ozima and Podosek, 1983; Hilton et al., 1993, 1994; Martelli et al., 2004; Shaw et al., 2006; Nuccio et al., 2008). Growing within magma, crystals can trap drops of melt and fluids containing helium isotopes that are representative of the magmatic conditions (Hilton et al., 2002).

3.1.1 Helium isotopes

Helium isotopes occupy a special place in mantle geochemistry studies: due to their low atomic weight and thus low atmospheric abundance, the air contamination effect that plague Ne-Ar-Kr-Xe analyses is extremely low. In addition the isotopic variability in mantle samples is enormous. As already seen above, relative to the atmospheric $^3He/^4He$ of 1.39×10^{-6} (Ra), mantle samples range from about 3 to 30 times higher (3 – 30 Ra). A great amount of data on the He isotopic composition of volcanic materials has been published over the years, providing what is probably a fairly complete representation of the variability of the mantle $^3He/^4He$, at least to the extent that such variability is expressed at the Earth's surface. To understand the evolution of the mantle-atmosphere system, the most important volcanic settings are mid-ocean ridges (MORB), which are believed to sample the uppermost part of the mantle, and ocean islands (OIB), derived from mantle plumes that drain deeper portions of mantle.

The mid-ocean ridge source is by far the most studied mantle environment, because quenched basalt glasses are ubiquitous and ready to be analyzed. As previously seen, the average He isotope composition of MORB show a narrow peak at 8 Ra, ranging between 6 and 16 Ra. It is generally accepted that MORB mantle displays a constant composition around the world, between 7 and 9 Ra, but the MORB source may be modified to higher or lower values, as a result of input from other sources. Commonly, higher He isotopic ratios are attributed to involvement of a component derived from a nearby hotspot. For example, the He isotope ratios along the ridges north and south of

Iceland are uniformly higher than other North Atlantic MORBs (Farely and Neroda, 1998). R/Ra increases approaching Iceland (Poreda et al., 1986), reaching the highest value of ~28 Ra on Iceland itself (Condomines et al., 1983; Kurtz et al., 1985). Off-axis plumes can also influence MORB He, as in Easter microplate basalts (~11 Ra; Poreda et al., 1993). MORB source interactions with hotpost characterized by lower $^3He/^4He$ are also known, in this case the ratio will be lower than 8 Ra. Several studies have highlighted also anomalous R/Ra ratios in MORBs far from hotspots. Mahoney et al. (1994) found ratios up to 11 Ra at 16° S on the East Pacific Rise, while Hanan et al. (1992) measured just 6.2 Ra at 33°S on the Mid-Atlantic Ridge. These unusual values are interpreted as punctual variation due to the presence of small isotopically distinct bodies within the upper mantle MORB source (Graham et al., 1996). Despite this variations, the sharp peaked distribution of $^3He/^4He$, suggests to refer to values between 7 and 9 Ra as the normal MORB isotopic range. In particular the value of 8 Ra, that corresponds to the peak of the distribution, may be diagnostic of a component derived from a MORB source, or at least that there is a communication with this source.

He isotope ratios of ocean island basalts (OIB) display a broader variation, ranging between ~4 and ~30-40 Ra (Fig. 3.1a). Iceland and Hawaii are the places on Earth where the highest He isotope values were measured, while the lowest values are found at several hot spot volcanoes including St. Helena (6 Ra), Guadalupe (4 Ra) and the Azores (4 Ra). Many hotspot volcanoes have $^3He/^4He$ ratios intermediate to these extremes, and as it is shown in *Fig. 3.2*, He isotope ratios in ocean island basalts extend to both higher and lower values than MORBs. In addition the prominent peak at the MORB values suggests that the depleted upper mantle plays an important role in the OIB He budget.
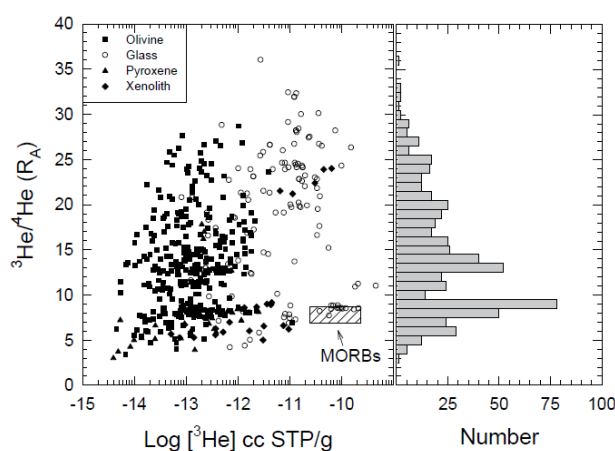

Fig. 3.2 – He isotope ratios versus ^3He concentration in ocean island basalts (OIBs) (from Farley & Neroda, 1998; data from Farley and Neroda (1998) and reference therein).

High ^{3}He/^{4}He ratios are thought to be carried by mantle plumes rising from a deep zone of the mantle (lower mantle or the core-mantle boundary). A deep mantle source provides a region to isolate high ^{3}He/^{4}He mantle from convective mixing with the lower ^{3}He/^{4}He MORB source. Wolfe et al. (1997) demonstrated a genetic relationship between a plume and high 3He/4He ratios under Iceland, with seismic tomography that suggests a hot zone upwelling from a depth of at least 400km.

Helium isotope ratios in volcanic gases along arc volcanoes, are close to those found in mid-ocean-ridge basalts, revealing the presence of primordial ^{3}He released from the wedge of mantle material above the sinking plate (Poreda and Craig, 1989). Craig et al. (1978) measured ^{3}He/^{4}He ratios in volcanic gases from Japan, the Marianas and Mt Lassen, showing that the dominant source of helium was the mantle wedge rather than subducted oceanic crust or sediment, both of which are rich in radiogenic ^{4}He. Poreda and Craig (1989) provided measurements of He isotopic ratios in free gases and fluid inclusions hosted in olivine and pyroxenes of many arc volcanoes around the circum-Pacific volcanic belt. They observed an arc helium signature of 6-8 Ra that points to a MORB source dominating the production of arc lavas. Craig et al. (1978) observed that if arc volcanics were simply remelted downgoing oceanic crust, very low ^{3}He/^{4}He ratios, ~2 Ra or less, would be observed because of radiogenic ^{4}He production in old oceanic crust which should retain little if any primordial ^{3}He. So old oceanic crust is low in ^{3}He, has a ^{3}He/^{4}He ratio dominated by radiogenic ^{4}He and cannot be the major source of helium in arc lavas. Stern (1981) supposed that an enriched source region produces arc lavas globally; however, Poreda and Craig (1989), suggested that no arc terrain has a ^{3}He/^{4}He ratio higher than that of normal mid-ocean ridge basalt. For this reason they suggested that helium in arcs associated with subducting oceanic crust, is almost entirely derived from a dominant MORB component in the mantle wedge, although local ^{3}He/^{4}He ratio variations could be related to local geodynamic complexities.

3.2 Sample preparation and analytical methods

Highly porphyritic lava and scoria samples belonging to the last 10ka activity of Turrialba were collected in the field and prepared for investigations (*Fig. 3.3* and *Fig. 3.4*). Basaltic-andesites samples (TU5 - TU6 - TU16) belong to bombs and scoriae from the most recent eruptive activity (1864-1866) and have been collected between the Central and the East Craters. Andesite samples (TU7 - TU8) belong to a lava flow dated ~7ka (G. Soto personal communication) and were collected on the southwestern flank of the volcano. Dacitic lava (TU4) has been sampled on the

western flank of the volcano and, according to Ruiz Cubillo et al. (2010), belong to a lava flow dated 3±3ka ($^{40}Ar/^{36}Ar$ method). All the volcanic rocks have been analyzed for chemical composition of bulk rock, mineral chemistry and Sr-Nd isotope ratio, with the analytical methods reported in *paragraph 2.3.2*. For each sample, we carried out noble gas analyses of fluid inclusions (FIs) hosted in olivine and pyroxene crystals. In this respect, samples were selected on the basis of the presence of mafic phenocrysts and of freshness.
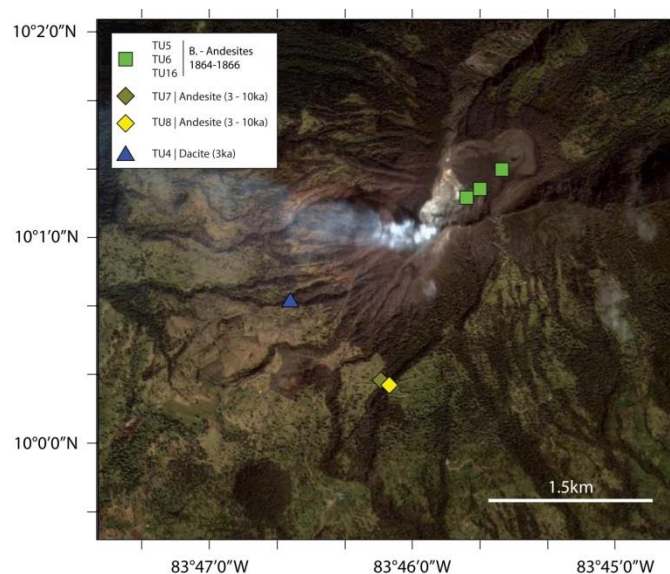

Fig. 3.3 – Location map of the collected Turrialba volcanic samples.
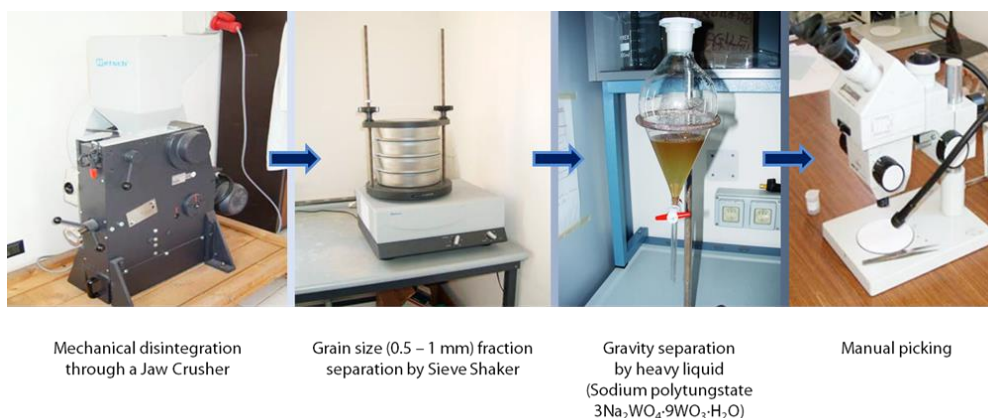
Fig. 3.4 – Summary of the working steps carried out for the separation and selection of crystals.

In order to perform noble gas analyses in FIs hosted in olivines and pyroxenes, rock samples were fragmented by mechanical disintegration through a crusher. In *Fig. 3.3* are summarized the different working steps carried out for the crystal separation. Then, the crushed sample was sieved, by selecting the fractions corresponding to the range size 0.5 mm - 1 mm. Olivine and pyroxene crystals were separated from the glass by using solution of sodium polytungstate ($3Na_2WO_4 \cdot 9WO_3 \cdot H_2O$) and then carefully handpicked under a binocular microscope; crystals with glassy and/or altered surfaces were discarded. The selected crystals were ultrasonically cleaned with successive treatments in diluted acid (6.5% HNO_3), deionized water and in high-purity acetone. A sieved and weighted aliquot of crystal (0.6 – 1.3g) was put in a stainless-steel bowl and placed in a crusher capable of loading up to six samples simultaneously. In order to reach ultra-vacuum conditions ($10^{-9} – 10^{-10}$ mbar), the system was heated under turbo-pumping conditions for 48-72h at 130°C. Gases were crushed in a single-step at a pressure of 200 bar, which avoids the release of both cosmogenic (^{3}He) and radiogenic (^{4}He) gases trapped in the crystal lattice (e.g., Correale et al., 2012). The gas mixture extracted from FI was purified in a stainless-steel preparation line, in order to remove all the species in gas mixture that are not interesting to be analyzed. CO_2, N_2, H_2O and H_2 were adsorbed by Zr-Al getter traps, then the residual gas mixture were adsorbed by charcoal traps that separate Ar from He+Ne fraction. The He and Ne mixture is absorbed and concentrated in another charcoal trap cooled down by liquid nitrogen at 12°K. Increasing progressively the temperature, helium is realeased at 40°K while neon at 85°K; then they are separately addressed in a split flight mass spectrometers for isotope analyses (Helix SFT). Argon previously trapped is released heating the trap to room temperature and then analyzed by a multi-collector mass spectrometer (Argon), equipped with 5 collectors for analyses of ^{36}Ar to ^{40}Ar.

Results are reported in terms of R/Ra with R the isotopic ratio of the measured sample and Ra the isotopic ratio of air:

$$\frac{R}{R_a} = \frac{\left(\frac{^3He}{^4He}\right)_m}{\left(\frac{^3He}{^4He}\right)_{air}} \qquad \text{where Ra= 1.39 x 10}^{-6}$$

Errors on R/Ra measurements are calculated combining analytical uncertainty of sample measurement with that of standard. Subsequently R/Ra can be corrected for air contamination on the basis of the difference between ^{4}He/^{20}Ne measured in the sample and the same ratio measured in the atmosphere (*X*):

$$X = \frac{\left(\frac{^4He}{^{20}Ne}\right)_m}{\left(\frac{^4He}{^{20}Ne}\right)_{air}} \qquad \text{with } ^4He/^{20}Ne \text{ of air} = 0.318$$

From which the He isotopic ratio is expressed as Rc/Ra as follows:

$$\frac{R_c}{R_a} = \frac{\left[\left(\frac{R}{R_a}\right)X\right] - 1}{(X-1)}$$

3.3 Fluid inclusions composition

Olivine and pyroxenes phenocrysts generally contain primary and secondary fluid inclusions that are trapped during the growth of the crystals in magmatic conditions. Thus, they can potentially preserve the pristine composition of noble gases originally dissolved in the silicate melt, and their investigation is useful to assess the features of the magma before the eruption. If compared to surface gases, which are representative of magma degassing at the collection date, the study of FI gives the opportunity to obtain information on the evolution that a magmatic system may have undergone over time. Data of noble gases measured in FI hosted in olivine and pyroxene crystals are reported in *Tab. 3.2*

On the basis of He and Ar relative abundances (*Fig. 3.11*), basaltic-andesites samples TU5 – TU6 – TU16, display the highest noble gases abundances with He varying between 7.35 x 10^{-13} and 3.09 x 10^{-14} mol/g and Ar between 9.49 x 10^{-12} and 2.58 x 10^{-12} mol/g. Xenocrysts of olivine in dacite TU4 lie in the same range displaying an He content of 2.31 x 10^{-13} mol/g and Ar of 2.68 x 10^{-12} mol/g. Olivines of andesite samples TU7 and TU8 show an He content comprised between 1.23 x 10^{-13} and 8.42 x 10^{-14} mol/g and an Ar content between 1.08 x 10^{-11} mol/g and 7.30 x 10^{-12} mol/g. He and Ar contents of basaltic-andesite (He = 3.14 x 10^{-14} mol/g; Ar = 3.27 x 10^{-12} mol/g) and andesites (He = 1.3 x 10^{-14} – 2.29 x 10^{-14} mol/g; Ar = 2.60 x 10^{-12}; 3.54 x 10^{-12} mol/g) are lower respect to the olivines of the same rock sample.

Plotting He abundances versus the He isotopic He (results are listed in *Tab. 3.2*) normalized to atmospheric value (R/Ra), olivine samples are arranged in three main groups (*Fig. 3.12*). The first group is represented by olivines of basaltic-andesites that range between 7.83 and 8.05Ra, displaying the highest He isotopic values. Olivine xenocrysts of dacite TU4 are characterized by similar values in He isotope composition (7.94 Ra). Andesites samples TU7 and TU8 represent the

second group, ranging between 7.03 and 7.18 Ra. Only clinopyroxenes of basaltic-andesite (TU6) and andesites (TU7 and TU8) were collected in a sufficient amount for analyses. Pyroxenes tend to have lower $^3He/^4He$ ratios (5.72 – 6.03 Ra) and lower He concentrations (1.63×10^{-14} – 3.14×10^{-14} mol/g) respect to cohexisting olivines (*Fig. 3.12*).
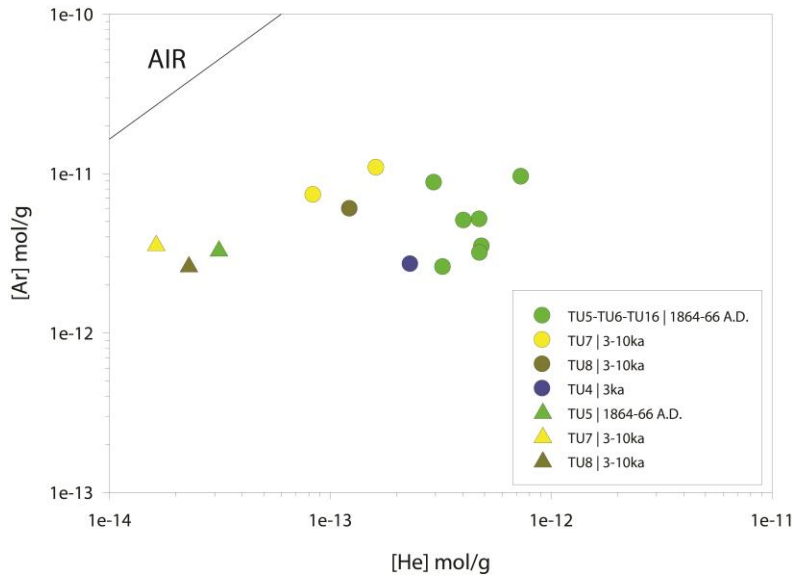

Fig. 3.11 – He and Ar abundances (mol/g) in fluid inclusions hosted in olivine and pyroxenes of the selected Turrialba rocks.
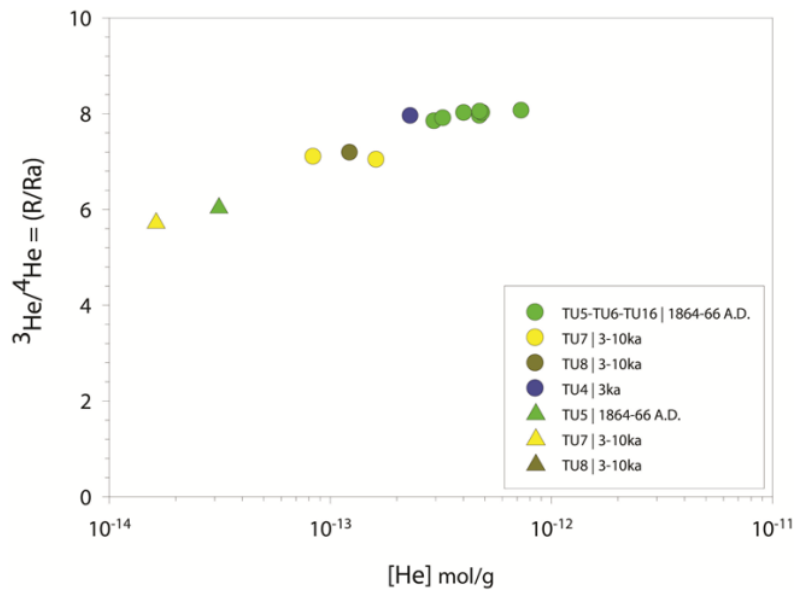

Fig. 3.12 – $^3He/^4He$ (expressed as R/Ra) ratio versus He concentration in the investigated samples.

Tab. 3.2 – Chemical and isotope composition of noble gases in fluid inclusions hosted in olivines and pyroxenes crystals of Turrialba rocks.

Sample	Bulk Rock[1]	Mineral[2]	Weight (g)	[He] mol/g (x10^{-13})	[Ne] mol/g (x10^{-15})	^{40}Ar mol/g (x10^{-12})	^{36}Ar mol/g (x10^{-14})	^{40}Ar* mol/g (x10^{-13})[3]	He/Ar*	He/Ne	R/Ra	Rc/Ra	Err $_{Rc/Ra +/-}$	^{40}Ar/^{36}Ar	Errore (%)	^{38}Ar/^{36}Ar	Errore (%)
TU5	BA	Ol	1.14	2.97	2.91	8.72	2.57	11.30	0.262	101.7	7.83	7.86	0.09	339.46	0.06	0.19	0.19
TU6	BA	Ol	1.06	3.25	1.23	2.58	0.60	8.12	0.400	263.5	7.90	7.91	0.08	431.55	0.12	0.19	0.19
TU6	BA	Ol	0.61	4.76	2.63	5.12	1.35	11.30	0.423	180.8	7.95	7.96	0.10	378.66	0.14	0.19	0.19
TU6	BA	Ol	0.61	4.04	2.99	5.04	0.14	9.14	0.442	135.2	8.01	8.02	0.11	360.92	0.08	0.19	0.19
TU6	BA	Px	0.97	0.31	1.37	3.27	1.05	1.59	0.197	23.0	6.03	6.11	0.28	310.61	0.08	0.19	0.19
TU16	BA	Ol	1.07	4.88	0.85	3.47	0.79	11.30	0.431	574.6	8.01	8.02	0.08	438.33	0.07	0.19	0.19
TU16	BA	Ol	1.08	4.78	1.13	3.15	0.71	10.70	0.445	422.6	8.03	8.04	0.07	447.68	0.07	0.19	0.19
TU16	BA	Ol	0.67	7.35	3.78	9.49	2.71	14.90	0.494	194.8	8.05	8.07	0.08	350.40	0.06	0.19	0.19
TU8	A	Ol	1.29	1.23	1.64	5.97	1.95	2.19	0.561	74.9	7.18	7.20	0.10	306.77	0.05	0.19	0.19
TU8	A	Px	0.28	0.23	7.26	2.60	0.82	1.64	0.140	3.2	-	-	-	315.43	0.29	0.17	0.17
TU7	A	Ol	1.22	0.84	1.48	7.30	2.43	1.05	0.800	56.9	7.09	7.13	0.11	299.82	0.64	0.19	0.19
TU7	A	Ol	1.18	1.62	2.34	10.80	3.57	2.59	0.628	69.4	7.03	7.06	0.09	302.75	0.04	0.19	0.19
TU7	A	Px	0.63	0.16	5.72	3.54	1.09	3.00	0.054	2.9	5.72	6.34	0.16	322.90	0.14	0.18	0.18
TU4	D	Ol	0.62	2.31	0.56	2.68	0.60	9.11	0.254	413.9	7.94	7.95	0.13	447.43	0.15	0.19	0.19

[1] Host rock chemical classification on the basis of SiO_2 and Alkali content. BA, Basaltic Andesite; A, Andesite; D, Dacite

[2] Mineral phases analyzed: Ol (Olivines), Px (Pyroxenes)

[3] ^{40}Ar* = ^{40}Ar$_{measured}$ -((^{40}Ar/^{36}Ar)$_{air}$ x ^{36}Ar$_{measured}$), with (^{40}Ar/^{36}Ar)$_{air}$ = 295.5

3.3.1 The effect of air contamination

The measured $^{40}Ar/^{36}Ar$ in Turrialba fluid inclusions (*Tab. 3.2*) are typical of subduction related volcanism (e.g. Fischer et al., 2005) and close to the atmospheric signature ($^{40}Ar/^{36}Ar = \sim 295$), ranging between 299 and 447. The Ar isotope value of fumarole collected during this study ($^{40}Ar/^{36}Ar = 329$; fumarole F1, West Crater, March 2011) represents the only available datum on Turrialba volcano at present day. This value falls in the range of Turrialba Ar isotope composition of fluid inclusions hosted in eruptive products, suggesting the hypothesis that this could be the Ar isotopic signature of the magmatic source beneath Turrialba volcano. This is confirmed by similar measurements in olivines and pyroxenes of other volcanoes of Central America: Fischer et al. (2005) measured in olivines and pyroxenes of Cerro Negro (Nicaragua) an average Ar isotopic ratio of $^{40}Ar/^{36}Ar = 306 \pm 76$, and in pyroxenes of Irazu volcano values of $^{40}Ar/^{36}Ar > 328$, asserting that this atmospheric-like Ar may potentially derive from subducted seawater stored in such sediments.
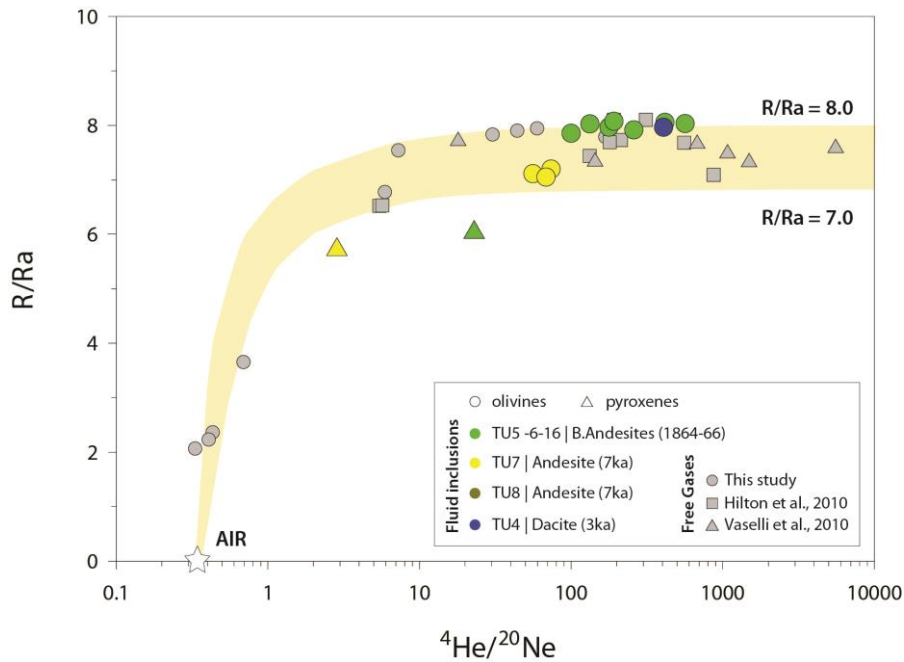
Fig. 3.13 – $^{3}He/^{4}He$ (R/Ra) vs $^{4}He/^{20}Ne$ ratios plot. Data of free gases and fluid inclusions hosted in olivines of Turrialba rock samples analyzed are plotted. Light orange area reports the binary mixing between air (white star) and a magmatic source with a He-isotopic composition comprised between 8 and 7 Ra. Data reference are indicated in figure.

Plotting $^{4}He/^{20}Ne$ with He isotopic ratio (Sano and Wakita, 1985) is it possible to assess the entity of the atmospheric contamination (*Fig. 3.13*). A low air contamination in Turrialba FIs is suggested

by the ^{4}He/^{20}Ne ratio, that ranges from 41 to 574 (^{4}He/^{20}Ne air = 0.318). This value is higher than in the fumarolic field during 2011 (^{4}He/^{20}Ne = 31 – 170) but it is extremely lower than the highest value ever measured at Turrialba (^{4}He/^{20}Ne = 5571, in March 2008; Vaselli et al., 2010). Assuming the last value as representative of the magmatic source, it is clear that some air contamination affected FIs in olivine crystals. Data from fluid inclusions and free gases are comprised in a range of 7.0 Ra and 8.1 Ra (*Fig. 3.13*), indicating a binary mixing between air and a magmatic end member with this He-isotopic range. Whilst air contamination of free gases is more easily explainable, noble gases with an atmospheric-like signature in pheocrysts fluid inclusions is still a matter of debate. Most authors think that air contamination occurs within the crust (Burnard et al., 2004), during eruption or in a post-magmatic stage (Nuccio et al., 2008; Correale et al., 2012).

The correction for air contamination of He isotopic ratio is expressed as Rc/Ra (see *paragraph 3.2* for details). At Turrialba differences between uncorrected (R/Ra) and corrected values (Rc/Ra) are insignificant (results in *Tab. 3.2*), indicating that He air contamination on the analyzed fluid inclusions is negligible.
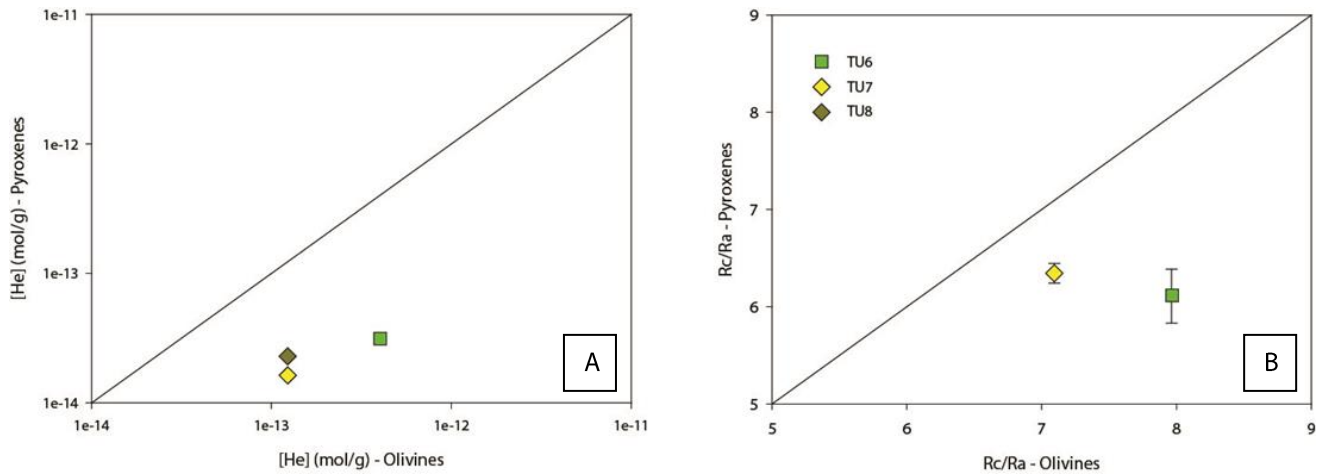
Fig. 3.14 – Comparison of He abundances (A) and He-isotopic ratios corrected for air contamination (B), in investigated olivines and pyroxenes.

As observed in the noble gases content, He isotope composition confirms that pyroxenes suffer a systematic disequilibrium with respect to cogenetic olivines, as indicated by their lower helium abundances and He-isotopic ratios (*Fig. 3.14*). This behavior has been already observed in other volcanic systems [i.e., at Etna (Marty et al., 1994; Nuccio et al., 2008; Correale et al., 2012, 2014) and in Central America (Shaw et al., 2006)]. Despite the most common hypothesis invoked to

explain this disequilibrium [i.e., post-entrapment in pyroxene crystals of contaminated/degassed fluids (Marty et al., 1994; Hilton et al., 1995; Shaw et al., 2006)], our dataset suggests that a preferential diffusive kinetic fractionation of He from such minerals occurred, as already suggested by Harrison et al. (2004), Nuccio et al. (2008) and Correale et al. (2012; 2014) in other volcanic systems. Accordingly, the Rc/Ra versus ^{4}He/^{40}Ar* plot (*Fig. 3.15*) shows that pyroxenes have systematical lower Rc/Ra and ^{4}He/^{40}Ar* ratios than cogenetic olivines, that is not compatible with more degassed conditions (i.e., ^{4}He/^{40}Ar* in pyroxenes higher than in olivines) as post-entrapment should imply. More likely, we infer that this behavior is due to the diffusive loss of He from the FI that affect both the elemental and isotope composition. In view of that, pyroxenes cannot be considered representative of the magmatic source, thus hereafter we will focus our discussion only on data from olivines.

3.4 Inferences on the local mantle source

As reported above, the ^{3}He/^{4}He ratio measured in olivines varies in the range 7.1-8.1 Ra, ratios similar to those measured in fumarolic gases (7.1-7.9 Ra) in 2011 and to the unique value of 7.5 Ra measured in FI by Shaw et al. (2006). In order to explain this variability we may look at the ^{4}He/^{40}Ar* ratio (*Fig. 3.15*), that is only available for FI and for the high temperature fumarole collected at SW crater (F1), compared to Rc/Ra.
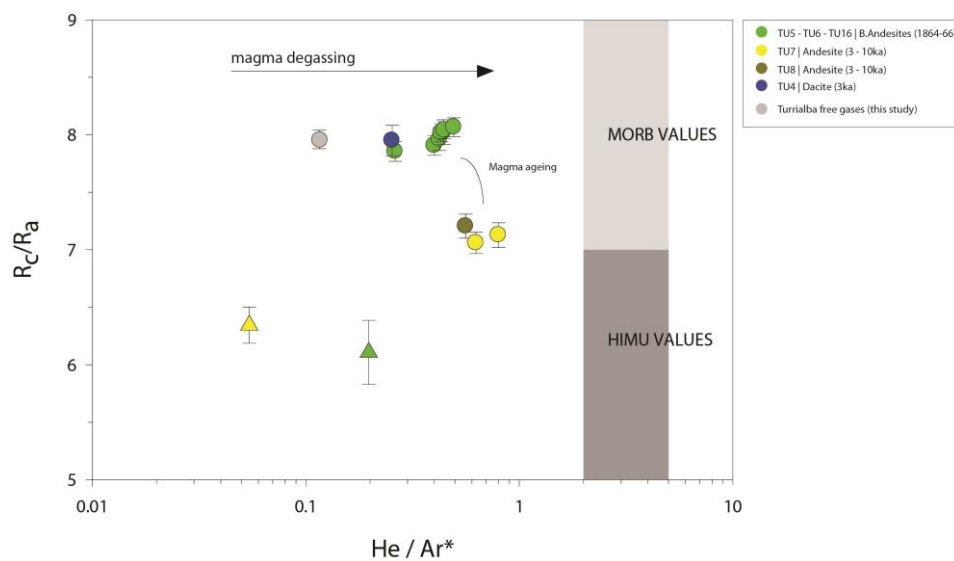
*Fig. 3.15* – ^{4}He/^{40}Ar* ratio versus ^{3}He/^{4}He isotope ratios (Rc/Ra) in fluid inclusions and in free gases. The straight arrow qualitatively indicates how magma degassing would affect the ^{4}He/^{40}Ar* ratio. Vertical error bars are shown.

The ^{4}He/^{40}Ar* ratio varies from 0.1 to 0.8, being below the typical range of radiogenic production in the mantle (^{4}He/^{40}Ar*=1–5; e.g., Ozima & Podosek, 1983; Marty, 2012). Considering the different solubilities of He and Ar in silicate melts (D_{He}/D_{Ar}~10; Iacono-Marziano et al., 2010; Paonita et al., 2012), these low ratios could be explained as an early degassing of Ar from magma, being this species preferentially exsolved with respect to He. Indeed, an increase of ^{4}He/^{40}Ar* indicates a greater extent of degassing (Iacono-Marziano et al., 2010; Correale et al., 2012; Paonita et al., 2012; Colin et al., 2013), while ^{3}He/^{4}He ratio does not vary during magma degassing. High temperature fumaroles and FI in olivines from basaltic-andesites do not show any variation of ^{3}He/^{4}He ratio, while ^{4}He/^{40}Ar* increases from 0.1 to 0.5. Also olivine xenocrysts hosted in TU4 dacite show isotopic ratios comparable to those of basaltic-andesites. This means that all these gases reflect a similar extent of degassing from a magma with the same He isotope signature. An appreciable decrease of ^{3}He/^{4}He ratio can be observed only in TU7 - TU8 andesites, that also display higher ^{4}He/^{40}Ar* values (from 0.5 to 0.8). This increase of ^{4}He/^{40}Ar* ratio is compatible with an higher extent of degassing, which is presumably accompanied by fractional crystallization (see also paragraph *3.3*). On the other hand, this process alone is not able to explain the lowering of ^{3}He/^{4}He ratio and other processes must be invoked: 1) post-eruptive ^{4}He in-growth; 2) crustal assimilation; 3) magma aging.

1) Considering that all the investigated products were erupted in the last 10ka and that olivine crystals contain a very low amount of U and Th, being these elements incompatible, a post-eruptive in-growth of radiogenic ^{4}He is not able to produce the decrease of Rc/Ra values recorded in andesites. A similar conclusion was also reached by Shaw et al. (2006). Moreover, the single-step crushing we adopted to release FI minimizes the contribution of those species trapped in the crystal lattice.

2) Crustal assimilation hypothesis assumes that the lower ^{3}He/^{4}He measured in andesites may reflect crustal contamination (i.e., assimilation) directly in the magma residing in the plumbing system. But the lack of any Sr-Nd variation (*Fig. 3.9*) in all the investigated products would lead to exclude also this process. In addition, we point out that the crustal thickness estimated below Turrialba (40 – 45 km; Carr et al., 2003) is among the highest for Central America, as the measured R/Ra values, which contrasts with what we should expect. Kim et al. (2008), in order to explain a similar behavior observed in Ulleungdo volcanic island (South Korea) invoked a direct contamination of magma by crustal fluids (R/Ra=0.02 and ^{4}He/^{40}Ar* up to 25; Andrews, 1985; Ballentine et al., 1994), that would affect only noble gas composition. Even if the variations observed in our andesites could be compatible with such a process, it is hard to hypothesize that a

crustal contamination would affect only He and no other geochemical/petrological tracers (e.g., Sr-Nd isotopes) and we prefer to consider this only as a minor possibility.

3) Magma aging process implies the in-growth of radiogenic ^{4}He due to the decay of U and Th directly in the magma, while it is residing in the plumbing system. Considering an initial average ^{3}He/^{4}He of 8 Ra and [He]=4 x 10^{-13} mol/g, as measured in FI from TU4-TU5-TU6-TU16, and an average U and Th content of 1.25 and 3.2 ppm respectively, as measured in TU7-TU8 lavas, we calculate that 5ka are necessary to produce a radiogenic ^{4}He of ~5 x 10^{-14} mol/g, which would lower the ^{3}He/^{4}He ratio from 8 to 7.1 Ra. This seems compatible to what observed in our dataset, also if we consider that andesites could represent a petrological evolution of basaltic-andesites due to fractional crystallization, that implies a period of residence (aging) of magma before erupting. We point out that this calculation is strongly sensible to the assumed initial He content. Indeed, for instance, Shaw et al. (2006) performed a similar calculation by assuming an higher value (i.e., MORB-like) that led the authors to exclude this process. We think that our assumption is more reasonable in this study-case because based on measured values, and that magma aging is thus the most likely process occurred to explain the variability in the dataset, even if more data and further investigations are necessary to validate this hypothesis.
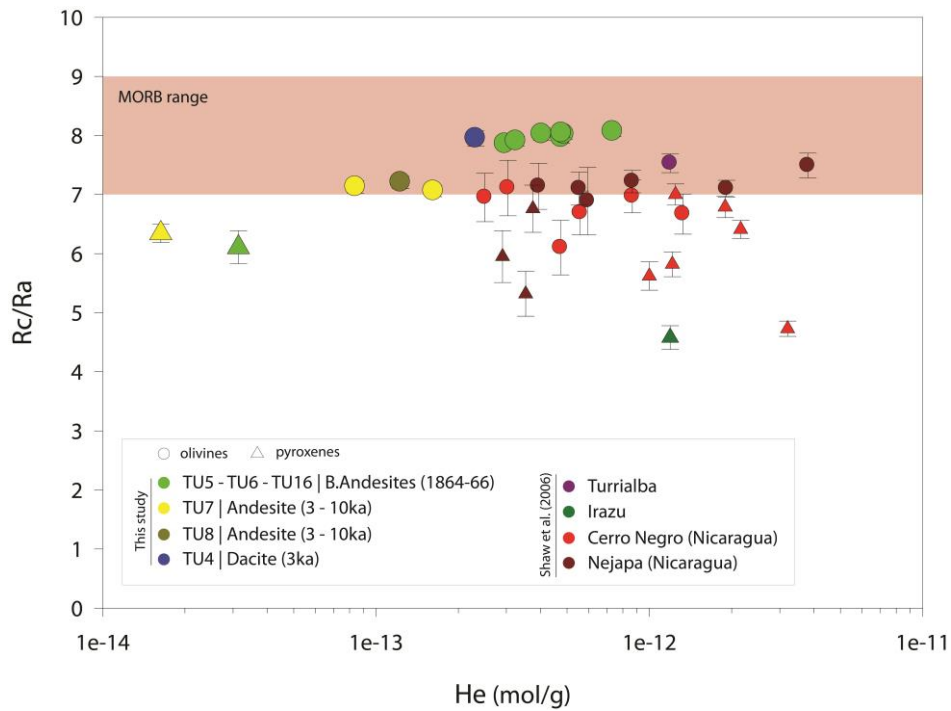

Fig. 3.16 – He concentrations (mol/g) against air corrected He-isotopic ratio basing on the ^{4}He/^{20}Ne ratio (Giggenbach et al., 1993). Data from this study and Shaw et al. (2006) are plotted. The reddish area indicates the He-isotope composition of MORB (Rc/Ra = 7 – 9; Graham, 2002).

Despite the observed variability, the $^3He/^4He$ ratio of fumarolic gases and FI from Turrialba volcano is well in the range of arc related volcanism (~7–8 Ra; Hilton et al., 2002), and represents the signature of mantle wedge below the area. If we compare these data with those from other volcanic systems of Central America (*Fig. 3.16*), it is possible to observe that Turrialba magmas derive from the most primitive source. Indeed, Cerro Negro and Nejapa are much more close to the boundary between HIMU-like and MORB-like values (i.e., 7 Ra), indicating that are slightly more contaminated at the source than Turrialba. This behavior is also suggested by the Sr-Nd isotope composition of Turrialba volcanics compared to those from Central America volcanism (*Fig. 3.9*). Many lavas from Central Costa Rica volcanoes (Reagan and Gill, 1989; Herrstrom et al., 2005; Feigenson et al., 2004) display an OIB-signature in their trace element geochemistry, whose origin is still a matter of debate. Feigenson and Carr (1993) proposed two different mantle reservoirs for this area, considering a MORB-like source and veins of enriched mantle cutting the former. Melting of this veined mantle source and its interaction with the subduction component produced magmas with typical arc signature (Carr et al., 2003; Feigenson et al., 2004). Abratis and Wörner (2001) suggest the presence of a slab window in the subducting Cocos Plate, allowing the Galapagos asthenosphere to rise through this window into the mantle wedge below south-central Costa Rica. Feigenson et al. (2004) consider the melting of the Galapagos modified mantle below Costa Rica and Panama as the cause of the formation of OIB signature. More recently Benjamin et al. (2007), Hoernle et al. (2008) and Gazel et al. (2009), explained this signature as due to the subduction of the Seamounts province, that originates from the Galapagos hotspot track. However they are in agreement that the transition from fluid-like slab, in the northern sector of the volcanic belt (e.g. Nicaragua), to melt-like slab in the south (Costa Rica), may be related to the influx of hot mantle through a slab window in the south (Abratis and Wörner, 2001). Turrialba volcano shows geochemical features related to an OIB-like source, as suggested in particular by trace elements pattern (e.g. Ba/La ratio = 20 − 34; see paragraph 3.3). The high He-isotope ratio measured in fumaroles and in fluid inclusions confirm the presence of a hot mantle source underneath the volcano. Coherently crustal tomography describes a large area of low crustal velocities underneath Turrialba and Irazu volcanoes (Husen et al., 2003). This zone narrows at shallow depth and extends directly beneath the two volcanoes. Lucke et al. (2008) found a low density body with gravimetric modeling, interpreted as a joint magma reservoir beneath Turriaba-Irazu volcanic complex at 1 - 10km depth. By anomalous receiver function conversions and tomography Husen et al. (2003) confirmed the presence of a magmatic body under Turrialba volcano and extended this zone to over 30km depth, where they estimate an absolute P-wave velocity of as low as 6.5 kms^{-1}. The presence of a hot mantle wedge underneath the volcano confirms that the contribution of radiogenic ^4He to

the mantle wedge below Turrialba by subducted sediments is negligible, as already inferred by Shaw et al. (2006).

A more general (i.e., worldwide) comparison of ^{3}He/^{4}He with ^{87}Sr/^{86}Sr ratios (*Fig. 3.17*) also supports what above stated and shows the coupling between these two tracers, which show a progressive decreasing of Rc/Ra values and contemporarily increase of ^{87}Sr/^{86}Sr ratios from MORB-like mantle toward a typical crustal end-member. Such a trend reflects a progressive increase of mantle contamination by crust, as generally observed in subduction-related environments. Likewise, Turrialba volcanism falls within the range of values measured at Etna (Italy), which is considered slightly affected by the subduction of African plate beneath the European one (e.g., Correale et al., 2012), and very close to a typical MORB mantle source.
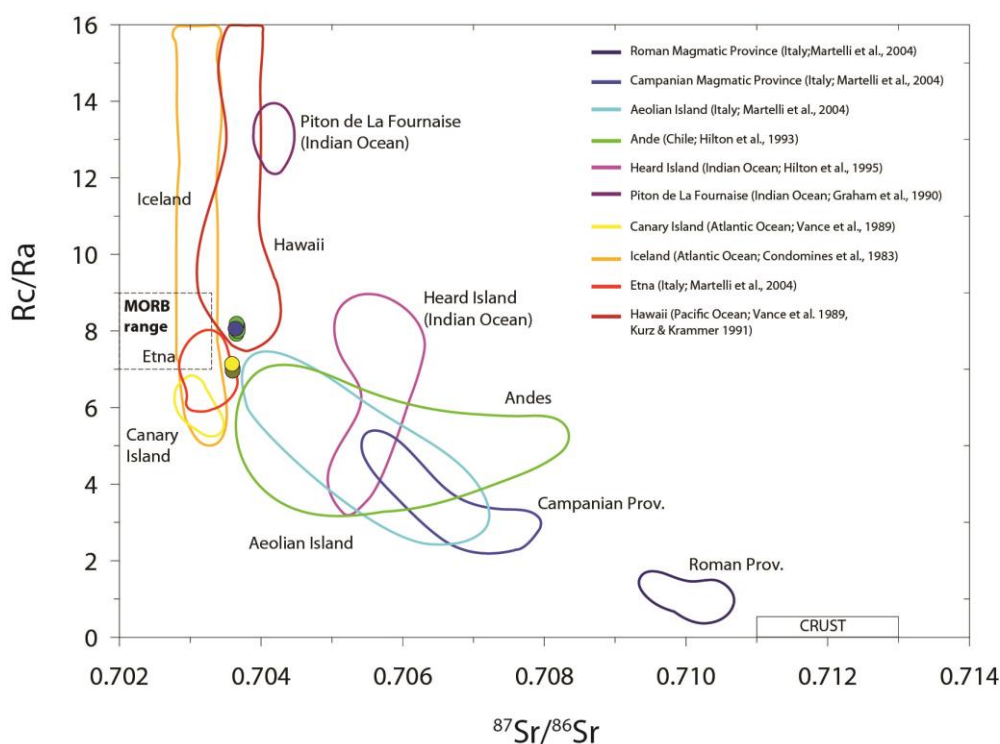
Fig. 3.17 – Rc/Ra ratio versus ^{87}Sr/^{86}Sr of some different geodynamic contests indicated by different colored fields. Data references are indicated in the figure.

3.5 Features of magma degassing at present day and inferences on the recent unrest phase

Since 1996, Turrialba volcano experienced a period of unrest, characterized by the broadening of the fumarolic field and the opening of new vents at the summit craters, associated also with phreatic

explosions. Geochemical and geophysical signals preceded and accompanied such period of unrest, as already shown by Tassi et al. (2004), Hilton et al. (2010) and Vaselli et al. (2010) towards magmatic-dominated conditions in its feeding system. *Figure 3.18* shows trends of some geochemical parameters during the last 15 years. In the upper part of the figure are shown changes in He isotopic ratio (corrected for air contamination) measured in free gases of West Crater (green line) and Central Crater (blu line), sampled also by Hilton et al. (2010), Vaselli et al. (2010).
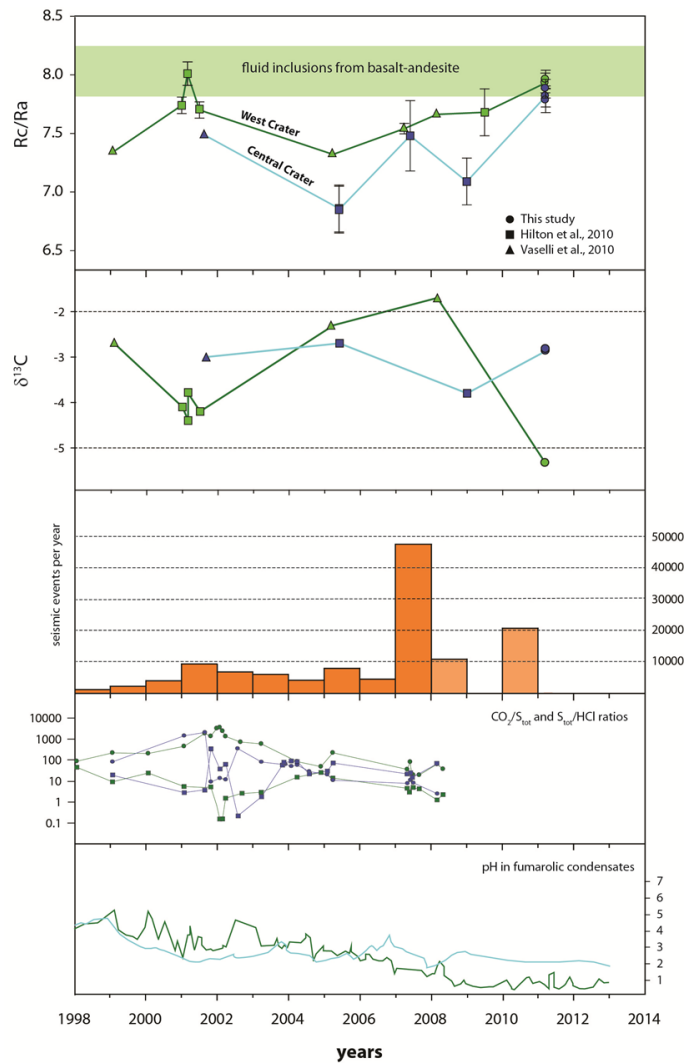
Fig. 3.18 - Geochemical and geophysical parameters variation through time (1998-2011). He isotopic ratios and C-isotope are from this study and Vaselli et al. (2010) and Hilton et al. (2010). Seismic events are from OVSICORI-UNA reports (http://www.ovsicori.una.ac.cr/). CO₂/S$_{tot}$ and S$_{tot}$/HCl ratios are after Vaselli et al. (2010). pH data are from Martini et al. (2010).

At the beginning of the unrest phase (1999), temperature of fumaroles was below 95°C at West Crater, and gas had an He isotopic ratio of 7.34 Ra. In coincidence with the seismic swarm occurred in 2001 (more than 9000 events per year; Martini et al., 2010), R/Ra increased to 8.01, reaching one of the highest values ever measured in Turrialba fumaroles. During this period a further increase in fumarolic activity and in the emission of magmatic gases was observed, even if not accompanied by a significant variation in fumarolic temperature (Tassi et al., 2004; Vaselli et al., 2010). In mid-2005 new fumaroles appeared along Ariete Fault (Martini et al., 2010; Vaselli et al., 2010), on the southern flank of the volcano. During this period He isotopic ratio decreases in both West and Central crater reaching values similar to the pre-unrest phase in West Crater (April 2005) and at the same time also a decrease in seismic activity was registered. Between 2005 and 2007 the He-isotopic ratio started to increase again in both craters. Peak in He-isotopic ratio were registered in Central crater fumaroles, in concomitance with two important seismic swarms recorded in mid-2007. In July 2007, the maximum activity to date, with 2000 event/day, was recorded for several days (Martini et al., 2010). At the same time the widening of the fumarolic field was accompanied by a strong increase in fumarolic activity, forming a plume that rose 2km high in the atmosphere (OVSICORI-UNA, 2007). After 2007 the contribution of magmatic gases to the crater fumaroles largely exceeded that of the hydrothermal fluids (Vaselli et al., 2010), with the result of a strong increase in gas temperature and concentrations of magmatic gases. Contemporaneously a strong acidification of condensates at fumarolic emissions was recorded (*Fig. 3.18*) and the interaction of acid gases with humidity allowed the precipitation of acid rains, mainly in the west sector of the volcano, that burned the vegetation and strongly affected the infrastructures downwind to the plume (OVSICORI-UNA, 2007, 2008; Martini et al., 2010). The He-isotopic ratio still increased after 2008, reaching in March 2011 some of the highest values ever measured on this volcano (West Crater, fumaroles SW1 = 7.93 Ra, F1 = 7.96 Ra). Temperatures at fumaroles and phreatic vents (the latter opened between 2010 to 2011) increased from ~ 300°C measured in 2008 to more than 600°C in 2011 (OVSICORI-UNA, 2012).

It's interesting to note that West Crater recorded over time an average He isotopic ratio higher than the Central one, but the common variation of this ratio at both craters suggest a common source for the degassing system of both craters. The difference in He-values between the two craters become negligible just in two separate occasions: in 2007, in coincidence with a major seismic swarm (in July 2007, when more than 30000 earthquakes in a month occurred; OVSICORI-UNA, 2007), and in 2011, one year after the phreatic explosion at the West crater. Moreover in both 2001 and 2011 He isotopic composition of fumarolic discharge matched the range measured in fluid inclusions of basaltic-andesites samples (7.86 − 8.07 Ra). During the 1998 - 2011 unrest period, the C-isotope

values were characterized by a wide variation at West Crater and a more constant trend at Central Crater (average $\delta^{13}C_{CO2}$ of -3.0‰V-PBD). At West Crater more negative $\delta^{13}C_{CO2}$ values were measured in 2001 $\delta^{13}C_{CO2}$ = -4.40‰V-PBD), in coincidence with peaks in $^3He/^4He$ ratio and seismicity, and in 2011 $\delta^{13}C_{CO2}$ of -5.34‰V-PBD).

Peaks in He-isotope ratios observed in 2001 and 2011 occurred in coincidence with negative values of $\delta^{13}C_{CO2}$, that reached values near to the typical C-isotope composition of a MORB-like source (-6.5±-2.5‰ V-PDB; Sano & Marty, 1995). As a matter of fact, in coincidence with these variations, peaks in seismic activity were also observed. Due to the strong limitations of the geodetic networks (Martini et al., 2010) and the relative lack of data, it is impossible to assess whether the unrest phase was characterized by magma uprising in the plumbing system. Martini et al. (2010) and Vaselli et al. (2010) agree in arguing that there has been no magma movement or injection of hot and fresh magma batches into the plumbing system of the volcano until 2008. Recently Conde et al. (2013) proposed a new interpretation of Turrialba unrest, combining SO_2 fluxes and different seismic signatures. From hypocenters distribution they identified two zone of magma storage, one at $4 - 6$ km, and a shallower one at roughly 1 km below the summit of the volcano. They suppose that during the period 2010 - 2011, the pulsating variations in gas discharge rates were most likely related to magma cycling by conduit convection and periodic injection of undegassed magma from below into the upper magma storage. In this view, the sharp increase in $^3He/^4He$ measured at fumaroles of the summit craters in 2001, could be related to the strong increase in seismicity that enhanced the formation of fractures, increasing the permeability of the gas discharge system. During this phase, the lack of SO_2 or magmatic gases in the fumarolic system (Vaselli et al., 2010) reinforces the hypothesis that no magma movements occurred. The increase in time of magmatic gas species, the appearance of SO_2 and halogens at fumaroles, the acidification fumarole condensates and the strong increase in fumarolic temperatures (from 90°C in 2002 to more than 600°C in 2011; Vaselli et al., 2010; OVSICORI-UNA, 2011, 2012) suggest an increase of magmatic fluids input in the plumbing system. About this phase, is not possible to know if there have been magma movement beneath the volcano, but as suggested by $^4He/Ar*$ and $^3He/^4He$ ratios during 2011, the refilling of the plumbing system by a less degassed, ^3He-rich and primitive magma, similar in composition with that involved in the last eruptive phase (1864-66 A.D.), may have occurred.

A similar behavior was observed in other volcanoes such as Etna (Rizzo et al., 2006; Nuccio et al, 2008; Paonita et al., 2012), Stromboli (Rizzo et al., 2009), El Hierro (Padrón et al., 2013) and Nysiros (Shimizu et al., 2005).

4. *Geochemical study of the degassing system of Turrialba volcano*

Geochemical monitoring of volcanic areas is crucial for assessing the state of activity of a volcano. In particular fluid geochemistry provides valuable insights into subsurface processes such as shifts in volcanic activity, the degassing behavior of a deep magmatic body, interactions between magmatic and hydrothermal fluids and evaluation on the geothermal reservoir (e.g. Rizzo et al., 2009; Chiodini et al., 2010; Paonita et al., 2012). During the uprising of a magma batch inside the volcanic feeding system, the dissolved volatiles in the magma are progressively released as a function of their relative solubility and decreasing confining pressure. Approaching the surface, the released magmatic fluids, rising along fractures and faults, can interact with hydrothermal systems or shallow aquifers. We present here a fluid geochemistry investigation of Turrialba volcano carried out during 2011 and focusing on fumaroles and diffusive soil degassing. The purpose of this study is to assess the degassing behavior of the volcano at the time of sampling, evaluating its state of activity and to increase the temporal dataset.

4.1 The Turrialba fumarolic discharge

The top of Turrialba volcano is characterized by three craters aligned NE-SW direction (*Fig. 4.1*), nested in a 1.2km long scissor-shape depression, at an altitude higher than 3000m a.s.l.. At the beginning of the unrest phase (in 1996) the crater summit contained only two small fumaroles (Vaselli et al., 2010): one in the southwestern part of the Central Crater (hereafter, CCr) and the other one in the northern rim of the West Crater (hereafter, WCr). In April 2002 a 4-m wide fracture, named "Quemada", opened between the WCr and the CCr discharging fluids at 90°C (*Fig. 4.1*; Tassi et al., 2004). Contemporaneously, new fumarolic vents and cracks opened in the northern and southern flanks of the WCr and within the CCr (Vaselli et al., 2010). In June 2005 the fumarolic activity increased strongly, discharging fluids at 90 - 92°C (OVSICORI-UNA, 2005). At the same time, the activity had propagated south to the top of the volcano, with the formation of new fumaroles at an elevation of 2600 - 2700m a.s.l., inside the NE-SW-oriented regional fault named "Falla Ariete" (Vaselli et al., 2010). But it is after the summer of 2007 that a dramatic increase in degassing activity was registered, with the extension of the fumarolic field and the relative formation of a gas plume that sometimes rose 1- 2km high in the atmosphere (OVSICORI-UNA, 2007, 2008). During 2008 the formation of a radial fracture system was observed in the outer southern rim of the WCr and contemporaneously, in the inner northern part of the same crater

(Vaselli et al., 2010). In January 2010 a phreatic explosion produced a 55 x 20m vent on the western rim of the WCr, discharging gas at high pressure and with temperature higher than 600°C (*Fig. 4.1*; OVSICORI-UNA, 2010). In January 2011, immediately before the investigation presented in this study (in March 2011), another ash discharge occurred at the 2010-vent. It is important to note that no juvenile materials has been recognized in the ash emitted by these events (OVSICORI, 2010, 2011).
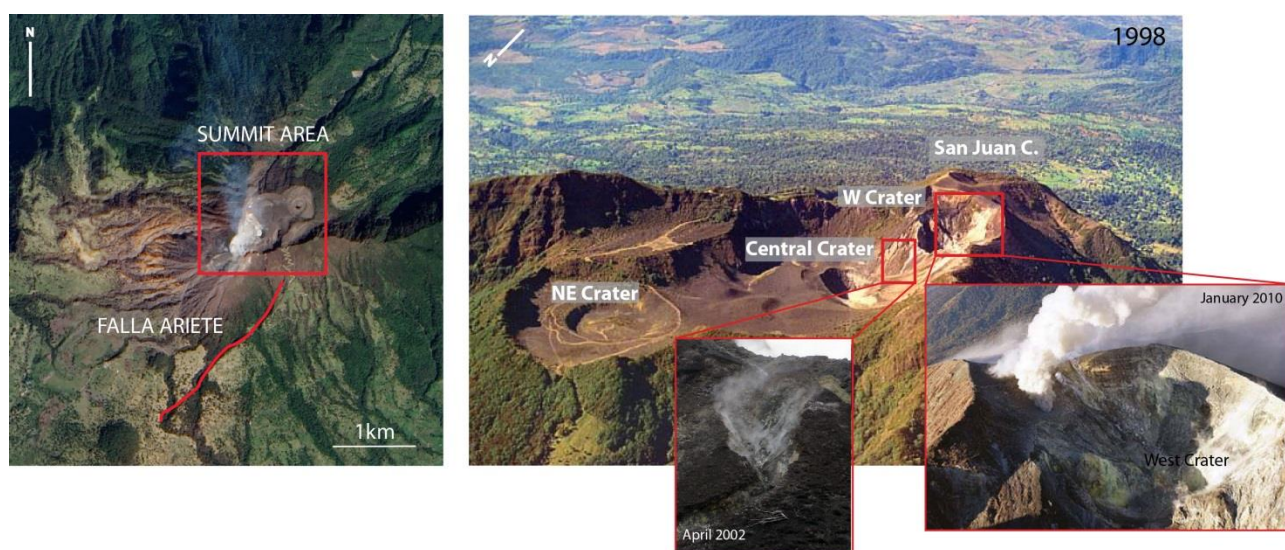
Fig. 4.1 – a) Satellite image of Turrialba volcano area. The red box indicate the summit crater area; the red line is the "Falla Ariete" tectonic lineament. b) Close-up of the summit area of Turrialba volcano shot in 1998; the red boxes show some changes occurred at the top of the volcano in the following 15 years.

4.2 Previous studies

The monitoring of fumarolic gas discharges at Turrialba volcano started in 1980 with weekly measurements by the OVSICORI-UNA team of fumarolic output temperature, sampling of condensates (pH, F and Cl; every month), rain waters (pH, electrical conductivity and main solutes), SO_2 fluxes and Radon. Since 1996 the geochemical monitoring was implemented, including periodical chemical (Tassi et al., 2004; Vaselli et al., 2010) and isotopic (Hilton et al., 2010; Vaselli et al., 2010) analyses of fumarolic gases. In particular data of WCr and CCr are available since 1998 (Tassi et al., 2004; Vaselli et al., 2010) and of peripheral gas discharge at "Falla Ariete" since 2007 (Vaselli et al., 2010). Regarding the temperature of fumaroles, Vaselli et al. (2010) measured fumarolic temperatures in the range of 86°C (CCr, 2001) to 94°C (Falla Ariete, 2008), corresponding approximately at the water boiling temperature at the respective sampling altitudes.

Only one site showed a high temperature of 282°C (in February 2008). Studying the evolution of SO_2/CO_2, HCl/CO_2 and HF/CO_2 ratios at the monitored fumaroles in the WCr and CCr, Vaselli et al. (2010) distinguished three main stages of activity (*Fig. 4.2*): 1) a "hydrothermal stage" (1998-2001), characterized by relative low fumarolic emissions with gas composition dominated by H_2O and CO_2, with significant amount of H_2S, N_2, HCl, H_2 and minor concentration of HF, CO and CH_4; 2) a "hydrothermal-magmatic stage" (2001-2002), marked by the appearance of SO_2 at the fumaroles of the CCr, in November 2001, dominated by strong input of magmatic gases into the hydrothermal reservoir; 3) the "magmatic-dominated" stage (2002 – 2008) was indicated by the increase of sulfur gas species at both WCr and CCr, the widening of the fumarolic field and the formation of new low-T fumaroles on the flanks of the volcano ("Falla Ariete").
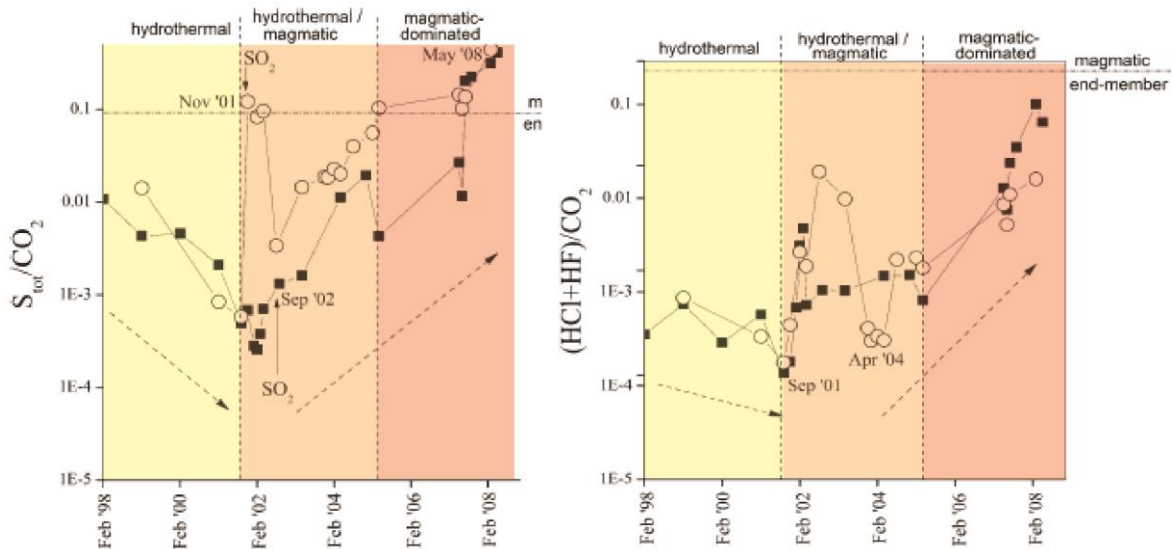
Fig. 4.2 – (Stot/CO₂) and (HCl+HF)/CO₂ vs. time measured in Central Crater (open circles) and West Crater (closed squares) fumaroles of Turrialba volcano between 1998 and 2008 (modified after Vaselli et al., 2010).

The He-isotopic signature (R/Ra= 7 – 8; where R is the $^3He/^4He$ measured in the gas sample and Ra is the same ratio measured in air = 1.39 x 10^{-6}) closely resembling that of mantle-related He in subduction zones (Poreda & Craig, 1989), suggests the presence of an active magmatic source beneath Turrialba volcano (Hilton et al. 2002; Shaw et al., 2003; Hilton et al., 2010; Vaselli et al., 2010). In particular Turrialba fumaroles display the highest He-isotope ratio measured in the Nicaragua – Costa Rica segment of the Central America volcanic belt (Shaw et al., 2003; Tassi et al., 2004; Shaw et al., 2006) and similar to values measured in other volcanoes such as Pacaya, Mombacho (Garofalo et al., 2006) and Poás (e.g. Shaw et al., 2003; Hilton et al., 2010).

Hilton et al. (2010) observed an important increase in He-isotopic ratio in coincidence with peaks in seismic activity. The carbon isotope record ($\delta^{13}C$) at Turrialba volcano shows broad variation from -4.8‰ V-PDB (CCr, in February 1999; Vaselli et al., 2010) up to -0.2‰ V-PDB (WCr, in March 2008; Vaselli et al., 2010), remaining slightly higher than the nominal range found in MORB (-6.5±-2.5‰ V-PDB; Sano & Marty, 1995). The relative proportion of CO_2 and ^3He (given as the $CO_2/^3He$ ratio), measured at Turrialba volcano, ranges between 5.2 x 10^9 (WCr, in February 1999; Vaselli et al., 2010) and 28.6 x 10^9 (WCr, in April 2005; Vaselli et al., 2010), and all values are averagely higher than those usually associated with MORB-mantle (~2 x 10^9; Marty & Jambon, 1987). The values are similar to those found at other subduction-related volcanoes worldwide (Sano & Williams, 1996).

These studies suggest that in the last decade Turrialba volcano experienced changes in the equilibrium between a hot deep magmatic source and a shallow aquifer, the latter operating as a buffer (Tassi et al., 2004; Martini et al., 2010). Gas geochemistry suggests a de-pressurization of the "degassing" magma body. However, if there have been magma movements (upraise) is still a matter of debate. Despite the few deformation data indicating a possible inflation pattern in 2007, reversed into deflation in early 2008, the characterization or quantification of this deformation is impossible due to the strong limitations of the geodetic network (Martini et al., 2010). Martini et al. (2010) and Vaselli et al. (2010) agree in arguing that there has not been any magma movement or new injection of hot and fresh magma batches into the plumbing system of the volcano until 2008. Recently Conde et al. (2013) proposed a new interpretation of Turrialba unrest, combining SO_2 fluxes and different seismic signatures. From hypocenters distribution they identified two zones of magma storage, one at 4 – 6 km, and a shallower one at roughly 1 km below the summit of the volcano. They supposed that during the period 2010 - 2011, the pulsating variations in gas discharge rates were most likely related to magma cycling by conduit convection and periodic injection of undegassed magma from below into the upper magma storage.

4.3 Methodology and sampling strategy

The March 2011 survey was a comprehensive and detailed geochemical study and it consisted of the repetition of the 2008 survey with the aim of comparing the two datasets and to define the new degassing path system in the summit area and in peripheral sites of the volcano. Moreover chemical and isotopic analyses of gas sampled from soil, fumaroles and peripheral sites were performed in order to implement the temporal dataset and to better define the evolution of the unrest phase.

The diffuse soil flux of CO_2 has been measured by portable accumulation chamber (a.c.; Chiodini et al., 1998; Carapezza and Granieri, 2004), with a net internal volume of 3 x 10^{-3} m^3, placed on dry soil, carefully avoiding any evident viscous degassing spots. The accumulation chamber was equipped with a LI-820 infrared detector (0 – 2 vol.%) for CO_2 (*Fig. 4.3*).
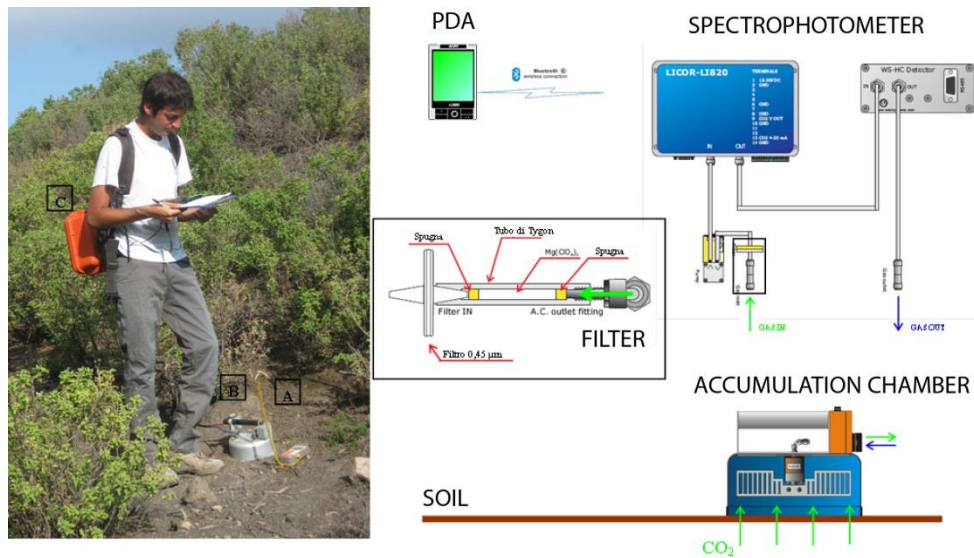
Fig. 4.3 – Illustrative sketch of the instruments adopted to carry out the CO_2 soil flux investigation.

For the production of gas flux contour maps and the calculation of total degassing rate, data were geostatistically treated using the kriging in Golden Software Surfer 8.0©. For the survey a model was selected that best fits the experimental semivariogram. Once a regular grid of flux values is obtained, total flux was calculated by multiplying the areas between selected isopleths by the average of the relative measured flux values. The normal probability plot graphical method was used to select anomaly thresholds (or flux isopleths). The normal scores of the data set are plotted versus measured fluxes: a linear trend indicates a normal distribution; a curved pattern indicates skewed distribution; straight line segments mark different population in the data set. The lowest flux class is usually attributed to the background, representing the biological CO_2 produced by soil respiration (Kucera & Kirkham, 1971). In the case of Turrialba volcano all the flux populations were attributed to an endogenous gas source, due to the complete absence of vegetation in the surveyed area. In order to obtain a detailed CO_2 soil flux map, a total of 973 measurements were performed in the summit depression of the volcano, drawing a 30m-spacing measurements regular grid and covering a surface of 0.807 km^2. Together with the CO_2 soil flux survey, soil temperature

measurements were carried out using the same 30m-spacing grid of carbon dioxide measurements, measuring temperature at 10cm depth into the soil. In order to produce a soil gas concentration map, we collected samples in 229 sites where CO_2 flux was higher than 15ppm/sec. Gas was collected inserting a probe in the soul at ~10cm depth.

Fluids collected consist of gases released by fumarolic emissions. We sampled 8 T-buffered (80 - 85°C) and 2 high-T sites (260 – 336°C), the latter at the bottom of the West Crater. Temperature was measured by inserting a thermocouple probe into the fumarole to a depth of ~ 20 cm. Gas was sampled following the methodology described in Sortino et al. (2006) and all the chemical analyses were performed at the laboratories of Istituto Nazionale di Geofisica e Vulcanologia sezione di Palermo. The CO_2 content was analyzed by potentiometric titration, whilst the concentration of He, H_2, O_2, N_2, CO and CH_4, were analyzed by portable gas chromatograph (Clarus 500, Perkin Elmer) equipped with a 3.5m Carboxen 1000 column and double detector (hot-wire detector and flame ionization detector), with analytical error lower than 3%. Dry gas samples were collected in two-way Pyrex bottles with vacuum valves at both ends, with the aim of determining the isotopic composition of C, He and Ne. The carbon isotope composition was measured by a dual-inlet mass spectrometer (Finnigan Delta Plus) after applying standard purification procedures to the gas samples. The isotopic compositions of CO_2 are expressed as $\delta^{13}C$ V-PDB (Vienna-PeeDee Belemnite), for which the analytical errors were lower than 0.2‰ V-PDB. The He-isotope composition, as well as the $^4He/^{20}Ne$ ratios, were determined separately admitting He and Ne into a split flight tube mass spectrometer (Helix SFT) after standard purification procedures. Helium isotope compositions were expressed as relative to He-isotopic ratio of air (R/Ra), and the analytical errors are lower than 0.3%. The R/Ra were corrected for the atmospheric contamination, using the $^4He/^{20}Ne$ ratio (Sano & Wakita, 1985).

4.4 Results

The geochemical survey was carried out between 9 and 20 March 2011, taking advantage of the dry season. The broader investigated area extends on the summit crater area, covering the entire scissor-shape depression opened to the NE. The zone was chosen due to the presence of two active degassing craters (WCr, CCr), involved in the most recent eruptive activity (1864-66 A.D.; Reagan et al., 2006), and to the high CO_2 soil flux degassing already ascertained by the March 2008 prospection. The comparison with similar past investigations is useful to better constrain the state of activity of the volcano and to assess the hazard from endogenous CO_2 emissions in this area frequented by tourists, coming to visit the Turrialba National Park. Another sector of the volcano was selected due to the opening of new fumaroles in 2007 (OVSICORI-UNA, 2007). These

fumaroles are situated along the NE-SW oriented "Falla Ariete", at 2600-2700m a.s.l., in the southwestern flank of the volcano.

4.4.1 The CO_2 soil flux surveys

The broader survey was performed on the top of the volcano, covering the entire summit region. The investigation was conducted by accumulation chamber method described in the previous paragraph. As a total 973 measurements were carried out with a spacing of 30m, over a surface of 0.807 km^2. Values of the CO_2 soil flux, display a wide variation, ranging from 0.4 to 52,090 gm^{-2}d^{-1} (*Fig. 4.4c*). In *Fig. 4.4a* the shape of the normal probability plot shows at least 7 flux populations. Assuming that the entire flux of CO_2 from the soil is related to an endogenous source, the different classes identified are due to variations in soil permeability and to the presence of degassing structures. The total flux of CO_2 from the soil is estimated to 3.43 t/ha per day. The distribution of CO_2 soil flux map of the investigated sector is shown in *Fig. 4.4*. It is clear that the zone affected by the highest degassing is that comprised between the West Crater and the Central Crater; in particular the highest values of CO_2 flux occur in the northwestern sector of the CCr and CO_2 anomalies tend to decrease moving toward northeast. As already observed in other studies (e.g. Barberi & Carapezza 1994; Giammanco et al., 1998) this kind of geochemical prospection is a useful tool to recognize buried volcanic structures or volcano-tectonic alignments. Looking at the entire CO_2 anomaly (*Fig. 4.4*), it displays an elliptical shape, slightly squashed, and oriented in a NE-SW direction, coherent with the main regional tectonic features.

Furthermore, observing carefully the geometry of the flux anomalies it is possible to distinguish at least four buried crater rims, nested one with the other, and located between the Central and the NE Crater. They could be related to the volcanic activity immediately preceding the most recent eruption occurred in 1866 A.D., whose products covered the entire summit of the volcano.

Along with the flux survey we carried out temperature measurements of soil at depth of 10cm and results are showed in *Fig. 4.5*. Temperature ranges between 5°C and 85°C and the highest values are concentrated between the West and Central Crater. The zones affected by soil temperature anomalies essentially coincide with those with soil flux anomalies. No temperature anomalies were registered during this survey in the northeastern sector of the summit terrace.
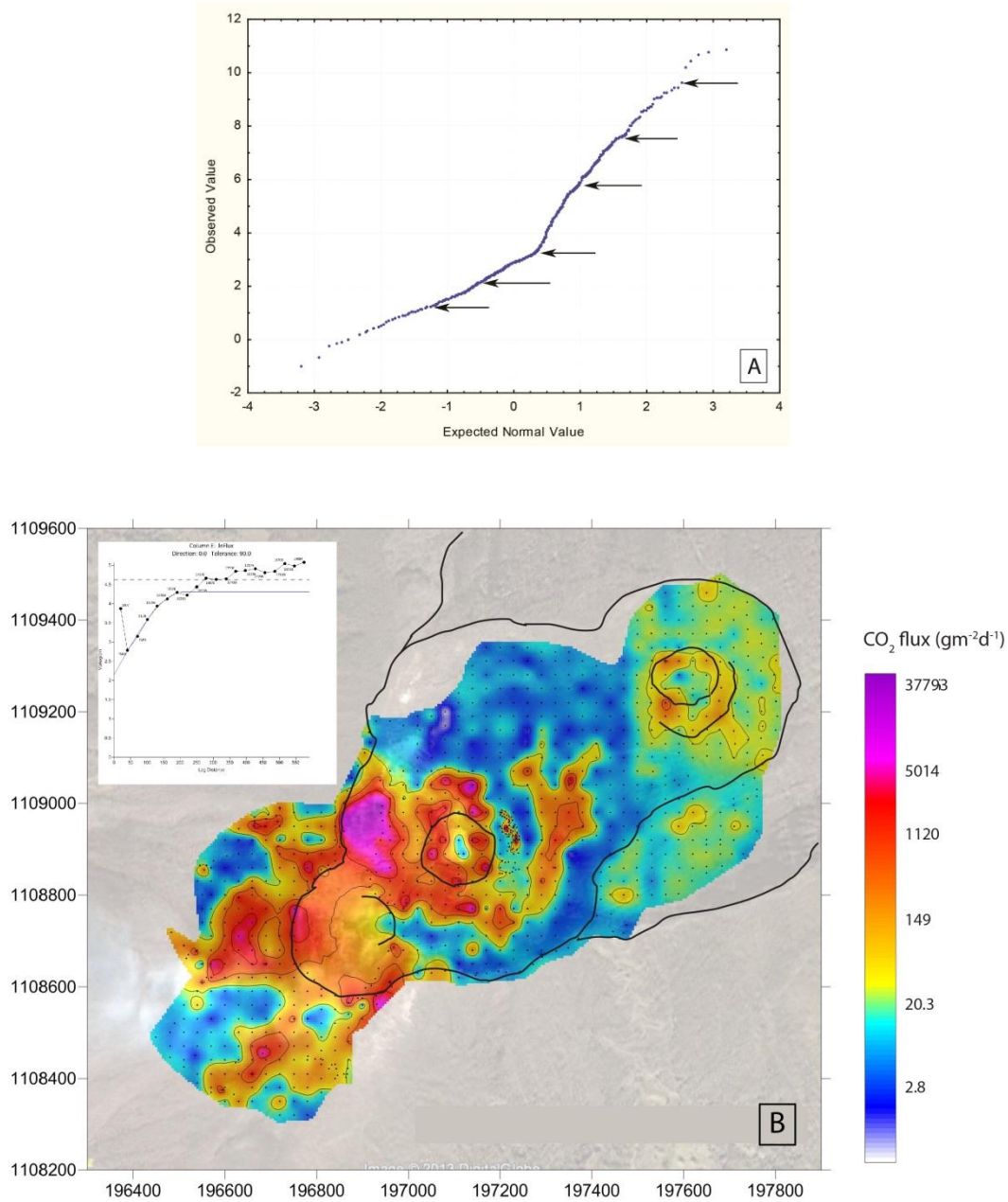
Fig. 4.4 – A) Normal Probability Plot of the measured CO_2 soil flux values with indication of the selected classes. B) CO_2 soil flux map of the crater area. The base map is a satellite image of the area. Black dots are measurements points.

A total of 5 profiles of soil CO_2 flux and temperature were performed at "Falla Ariete" (*Fig. 4.6*), a tectonic structure N40°E oriented, forming a narrow watershed completely covered by vegetation. This tectonic feature cut the entire south-southwestern flank of the volcano, forming a scarp ~20m high. The survey was performed between 2600 – 2800m a.s.l., and due to the irregular morphology generated by the fault, the profiles were not perfectly perpendicular to the tectonic structure. In addition these measurements were performed in proximity to where similar investigations had been
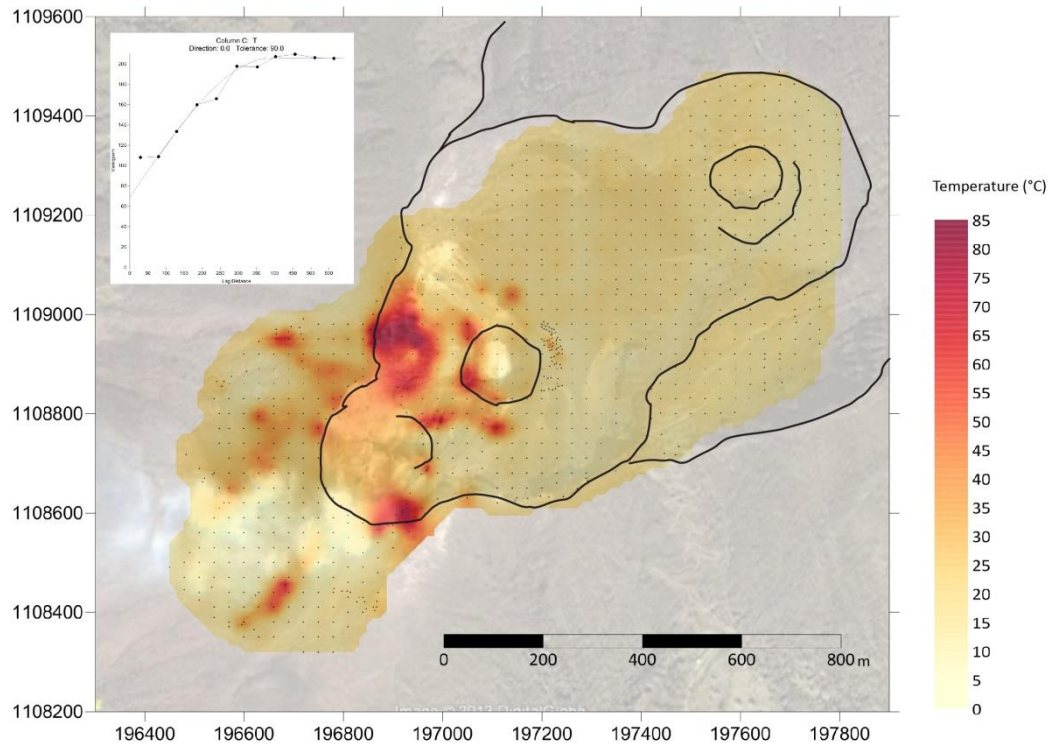
Fig. 4.5 – Distribution of soil temperature (-10 cm depth) in the crater area and related semivariogram with the calculated fit line (blue), used to obtain the map.

made in 2008; the comparison between the two investigations will be discussed in a next section. CO_2 flux anomalies were identified in three out of five profiles.

First and fifth profiles do not show any anomaly with the exception of a single point along the first profile where a CO_2 soil flux of 751 $gm^{-2}d^{-1}$ was measured. Profiles second to forth display the highest anomalies which occur in an area characterized by the junction of two tectonic structures. The second profile is characterized by two different peaks of CO_2 flux and soil temperature anomaly, reaching a maximum value of respectively 2112 $gm^{-2}d^{-1}$ and 73.7°C; this profile was made in an area with a high density of fractures. The third profile showed the highest peak in flux anomaly, with a value of 5375 $gm^{-2}d^{-1}$, that was measured in the bottom of the watershed. The forth profile displays a narrow peak with a single high value of CO_2 soil flux of 3645 $gm^{-2}d^{-1}$. Simultaneously temperature profiles were carried out, inserting a thermocouple at ~10cm into the soil. Temperatures varied from 9.2°C and 73.7°C, with the highest values measured close to the fumarolic emissions and coincident with the highest CO_2 soil flux (profile 2, *Fig. 4.6*).
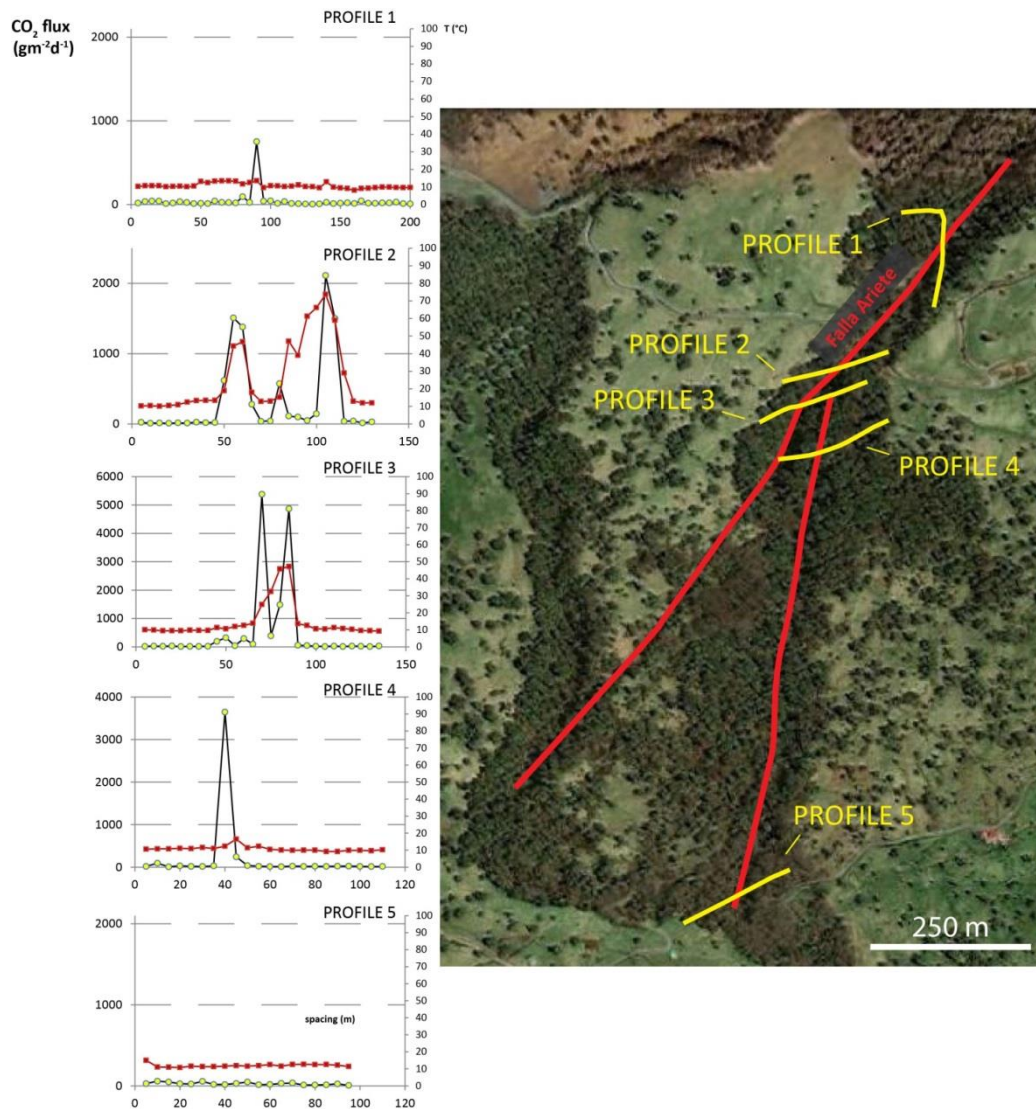
Fig. 4.6 – CO_2 soil flux (yellow circles) and soil temperatures (red squares) measurements along Ariete Fault.

4.4.2 Soil gases concentration

As a total 229 measurements were performed in the summit crater area with the aim of mapping the gas concentration distribution in the soil. The sampling sites were chosen by discarding those with CO_2 soil flux lower than 15 ppm/sec, for this reason the array was locally not regular. The sampled sites are shown in *Fig. 4.7*.

CO_2 soil concentration ranges between 3% and 100%. The highest values were measured in a wide area between West and Central Crater, where some of the highest CO_2 soil flux and soil temperature had been measured. The Western Crater could not be investigated due to the strong degassing in its inner part, but its outer rim was covered, displaying punctual anomalies near San Juan Crater and in the northern flank, where respectively 98% and 100% of CO_2 were measured. He soil concentration varies between 2.4 and 18.5 ppm. The area between WCr and CCr is still the zone where He concentration anomalies are more widespread. Surprisingly the highest He value was measured in the outer northern flank of the WCr (He= 18.5 ppm). The concentration of H_2 in the crater area ranges between 0.1 and 2320 ppm. The highest values were measured in the southern rim of the WCr and in the western side of the CCr, where a large H_2 anomaly was observed.
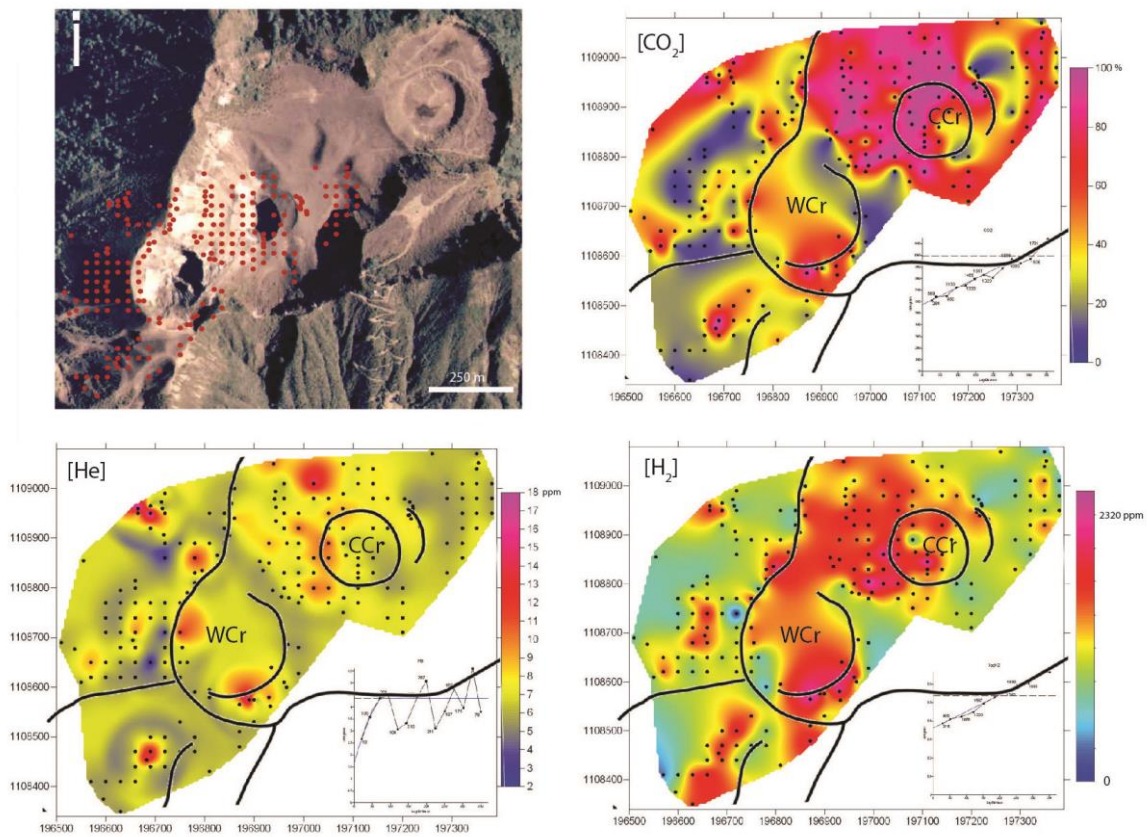
Fig. 4.7 – Site sampling location and maps of CO_2 concentration (%), He (ppm) and H_2 (ppm), in the soil.

4.4.3 Chemical composition of fumaroles

The chemical composition of 9 fumaroles located between the West and Central Crater was and data are listed in *Tab. 4.2*. Seven fumaroles are T-buffered, showing a temperature lower than 90°C (maximum measured temperature), whilst two fumaroles have high-temperature (140 – 456°C); the latter were sampled at the bottom of the WCr. The sampled fumaroles are CO_2-dominated emissions (CO_2 = 72 - 97%) in dry gases, with low to significant concentration of CO (0.3 – 54 ppm), low helium content (3.4 – 5.8 ppm) and very low methane (CH_4 = 0.1 – 0.5 ppm). Atmospheric contribution is negligible as attested by O_2 and Ne concentration (O_2 = 0.006 – 0.01 %; Ne = 0.07 – 0.8 ppm). In the fumaroles sampled outside the crater area, a decrease in CO_2 content (CO_2 = 17 – 45 %) and an appreciable increase of the atmospheric-related components (O_2 = 0.4 –14 %; Ne = 0.9 – 13.4 ppm) was noticed. Ternary diagram He-N_2-CO_2 (*Fig. 4.8*) displays an appreciable air contamination in fumaroles of the Central Crater sampled during March 2011. Our data are plotted with those of Vaselli et al. (2010) for comparison. All fumaroles are strongly enriched in CO_2 and lies on a mixing line between an atmospheric and a magmatic end member.
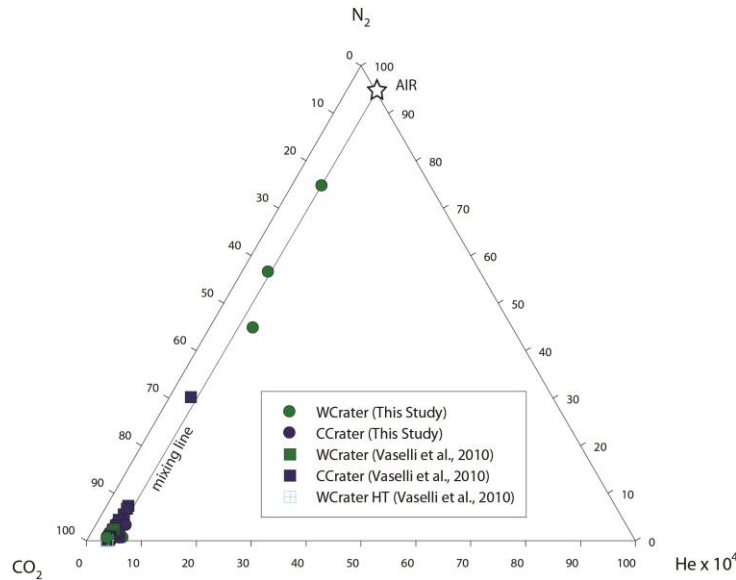
Fig. 4.8 - He–N_2–CO_2 ternary diagram showing the mixing between the magmatic and atmospheric components. Central Crater fumaroles sampled in 2011 (this study) are always strongly air-contaminated, while West Crater fumaroles (this study and data from Vaselli et al., 2010) are generally air-free.

The He-isotope composition of free gases measured in samples collected during this investigation (*Fig. 4.9*), was extremely high at both West and Central Crater (respectively 7.93 – 7.96 Ra and 7.78 – 7.88 Ra). As previously noticed for gas composition, also the He-isotope ratio decreases

significantly moving away from the West and Central Crater. In particular ratios of 5.82 Ra and 5.87 Ra were measured in the outer rim of the Western Crater, and a value of 7.08 was measured east to the Central Crater.
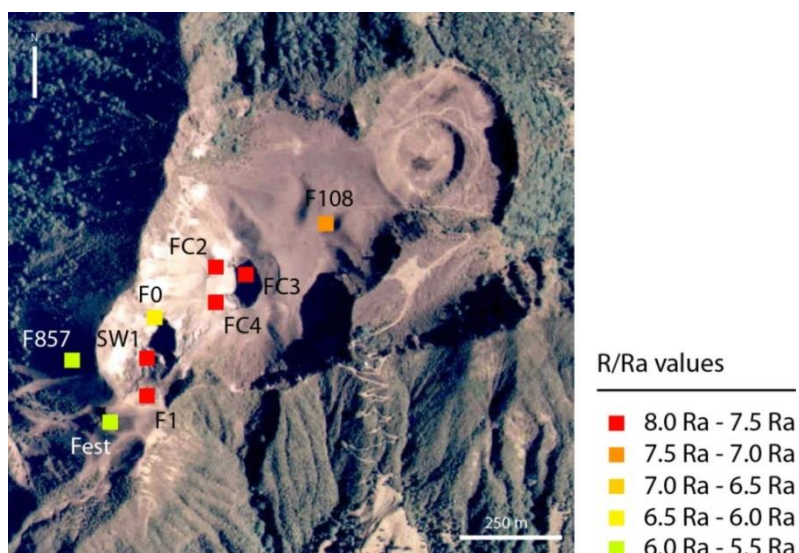
Fig. 4.9 – Location and He-isotope composition of the sampled fumaroles

The $\delta^{13}C_{CO2}$ measured in low-temperature fumaroles varies between -1.8‰ and -2.9‰ V-PBD (*Tab. 4.3*). Only one high temperature fumarole (456°C), inside the West Crater, shows a significantly more negative $\delta^{13}C$ value of -5.34‰ V-PBD (the sample shows also a lower CO_2 concentration with respect to the other fumaroles; see *Tab. 4.2*).

Tab 4.2 – Chemical composition of the analyzed fumaroles

Sample	Sector	Coordinates	He ppm	H_2 ppm	O_2 %	N_2 %	CO ppm	CH_4 ppm	CO_2 %
Turrialba SW1	SW Crater	10°01'07"N 83°45'53"W	2.7	132	0.0069	0.39	5.3	-	72.26
Turrialba F1	SW Crater	10°01'01"N 83°45'54"W	6	684	0.011	0.52	45	0.5	87.16
Turrialba F0	SW Crater	10°01'09"N 83°45'53"W	4.5	9	12.4	51.47	10	2.3	35.15
Turrialba F857	SW Crater	10°01'05"N 83°46'00"W	7.7		10.64	42.72	0.4	1.1	45.1
Turrialba Fest	SW Crater	10°01'00"N 83°45'57"W	5	-	14.67	66.3	2.1	2.1	17.54
Turrialba FC4	Central Crater	10°01'14"N 83°45'47"W	6	9	-	0.52	4.1	0.1	95.38
Turrialba FC2	Central Crater	10°01'14"N 83°45'43"W	6	97	0.059	3.36	0.9	0.1	96.37
Turrialba FC3	Central Crater	10°01'12"N 83°45'45"W	-	5	0.3	1.43	6.8	1.1	94.02
Turrialba 108	NE to CCr	10°01'18"N 83°45'37"W	5.5	5.5	0.44	1.75	0.5	-	97.56

Tab. 4.3 – Temperature and isotopic composition of the analyzed fumaroles

Sample	Sector	date (dd/mm/yy)	Temp.	He ppm	H$_2$ ppm	O$_2$ %	N$_2$ %	CO ppm	CH$_4$ ppm	CO$_2$ %	R/Ra[1]	[He] ppm	[Ne] ppm	He/Ne	Rc/Ra[2]	Rc/Ra$_{ERR +/-}$	δ^{13}C$_{CO2}$ (‰ PDB)
Turrialba SW1	W Crater	16/03/11	456°C	2.7	132	0.0069	0.39	5.3	-	72.26	7.88	3.43	0.08	44.8	7.93	0.084	-5.34
Turrialba F1	W Crater	20/03/11	90°C	6	684	0.011	0.52	45	0.5	87.16	7.92	5.41	0.09	60.6	7.96	0.080	-
Turrialba F0	W Crater	20/03/11	140°C	4.5	9	12.4	51.47	10	2.3	35.15	2.21	5.55	13.43	0.4	6.24	0.096	-1.89
Turrialba F857	W Crater	20/03/11	-	7.7		10.64	42.72	0.4	1.1	45.1	3.63	7.41	10.57	0.7	5.82	0.078	-2.39
Turrialba Fest	W Crater	20/03/11	84.5°C	5	-	14.67	66.3	2.1	2.1	17.54	2.35	5.88	13.38	0.4	5.87	0.081	-2.8
Turrialba FC4	Cent. Crater	20/03/11	85°C	6	9	-	0.52	4.1	0.1	95.38	7.81	5.54	0.18	30.8	7.88	0.080	-2.83
Turrialba FC2	Cent. Crater	20/03/11	83°C	6	97	0.059	3.36	0.9	0.1	96.37	7.52	5.87	0.80	7.4	7.82	0.090	-2.87
Turrialba FC3	Cent. Crater	20/03/11	70.3°C	-	5	0.3	1.43	6.8	1.1	94.02	7.77	5.06	0.03	170.7	7.78	0.103	-2.89
Turrialba 108	NE to CCr	20/03/11	-	5.5	5.5	0.44	1.75	0.5	-	97.56	6.76	5.70	0.95	6.0	7.08	0.095	-2.94

[1] R/Ra is the measured ^{3}He/^{4}He ratio divided by the ^{3}He/^{4}He in air = 1.4 x 10^{-6}

[2] Rc/Ra is the air corrected He isotopic ratio basing on the ^{4}He/^{20}Ne ratio (Giggenbach et al., 1993)

4.5 Discussion

Previous works on Turrialba volcano described a strong variation in temperature and composition of fumarolic gases suggesting an increasing input of magmatic fluids (Vaselli et al., 2010; Martini et al., 2010). All the geochemical parameters collected during our survey confirm that in 2011 there was still a strong input of magmatic gases, with some variations compared to previous surveys. In particular the CO$_2$ flux survey shows some differences with respect to that performed in March 2008 (*Fig. 4.10*). In spite of only a slight decrease in total flux (3.43 t/ha per day in 2011 and 3.96 t/ha per day in 2008), the spatial distribution of the anomalies is fairly different. In particular, the extensive CO$_2$ flux anomaly around the WCr observed during the 2008 survey, resulted reduced during 2011-survey. Something similar happened at the CCr, where the flux anomaly of 2011 is more restricted and concentrated northwestward to the bottom of the crater. A new degassing structure is evidenced by 2011-survey, between the Central and the NE crater. The shape of this anomaly could suggest the presence of a buried crater rim in this sector. Generally the CO$_2$ flux anomaly during 2011-survey appears to be more fragmented respect to the 2008-survey, when the soil gas flux seemed more uniform in the crater area.
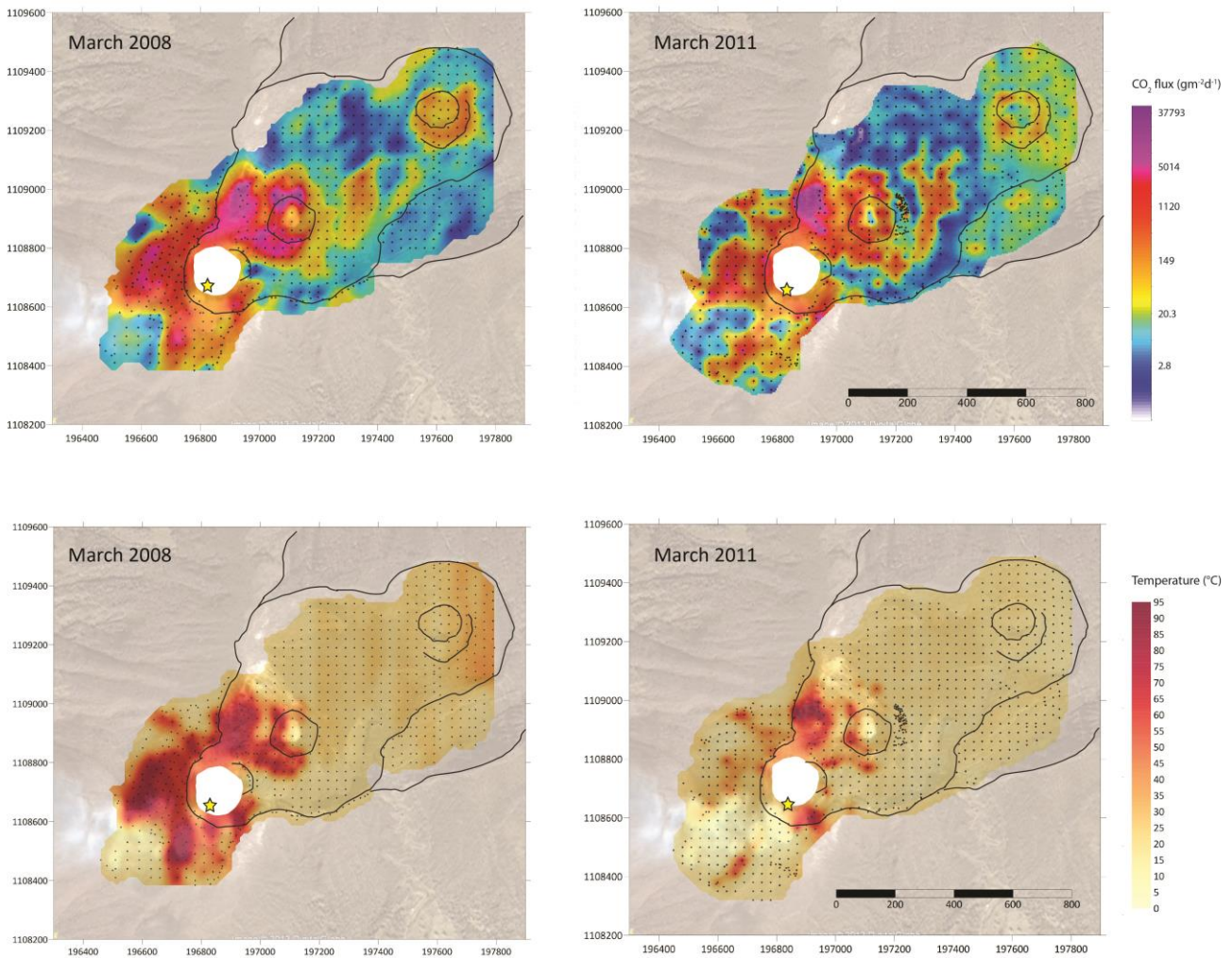
Fig. 4.10 – Comparison between CO_2 soil flux and soil temperature at -10cm depth of the 2008 and 2011 surveys. Black lines reproduce the geometry of the crater terrace.; the yellow star indicates the 2010 phreatic vent. The white-colored area was not investigated.

The difference between the two surveys is even more relevant comparing soil temperature data. In March 2008 the area affected by temperature anomaly was much larger than that observed in March 2011. In particular the western and southwestern sectors of the WCr, show a sensible lowering in temperature, with the main anomaly concentrated in the northern sector of the CCr. It is important to remember that just one year before the 2011-survey a phreatic explosion occurred in the WCr, with ash emission continued until January 2011. The coinciding decrease of CO_2 soil flux anomaly and soil temperature could be explained with the opening of this vent that substantially would have acted as a drain for the fluids rising inside the shallower feeding system of the volcano. It is interesting to note that during the March 2011-survey the main anomalies were clustered in a sector

comprised between WCr and CCr, where a new phreatic vent opened in May 2011 (OVSICORI-UNA, 2012).

Fumaroles of West and Central crater display a similar chemical composition, with CO_2-dominated emissions, suggesting a common source feeding both craters with a strong magmatic signature. No remarkable compositional variations were observed with respect to the gas samples collected by Vaselli et al. (2010) in 2008. This would suggest that during our 2011-survey Turrialba was still in the "magmatic-dominated" stage identified by these authors.

The He-isotopic values measured in 2011 (see *Tab. 4.3*) confirm the magmatic signature of crater fumarolic gases. R/Ra ratios are higher than those measured by Vaselli et al. (2010) in the "magmatic-dominated" phase (7.58 − 7.71 Ra) and show slight differences between the West Crater and the Central Crater. In *Fig. 4.11* the time variation of He-isotopic ratio of West Crater (green line) and Central Crater (blue line), fumarolic gases is shown, (data from Hilton et al. (2010), Vaselli et al. (2010), and this study). At the beginning of the unrest phase (1999) West Crater fumaroles displayed an He isotopic ratio of 7.34 Ra, but in coincidence with a seismic swarm occurred in 2001, the ratio increased to 8.01 Ra, reaching one of the highest values ever measured at Turrialba. In the following years He ratio decreased in both West and Central crater reaching values similar to the pre-unrest phase (e.g. in 2005). But since 2006 the He isotopic ratio steadily increased in both craters reaching again values close to the maximum of 2001 (7.93 − 7.96 Ra, West crater; 7.78 − 7.88 Ra, Central crater). It is interesting to note that West crater shows an average He-isotopic ratio higher than the Central crater, perhaps suggesting an higher contribution of magmatic fluids. However, the contemporaneous variations of He isotopic composition at both craters suggest a common gas source. The difference in He-isotopic values between the two craters becomes negligible just in two occasions: in 2007, in coincidence with a major seismic swarm (in July 2007, when more than 30000 earthquakes occurred in a single month), and in 2011, in the gases firstly sampled after the phreatic explosion occurred at the West crater. At the same time a strong negative peak in $\delta^{13}C_{CO2}$ is measured in 2001 and 2011 in fumaroles of the West Crater. This would confirm that during these years the volcano experienced a significant input of magmatic fluids. The high He-isotope values measured at Turrialba volcano suggest a [3]He-rich fluid source and reflect a negligible effect of [4]He-crustal contamination.
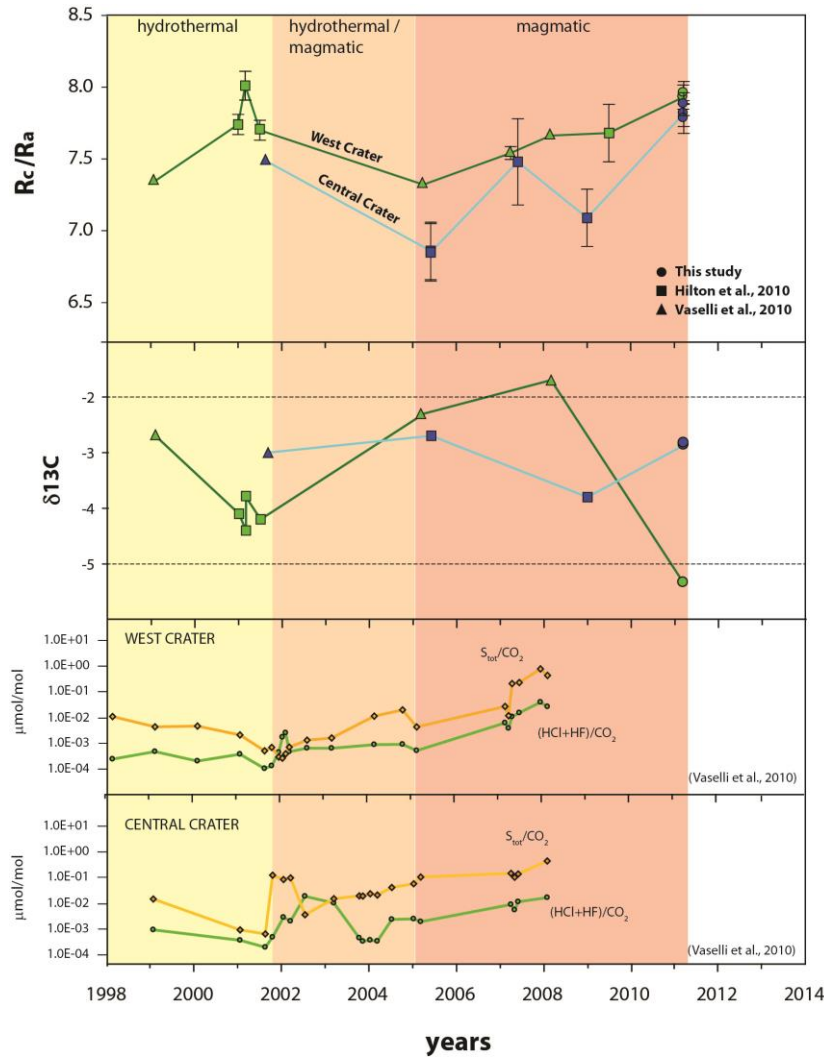
Fig. 4.11 – Temporal variation of He-isotopic ratio (corrected for atmospheric contamination); C-isotope ($\delta^{13}C_{CO2}$); S_{tot}/CO_2 and $(HCl+HF)/CO_2$ ratios, measured in crater fumarolic gases. The colored fields are modified after Vaselli et al. (2010). Green line = West Crater, blu line = Central Crater.

According to other studies (Snyder et al., 2001, 2003; Tassi et al., 2004; Shaw et al., 2003, 2006; Vaselli et al., 2010) Turrialba volcano displays the highest He-isotopic ratio with respect to other volcanoes of Nicaragua and Costa Rica (e.g. Mombacho 7.62 Ra, Garofalo et al., 2006; Poás 7.56 Ra, Hilton et al., 2010) showing values close to the typical He-isotopic ratio of MORB-like source (8.0 Ra±2.0). In this regard the relative proportions of CO_2 and He (given as the $CO_2/^3He$ ratio) varies between 1.8×10^{10} and 2.56×10^{10} with a good correspondence between West and Central craters. Based on the relation between $\delta^{13}C_{CO2}$ values and $CO_2/^3He$ ratio (*Fig. 4.12* ; Sano and Marty, 1995), the origin of fluids seems to be related to a source where a MORB-like mantle component is mixed with a carbonate-rich end member (limestone-like). As shown in *Fig. 4.12*,

Turrialba values of $\delta^{13}C_{CO2}$ and $CO_2/^3He$ ratio are consistent with those measured in other volcanoes of Costa Rica and Nicaragua, reflecting the carbonate-rich nature of the sediments of the downgoing slab (Shaw et al., 2003).
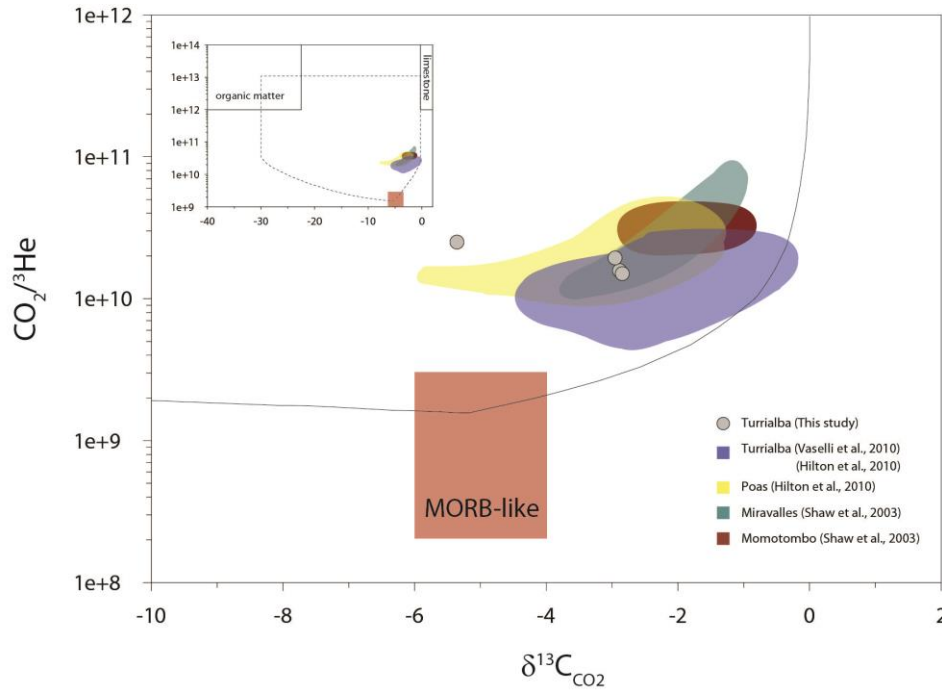
Fig. 3.11 – $\delta^{13}C_{CO2}$ vs. $CO_2/^3He$ ratio for Turrialba, Poás, Miravalles and Momotombo volcanoes. End-members compositions are from Sano & Marty (1995).

Data of CO_2 soil degassing in the Ariete Fault, collected during 2011, are compared with those of the survey performed in 2008 in the same area in *Fig. 4.13*. Anomalies were observed in both surveys, but they appear to be more intense in 2011. A maximum flux value of 5375 $gm^{-2}d^{-1}$ was measured during the 2011-survey, whereas the maximum flux of 2008 was 1994 $gm^{-2}d^{-1}$. In addition the anomalous flux profile 2 in the proximity of the gaseous emissions, appeared to be wider in the 2011-survey, suggesting an expansion of the fractured zone near the fault. The last noticeable difference between the two surveys is the appearance, in 2011, of a narrow CO_2 peak anomaly along the profile 4. In the interval time between the two surveys, in Falla Ariete sector, there has been a significant increase of degassing activity at surface.
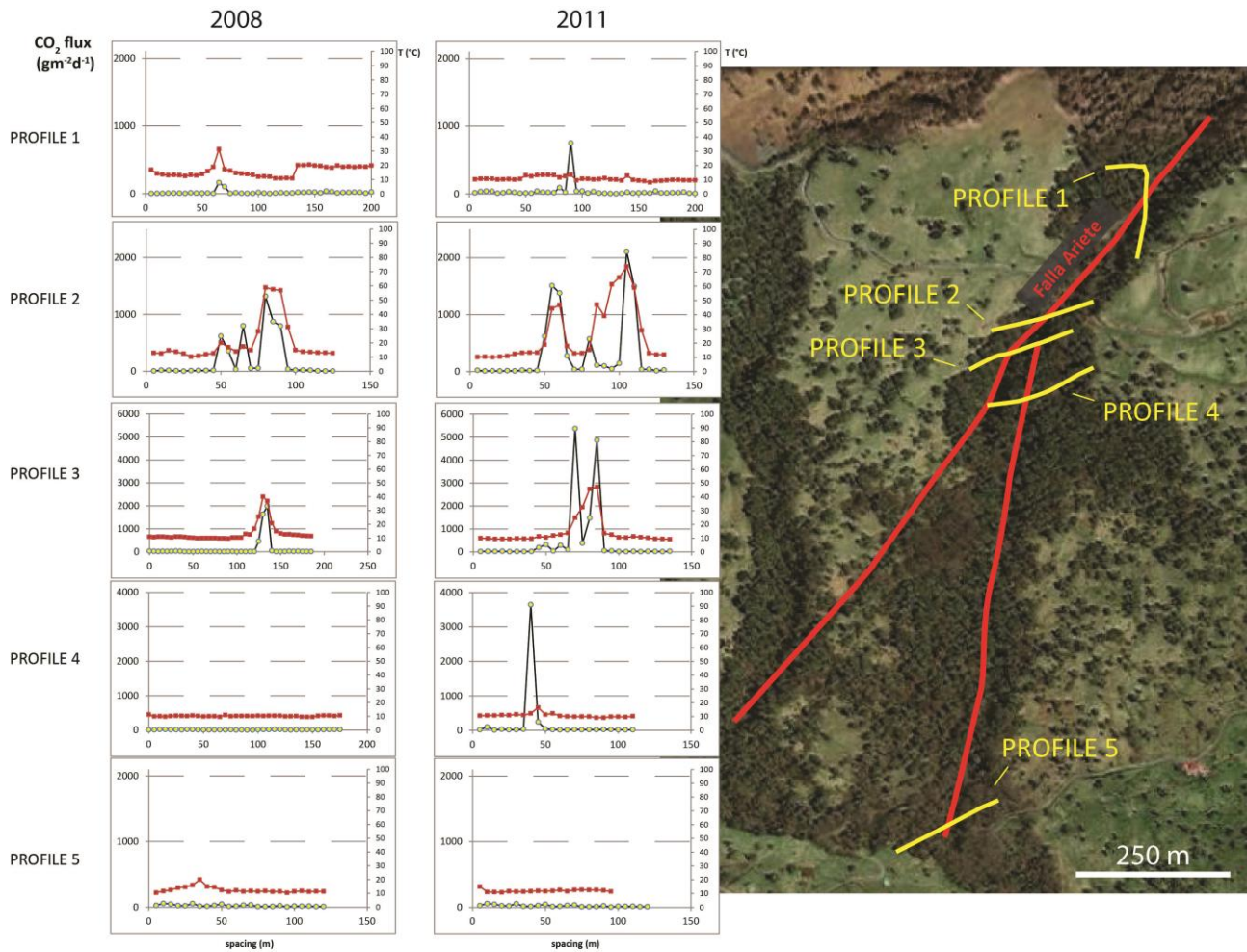
Fig. 4.13 – CO_2 soil flux (yellow circles) and soil temperatures (red squares) measurements along Ariete Fault. Comparison between 2008 and 2011 surveys.

Furthermore He-isotopes measurements performed in Falla Ariete fumarolic gases, in March 2008 (Vaselli et al., 2010), display a value of 7.71 Ra, confirming a common source for fluids feeding both craters and Falla Ariete area. All these data suggest that this sector is experiencing a process of downslope expansion of hydrothermal activity at surface.

4.6 **Constraints on the Turrialba unrest phase**

When a volcano becomes restless, one of the primary questions asked by scientists is whether the unrest will lead to an eruption. To address this question, many factors are taken into account, including seismicity, deformation, gas emissions, the geologic and/or historic record of past

eruptions, and analogues from the global record of volcanic unrest and eruptions. Based on the geochemical measurements conducted during 2008 and 2011 at Turrialba, and on the comparison with the temporal evolution of geochemical parameters (Vaselli et al., 2010) since 1998, it is possible to better understand the evolution of the unrest phase of the Turrialba volcano. The progressive increase in gas output, temperature and extension of the fumarolic field on Turrialba summit craters, culminated on January 5th 2010 with a phreatic explosion that opened a large vent on the southwestern inner rim of the West Crater. This vent has allowed since then to passively decompress the volcanic system as suggested by the lowering of CO_2 soil flux anomalies and temperatures (this study) and by the large increase in the SO_2 flux in the vent observed between January 2010 and May 2011 (OVSICORI-UNA, 2013). The opening of this vent could be attributed to movements of magmatic fluids from deep to shallow levels through cracks (Avard et al., 2013). Other two vents opened in May 2011 and in January 2012, both generated by the pressurization of a shallow hydrothermal system, as suggested by the absence of changes in the seismic patterns and in the flux of CO_2 and H_2S diffused through the soil (OVSICORI-UNA, 2012, 2013). The temperature of gas emitted by these vents rose from 600°C (2010 vent) to around 800°C (2012 vent), confirming that the hydrothermal system had partially rarefied. In this view, the degassing system of the volcano, in 2011-2012, has been characterized by narrow zones were the hydrothermal system was opened, and where magmatic fluids were discharged to the atmosphere at high temperatures (up to 800°C), maintaining their chemical and isotopic magmatic signature (presence of SO_2, HCl and HF, and R/Ra up to ~8). The low temperature fumarolic fields of the summit craters were the surface manifestation of purely shallow-level hydrothermal activity. The presence of the hydrothermal system is testified in peripheral zones of the volcano, such as the Falla Ariete sector, where low temperature fumaroles and high CO_2 flux from the soil were observed and measured during this study.

The opening of vents was accompanied by LP events that were generated by a crack mechanism dipping at shallow angle and located at shallow depths between the West and Central Crater (Eyre et al., 2013). These events are most likely to be generated in the hydrothermal system, either by resonance of a fluid-filled crack due to pressure fluctuations in the fluid or the fluid "pulsing" through the crack. Eyre et al. (2013) hypothesized that a crack containing hydrothermal fluid is pressurized by heating due to the presence of an underlying magma body. When the crack reaches a critical pressure level, there is a rapid discharge of the fluid, triggering the resonance of the crack. A similar crack mechanism is believed to be the cause of LP events in a hydrothermal source of Kilauea volcano, Hawaii (Kumagai et al., 2005) and Kusatsu-Shirane volcano, Japan (Kumagai et al., 2002). During this stage of the unrest phase also VT events were registered and associated to

high-frequency signals caused by brittle failure of the wall-rocks surrounding the plumbing system, in response to stresses associated with possible magma movement (Shaw, 1980). Conde et al. (2013) studied the chronology of degassing and seismic events suggesting that the pulsating variations in gas discharge rates at Turrialba volcano are most likely related to magma cycling by conduit convection and periodic injections of undegassed magma into the upper magma storage, in combination with an opening-sealing dynamic of the conduit by solidified magma and mineral precipitation on degassing pathways (Casadevall, 1981). Unfortunately ground deformation data at the Turrialba are available only for a short period of time, they have been collected only from few tiltmeter and are not sufficient to completely define the volcanic deformation pattern (Martini et al., 2010) and thus the entity of magma movement.

But why the unrest phase has not led to an eruption of the volcano? Over the last several decades, unrest episodes leading to an eruption have included various combinations of increased degassing and thermal output, phreatic explosions, shallow earthquake swarms (some with felt and/or low-frequency events) and notable ground deformation. Examples include Soufrière Guadeloupe, 1975-1976 (Hirn and Micheal, 1979; Doreal and Feuillard, 1980; Beauducel and Besson, 2008), Mount Baker, Washington, 1975 (Crider et al., 2011), Paricutin, Mexico, 2006 (Gardine et al., 2011), La Fossa Volcano, 1977-2005 (Martini et al., 1980; Barberi et al., 1991; Capasso et al., 1997; Granieri et al., 2006), Santorini, Greece, 2011-2012 (Newman et al., 2012; Parks et al., 2012; Parks et al., 2013; Tassi et al., 2013). A few cases are well studied, but many are poorly documented in the literature and so details of such events are often unavailable for comparison during an unrest stage. Moran et al. (2011) defined "failed eruptions" as instances in which magma reaches but does not pass a "shallow intrusion stage", generally < 2-3 km below the surface, accompanied by anomalous seismicity, deformation, degassing and in some cases phreatic explosions, but ultimately fails to reach the surface and erupt. These authors recognized three main variants in the nature of unrest associated with "failed eruptions": 1) volcanoes that exhibit only strong steaming, changes in gas flux, composition and/or elevated fumarole temperature, e.g. Vulcano, 1977-2006 (Martini, 1993; Granieri et al., 2006):

La Fossa cone at Vulcano island (Aeolian Island, Italy), is the volcano whose historic activity gave name to the "vulcanian" type of explosive eruptions. Since it last erupted in 1888-1890, it has been affected by two main episodes of increasing fumarolic activity (so called "volcanic unrest") none of which was followed by eruption. The first one occurred in 1912-1923 and the maximum temperature of the crater fumaroles reached 615°C (Sicardi, 1941). The second episode began in 1977 and the temperature progressively increased from 210°C to 690°C in May 1993 (Chiodini et

al., 1995). Then temperature decreased to values of 340-360°C (2004), and now is increased again up to ~ 500°C (Paonita et al., 2013). It was recognized that during crises the magmatic component (richer in CO_2, N_2 and He) dominated the fumarolic composition (Chiodini et al., 1995; Nuccio et al., 1999; Capasso et al., 1999). In particular inputs of magmatic fluids were detected in 1979-1981, 1985, 1988 and 1996. The associated seismic activity was characterized by swarms of low-magnitude shocks (M<2.5) with generally shallow foci (< 4km). Waveform feature and frequency of events indicate that they were linked to rising gases in the fumarolic feeding system (Chiodini et al., 1991; Bonaccorso, 2002). The chemical changes recorded in 1988-1998 at the fumaroles have been attributed by Nuccio and Paonita (2001) to an upraise of rhyolitic magma that in 1998 would have reached a depth of only 2.5km. Granieri et al. (2006) suggested that the inferred felsic composition is in contrast with the high He isotopic ratios measured at fumaroles (R/Ra ~ 6) and with the sulphur content of melt inclusions in the phenocrysts of the magma erupted at La Fossa. The sulphur content of melt inclusion, if compared with SO_2 output from the fumaroles, led to infer that the present gas source was likely to be a primitive basaltic magma, rich in volatile (Clocchiatti et al., 1994). Granieri et al. (2006) indicated that the increasing gas output would reflect the permeability increase by seismic fracturing of the impervious rock pile above a continuously degassing deep magmatic source. An interpretation that did not require any magma movement or upraise, as suggested also by the absence of significant uplift of La Fossa cone (Barberi et al., 1991; Bonaccorso, 2002). More recently Paonita et al. (2013) interpreted these "crises" as the evolving conditions in the magmatic system, such as gas buildup at the top of magma batches followed by massive discharge, activation of new degassing levels due to reorganization of the magma system, and its interplay with the stress field.

2) cases in which seismic swarms, inflation and other evidence of pressure buildup simply stops, abruptly or slowly, e.g. Santorini (Newman et al., 2012; Parks et al., 2012; Tassi et al., 2013):

Santorini (Greece) is the most active volcanic system of the South Aegean Active Volcanic Arc (Southern Aegean Sea). Since January 2011, several earthquakes (M<3.5) have been recorded beneath the Santorini caldera, and significant intra-caldera ground deformation (up to 15-20cm of radial extension and vertical uplift) has affected the Santorini islands (Newman et al., 2012; Parks et al., 2012). The main magma pressure source has been identified at a depth of 4 km north of the Nea Kameni island with an estimated volume of ~1.5×10^7 m^3 (Newman et al., 2012; Parks et al., 2012). At the same time significant changes of gas chemistry were measured in the fumarole emissions from the Nea Kameni summit craters, concomitant with the increase in seismic activity and ground deformation episodes between 2011 and 2012. Newman et al. (2012) and Parks et al. (2012)

interpreted this unrest phase as due to the injection of a new magma batch at depth. This could explain the increasing trends of H_2 and CO_2 concentrations observed from May 2011 to February (2012) (Tassi et al., 2013). However, Tassi et al. (2013) pointed out that a similar geochemical behavior could also be expected in case of increasing permeability at depth due to the seismic activity.

3) cases in which unrest culminates in phreatic explosions, e.g. La Soufrière Guadeloupe, 1976 (Feuillard et al., 1983; Beaducel and Besson, 2008).

La Soufrière lava dome is the highest mountain of the Lesser Antilles (1467m) and was emplaced during the last magmatic eruption that took place in 1580 AD (Semet and Vatin-Pérignon, 1979; Vincent et al., 1979). Since 1975 an increase in seismic activity was registered. A total of 26 phreatic eruption took place during 1975-1976. The steam blasts that characterized the eruptions gave rise to particle- and sometimes block-charged plumes that deposited an estimated 10^6 m^3 of solids (Feuillard et al., 1983). All materials were erupted at temperature of the order of 100 – 200°C. Most of the steam and the tephra were originated from superficial levels of the hydrothermal system, and the occurrence of a truly magmatic eruption was probably inhibited by an extensive hydrothermal system. Seismic activity was characterized by random occurrence of a few small-magnitude events per week, fumarole temperature reached 180°C during the 1975-1977 crisis and returned to water saturation temperature (96°C) in 1979 (Feuillard et al., 1983). If there was a magmatic intrusion at La Soufrière during this unrest phase is still a matter of debate. Beaducel and Besson (2008) assumed that if there was an intrusion, magma already reached a depth of only 2 km, as revealed by evidences for migration of seismic events (Hirn and Michel, 1979) and by the magnitude of seismicity and the entity of the magnetic anomaly (Feuillard et al., 1983).

In all these cases the possible magmatic intrusion failed to approach the surface. Magmatic eruptions can be inhibited by numerous factors such as loss of driving force (decrease of magma supply rate or gas pressure), increase in viscosity due to cooling or degassing/loss of water from the melt and associated formation of microlites (e.g. Cashman and Blundy, 2000), presence of a physical barrier (e.g. Taisne et al., 2011) and change in local stress conditions with consequent magma migration (e.g. Gudmundsson and Brenner 2004; Taisne et al., 2011). It is not easy to determine which geophysical and/or geochemical signs are indicative for the possible "failed eruption". Decreasing rates of seismicity, deformation and gas emission over timescales of weeks to months, or longer pauses between phreatic explosions, are all sign indicating waning driving forces and/or increasingly sluggish magma ascent (Moran et al., 2011). In addition phreatic explosions are not necessarily followed by magmatic eruptions, as evidenced by Barberi et al. (1992). Tazieff

(1977) pointed out that absence of significant SO_2 and juvenile glass shards in the phreatic explosions could be an evidence that magma will not erupt. However recent studies (e.g. Doukas and Gerlach, 1995) showed that SO_2 emissions could be masked if groundwater is absorbing (or "scrubbing") all the SO_2 and other acid gases, even if magma is near the surface and close to eruption.

All these cases suggest the hypothesis that Turrialba volcano might have experienced a "failed eruption" stage. The unrest of Turrialba, characterized by the increase of gas temperature, the extension of the fumarolic field, the clear magmatic signature of chemical composition of gases, and the opening of degassing vents, share many similarities with the case of La Fossa di Vulcano (Italy). Unfortunately data on ground deformation available for Turrialba are not very reliable, so it is not possible to ascertain if a magma intrusion took place in the plumbing system of the volcano. The appearance and increase in SO_2 observed at Turrialba since 2007-2008, was interpreted by Conde et al. (2013) as linked to the replenishment of the shallower magma chamber of Turrialba volcano (3-4 km of depth), by a relatively undegassed magma rising from greater depths. But this increase could also reflect simply dry pathway through which the gas can escape and reach the surface (e.g. Werner et al., 2011). The decrease in SO_2 and seismic activity observed since 2011-2012 would indicate that the accumulated magma had exsolved enough gas to reach a phase of enhanced crystallization and a higher viscosity (Conde et al., 2013). In addition, the low-explosive events due to seismic activity which occurred at Turrialba volcano between 2010 and 2013 are probably the cause of the increasing permeability of the overlying cap of rock, promoting gas escape to the surface and also progressive and periodic depressurization of a stationary magma body.

The entity of the fracturing of the cap rock and the opening of the hydrothermal system, has not been large enough to trigger a magmatic eruption. As erroneously reported by the press and media, these were not properly phreatic events. However, as testified by ${}^{3}He/{}^{4}He$ ratio measured at Turrialba fumaroles, the plumbing system has been recharged by a ${}^{3}He$-rich mafic magma that could be involved in a future eruption. Maybe deeper event, such as the reactivation of a the regional fault system, would trigger depressurization and eruption of the magma.

5. Textural analysis on two explosive eruptions of the last 2ka of Turrialba volcano

Textural analysis of vesicles and crystals, in addition to field and petrographic observations, were carried out in order to better constraint the degassing history experienced by the magma, and thus the eruptive behavior. For this investigation, two end member eruptions were chosen, basalts pertaining to the last unrest phase of Turrialba volcano and andesites related to the most important explosive eruptions.

The rationale behind this choice was to investigate products related to the most likely eruptive event in case of reactivation of volcanic activity, and the most explosive event expected. Through the study of fluid inclusions hosted in olivine and pyroxenes of products belonging to the last 10-ka activity of Turrialba volcano, it was observed that the last unrest phase of Turrialba was fed by a ^{3}He rich magma, possibly mafic or similar in composition with magma erupted between 1864 and 1866. Basaltic magmas and eruptive style similar to that of the eruption which occurred between 1864 and 1866 are therefore the most likely eruptive event in case of reactivation of activity.

The more explosive end member that we chose to investigate is the most important explosive eruption occurred at Turrialba volcano, according also with Soto (1988) and Reagan et al. (2006). This eruption is a 1.9ka explosive event fed by andesitic magma, classified as a sub-Plinian eruption (Reagan et al., 2006).

5.1 Crystal and Vesicle Size Distributions: brief background theory

Textural characterization of pyroclastic rocks from explosive volcanic eruptions has proven to be an important support to other approaches (e.g. field, theoretical observations and experimental) in studying the physical processes that control the eruptive styles, magma vesiculation, fragmentation and conduit ascent to the Earth surface (Houghton and Wilson, 1989; Klug and Cahsman, 1994, 1996; Gardner et al., 1996, 1998; Hammer et al., 1999; Polacci et al., 2001; Klug et al., 2002). Quantification and interpretation of vesicles have been an important research topic in volcanology. Vesicles in pyroclasts and lava flows document processes of gas exsolution, expansion and escape that drive most volcanic eruptions. Nucleation and growth rates are related to both intensive magma properties (e.g. initial volatile content and melt viscosity) and extensive properties (e.g. magma ascent rate, fragmentation and quenching) and the relative rates of bubble nucleation and growth control primary vesicle textures. These textures may be further modified by bubble deformation,

coalescence, expansion or gas escape (e.g. Sparks, 1978; Cashman and Mangan, 1994; Simakin et al., 1999; Polacci et al., 2003; Gurioli et al., 2005; Sable et al., 2006; Adams et al., 2006; Lautze and Houghton, 2007). Similarly the analysis of crystal size distributions (CSD) may provide information on the nucleation and growth rate of crystals, and their residence time in the magmatic systems (Marsh, 1988). Variations in nucleation and growth rate with time can be identified, providing a link between the kinetics of crystallization and physical processes which may be operating in the magmatic system. Here is a brief introduction on background theory of both Crystal and Vesicle Size Distributions.

5.1.1 *Crystal Size Distribution*

Crystal size distribution (CSD) provide a way of quantifying crystal populations, which can yield valuable information on the crystallization history of an igneous rock (Marsh, 1998). Born in chemical engineering environment (e.g. Randolph & Larson, 1971), it was then applied in geological context by Marsh (1988) and Cashman & Marsh (1988).

The CSD theory is based on a set of equations that represent a balance describing the change in number and size of crystals as a function of their residence time in the system and as a function of the influx and loss of crystals to the system. In order to establish this balance, the number density of crystals, n(L), must be known as a function of crystal size. A simple histogram of the number of crystals per unit volume, N(L), is inadequate as the shape of the histogram curve will be dependent on the width of the chosen size class (Cashman, 1990). The cumulative number density curve at any given size class is then used:

$$N(L) = \int_0^L n(L) \ d(L) \quad (1.4)$$

with N(L), the total number of crystals of L size and smaller; n(L), the number density of crystals. The population density, n(L) can be defined as the slope of the cumulative density curve at any given size class:

$$n(L) = \frac{dN(L)}{d(L)} \quad (1.5)$$

where n(L) is the number of crystals per unit length L, per unit volume of magma.

Two populations of crystals (n1,2), with different sizes (L1, and L2 = L1 + □wo populations of crystals (n1,2),[-1]) and contained within magma volumes $V_{1,2}$ (cm³), are related through a number of conservation equations. The change with time of the volume of the system and the number density

of crystals within the size range ΔL is governed by the rate at which crystals grow into and out of this size range in a time Δt (e.g. $G_1V_1n_1$ and $G_2V_2n_2$) and by the influx ($Q_in_i\Delta L\Delta t$) and outflux ($Q_0n_0\Delta L\Delta t$) of crystals from the system. The equation that link this terms is

$$(V_2n_2 - V_1n_1)\Delta L = (G_1V_1n_1 - G_2V_2n_2)\Delta t + (Q_in_i - Q_0n_0)\Delta t\Delta L \quad (1.6)$$

which is equivalent to:

(net accumulation) = (growth input − growth output) + flux in − flux out.

Dividing by Δt and ΔL, letting then both approaching to zero, and assuming $Q_in_i \ll Q_0n_0$, it results:

$$\frac{\delta(V_n)}{\delta t} + \frac{GV_n}{\delta L} + Qn = 0 \quad (1.7)$$

This equation is an average population balance for a system with volume V, indeed does not consider any spatial variation in crystallinity which may occur in an active magma chamber (e.g. convection). Considering constant the volume of the system, Eq. 1.7 becomes:

$$\frac{\delta n}{\delta t} + \frac{\delta(Gn)}{\delta L} + \frac{n}{\tau} = 0 \quad (1.8)$$

Where τ the effective residence time of crystals in the system. If growth rate is assumed to be independent of the crystal size, at steady state (so with dn/dt = 0), Eq. 1.8 can be expressed as:

$$\frac{\delta Gn}{\delta L} + \frac{n}{\tau} = 0 \quad (1.9)$$

Integrating this is it possible to obtain:

$$n = n_0 \exp\left(-\frac{L}{G\tau}\right) \quad (1.10)$$

where L is the crystal size, G is the growth rate, τ is the residence time and n_0 s the nucleation density. Thus plotting crystal size, L, versus ln (population density), the slope of the curve provide a measure of the growth rate and residence time of crystals in the magmatic system, and the intercept gives the nucleation density (Cashman & Marsh, 1988; Marsh, 1988, 1998) (*Fig. 5.1a*).

The shape of the Crystal Size Distribution can provide information about processes occurring deeper in the magmatic system and can represent a tool to evaluate the relationship between the kinetics of crystallization and any physical processes experienced by the magma (Cashman, 1990). A straight CSD (*Fig. 5.1a*) indicates a "simple" crystallization history preserved in the rock, while a kinked or curved CSD (*Fig. 5.1b*) reflects a complex crystallization history due to the mixing of

different crystal populations, crystal accumulation or a change in the crystallization environment (e.g. Higgins, 1996a,b; Marsh, 1998).
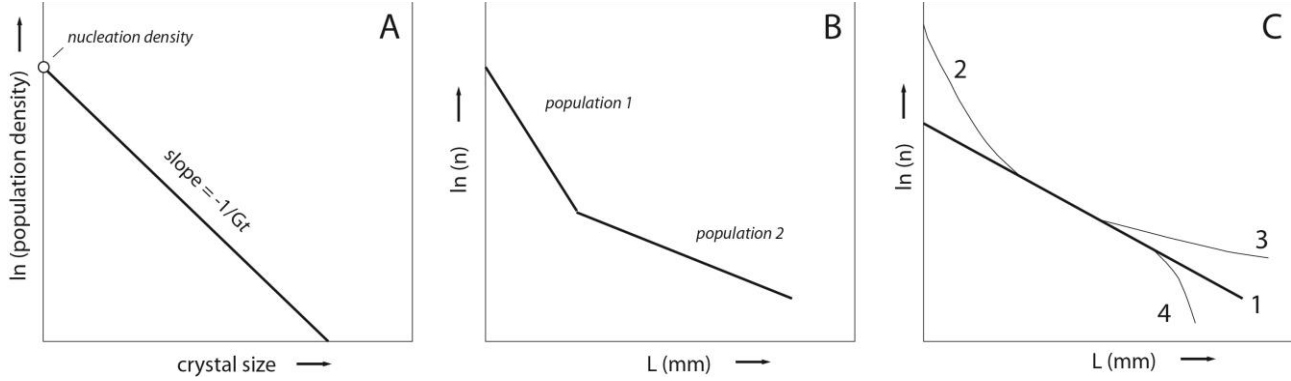
Fig. 5.1 – Sketch CSD ln(population density) vs crystal size with linear (A), kinked (B) andvarious patterns (C):log linear CSD (1) modified by rapid undercooling (2); by crystal accumulation (3); and by crystal removal (4).

Another important parameter describing the crystallization history of a rock sample, is the nucleation rate (J). Considering L = 0, from Eq. 1.2 the nucleation rate is derived:

$$J = n_0 G$$

Many authors (e.g. Lofgren, 1980; Kirkpatrick, 1981; Couch, 2003) performed experimental works on plagioclase crystallization observing that the crystallization rate is dependent on the degree of undercooling (ΔT) experienced by the magma. Coherently with the increase of undercooling degree, also the crystal fraction, crystal number density, nucleation rate and growth rate of crystals increase. Thess features peaks at various degree of undercooling and, increasing more ΔT, they start to decrease (e.g. Cashman & Blundy, 2000).

Fig. 5.2 shows relative rates of crystal growth (G) and crystal nucleation (J) as a function of the undercooling (ΔT). At slow to moderate cooling rates (ΔT), the crystal nucleation rate is slow, thus the growth rates are relatively high, reaching a peak, and crystallization occurs primarily by the growth of existing crystals. The resulting texture of the rock is characterized by few and large crystals. Increasing the ΔT nucleation is favored over growth, the resulting texture is dominated by numerous small crystals. At highest ΔT rates the melt may quench to glass without the nucleation of any new crystals (Cashman & Blundy, 2000) and the driving force for nucleation is countered by limiting rates of diffusion caused by large increases in melt viscosities at low water contents (i.e.

Hess &Dingwell, 1996). So the size distribution of crystals in a rock is a direct result of the undercooling at witch a magma crystallized (e.g. Cashman & Marsh 1988), and different stages in the crystallization history of the rock may be preserved in the textures.
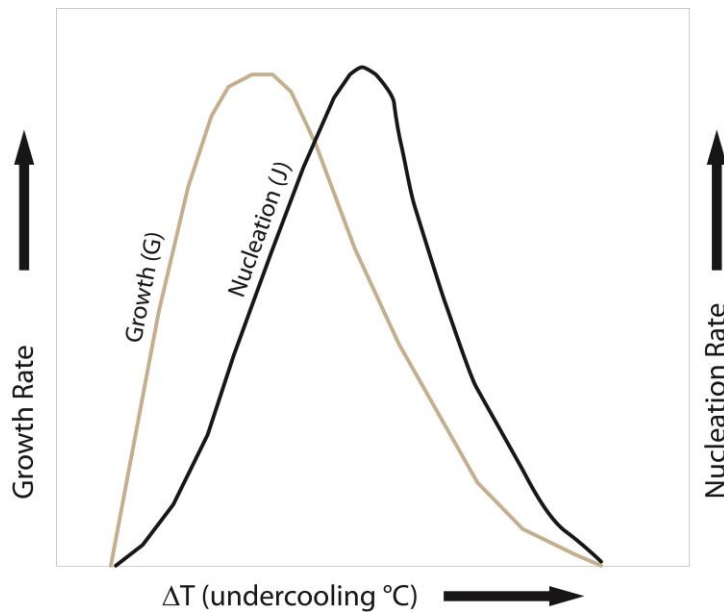
Fig. 5.2 – Sketch diagram illustrating variations in the rates of crystal growth (G) and nucleation (J) as a function of undercooling (ΔT). For small degrees of undercooling the nucleation rate will be low and the growth rate moderate. At larger degrees of undercooling the nucleation rate will be high and the growth rate also high. This will result in many crystals growing rapidly, with the result of a fine grained texture. At high degrees of undercooling, both the growth rate and nucleation rate will be low.

Qualitative information on the thermal regime prevalent during the crystallization processes may be derived by the examination of crystals habits. Experimental studies (e.g. Lofgren, 1974) on plagioclase crystals reveal that plagioclases develop different habits at different undercoolings and that there is a strong correlation between the ΔT rate and crystal size (e.g. Couch, 2003). As the morphology of plagioclase crystals changes from tabular to acicular with increasing the degree of undercooling, the aspect ratio of the resulting crystal also increases (Armienti et al., 1994). During cooling experiments performed by Lofgren (1974), variation in plagioclase morphology were observed. In particular, at ΔT under 150°C tabular crystals 2 mm long were found. Acicular or skeletal crystals occurred between ΔT 100 - 200°C, and dendritic morphologies for values between 150 and 250°C. At ΔT > 250°C plagioclase spherulites are dominant.

Armienti et al. (1994), studied lavas from the 1991-93 eruption of Mount Etna (Sicily). They observed that plagioclase crystals with sizes larger than about 0.015 cm are always tabular. In this interval, the mean elongation ratio between the major axes in exposed sections correlates inversely with size and varies from a mean of 1.8 for crystals over 0.05 cm to 2.2 for those between 0.05 – 0.015 cm. Crystals smaller than 0.015 cm develop acicular shapes with an even larger elongation. These observations strongly suggest that crystallization of the studied lavas took place at increasing undercoolings, with mild undercooling reflected by the largest crystals and stronger undercooling driving growth of the smallest. Crystal size distributions revealed three distinct populations of crystals, corresponding to three distinct cooling regimes explained as follows: 1) a nearly horizontal trend of CSD suggesting storage of the magma in a deep reservoir; 2) an increase in nucleation related to magma ascent, when undercooling shows an increase; 3) quenching phase after the eruption, developing very small (0.003 cm) and mainly acicular crystals. It is clear that low degrees of undercooling are reflected by the largest crystals (stage 1), while higher undercoolings drives the growth of the smallest populations (stage 3).

During ascending magma conditions, crystallization is enhanced by decompression and degassing as the magma become strongly undercooled. Degassing-induced crystallization has been inferred for several volcanic systems (Cashman, 1992; Nakada and Motomura, 1995; Swanson et al., 1989). Experimental verification that it can occur over eruptive time scales in sicilic magmas has been obtained for Mount St Helens eruption (Geschwind and Rutherford, 1995), where plagioclase microlites grew in response to rapid isothermal decompression of an H_2O-saturated dacite from 160 to 2 MPa. Isothermal decompression-induced crystallization has been inferred in natural systems where rates of supersaturations due to decompression are substantially greater than cooling rates (Swanson et al., 1989; Gardner et al., 1998; Hammer et al., 1999). Pressure conditions and water content of the magma seem to be first-order factors in influencing kinetic parameters, as growth rates may vary several orders of magnitude during ascent and degassing of magmas along a conduit.

In this study, we performed crystal size distribution analyses on the mineral assemblage of our samples, with particular attention to the plagioclase crystals, which are the dominant phases in all analyzed rocks.

5.2.2 *Vesicle Size Distribution*

Over the last two decades the detailed analysis of the structure of volcanic rocks such as pumice, scoria and lava has become a standard tool in the deduction of eruption parameters. One of the most common textural parameters measured is the vesicle size distribution (VSD) of the solid rock,

which is used to infer the bubble size distribution (BSD) generated during the liquid process of magma vesiculation.

During magmatic ascent, bubbles in magma nucleate and grow, as volatiles are exsolved. The final number density and size distribution of bubble populations in a volcanic rock erupted at the surface depends not only on the available volatile concentrations, but also on the ability of this volatile phase to diffuse through the melt, as well as the time available for expansion (i.e., time spent by magma in the conduit and/or at the surface) (Toramaru 1995; Lyakhovsky et al. 1996; Proussevitch and Sahagian 1996). Hence, investigating vesicle sizes and numbers can prove invaluable to characterizeing storage, ascent and eruption conditions (e.g. Klug and Cashman, 1994). Vesicle number densities per volume (VNDs) are typically higher in explosive eruptions than in effusive eruptions (Toramaru 1989; Cashman and Mangan 1994; Toramaru 1995; Mangan and Cashman 1996; Polacci et al. 2001; Sable et al. 2006; Toramaru 2006; Sable et al. 2009; Shea et al. 2010). The tendency of VND to increase with eruption intensity has been experimentally and numerically linked to the dependence of VND on decompression rate, and on other properties such as diffusivity, viscosity and surface tension (Mangan and Sisson 2000; Lensky et al. 2004; Mourtada-Bonnefoi and Laporte 2004; Namiki and Manga 2006; Toramaru 2006; Cluzel et al. 2008). Hence, VND is expected to scale with SiO_2 content (e.g., Sable et al., 2006) and physical eruption parameters such as magma discharge rate or column height (e.g., Gurioli et al. 2008). As a consequence, obtaining accurate measurements of both vesicle size number is crucial if valid physical comparisons are to be made between different eruptions. Because vesicles vary significantly both in size and in number, textural data are always displayed as distributions. The four most recurrent plots in the size distribution literature are used either to display vesicle volume information (vesicle volume distributions VVD and cumulative volume distributions CVVD), or number of vesicles per class size information (vesicle size distribution VSD and cumulative size distributions, CVSD).

Vesicle Size Distributions (or ln(n) vs. L plots, with L equivalent diameter in mm) are used commonly to infer kinematics of nucleation density and growth rate of crystals or bubbles (e.g. (Marsh 1988, 1998, 2007) According to Mangan and Cashman (1996), linear distributions denote steady-state nucleation and growth while an upward inflexion towards smaller sizes reflects ripening processes and a downward inflexion towards larger objects may be caused by coalescence (*Fig. 5.3*). In turn, bubble collapse may produce a curve that plunges rapidly in the larger size classes. Hypothetically, if the data within a VSD plot follows a linear trend, growth rates (G, mm s^{-1}) can be determined from the slope of the curve and initial number density (n_0, mm^{-3}) calculated

from the intercept at L=0, providing that some constraint exists on the time scale for nucleation and growth (τ). From the latter parameters, it is then possible to obtain nucleation rates (J, mm^{-3} s^{-1}). If no time constraint exists, only the total vesicle number density (N_{tot} in Mangan and Cashman, 1996; written NV_{fit} herein to describe better its origin) and dominant diameter L can be derived from the slope.
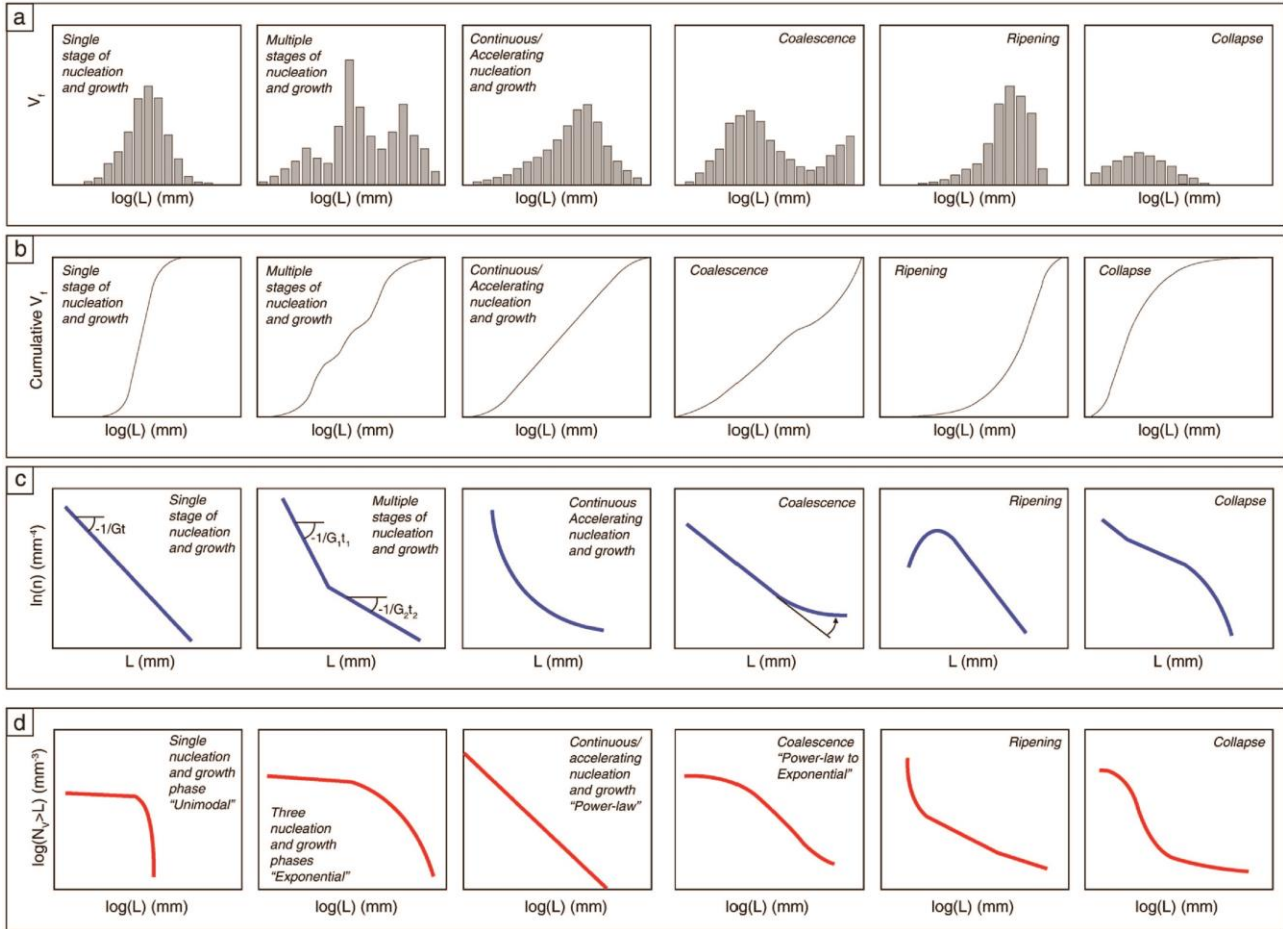
Fig. 5.3 – Various ways to display textural characteristics through size (L) and number density (n or NV) plots, and processes that they may be associated with (single or few nucleation events, multiple nucleation and growth events, continuous nucleation and growth, coalescence, ripening, and collapse, see text for explanation). (a) Simple volume fraction (Vf) size distribution (VVD), (b) cumulative volume fraction size distribution. (CVVD), (c) vesicle size distributions (VSD) in terms of number density n, and (d) cumulative number density plots log(NVNL) vs. log(L) (CVSD). Because during magmatic ascent multiple vesiculation and degassing processes may occur simultaneously and overprint each other, such plots call for interpretative prudence. G is growth rate and t is time.

In theory, assuming that nucleation and growth rates are constant throughout the vesiculation process, numerous physical parameters can be derived from segments of VSD curves. These include nucleation rates (J), growth rates (G), number of initial nuclei (n_0), the total number of

vesicles per unit volume (N_{Vfit}) and the characteristic bubble diameter (L). These parameters are found using the steady-state conservative exponential equation:

$$n = n_0 exp\left(\frac{-L}{G\tau}\right)$$

Then nucleation rates (J, mm^{-3} s^{-1}) are simply:

$$J = n_0 G$$

In theory, if the data are linear on an ln(n) vs. L plot, the total number density of vesicles per volume melt can be retrieved through the zeroth moment of the previous equation (Cashman and Mangan, 1994):

$$N_{Vfit} = n_0 G\tau$$

In turn, the first moment gives the dominant diameter:

$$L_{fit} = G\tau$$

The value of N_{Vfit} can be compared subsequently to the VND directly measured within the sample to test whether the trend adequately represents the actual data. If they are similar, then the fit can be considered robust.

Cumulative Volume Size Distributions (or log(NV>L) vs. log(L) plots) make use of population number density, and consider the number of objects per cubic mm with diameter greater than L. Gaonac'h et al. (1996; 2005) and Blower et al. (2001a; 2001b; 2003) developed the idea that power-law distributions could better accommodate certain types of vesicle size distributions produced by continuous/accelerating nucleation (i.e. data generating curves on VSD plots).

Numerical models by Blower et al. (2002) demonstrate that in log(NV>L) vs. log(L) plots, one to three nucleation events are able to generate exponential curves of form:

$$\log(N_V > L) \propto e^{-L}$$

Whereas numerous nucleation events or continuous nucleation and growth produce power law linear trends:

$$\log(N_V > L) \propto L^{-D}$$

where D is the power-law exponent. This type of plot was used to differentiate between exponential and power-law distributions, and between single, multiple or continuous nucleation (Gaonac'h et al., 1996; Gaonac'h et al., 2005; Blower et al., 2001, Blower et al., 2002, Polacci et al., 2008).

Power-law fitted distributions are usually only valid for a certain size range (Blower et al., 2002), and are seemingly applicable to most volcanic rocks as they represent multiple or continuous nucleation events. Gaonac'h et al. (1996, 2005) predicted that a single value of exponent D~2.5, close to the value anticipated for Apollonian packing (Blower et al., 2001), could apply to most vesicular samples, from lava flows to pumice. In contrast, exponential fitted distributions are applied in log(NV>L) vs. log(L) plots when the trend is nearly horizontal towards smaller class sizes and curves down towards larger objects. These fits do not seem to apply to many situations, however, and are thought to represent cases in which one or only few nucleation events have occurred (Blower et al., 2002; Bai et al., 2008). Coalescence tends to produce curves looking fairly similar to exponential trends, with the distinction nonetheless that a more horizontal tail may exist towards large size classes (Polacci et al., 2008; Bai et al., 2008). In turn, collapse textures may produce a curve which rapidly decreases towards low NV values and quickly becomes near-horizontal as largest sizes are approached.

Vesicle Volume Distributions are generally used to infer the nature of nucleation and/or coalescence events during the vesiculation history of pyroclasts (e.g. Klug and Cashman, 1994). Typically, each mode is interpreted to illustrate a distinct pulse of nucleation and growth (Klug et al. 2002; Polacci et al. 2003; Lautze and Houghton 2008); coalescence tends to skew the data positively or even produce a distinct larger mode (Gurioli et al., 2008; Adams et al., 2006), ripening produces a negative skewness (Mangan and Cashman, 1996), and bubble collapse dramatically reduces total vesicle volume fraction and modal size (Burgisser and Gardner 2004; Sable et al. 2006).

Cumulative Vesicle Volume Distribution plots are complementary to VVDs as they provide essential knowledge about the contribution of each size range to the total vesicularity. A unimodal distribution produces a sigmoid-shaped curve, multiple modes add bulges to the curve, coalescence tends to reduce the slope of the upper portions of the sigmoid, ripening shifts the curve to the right and accentuates the lower portion of the curve, while collapse likely results in a curve shifted towards smaller sizes, with lessened contribution of large vesicles (Klug et al. 2002; Adams et al. 2006; Mongrain et al. 2008).

5.2 Methodology

In order to perform textural characterization of the eruptive products, key stratigraphic sections were chosen for the selected eruptions. The vertical sampling intervals where chosen on the basis of shifts in intensity or style of the eruption, where macroscopic variation in the deposits were observed.

About the silicic 1.9ka explosive eruption, samples from three key outcrops in proximal, intermediate and distal position with respect to the summit of the volcano were sampled. A total of 9 samples were collected (3 samples for each stratigraphic section), choosing the most fresh and representative pumices, scoriaceous bombs and dense clasts of the analyzed deposit. Regarding the 1864 – 1866 explosive eruption, due to the lack of fresh outcrops related to this eruption and due to the limited areal dispersion of the deposit, we decided to choose section TU36 as the key section for the entire eruption. A total of 4 samples belonging to this eruption were collected. They are scoriae, and bombs.

Juvenile clasts where then sieved and 50 clasts pertaining to the grain size class 8 – 16 mm, for each level , were chosen. The selected clasts were then cutted with a saw and shaped in cubes, trying to minimize the asymmetries between each side. Samples were then cleaned and dried at T = 100°C for 24h. Two methods were followed in order to performed density measurements. Initially we measured the density following the method described by Houghton and Wilson (1989). Clasts were weighted in air (m_{air} in g) and successively drowned in hot wax, in order to make their surface totally impermeable. Then they were weighted once more in air (m_{wax}), and then in water (m_{water}). Thereby density is expressed as:

$$\rho \, bulk = \frac{m_{air}}{m_{air} - (m_{water} - m_{wax})}$$

Then the dense rock equivalent (DRE) density of the magma were measured with the sample powdered and measured in the He-pycnometer. Vesicularity was then calculated as follows:($\square$ expressed in percentage):

$$\phi \, (\%) = \frac{100 \times (DRE \, density - \rho \, bulk)}{DRE \, density}$$

The values of porosity obtained using this method (mode around 40-45 % vol.), were anomalously low for the considered samples, when compared with vesicle size distributions. This could be due to the different capacity of the wax to penetrate samples, depending on its temperature. If wax

temperature is too high, it acquires a very low viscosity, and it becomes capable of permeating and penetrating very easily into the sample, filling the vesicles, and decreasing the apparent porosity of the sample. Thus we decided to discard these initial measurements and to measure density/porosity directly using a He-pycnometer, yielding both connected and isolated vesicle fractions (Rust & Cashman, 2004). These measurements show an increase in porosity of more than ~ 20% vol with respect to the initial measurements..

For juvenile samples datasets, density or porosity is plotted on a histogram in order to choose a statistic number of clasts representative of the different end-members from the entire distribution. In particular a selected number of clasts for the low, modal and high vesicularities were chosen. The chosen clasts are made into thin sections or embedded into epoxy resin.

In order to perform textural analysis and cover all the ranges of vesicles and crystals presented in our samples, thin sections were scanned to image adequately the largest vesicles or crystal populations. For larger magnification (i.e. greater than 25x), image acquisition were performed through Field Emission Scanning Electron Microscopy (FESEM) at Istituto Nazionale di Geofisica e Vulcanologia Roma-1. In some cases, it was possible to map the entire surface of the sample through a mosaic of 100x images. Images were acquired in back-scattered electron imaging mode (BSEI); working distance was set at 50mm for 25x images and at 20mm for images at higher magnifications (>100 x). During the image acquisition, brightness and contrast were adjusted in order to obtain the best representation of bubbles and crystals. As indicated in many studies (e.g. Gurioli et al., 2005; Sable et al., 2006; Lautze and Houghton, 2007), characterizing the full range of vesicle sizes or crystal sizes in a rock requires image acquisition over a similar range of scale. The magnification ranges needed to cover the range of vesicle sizes of the rock, were determined by identifying the smallest and largest vesicles within the sample. So the lowest or the highest magnification had to record respectively the biggest or the smallest vesicle at a resolution that is sufficient to represent individual vesicles (Shea et al., 2010). The chosen imaging strategy for this study is the 15 image "Exponential" Nest, a grid strategy that predicts the increase of number of images with magnification (25x – 100x – 250 x – 1000x), with an Image Magnification Ratio of 2:1 between each magnification.

Acquired images were then digitized and binarized, in order to be edited manually with an image analysis software (Image J 1.47f®), to allow for the full range in size and shape of vesicle and crystal populations to be represented. To characterized the vesicle populations in acquired images, we employ a new Matlab-based software named "FOAMS" (Fast Object Acquisition Measurement System; Shea et al., 2010), that allows the calculation of parameters describing the spatial

arrangement, as well as the size and number of vesicles in our samples. The analysis of crystal populations were performed using CSDslice5, an excel-based program used to evaluate the crystals shape parameters, and CSD corrections v. 1.4.0.2, a free software allowing the stereological conversion of crystals and the calculation of the crystal size distribution of each population.

5.3 1.9ka eruption of Turrialba volcano

5.3.1 Field observations

The location map of the collected samples, along with a brief description, is shown in *Fig. 5.4*.

This eruptive unit consists of air fall, surges and pyroclastic flow deposits erupted from a vent located in the proximity of Central crater (Reagan et al., 2006). It is useful as a marker horizon for Central Costa Rica (Clark et al., 2006). The deposits are up to 30 – 40m thick on Cerro San Carlos, 1.3m thick 2.5 km from the summit and 0.1 m thick at 20km west of Turrialba summit. Pyroclastic flows and surges outcrop on the south and west flank of the volcano, overlying the fallout stage. Radiocarbon ages of the fallout and pyroclastic flow deposits range from 2330 ± 90 yr B.P. to 1860 ± 100 yr B.P. (Reagan et al., 2006). The most precise age (1975 ± 45 yr B.P.) is from a 3-cm-thick charcoalized branch found in the fallout pumice deposit near the summit of Turrialba. Melson et al. (1985), report a similar radiocarbon age (1970 ± 90 yr B.P.) for a phreatic explosion layer that is overlain by a pumiceous fall deposit and underlain by a paleosoil bearing ceramic fragments aged 2000 B.P.. The minimum value of volume of the fallout deposit was calculated to be 0.2 km^3. Considering the isopachs calculated by Reagan et al. (2006), this eruption was sampled in three outcrops considering proximal, intermediate and distal facies.

The key stratigraphic outcrop in proximal position with respect to the vent is located close to the summit of Turrialba volcano (10°01'05.42"N – 83°45'34.97"W), under the radio station, at an altitude of 3282m a.s.l., and has a thickness of 7 meters. Stratigraphic column with samples and detailed outcrop characteristics are shown in *Fig. 5.4.*

The base of the outcrop is constituted by 50 – 60 cm of an altered layer made of yellowish to reddish clasts altered by fumarolic activity (P$_1$). Lithic clasts are cm-size and are drowned in a compact grey ash matrix. Subordinately grey pumiceous lapilli are present, but represent only 10 - 15 % of the entire deposit. Charcoal fragments are also present. The layer could represent the opening phase of the eruption, where the occurrence of fumarolic altered clasts suggest the presence of fumaroles and hydrothermal activity prior to the eruption. This layer is followed by a ~ 260cm

fallout deposit (P_2), composed by grey to yellow pumices of various dimensions with a D_{med} $5 - 7$ cm and a D_{MAX} of 80 cm. The biggest juvenile clasts often present scoriaceous morphologies or aerodynamic shape with impact sags associated. Dense juvenile fragments are dark-colored and porphyritic with a D_{med} of $5 - 6$ cm and D_{MAX} of 12 cm. This fallout phase is overlaid by a 90 cm-thick dense clasts layer (P_3), composed by dark and porphyritic massive clasts with D_{med} of $6 - 8$ cm and D_{MAX} of 24 cm. It is possible to recognize loose yellowish to grey pumices cm-size and pumiceous lapilli. Dense clasts display homogeneous characteristics, but some fragments with reddish alteration were recognized. This deposit is followed by a 40 cm-thick fallout deposit(P_4), composed of yellowish to grey pumices with D_{med} of $4 - 5$ cm and D_{MAX} of 20 cm. The deposit presents a high sorting degree, and displays dense clasts of various dimension with D_{MAX} of 26 cm. Sample belonging to this deposit is TU37/5. This deposit is overlaid by a 90 cm-thick level made of dark scoriaceous and dense bombs (P_5), with a lot of impact structures affecting the top of the underlying layer. Vesicular bombs occurred very often and have a D_{MAX} of 120 cm, they present frequent squashed shapes; dense bombs are porphyritic and have a D_{MAX} of 60 cm. The upper part of the deposit is made of a fallout layer 210cm-thick(P_6), characterized by yellowish to grey pumices with D_{med} of $2 - 3$ cm and D_{MAX} of 18 cm. Occasionally, also black and porphyritic scoriacous bombs with D_{MAX} of 80cm occurred in the deposit, forming bomb sag or deformations structures of the deposit. Black porphyritic dense clasts also are present, chaotically dispersed, with D_{med} of $1.5 - 2$ cm and D_{MAX} of 8 cm. Samples belonging to this unit are TU37/7 and TU37/9, collected respectively in the lower part and in the upper part of the deposit. The outcrop ends with this unit and is overlaid by vegetation.

The intermediate outcrop selected for this eruption is located on the road to Finca Silvia (10°00'56.48"N – 83°46'59.76"W), ~3km W to Turrialba summit (*Fig. 5.4*). The entire outcrop has a thickness of 140cm and is cut by the road. The deposit starts with a brownish paleosoil very rich in charcoal fragments; it was not possible to recognized the bottom of this layer that represents the very base of the eruption. The paleosoil is followed by 88 cm-thick fallout deposit (I_1), well sorted, with a showy change in clasts diameters, describing a reverse and subsequent normal gradation. In the first 20-22 cm, clasts are yellowish to pink pumices with D_{med} of 1 cm $- 2$ cm and D_{MAX} of 3 cm and dense black porphyritic clasts with D_{med} $0.5 - 2$ cm. Samples belonging to this layer are TU31/2. Pumices progressively increase their medium diameter going upward (I_2), reaching a D_{med} of 3 cm and D_{MAX} of 6 cm. Dense blocks are ubiquitous, and are in dimensions range of pumices. Samples collected in this unit are TU31/3. In the upper part of the deposit the dimension of clasts are smaller and more similar to the lowermost part (I_3), with a D_{med} of 1 cm. A ~10cm thick deposit
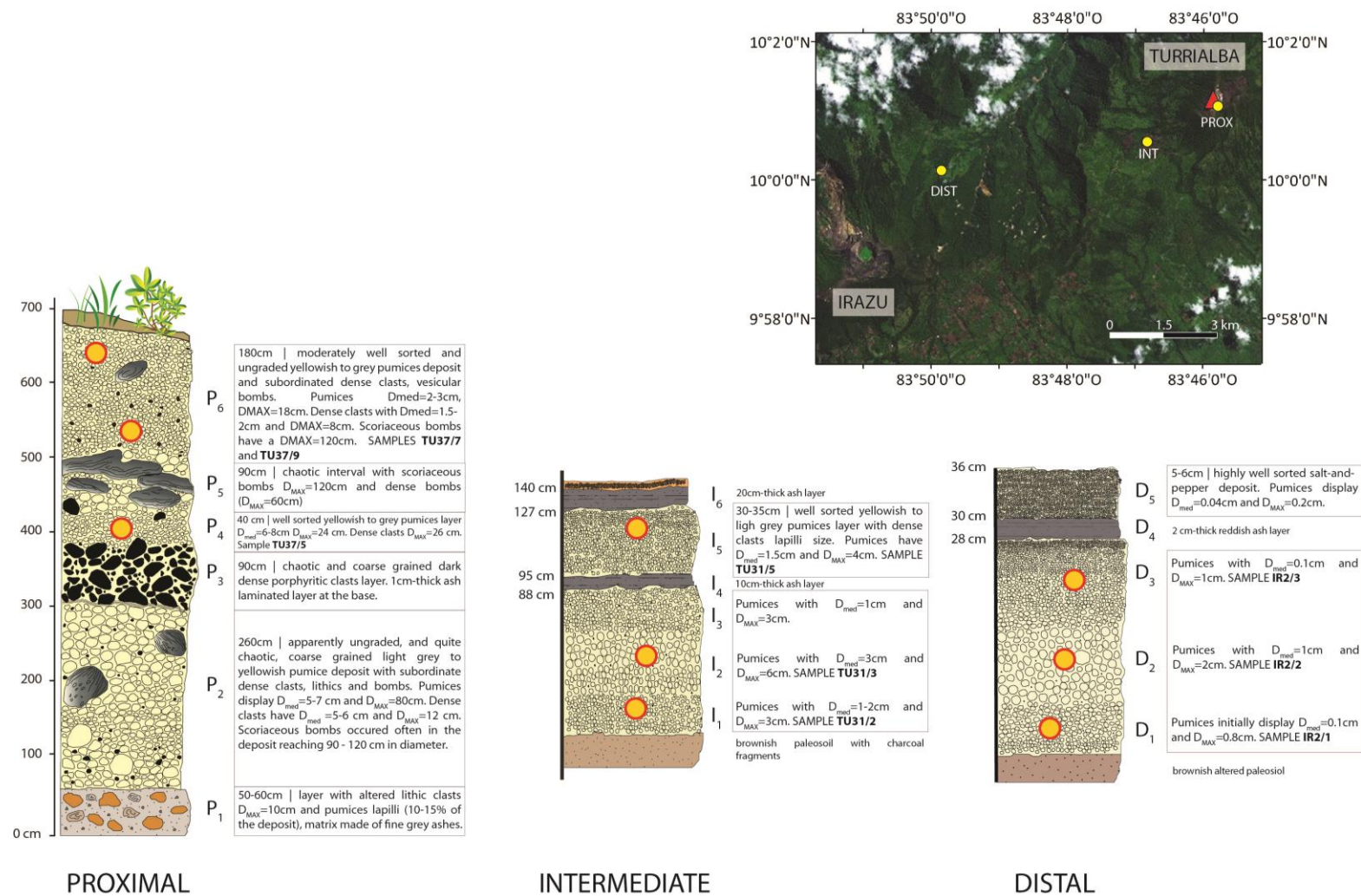
Fig. 5.4 – Location map of proximal, intermediate and distal outcrops of 1.9ka eruption. Insets contain stratigraphical information on the analyzed deposits.

of brown to gray ashes follow upward (I_4). Drawn in the matrix it is possible to recognize juvenile black to reddish lapilli and pyroxenes crystals. A 30 – 35 cm-thick fallout deposit overlies the ash interval (I_5). This layer is well sorted and made of yellowish to creamy colored pumices with D_{med} 1.5 cm and D_{MAX} of 4 cm (sample TU31/5). Dense blocky juvenile clasts are associated with pumices, giving a typical salt and pepper aspect to the deposit. Upward the deposit is overlaid by 20cm-thick compact ash layer (I_6).

The distal outcrop was sampled near Cerro Alto Grande, on the NE flank of Irazu volcano at 2503 m a.s.l. (10°00'38.49"N – 83°50'08.97"W) and 8km west to the summit of Turrialba volcano (*Fig. 5.4*). The outcrop was covered by vegetation and when cleaned, it displays a thickness of ~ 40 cm. The very base consisted of a brownish fine grained altered soil, followed by a fallout layer 28cm-thick (D_1). Initially pumices show a very light coloration and have a D_{med} 0.1 cm and D_{MAX} of 0.8 cm. This is the first unit sampled (IR2/1). Upward pumices display a reverse gradation and are characterized by an average increase in diameter displaying a D_{med} 1 cm and D_{MAX} of 2 cm (D_2). Samples belong to this unit are named IR2/2. More upward a decrease of the average and maximum diameter is registered with a D_{med} 0.1 cm and D_{MAX} of 1 cm(D_3). Samples belonging to this unit are named IR2/3. The first fallout deposit is interrupted at the top by a continue 2 – 3 cm-thick grey ash layer (D_4). This is composed by fine ash organized in very thin blades. The top of the outcrop is characterized by a 6 cm fallout deposit composed of well sorted yellowish pumices with a D_{med} of 0.04 cm and D_{MAX} of 0.2 cm (D_5). This level is very rich in dense blocky juvenile, porphyritic and dark colored, giving the typical salt and pepper aspect.

5.3.2 Petrographic observations

All the analyzed samples have a quite constant SiO_2 content varying between 58.4 and 59.5 wt % and present a glassy to porphyritic texture with phenocrysts of plagioclase (20 - 25 % vol.), pyroxenes (10 – 15 % vol. %) and rare olivine (< 5 vol %). Mineral chemistry classification diagrams are shown in *Fig. 5.5*. Fe-Ti oxides are present in different amounts and occurr essentially as microphenocrysts or microlites. The petrographic characteristics are similar for all the analyzed samples, with some samples presenting glomerophyric aggregates composed of clnopyroxenes, orthopyroxenes and oxides. The glassy texture is typical of pumiceous or highly vesicular clasts, while the porphyritic texture is characteristic of denser clasts that display an high percentage of microlites with respect to the former.

Plagioclase phenocrysts are ehuedral and reach maximum 5 - 6 mm length. They display mainly labradoritic composition (An45 - An66) with no substantial compositional differences between

phenocrysts and microlites. Only one sample presents some bytownitic plagioclases as phenocrysts and microphenocrysts (An83 – An85). Zoning is rare with more An-rich core (e.g. An68) and more sodic-rich rims (An53) and occurr especially in phenocysts.
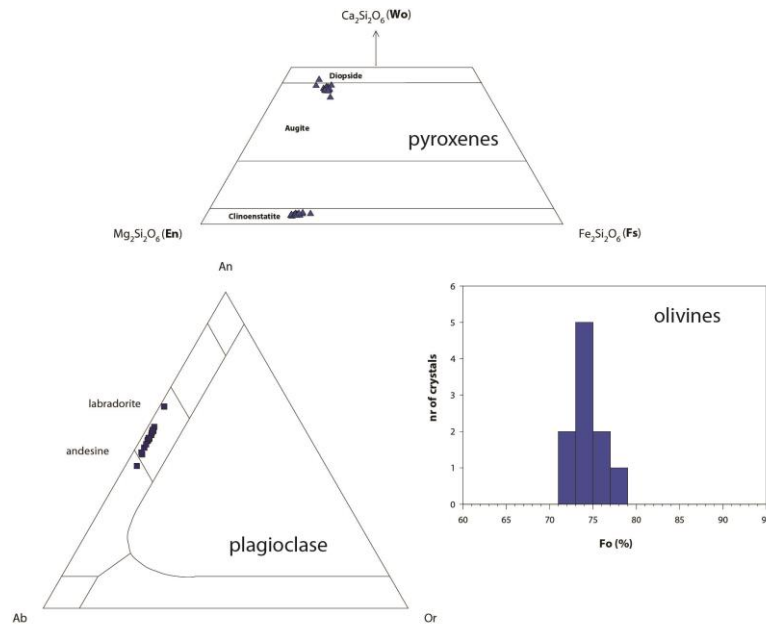
Fig. 5.5 – Classification diagrams of plagioclase, pyroxenes and olivine belong to the eruptive products of 1.9ka eruption.

Pyroxenes are ehuedral to subhedral and reach maximum 4 – 5 mm length. They are both augites and high-Mg orthopyroxenes (*Fig. 5.5*). Clinopyroxenes occurr as phenocrysts and in groundmass, they display a very homogeneous composition in all the analyzed samples, expressed in formula units as $Wo_{43-45}En_{42-43}Fs_{13-14}$. Hyperstene - orthopyroxenes are present as phenocrysts and microlites and are rich in Mg (En = 69 % - 78 %). Sometimes pyroxenes phenocrysts are organized in glomerophyric clusters, where also Fe-Ti oxides are present.

Olivine crystals are very rare and they occur as phenocrysts or microphenocrysts and always display alteration rims, orthopyroxene in composition, due to a high degree of disequilibrium with the liquid. The Fo content of the analyzed crystals is comprised between Fo70 and Fo75.

5.3.3 Density and vesicularity

The vesicularity of 50 clasts, randomly selected from the grain size interval 8 – 16 mm, was calculated from the bulk density using a dense rock equivalent (DRE) value, measured through He-pycnometry, of 2.784 g/cm^3. This value was obtained by averaging 20 DRE measurements on products belonging to this eruption. The analyzed samples display a range of density comprised between 0.6 and 1.4 g/cm^3.

The density distributions of proximal, intermediate and distal outcrop are shown in *Fig. 5.6.* and listed in *Tab. 5.1*. Samples belong to the proximal outcrop (TU37/5 – TU37/7 – TU37/9) are characterized by a unimodal peak at 0.9 g/cm^3 with a small tail of denser clasts (1.3 – 1.4 g/cm^3). Intermediate and distal outcrops (TU31 and IR series) display a common narrow density distribution with well-defined modes at 0.8 – 1 g/cm^3 and higher densities at 1.1 – 1.2 g/cm^3. The tail of denser clasts was noticed only in the proximal outcrop, maybe suggesting a density selection with increasing distance from the main vent. At a first interpretation, the distribution could suggest a common vesiculation history for all the analyzed juvenile products, however, further observations show that the degassing history of these products is more complex as suggested by the presence of high density clasts, characterized by low vesicularity. The mean bulk density and vesicularity of the proximal samples, along the stratigraphic column is the following: TU37/5: 0.9 g/cm^3 (66.82 %); TU37/7: 0.8 g/cm^3 (66.19 %); TU37/9: 0.9 g/cm^3 (69.08 %). For the intermediate outcrop the following values are measured: TU31/2: 1.0 g/cm^3 (65.54 %); TU31/3: 0.7 g/cm^3 (71.47 %); TU31/5: 0.9 g/cm^3 (67.57 %). Distal outcrop displays the following density/vesicularity values: IR2/1: 0.8 g/cm^3 (70.14 %); IR2/2: 0.7 g/cm^3 (75.80 %); IR2/3: 0.9 g/cm^3 (71.72 %).

Tab. 5.1 – Bulk density and porosity of 1.9ka eruptive products

		bulk density			Mean porosity
		min	mode	max	(%)
proximal	TU37/9	0.5	0.9	1.4	69.08
	TU37/7	0.6	0.8	1.4	66.19
	TU37/5	0.7	0.9	1.3	66.82
interm.	TU31/5	0.6	0.9 - 1	1.4	67.57
	TU31/3	0.6	0.7	1.1	71.47
	TU31/2	0.7	1	1.2	65.54
distal	IR2/3	0.6	0.8	1.1	71.72
	IR2/2	0.5	0.7	1	75.8
	IR2/1	0.6	0.8 - 0.9	1	70.14
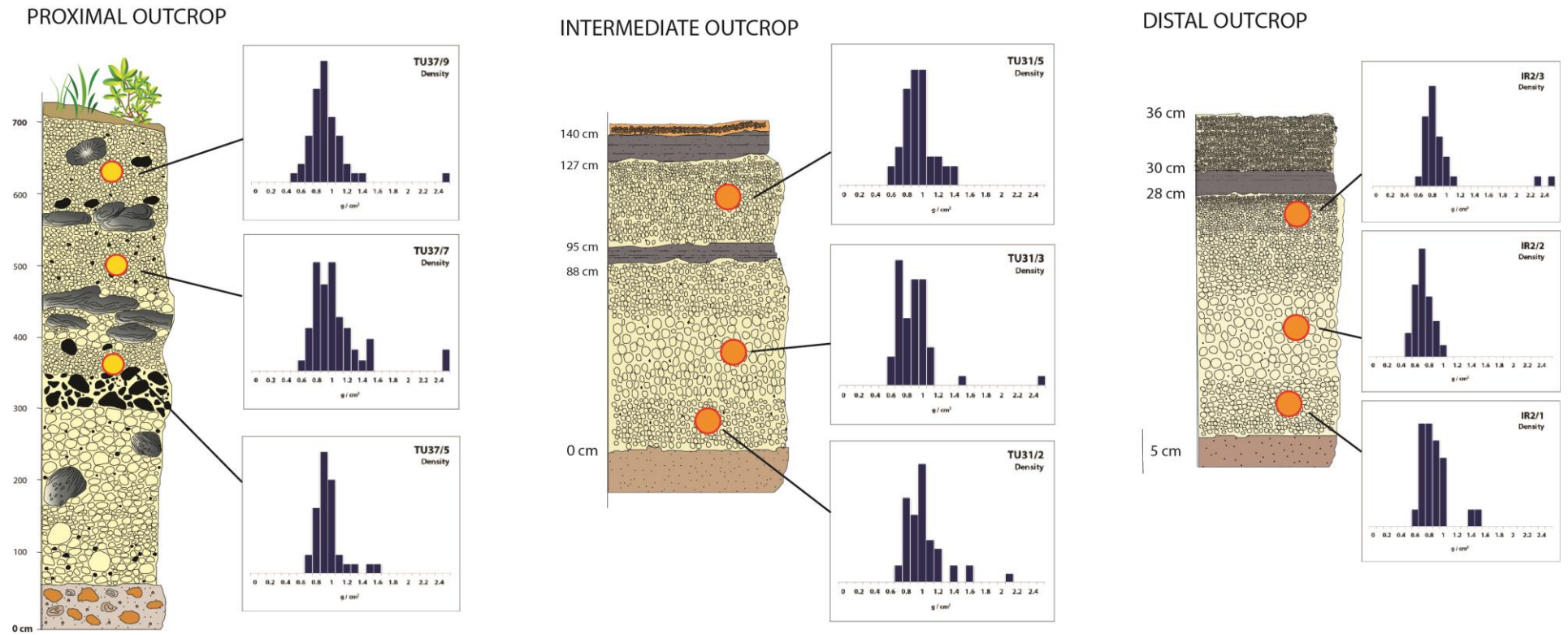
Fig. 5.6 – Density distributions of proximal, intermediate and distal outcrop of 1.9ka eruption.

5.3.4 Vesicles textural observations

From low density to high density clasts, through image analysis, it was possible to observe variations in shape, size and thickness of septa. Sometimes the presence of collapse and coalescence structures were observed. These variations were more appreciable in samples belonging to the proximal outcrop, due to the widening of density values

Similar features were observed in all samples pertaining to proximal, intermediate to distal outcrops, so, for the sake of brevity, in the following discussion, only the features pertaining to a representative sets of samples relative to the proximal product TU37/5 will be given. For this case, we considered the entire density distribution from low to high density pumices (*Fig. 5.7*).
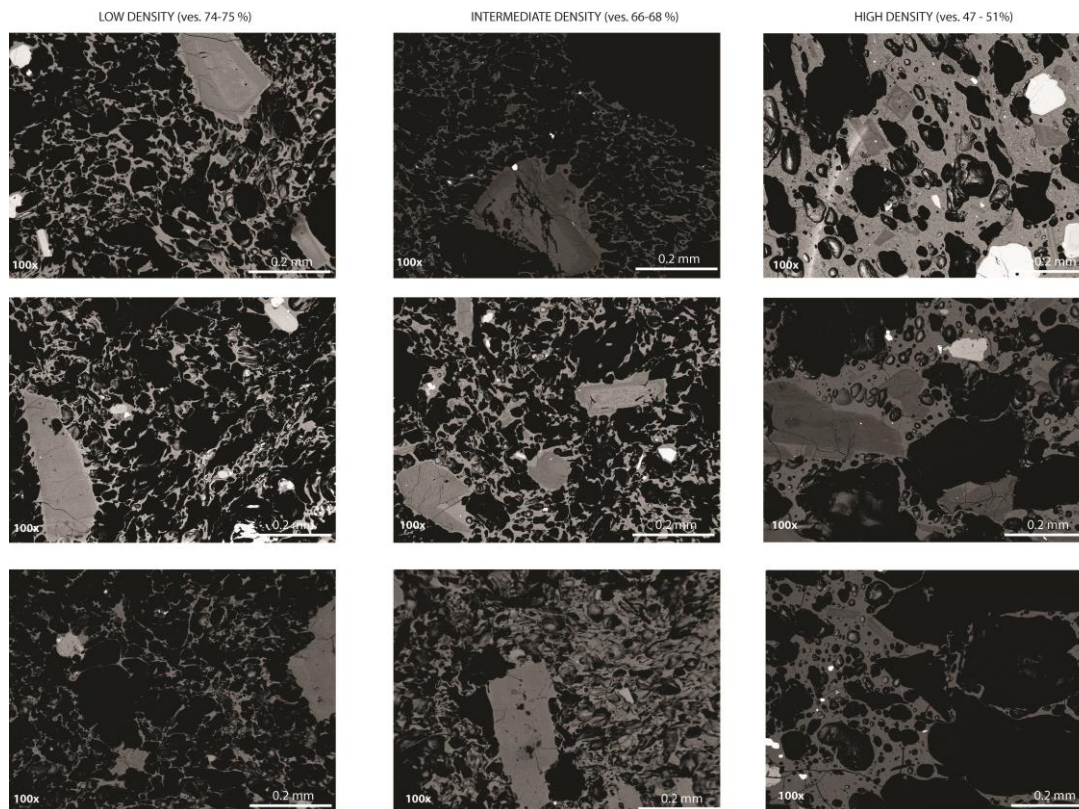
Fig. 5.7 – Back Scattered Electron Microscope images of clasts belong to sample TU37/5, on the left the low density and on the right the high density.

Low density samples (vesicularity > 73%) display vesicles with a wide range of shapes, from rounded to polygonal or strongly elongated. An average septa thickness was estimated to be in the

order of 0.011 – 0.019 mm. There are no signs of coalescence or collapse, bubbles are deformed and usually septa appear highly stretched, forming extremely thin glass wall.

Mode density samples differ slightly from the low density samples, having a vesicularity comprised between 69 and 73%. Vesicles appear to be slightly more rounded, but polygonal or elongated shapes are also present. Collapse texture are observed and sometimes episodes of coalescence can be inferred by "cuspidate" septa. Often vesicles form radial textures around phenocrysts, with the axis of maximum elongation perpendicular to the face of the crystal (Fig. 5.8). Average septa diameter is between 0.020 and 0.025 mm. High density clasts (vesicularity < 65 %) are characterized by an average widening of bubbles diameter. Bubble coalescence and elongated or squashed structures associated with bubble collapse occurred, especially in larger sizes, where wall rupture forms cuspidate septa. Bubbles appears more rounded, but some deformed samples are still present. Average septa diameter is up to 0.035 mm.
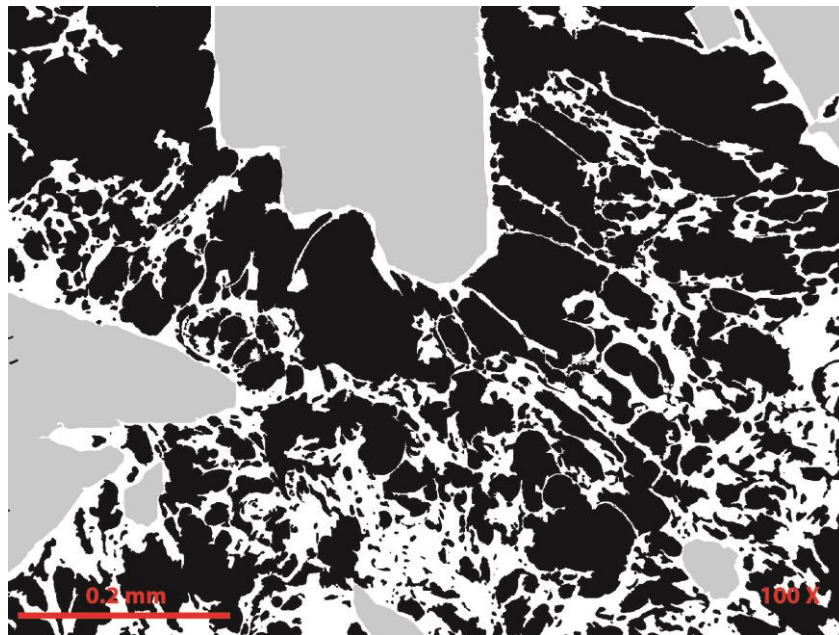
Fig. 5.8 – Binary image of sample IR2/3 in which vesicles (in black)form radial textures around plagioclase phenocryst (in light grey).

5.3.5 Vesicles Volume Distributions

Vesicle Volume Distributions were calculated with FOAMS software (Shea et al., 2010). The proximal outcrop displays the widest density/vesicularity distribution with respect to outcrops

investigated, for this reason VVDs and successively Vesicle Number Density were calculated for each density mode, by averaging measurements of selected clasts for each modes. Due to the narrower density distributions of intermediate and distal outcrops, ,for these outcrops, only modal density samples were considered and compared.

Considering the VVDs of samples belonging to the proximal outcrop (*Fig. 5.9*), it is possible to divide samples in three groups, on the basis of their vesicularity. Intermediate density samples display a quite narrow mode of VVD range between 0.23 and 0.38mm,however, the polimodal distribution is less evident but still recognizable. High density samples are characterized by the lowest vesicularity values (47–51%) and VVDs are characterized by the decline of volume fractions of the smallest vesicle sizes and by the increasing volume fraction of the largest bubbles in all the three analyzed samples.

Samples belonging to intermediate and distal ouctrops (*Fig. 5.10)* display always a polimodal distribution with at least two modes, the first on the small sizes (between 0.09 and 0.23 mm) and the second on larger bubbles (0.93 mm). Vesicles dimensions range between 0.010 and 0.9 mm.

Tab. 5.2 – Textural parameters of vesicles of 1.9ka eruptive products.

		Vesicles dimensions						Av. porosity	Vesicles Number Densities			D parameter
		Low density		Mode density		High density			Low density	Mode density	High density	Mode density
		max	min	max	min	max	min	(%)	(10^8cm^{-3})	(10^8cm^{-3})	(10^8cm^{-3})	
proximal	TU37/9	0.956	0.003	1.184	0.005	1.139	0.009	69.08	4.69	2.11	0.608	-
	TU37/7	0.932	0.005	0.929	0.005	1.154	0.007	66.19	4.39	2.29	0.687	-
	TU37/5	0.943	0.005	0.930	0.005	1.478	0.009	66.82	4.05	2.4	0.89	-
interm.	TU31/5	1.139	0.008	1.139	0.008	-	-	67.57	4.18	2.19	0.658	2.80
	TU31/3	1.168	0.005	1.168	0.005	-	-	71.47	5.16	3.27	1.99	2.91
	TU31/2	1.128	0.003	1.128	0.003	-	-	65.54	3.88	1.98	1.84	2.88
distal	IR2/3	0.927	0.009	0.927	0.009	-	-	71.72	4.3	2.05	1.98	2.90
	IR2/2	1.168	0.007	1.168	0.007	-	-	75.8	5.76	3.34	2.1	2.92
	IR2/1	0.930	0.009	0.930	0.009	-	-	70.14	3.95	2.26	1.97	2.81

5.3.6 Vesicles Number Density

The cumulative volumetric density number (N_{Vtot} = number of vesicles per unit volume; Cashman and Mangan, 1994) was calculated considering some selected pumices characteristics of the low density domain, the modal domain, and the high density domain. The calculations were performed using FOAMS software (Shea et al., 2010). The N_{Vtot} was calculated subtracting the phenocrysts
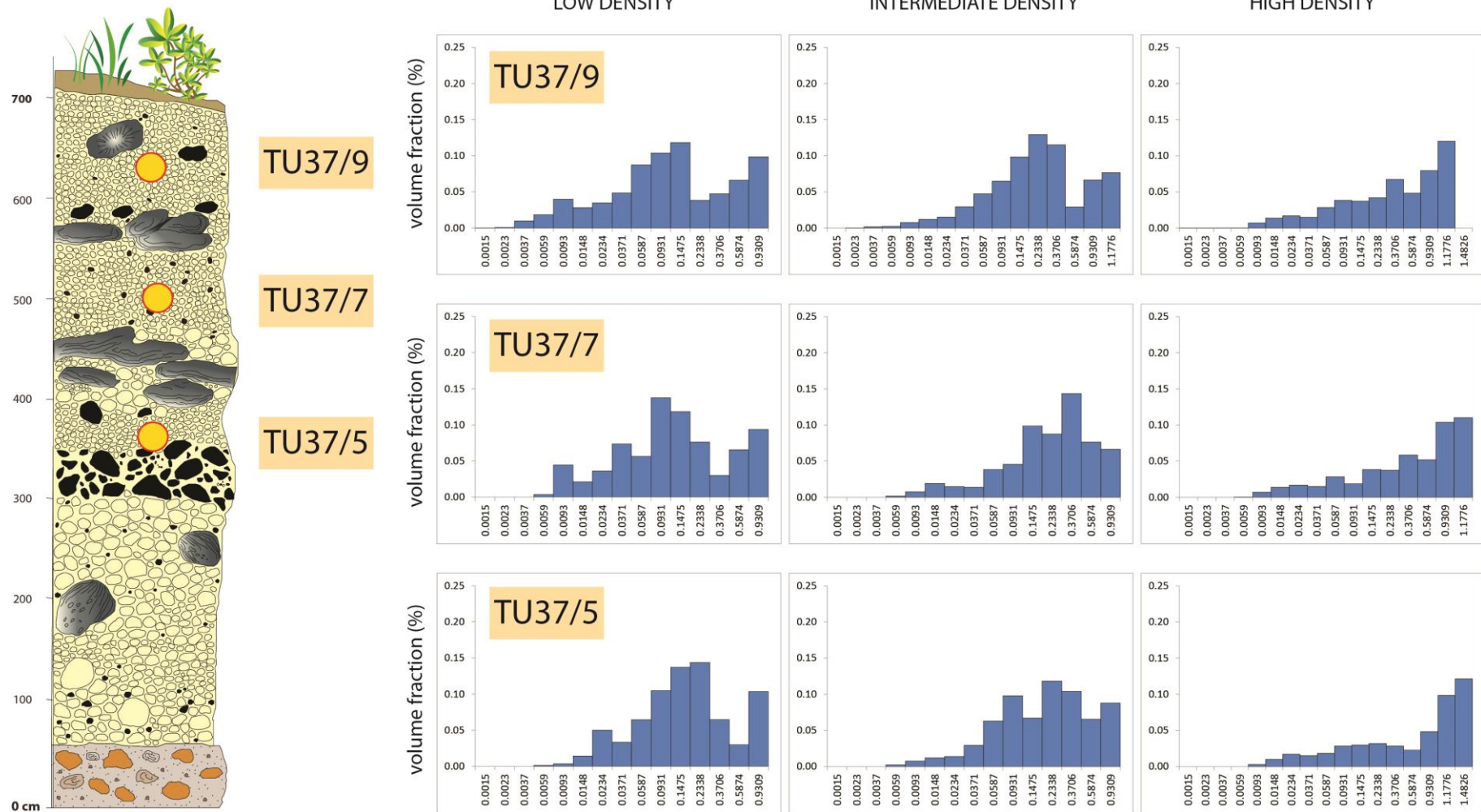
Fig. 5.9 – Vesicle Volume distribution for samples belong to proximal outcrop.

volume and so it refers to the number of vesicles per unit volume of clast matrix (melt-referenced) and are expressed in cm^{-3}. Results are listed in *Tab. 5.2*.

Vesicle Number Density ranges between 6.07 x 10^7 cm^{-3} and 5.76 x 10^8 cm^{-3}. The lowermost density samples display the highest VND, in the order of 10^{8}cm^{-3}. Modal density samples have quite constant VND values between 1.98 x 10^8 cm^{-3} and 3.34 x 10^8 cm^{-3}. The high density samples belonging to upper intermediate and proximal outcrops, show the lowermost VND values ranging from 6.08 x 10^7 cm^{-3} and 8.90 x 10^7 cm^{-3}.
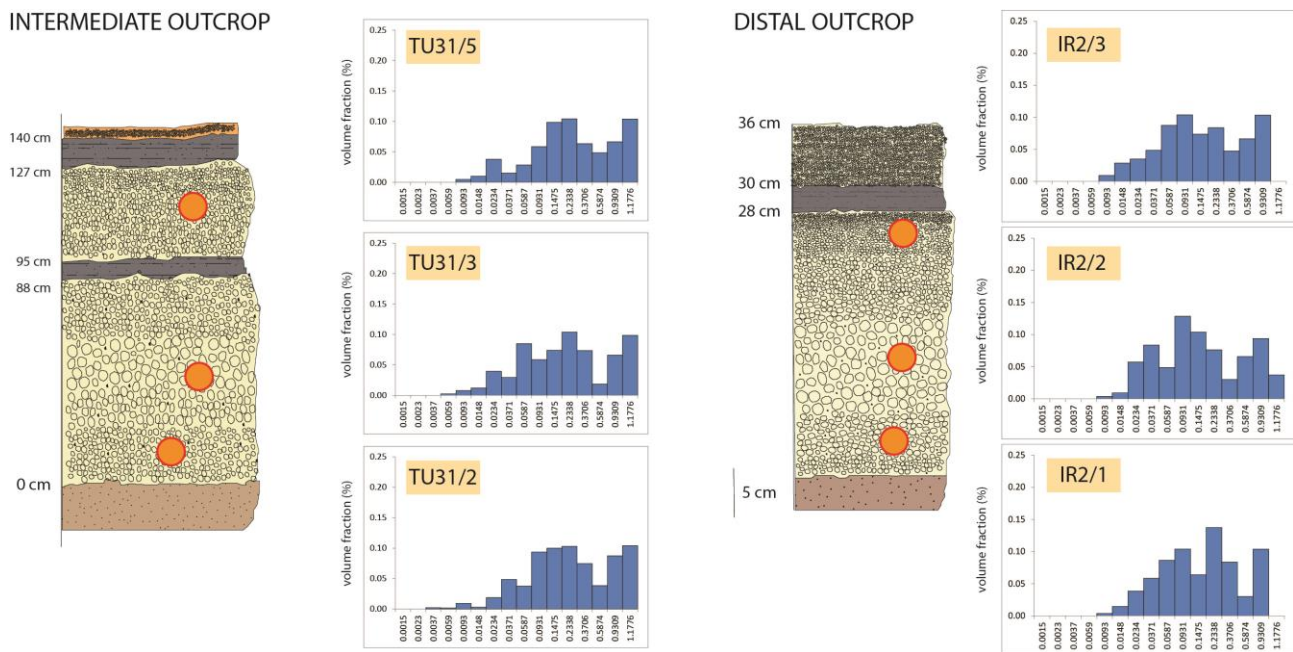
Fig. 5.10 – Vesicle Volume distribution of samples belong to intermediate and proximal outcrops of 1.9ka eruption. Data relative to modal density samples are plotted.

5.3.7 Crystal Size Distribution

Crystal size distribution was performed on plagioclase crystals, the most abundant mineral phases found in our samples. The most interesting and significant variations were observed on samples belonging to proximal outcrop and displaying the widest density/vesicularity variations. Such variations were not observed in intermediate and distal samples, thus CSD was performed only on a selected suite of samples belonging to the proximal section (TU37/5, data are listed in *Tab. 5.3* and CSDs are shown in *Fig. 5.11*). An appreciable difference in crystal size distribution is observable from low to high density clasts; indeed the reduction in vesicularity is balanced by an increase in

crystals content. CSD were performed averaging measurements of two samples for density class considered.
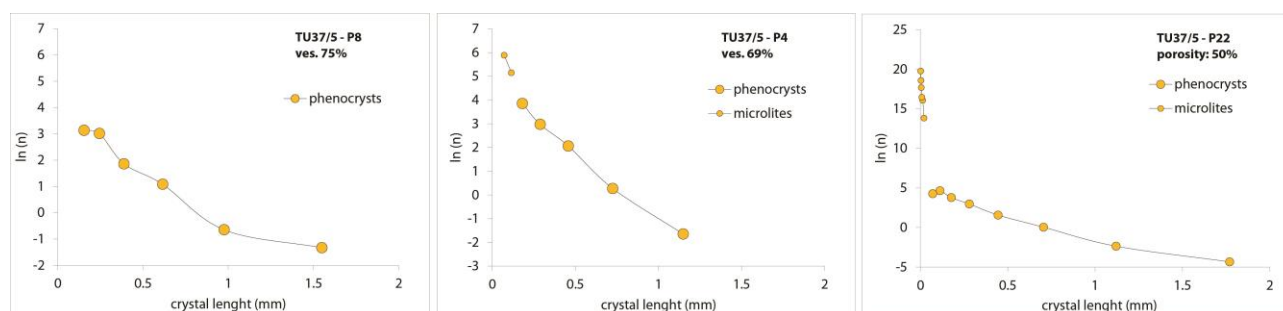
Fig. 5.11 – Crystal Size Distributions of the 1.9ka pumices. From left to right CSDs of low, intermediate and high density pumices are plotted.

Higher vesicular sample is characterized by quite linear plagioclase CSD, with R^2 value of 0.93. Intercept (n_0) value is of 3.4 and the slope is -3.39. Crystal length ranges between 1.41 and 0.019 mm. Intermediate vesicular samples (vesicularity = 69%) show a mild kink plagioclase CSD with two distinct segments. That represent phenocrysts population has a R^2 value of 0.99, intercept value of 4.67 and slope value of -5.65. The observed change in the slope of CSD occur in correspondence of sizes 0.18 – 0.11 mm, which could be considered the limit between phenocrysts and microlites populations. Thus microlites are characterized by larger slope and intercept values (-17.4 and 7.15 respectively), with R^2 value of 0.93. Low vesicular clasts (vesicularity = 50%) are characterized by a strongly kinked, concave upwards plagioclase CSD, implying a disproportionate number of large crystals and thus reflecting the presence of both groundmass and phenocrysts populations of plagioclase. Phenocrysts CSD display values similar to the previous samples (intercept = 4.50 and slope = -5.44), with R^2 of 0.96. Crystals length varies between 0.07 and 1.77 mm. Microlites population is characterized by a steep linear CSD with a very high slope (-283.4) and intercept (19.56) and display an R^2 of 0.93. These crystals are characterized by very small length ranging between 0.02 and 0.002 mm.

Tab. 5.3 – CSD data for 1.9ka eruptive products.

Sample	Nr crystals	Plg fraction (%)	large crystal populations					small crystal population				
			L_{MAX}	L_{min}	Intercept	Slope	R^2	L_{MAX}	L_{min}	Intercept	Slope	R^2
P_8	65	8.50	1.41	0.02	3.4	-3.39	0.93	-	-	-	-	-
P_4	224	9.30	1.15	0.18	4.67	-5.65	0.99	0.115	0.07	7.15	-17.45	1
P_22	380	11.75	1.77	0.11	4.5	-5.45	0.96	0.07	0.002	19.56	-283.4	0.93

All the phenocrysts analyzed display the same range of shapes, with an average ratio of the three geometric dimensions of 1:00 – 2:20 – 4:00, corresponding to a rectangular prism. In the contrary, microlites of the low vesicularity samples show more an acicular shape, based on their x - y - z ratio (1:00 – 2:50 – 2:60).

At small crystal sizes, some CSDs plot show a typical kinked downward trend, therefore a reduction in the contribution of small crystals compared to the simple log-linear distribution. This can be considered an artifact of the measuring process, and simply reflects the difficulty in measuring crystals in the smaller crystal size classes. In the similar way, the CSDs tend to diverge and form a fan shape at larger crystal sizes due to the small number of crystals pertaining to those classes, and resulting in larger uncertainties in their population density (e.g. Higgins, 2002).

5.4 1864 – 1866 eruption

5.4.1 Field observations

The eruptive products linked to this eruption mantle most of Turrialba's summit region. For this reason, the greatest part of this deposit underwent strong fumarolic alteration, due to the increase in degassing activity on the top of the volcano during recent years. The thickness of these products is very irregular, reflecting syn- and post-eruption erosion, as well as variable depositional thickness. Deposits related to this eruption are beds of well to poorly sorted juveniles, rootless lava flows and near-vent flowage deposits (Reagan et al., 2006). The explosive eruption began on 17 August 1864 and lasted into February 1866. The detailed description of the eruption is presented in Chapter 2 and will not be reitereted here. It was not possible to select outcrops at different distances for this eruption, due to lack of fresh and unaltered exposures. For this reason, we decided to investigate only one key outcrop as representative of the entire eruption (*Fig. 5.12*).

-cm to -m size breadcrust bombs, dense and porphyric (**TU16**).

80cm | moderately well sorted and coarse grained black vesicular scoria layer. Scoriae have D_{med}=3cm and D_{MAX}=20cm (**TU36/4**). Impact sags by scoriaceous bombs and lithics were observed.

145cm | complex ashes and lapilli beds rythmically alternated. Two cm-size layer with scoriae occurred. The lowermost is 15-20cm thick, unsorted and coarse grained. Scoriae have D_{med}=3-4cm and D_{MAX}=12cm (sample **TU36/2**). Upper scoria layer is characterized by scoriae with D_{med}=2-3cm and D_{MAX}=15cm (**TU36/3**).

1cm | ash layer with altered pumices

55cm | alternation of lapilli and ash layers with the rare occurence of 2-6cm in diameters scoria bombs.

8-10cm | layer with white to light grey ashes and altered clasts of various tipology, from rounded to subangular.

Fig. 5.12 - – Location map of key outcrop of 1864 - 1866 eruption. Insets contain stratigraphical information on the studied deposits

The key outcrop of 1864 – 1866 eruption was found on the summit of Cerro San Carlos at 3325m a.s.l. (10°01.21.80''N – 83°45'32.49''W). The total thickness of the outcrop is about 280 cm and the entire succession appears to have deposited in a small valley. The stratigraphic succession begins with a 5 – 6 cm layer composed of laminar yellowish to pink ashes with altered lapilli and blocks full of veins and altered by fumarolic activity. The presence of altered clasts suggests the occurrence of fumarolic activity prior the eruption, as observed from the chronicles (Gonzalez – Viquez, 1910). The first 60 cm of the deposit are characterized by an alternation of lapilli-size to ash layers rhythmically spaced. Juvenile clasts are essentially dark grey colored lapilli but sometimes porphyritic scoriaceous bombs occurr red with dimensions comprised between 2 and 6 cm. The deposit is interrupted upwardly by a thin white layer 1 cm-thick, with few sub-angular altered clasts, that could be representative of a phreatic phase occurred during the eruption. This layer is overlaid by a 145 cm-thick fallout deposit, that is characterized by an alternation of lapilli size to ash layers and sometimes by the occurrence of vesicular and porphyritic scoriae beds that were sampled for textural analysis (TU36/2, TU36/3). A drastic change in macroscopic

characteristics of the deposit occur in the uppermost part of the outcrop. This part is characterized by dark vesicular and porphyritic scoriae with D_{med} of 3 cm and D_{MAX} of 20 cm (TU36/4). Sometimes scoriaceous bombs and cm-size lithic fragments occurr, deforming with impact sags also the underlying deposits. The end of the eruption coincides with the emission of m-size breadcrust bombs, covering the entire summit region and outcropping specially on the crater terrace. These bombs are dark grey colored, highly porphyritic and dense, with an outer glassy carapace broken by fractures formed for the expansion of gases after their deposition.

5.4.2 Petrographic observations

Samples belonging to this eruption are basaltic – andesite in composition (SiO_2 = 52 – 53 wt %) and are glassy scoriae and dense porphyritic bombs. All the samples displays a medium grained hypocrvstalline porphyritc texture, with rounded vesicles (45-50% vol). Also in this case, all the analyzed samples display very similar petrographic and thus mineral chemistry features (*Fig. 5.13*).

Phenocrysts mineralogy consists of abundant plagioclase crystals (up to 25% vol.), essentially heuedral with normal zoning. Phenocryst cores exhibit a wide range of composition with Ca-rich samples (An80 – An81) and more sodic ones (An51), while rims show a narrow anorthitic content (An60 – An69) (*Fig. 5.11*). Compositionally they are labradoritic to bytownitic in composition. Microlites are less An-rich with respect to phenocrysts, showing a composition between An68 and An50.

Pyroxenes are green colored, ehuedral to subhedral and ubiquitous (~20% vol.). Phenocrysts are augitic to diopsidic in composition (Wo_{37-46} - En_{42-46} - Fs_{7-15}) (*Fig. 5.11*). Microlites are also in this range of composition. Clinopyroxenes from dense samples (TU16) appear to be more diopsidic on average compared to those from scoriaceous samples (TU36 group).

Olivine phenocrysts (~10% vol.) are colorless and ehuedral to subhedral. Phenocrysts display a broad range of composition at cores (Fo75 - Fo88) and normal zoning (rims: Fo70 – Fo75) (*Fig. 5.11*). Microphenocrysts and microlites composition is more Fa-rich (Fo71 – Fo75).
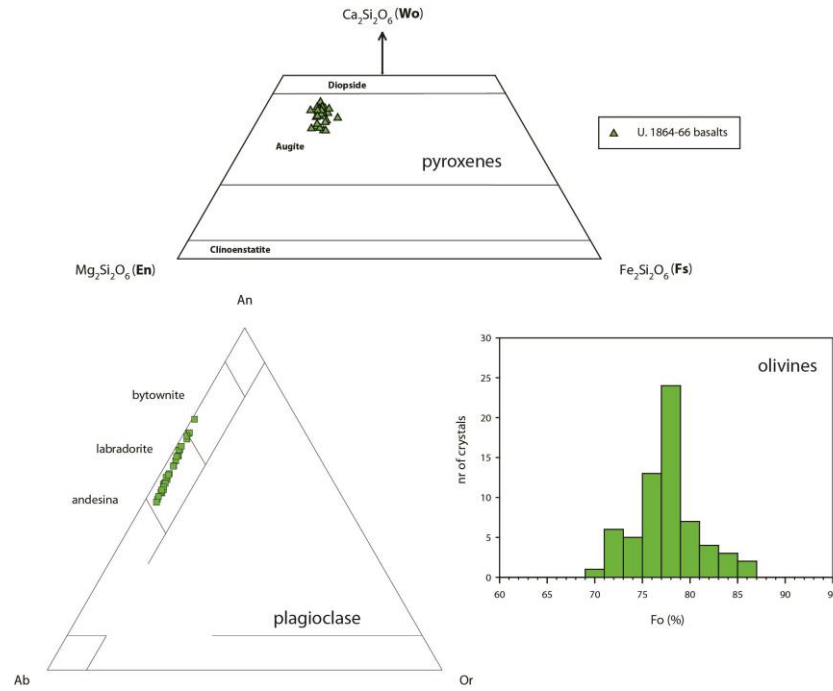
Fig. 5.13 - Classification diagrams of plagioclase, pyroxenes and olivine belong to the eruptive products of 1.9ka eruption

5.4.3 Density and vesicularity

In order to perform density measurements and vesicularity calculations on basaltic samples, selected samples of scoriae and bombs were broken with a hammer; the broken pieces were cut with a saw to obtain regular cubes. Geometric volumes of these samples were then calculated from averaging replicate micrometer measurements of diameter and length. Density values show an appreciable variation along the stratigraphic section, ranging from 1.21 g/cm^{-3} to 2.46 g/cm^{-3}. The Dense Rock Equivalent used for vesicularity calculation was measured by averaging 5 measurements on samples belonging to the same eruption (2.81 g/cm^3).

Density measurements display always narrow unimodal distributions with modal density values showing a progressive decrease from the base of the outcrop (TU36/2, 1.55 g/cm^3) to the uppermost scoria sample analyzed (TU36/4) (*Fig. 5.14*); similarly, vesicularity increase from 44.7 % to 56.3 %. Bombs related to the explosive phase at the end of the eruption, display the highest density values (2.46 g/cm^3) and the lowermost vesicularity (12.3 %).
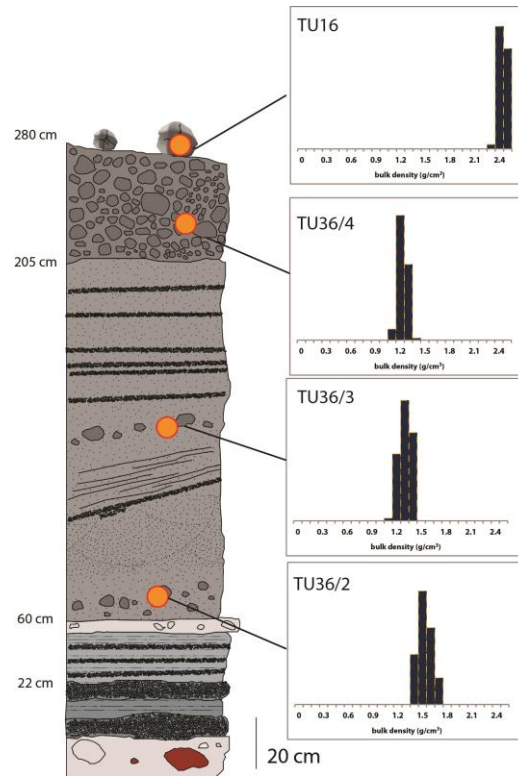
Fig. 5.14 - Density distributions of key outcrop of 1864-1866 eruption

5.4.4 Vesicles textural observations

Vesicles of scoriae samples (TU36/2 – TU36/3 – TU36/4) are characterized by rounded shapes and usually display features suggesting coalescence episodes (*Fig. 5.15*). Sample TU36/3 and TU36/4 display the most elongated bubble, with evidence of coalescence and collapsing episodes. Sample TU36/3 display also polygonal to cuspidate shapes affecting the biggest bubble population. Often the smallest vesicle populations display milled outlines due to microlites crystallization. Vesicle population of scoriae samples reach maximum dimensions of 2.16 – 2.38 mm and minimum dimension of 0.01 – 0.02 mm.

Sample TU16 is a dense bomb and thus display features completely different from the latter samples. Macroscopically the sample appear completely dense. Microphotographs at Scanning Electron Microscope reveal larger vesicle populations with boxy shape; they are elongated, squashed between crystals and with jagged outlines due to the strong crystallization of the rock. Trains of vesicles forming sort of channels between phenocrysts are visible sometimes interrupted by the presence of microlites. This sample is characterized by the smallest vesicles maximum dimension of 0.27 mm, with respect to the other analyzed samples.
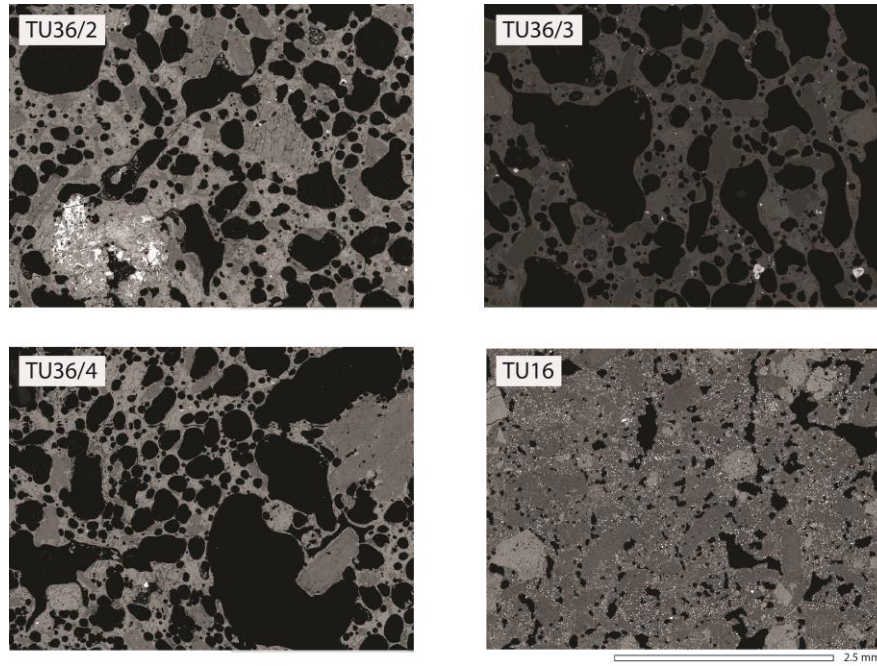
Fig. 5.15 – Back Scattered Electron Microscope images of 1864-1886 analyzed samples (mag. 25X).

5.4.5 Vesicles Volume distribution

Results of vesicles volume distribution calculations are shown in *Fig. 5.16*. For each deposit some selected sample belonging to the modal density were chosen. Scoria samples TU36/2 and TU36/3 display similar vesicles volume distribution, with polymodal patterns and modes respectively at 0.74 – 2.54 mm and 0.46 – 2.54 mm. TU36/3 is characterized also by an important mode of very large vesicles at ~4mm in diameter. Sample TU36/4 displays a more unimodal distribution with a mode at 0.29mm, while larger sizes are characterized by a weaker mode at 4.59 mm. Sample TU16 is a volcanic bomb and display a completely different vesicle volume distribution, with a narrow unimodal shape and a mode around 0.18 mm. Vesicles textural parameters are indicated in *Tab. 5.4*.

5.4.6 Vesicle Number Density

The cumulative volumetric density number (N_{Vtot} = number of vesicles per unit volume; Cashman and Mangan, 1994) was calculated by averaging 2 samples of modal density clasts. The calculation were performed with the use of FOAMS software (Shea et al., 2010). The N_{Vtot} was calculated subtracting the phenocrysts volume and so it refers to the number of vesicles per unit volume of clast matrix (melt-referenced) and expressed in cm^{-3}.

Tab. 5.4 - Textural parameters of vesicles of 1864-1866ka eruptive products.

	Vesicularity	Vesicles dimensions		VVD modes
	(%)	Max dim. (mm)	min dim. (mm)	(mm)
TU16	12.3	0.87	0.012	0.18
TU36/4	56.3	4.06	0.007	0.29 - 4.59
TU36/3	54.4	4.19	0.0014	0.4 - 2.54
TU36/2	44.7	2.39	0.018	0.74 - 2.54

Vesicle Number Density ranges between 9.74×10^4 cm^{-3} and 3.9×10^6 cm^{-3}. Scoria samples display a quite constant VNDs , between $1.4 – 3.9 \times 10^6$ cm^{-3} and a slight increase in VND is observed from the base to the top of the analyzed deposit. Bomb TU16 display the lowermost VND (9.74×10^4 cm^{-3}) suggesting a completely different vesiculation history with respect to the other samples.
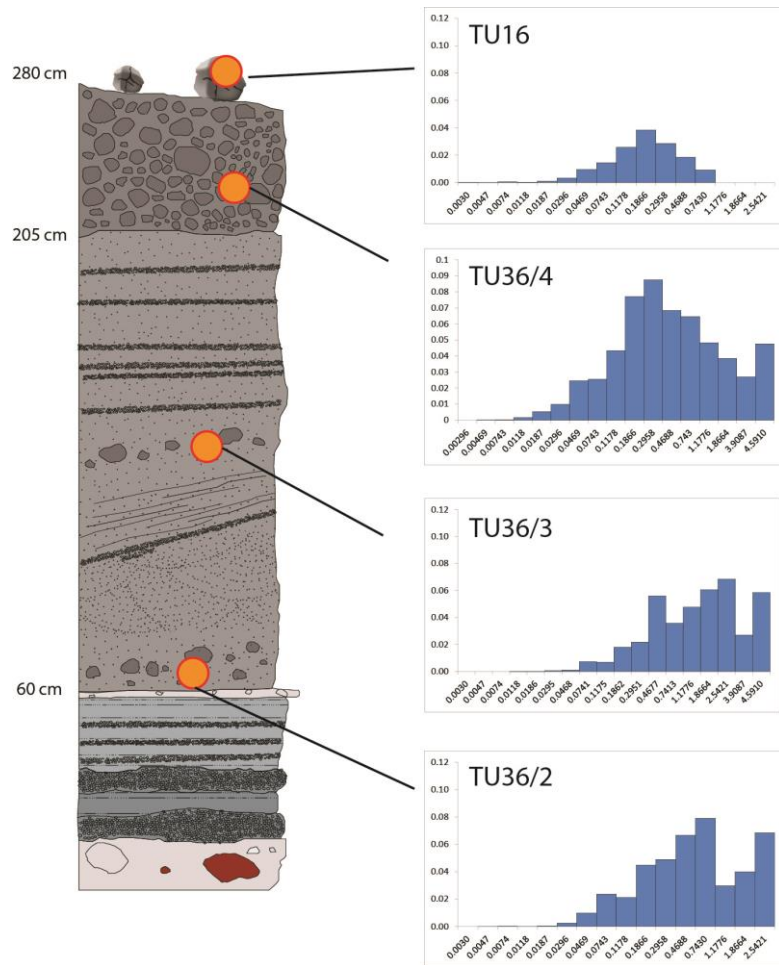
Fig. 5.16 - Vesicle Volume distribution of samples belong to the key outcrop of 1864 – 1866 eruption. Data relative to modal density samples are plotted.

5.4.7 Crystal Size Distributions

Crystal size distribution was performed on plagioclase crystals, which represent the most abundant mineral phases characterizing these samples. Size distributions were calculated on a high number of crystals, from 462 to 1226 samples. Results are listed in *Tab. 5.4* and distributions are shown in *Fig. 5.17*. All the analyzed samples display concave upward CSDs with at least three different crystals populations, that are characterized by different slope and intercept values. In addition, the shape of phenocrysts and microlites in all the samples studied are similar to each other.
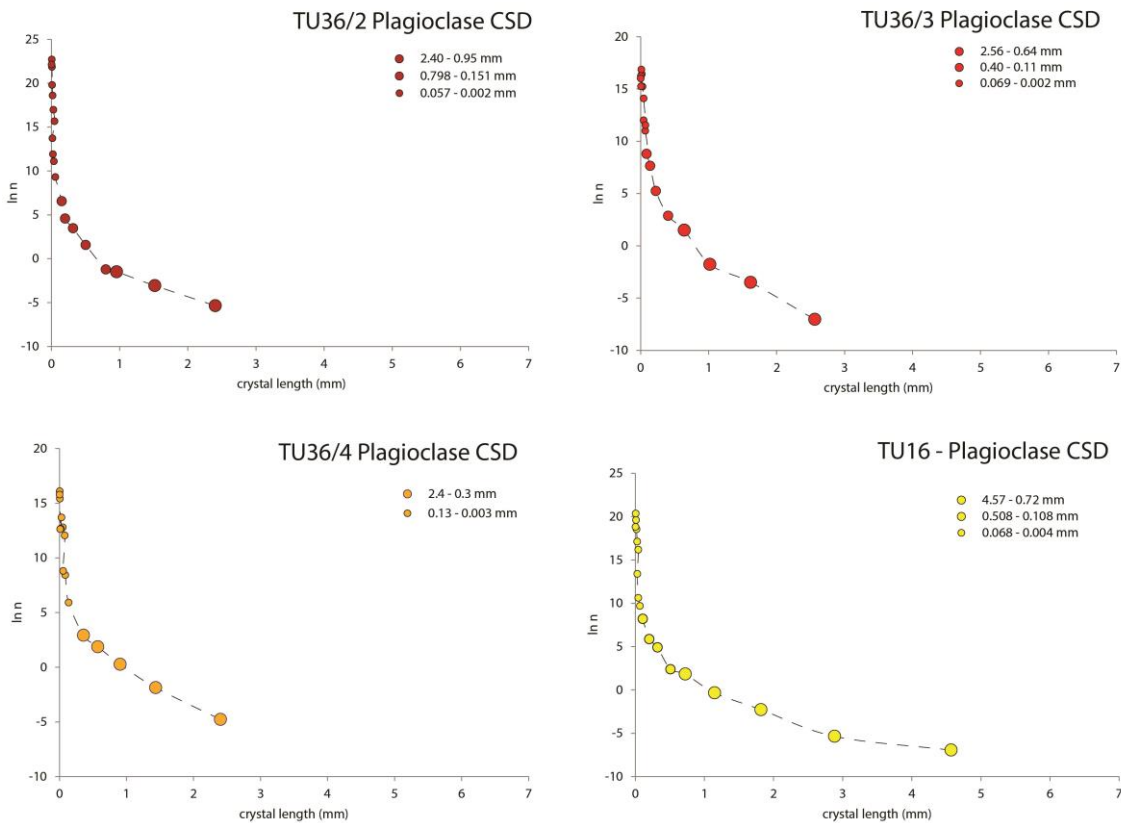
Fig. 5.17 – Crystal Size Distributions of the 1864 – 1866 eruptive products.

Scoria sample TU36/2 is characterized by continuous concave upward CSD reflecting at least three different plagioclase populations (*Fig. 5.16*). In the large size classes, phenocrysts range between 2.4 and 0.95 mm in size, they display an intercept value of 1.02 (n_0) and a slope value of -2.66. A second population of crystals ranges in size between 0.79 and 0.15 mm; these crystals have an intercept of 7.34 and a slope value of -11.04. Microlites population is characterized by sizes between 0.057 and 0.002 mm, and has very high intercept value of 21.5 and slope value of -214.8.

R^2 values are high for both phenocrysts and intermediate-size populations (0.99 – 0.96), whereas they are lower for the microlites population ($R^2 = 0.64$).

Scoria sample TU36/3 displays a concave upward CSD with three distinctive crystals populations (*Fig. 5.16*). Phenocryst sizes range between 2.56 and 0.64 mm, they show an intercept value of 3.37 and slope of -4.15 ($R^2 = 0.96$). Intermediate size plagioclase population ranges in sizes between 0.40 and 0.11 mm, displays an intercept of 10.14 and a slope value of -18.64 ($R^2 = 0.96$). The crystals population characterized by the smallest sizes (0.069 – 0.002 mm) has both high intercept (16.80) and slope values (-76.78), and a R^2 value of 0.84.

Tab. 5.5– CSD data for 1864 – 1866 eruption

Sample	Nr crystals	Plg fraction (%)	large crystal populations					intermediate crystal population					small crystal population				
			L_{MAX}	L_{min}	Intercept	Slope	R^2	L_{MAX}	L_{min}	Intercept	Slope	R^2	L_{MAX}	L_{min}	Intercept	Slope	R^2
TU16	1226	26.73	1.40	0.50	2.35	-2.23	0.92	0.50	0.10	9.25	-13.74	0.96	0.068	0.004	20.75	-164	0.77
TU36/4	462	15.16	2.40	0.30	3.93	-3.74	0.98	-	-	-	-	-	0.13	0.003	15.25	-68.7	0.79
TU36/3	1084	14.23	2.56	0.64	3.37	4.15	0.96	0.40	0.11	10.14	-18.64	0.96	0.069	0.002	16.8	-76.78	0.84
TU36/2	687	16.58	2.40	0.95	1.02	-2.66	0.95	0.79	0.15	7.34	-11.04	0.96	0.057	0.002	21.5	-214.88	0.99

Sample TU36/4 has a kinked upward CSD with at least two populations, identified by one distinctive knee (*Fig. 5.16*). Larger crystals range in size between 2.4 and 0.3 mm, and display an intercept value of 3.93 and a slope value of -3.74, with R^2 of 0.98. Microlites have sizes between 0.13 and 0.003 mm, are characterized by intercept value of 15.25 and a slope of -68.70 ($R^2 = 0.79$).

Volcanic bomb TU16 is constituted by a continues concave upward CSD, with three breaks in slope (*Fig. 5.16*), reflecting three different stages of crystallization. Phenocrysts display slightly lower values of intercept (2.35) and slope (-2.23) with respect to the other analyzed samples; R^2 value is high (0.92). An intermediate population has been recognized, with sizes between 0.50 and 0.10 mm, having an intercept value of 9.25 and slope of -13.74 ($R^2 = 0.96$). The smallest population of plagioclase crystals, is characterized by 0.068 to 0.004 mm-size crystals, with very high slope (-164) and intercept (20.75) values.

All the analyzed plagioclase phenocrysts belonging to scoria samples (TU36/2 – TU36/3 – TU36/4) are characterized by the same shapes and dimensions, displaying a quite constant long-intermediate-short axis ratio (1:00 – 1:40 – 3:20), indicating a rectangular prism shape, and ranging in size between 1.7 and 2.6 mm. Phenocrysts of TU16 slightly differ in intermediate axis (1:00 – 2:10 –

3:60), but substantially preserve the shape observed in crystals of scoriae samples. The intermediate size crystal populations have rectangular prism shape too (1:00 – 1:50 – 3:00) in all the analyzed samples. A different shape characterize the smallest crystals population that display long-intermediate-short axis ratio of 1:00 – 4:00 – 10:00 indicating an acicular shape.

5.5 Discussion

5.5.1 The 1.9ka andesitic eruption

The explosive eruption dated 1.9ka by Reagan et al. (2006) was fed by andesitic magmas. For a better comprehension of the development of this eruption, only intermediate and distal outcrops will be considered. The position of the chosen proximal outcrop is too close to the main vent, suffering the deposition of many different products that complicate the stratigraphic sequence. The stratigraphic record of intermediate and distal outcrops suggests the occurrence of at least two pulses of magma output with a slight variation in the eruption style during the first event. Labels indicated in the text are referred to different stratigraphic levels shown in *Fig. 5.4*.

The first eruptive event begin with a phreatic layer that was recognized only at the base of the proximal outcrop (P_1); in intermediate and distal outcrops, the base of the eruption is constituted by a brownish altered paleosoil. After the initiation of the eruption by phreatic events, the eruption continued by magmatic input only and an eruptive column was generated, as testified by the deposition of the fallout pumices of the level I_1 and D_1 (represented respectively by samples TU31/2 and IR2/1).

Pumices of the levels I_2 and D_2 show reverse gradation with respect to level I_1 and D_1, (samples respectively TU31/3 and IR2/2) suggesting an increase in eruption intensity and thus column height, although a shift of the dominant wind could also partly contribute to the stratigraphic observations. The progressive reduction in pumices diameter in levels I_3 and D_3 (sample collected IR2/3) suggests a decrease in eruptive activity, confirmed by the overlaying ash layer that closes this first stage of the eruption, characterized essentially by an oscillating column. The second eruptive impulse is composed by the deposition of lapilli-size juveniles and a final ash-dominated phase, that possibly records a prolonged phase of ash emissions which closes the eruption (levels I_5 and D_5; sample belonging to this phase were sampled only in intermediate outcrop, TU31/5).

Both the homogeneous bulk rock composition and mineral assemblage (Fig. 5.2 and Table Y) indicate that all of the studied juvenile products were discharged from a nearly unzoned magma

body. This result suggests that the textural heterogeneities observed both among and within pumices clasts, characterized by a sensible difference in density and/or vesicularity, cannot be attributed to different physical or chemical conditions in the pre-eruptive magma chamber, but more likely reflect changes in the physical properties of the magmatic mixture during the eruption.

In addition, the presence of narrow density distributions, with well-defined peaks (observed in particular in the distal and intermediate deposits of the second stage of activity) are thought to indicate that the magma fragmented over a narrow vesicularity range. However, when looking in more detail over the entire eruption, we can observe that the deposits of the most proximal outcrops, present a broader density distribution with the presence of high density clasts (d= 1.3-1.4 g/cm^3; *Tab. 5.1; Fig. 5.9*) which could reveal a more complex vesiculation pattern of magma ascent (Mangan et al., 2003; Houghton et al., 2004; Adams et al., 2006).

The higher density clasts are not well represented in density distributions of intermediate and distal outcrops, maybe due to a density selection, increasing distance from the eruptive vent. Values of mean porosity of 1.9ka Turrialba eruption are listed in Tab. 5.1. Maximum values are measured in levels I_2 (71.4 %) and D_2 (75.8 %) respectively from intermediate and distal outcrop; this confirms the increase in eruptive intensity as already observed from stratigraphic observations.
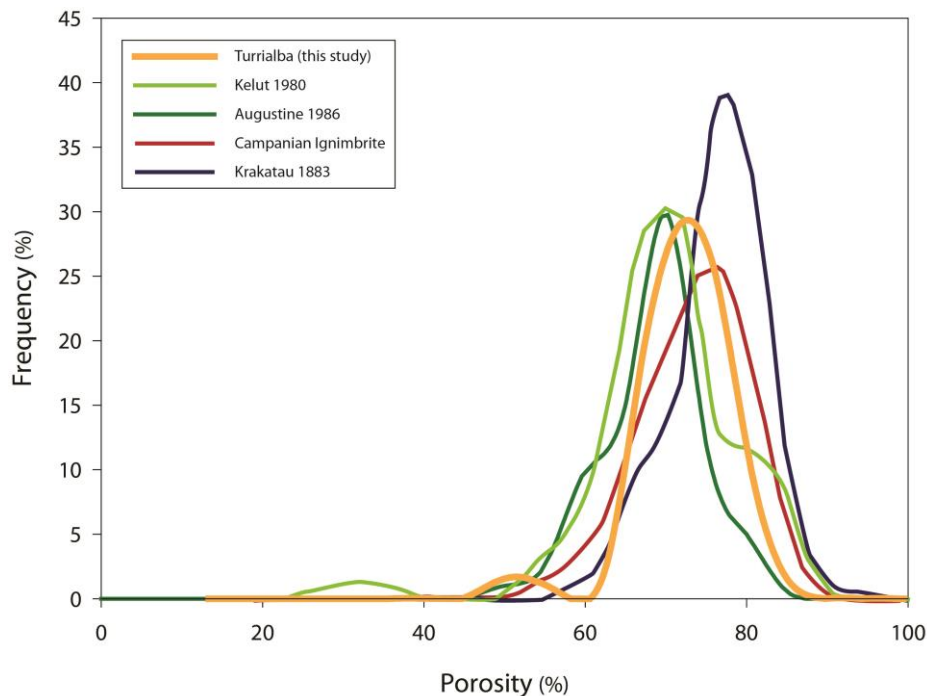
Fig. 5.18 – Porosity distribution of Turrialba 1.9ka eruptive products compared to eruption of similar intensity from literature eruptions (data from Mueller et al., 2011).

In *Fig. 5.18* the average porosity distribution of the 1.9ka andesitic eruption is shown. The average value of porosity is 69.4 % and was obtained by averaging porosity measurements of pumices from intermediate and distal outcrops. The distribution is symmetric, with a mode around 68.4 % and a small tail at lower porosities (43 – 45 %). Mean porosity values of Turrialba 1.9ka eruption are comprised between values typical of Subplinian events, such as the 1986 eruption of Augustine volcano (61.4 %; Mueller et al., 2011), or the 1990 eruption of Kelut volcano (65.8 %; Mueller et al., 2011) and those of other Plinian event such as the Novarupta eruption of 1912 (68.5 %; Mueller et al., 2011).

Vesicles dimensions of low to intermediate density pumices show similar values, with maximum dimensions between 1.18 and 0.93 mm and minimum dimensions between 0.003 and 0.009 mm. High density clasts display the same range of dimensions, with maximum values comprised between 1.47 and 1.19 mm (*Table 5.2*). Intermediate and low density clasts display dimension values that are well in the range of those typical of other Subplinian events, such as the 512 AD eruption of Vesuvius (maximum vesicles dimension between 0.79 and 1.0 mm and minimum between 0.04 and 0.001 mm; Cioni et al., 2011). These values are also in the range of those measured in other Plinian eruptions such as the 79 AD eruption of Vesuvius (maximum dimension of vesicles (maximum dimension between 1.51 and 0.001 mm).

Vesicle volumes are characterized by polymodal distributions with two distinctive modes at 0.09 and 0.93mm, observed in samples belonging to the distal outcrop (IR2/1, IR2/2 and IR2/3), and between 0.14-0.23 and 1.17 mm in samples of intermediate outcrop (TU31/2, TU31/3, TU31/5). These values are comparable to modes measured in other Suplinian to Plinian events, such as the 1875 eruption of Askja volcano (modes between 0.079 and 0.79 mm; Carey et al., 2009) or the 79 AD explosive event of Vesuvius (modes between 0.01 and 0.09 mm). As observed Vesicles Volume Distributions of intermediate and low density samples display polimodal patterns in all the analyzed clasts, with the occurrence of two or multiple modes. These scattered distributions suggest multiple population of vesicles and thus nucleation events, also typical of high disequilibrium conditions.

Pumices of Turrialba 1.9ka eruption display Vesicle Number Densities that cover one order of magnitude ($10^7 – 10^8$ cm^{-3}), ranging between 6.8 x 10^7 cm^{-3} to 5.76 x 10^8 cm^{-3}. In intermediate and distal outcrops slight vertical variations of VNDs along the stratigraphic column are observed. The initial fallout phase is characterized both in intermediate and distal outcrops by similar VNDs, respectively 1.98 x 10^8 cm^{-3} (sample TU31/2; level I_1) and 2.26 x 10^8 cm^{-3} (sample IR2/1; level D_1). Upward in the stratigraphic succession, both levels I_2 (sample TU31/3) and D_2 (sample IR2/2) show

119

an increased Vesicle Number Density, respectively 3.27 x 10^8 cm^{-3} and 3.34 x 10^8 cm^{-3}, suggesting an increase in the eruption intensity, which is in agreement with field observation of reverse gradation. The upper levels of both intermediate and distal outcrop display a decrease in VNDs values, respectively 2.19 x 10^8 cm^{-3} (sample TU31/5; I_5) and 2.05 x 10^8 cm^{-3} (sample IR2/3; D_3).These VNDs values are in the range of other Subplinian eruptions such as the 572 AD Vesuvius eruption (1.2 x 10^8 - 1.3 x 10^9 cm^{-3}) and slightly smaller than those of the Plinian eruption of Vesuvius 79 B.C. (5.2 – 8.8 x 10^8 cm^{-3}; Gurioli et al., 2005), of St Helens 1980 (8.2 x 10^8 – 9.2 x 10^9 cm^{-3}; Klug and Cashman, 1994) and 1875 Askja eruption (7.1 x 10^8 – 2.0 x 10^9 cm^{-3}; Carey et al., 2009) suggesting nucleation rates similar to Subplinian to Plinian events. In addition D parameter, calculated from the Cumulative Vesicle Size Distribution, displays values ranging between 2.81 and 2.92 (*Table 5.2*), suggesting evidences of disequilibrium conditions during magma ascent.
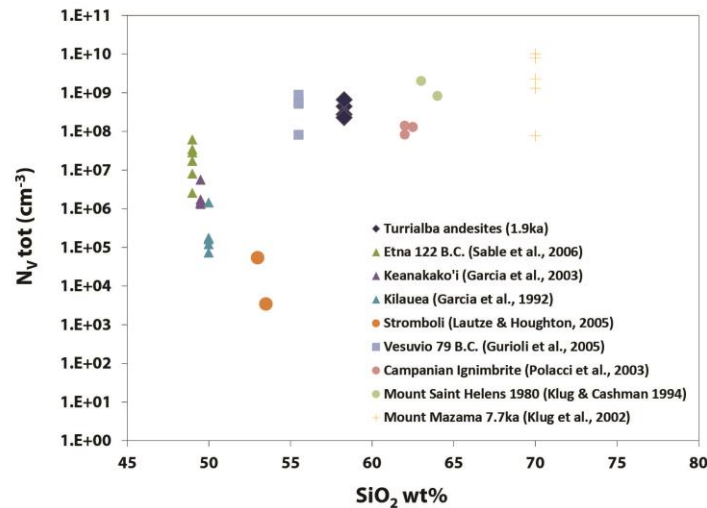
Fig. 5.19 – VND (cm^{-3}) against Silica content (wt %) for Turrialba 1.9ka samples and comparison with data from other eruptions (modified after Sable et al., 2006).

The presence of stretched and deformed textures within bubble populations in both the modal and low density clasts, could imply conditions of high shear and acceleration of magma in the conduit rather than post-fragmentation deformation.

In summary, all the textural features here presented, the elevated VND, the narrow porosity distribution, the polymodal volume distribution, the minimum and maximum size of bubbles, the high D numbers and lastly the highly elongated and deformed bubbles all concur to classify this eruption as a very high energy sub-plinian eruption. Very high disequilibrium conditions, due to

elevated ascent velocities are responsible for disequilibrium nucleation and growth processes, giving rise to several nucleation events, and the development of high VND and D numbers. Small changes in the eruption ascent velocity and intensity are recorded in the stratigraphy (reverse gradation) and also testified by higher VND and D pertaining to levels D_2 and I_2.

When considering the proximal outcrops, a certain diversity of textures can be observed, compared to the relative homogeneity of textures illustrated in the intermediate to distal outcrops. In particular, the vesicle volume distribution for samples belonging to proximal outcrops is broader an a mode at higher density is present (*Fig. 5.4*). These clasts present an absence of small bubbles, larger bubble population (1.1 – 1.7 mm) that strongly dominate the volume fraction and the presence of an important microlite population. Microlite populations was investigated in particular for the proximal outcrop.

Mineral assemblage is composed by dominant plagioclase, clinopyroxenes and ortopyroxenes and oxides. CSD were performed only on the dominant plagioclase phase and for the proximal outcrop. Investigation of crystal size distribution for intermediate and distal outcrops and for the other phases is currently underway.

CSDs trends of the analyzed samples show the existence of a population of plagioclase phenocrysts related to a growth-dominated crystallization in magma chamber, observed in all the analyzed samples, and a population of plagioclase microlites related to cooling in the volcanic conduit. The latter occurred only in the modal and high density samples of the proximal outcrop, showing a progressive increase in intercept and slope values and decrease in groundmass grain size increasing the density of the juvenile.

All the textural features illustrated are compatible, as already observed, with a very high energy sub-plinian eruption.

The external shapes of the juvenile clasts can give us some insights on the mechanism of the eruptions. The coexistence of variably crystalline, vesicle-rich clasts and crystal-rich, dense blocky clasts could support an important involvement of external water. Morphological features of the juvenile clasts are not indicative of fragmentation by magma-water interactions, as suggested by the lack of hydratation cracks, chemical pitting, adhering particles, depositions of secondary mineral phases, or alteration of the external surface of the fragments (Heiken and Wohletz, 1985; Cioni et al., 1992). Juvenile clasts display three main morphologies: fluidal, spongy and dense. Fluidal clasts are glass bearing and vesicular juveniles, sometimes displaying the shape of tubes, with strongly stretched and elongated vesicles. Spongy clasts are moderately vesicular with rounded to slightly

deformed bubbles intersecting the external surface of the clast. Dense clasts are blocky, sub-angular, massive and porphyric juveniles with microcrystalline surfaces intersecting few vesicles. The large heterogeneity observed in the texture of the juvenile clasts, is consistent with a magma experiencing rapid ascent under a marked lateral velocity gradient (Cioni et al., 2011), being able to shear the melt and deform the vesicles before reaching glass transition. In order to verify that conditions for fragile fragmentation could be reached within the conduit during the eruption, we calculate viscosity as a function of crystal and bubble contents following the model of Vona et al., (2011) for the effect of crystal on the viscosity of a magmatic suspension and the model of Lewelling and Manga (2005) for the effect of bubble.

In order to constrain the fluid-dynamic behaviour of a magma during the eruption, eruptive temperature and volatile content should be known in detail. Unfortunately, the lack of literature data does not allow us to quantify the evolution of viscosity during the course of the eruption, but only a first approximative interpretation can be given.

In *Fig. 5.20*, the viscosity variation versus water content for two eruptive temperature of T= 1050°C and T= 1000°C is shown.
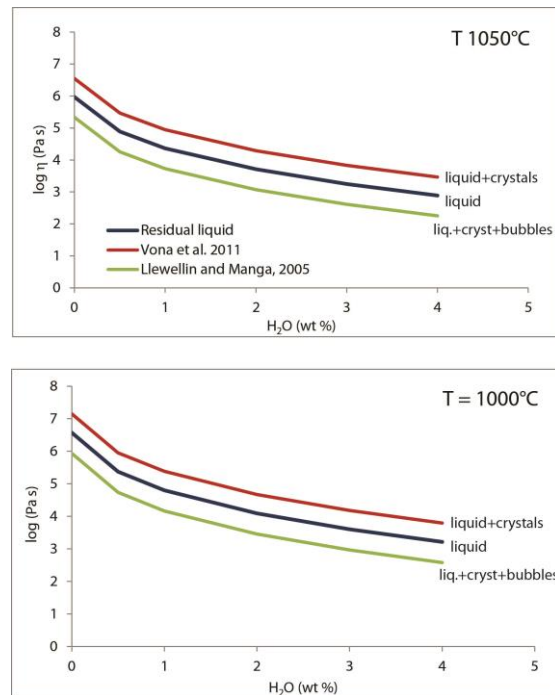
Fig. 5.20 – Plots of viscosity calculations of the natural products for the TU37/5 sample as a function of the water content.

In general, as it can be observed in *Fig. 5.20*, the viscosity that such andesitic magma can experience are very high, certainly high enough to reach brittle fragmentation due to high elongational strain rate (Papale et al., 1999). According with the strain-induced fragmentation criterion, which is achieved when the strain rate exceeds the relaxation time of the melt (Papale 1999), viscosities values normally invoked for reaching conditions for brittle magmatic fragmentation are on the order of 10^8–10^9 Pa s. In particular, the brittle criterion provides the theoretical framework to determine the conditions for the magma fragmentation, based on the Maxwell relation (Maxwell 1866; Dingwell and Webb 1989; Papale 1999):

$$\frac{dv_z}{dz} > k\frac{1}{\tau} = k\frac{G_\infty}{\eta_s}$$

where v is velocity, z is the elongation direction ($dv_z/dz = \dot{\gamma}$ is the elongational strain rate), k is a constant experimentally determined equal to 0.01 (Dingwell and Webb, 1989; Webb and Dingwell, 1990), τ is the magma structural relaxation time, η_s is the newtonian mixture viscosity at zero frequency, and G_∞ is the elastic modulus at infinite frequency. For a wide range of compositions including nephelinite, tholeiite, andesite and rhyolite, brittle magma failure occurs at a strain rate two orders of magnitude below the critical strain rate equal to the inverse of the structural relaxation time, corresponding to $k = 0.01$. G_∞ is found to be scarcely dependent on magma composition and temperature, and is in the range 3±30 GPa (Dingwell and Webb, 1989). So, assuming G_∞ on the order of 10^{10} Pa and k equal to 0.01, we obtain viscosities on the order of 10^8 Pa s for $\dot{\gamma}$=1 s and on the order of 10^6 Pa s for $\dot{\gamma}$=100 s, with 1 to 100 s representing the typical strain rate range for Plinian eruptions.

The heterogeneity observed in the texture of the juvenile material reflects fragmentation of a magma body with lateral and/or vertical gradients in vesicularity and crystal content. Highly vesicular clasts are derived from syn-eruptively vesiculating portions of the magma, while the microlite-rich, high density clasts with more mature textures, are the products of the passive fragmentation of degassed magma. Thus these clasts could represent a portion of magma that experienced a slower rise inside the conduit, allowing time for degassing and crystallization. The elongate shape of the vesicles and the low porosity values could suggest permeability development in the magma during its ascent (Klug and Cashman, 1996; Blower et al., 2001).

Thus we have evidence of lateral hetereogeneity in vesicularity which result in crossing the permeability threshold during the eruption that could produce instabilities in magma discharge and thus variability in conduit pressure and thus in column height.

5.5.2 The 1864 – 1866 basaltic eruption

The explosive eruption occurred between 1864 and 1866 was fed by basaltic-andesite magmas. Due to the strong hydrothermal alteration of the deposits related to this eruption, and their smaller areal extension, only one key outcrop was chosen and studied as representative for the entire eruption event. The stratigraphic record suggests the occurrence of two different eruptive phases, separated by two phreatic layers, within which many short-lived pulses are distinguished. Scoriae belong to the second eruptive phase were collected. This phase is characterized by and alternation of fall-out deposits (samples TU36/2 – TU36/3 – TU36/4) and surges.

Sample TU36/2 represents the initial fall-out occurring after the phreatic event considered as the opening phase of the eruption. This fall out is mainly characterized by the emission of scoriae and ashes followed by the deposition of surge beds. The eruption continued with another fall-out deposit (TU36/3), followed by an alternation of ashes and lapilli beds, with some of these beds indurated and vesicular. This stage is related to phreatomagmatic activity (Reagan et al., 2006). The last part of the eruption is characterized by the deposition of scoriae (TU36/4) and bombs (TU16) emitted from the central and west craters of the volcano.

Scoriae samples are characterized by rounded vesicles and vesicularity comprised between 44 and 56 vol. %. Bombs related to the last stage of activity have the lowest vesicularity measured(12 vol. %). There is quite more than one order of magnitude difference in vesicle number density ($10^4 – 10^6$ cm^{-3}) suggesting differences between scoriae and bombs. The vesicle texture and shape of the former, is a strong indication on the low viscosity that characterize these magmas. Indeed the low viscosity of magma, together with low ascent rates, must have favored the roundness of vesicles and the growth of relatively undeformed sub-spherical vesicles. Scoria samples display a polimodal volume vesicle distribution, with generally two to three modes per sample. Sample TU36/2 displays modes between 0.74 and 2.54 mm, while scoriae TU36/4 between 0.29 and 4.59 mm. Sample TU36/3 display a third mode at 4.59 mm. These values suggest the presence of vesicles of large dimensions due to growth and coalescence processes as suggested also by Vesicle Volume Distributions. Vesicles of the bombs TU16 are small and collapsed, as inferred by the shape of VVD, displaying the lowest volume fraction of all the analyzed samples. Vesicles of this sample are often obliterated by crystals, with the smaller populations displaying reeded borders due to the strong crystallization and growth of microlites. Vesicle Number Density increases with the stratigraphic height, from 1.4 x 10^6 cm^{-3} of level TU36/2 to 2.18 x 10^6 cm^{-3} of TU36/3, and then to 3.91 x 10^6 cm^{-3} in sample TU36/4. Bombs of the last phase of the eruption (sample TU16) display the lowermost VND of 9.74 x 10^4 cm^{-3}. Values of vesicle number density of the entire 1864-1866

eruption are in the range of Strombolian eruptions such as the 2002 Stromboli eruption (VNDs = 7.4 x 10^5 – 1.4 x 10^7 cm^{-3}; Lautze and Houghton, 2007), or the Villarica Strombolian activity (VNDs = 7.4 x 10^5 – 1.4 x 10^7 cm^{-3}), and of Hawaiian activity with values similar to the Pu'u 'O¯'o¯ tephra (VNDs = 1.9 x 10^5 – 3.4 x 10^6 cm^{-3}; Mangan and Cashman, 1996), Mauna Ulu 1969 eruption (VNDs = 2.3 x 10^4 – 2.0 x 10^6 cm^{-3}; Parcheta et al., 2013) and the Episode 16 of Kilauea Iki volcano (VNDs = 4.5 x 10^6 – 1.0 x 10^7 cm^{-3}; Stoval et al., 2011). Modes of vesicle volume fractions of scoria samples (TU36/2, TU36/3 and TU36/4) are comprised between 0.23 and 0.75 mm and are similar to modal values of VVDs of other Hawaiian eruptions such as the Mauna Ulu 1969 eruption (modes at 0.31 and 0.79 mm; Parcheta et al., 2013) and Villarica Strombolian eruptions (mode around 0.40 mm; Gurioli et al., 2008). The coalescence structures observed in these samples and the occurrence of a strong crystallization, can be interpreted as a combination of magma withdrawal from a static upper magma layer, in which bubbles had accumulated, coalesced, and in which magma had the time to crystallize in a medium-shallow reservoir.

Plagioclase CSDs of 1864 – 1866 products are characterized by three distinct patterns, with the most significant break of slope occurring at around 0.1 – 0.2 mm: larger crystals are distributed along nearly horizontal trends; crystals with intermediate dimensions exhibit steeper distribution with respect to their dimension; crystals with dimensions < 0.15 mm show the steepest distribution reaching high intercept and slope values. Qualitative information on the thermal regime prevalent during the crystallization processes may be derived by the examination of crystals habits (Armienti et al., 1994). The experimental observations of Lofgren (1974) reveal that plagioclase develops different habits at different undercoolings. In particular low undercooling (< 30°C) favours the growth of tabular crystals, whilst higher undercoolings causes an increase in the elongation of crystals, which start to develop acicular and skeletal habits. We observed that plagioclase crystals with sizes larger than about 0.13 – 0.15 mm display a rectangular prism shape, based on their long-intermediate-short axis ratio (Morgan and Jerram, 2006). Crystals smaller than 0.13 mm, which are characterized by the steepest size distribution, develop acicular shapes with an even larger elongation. These observation strongly suggest that crystallization took place at increasing undercoolings, with mild degree reflected by the larger crystals and stronger undercooling driving growth of the smallest. This could suggest that crystals belong to the largest populations are intratelluric and reached their larger size in deep seated conditions. Thus the slope of the CSD that is close to the horizontal, suggests that J/G ratio remain quite constant, as expected for a system resting in a deep reservoir and in near thermal equilibrium. The intermediate dimension population could be representative of the growth of crystals during magma ascent in the conduit; indeed effects related to degassing-induced crystallization can increase the undercooling and therefore J/G ratio.

The smallest population of crystals could be related to quenching , as suggested by the shape and the dimension of these crystals (Armienti et al., 1994).
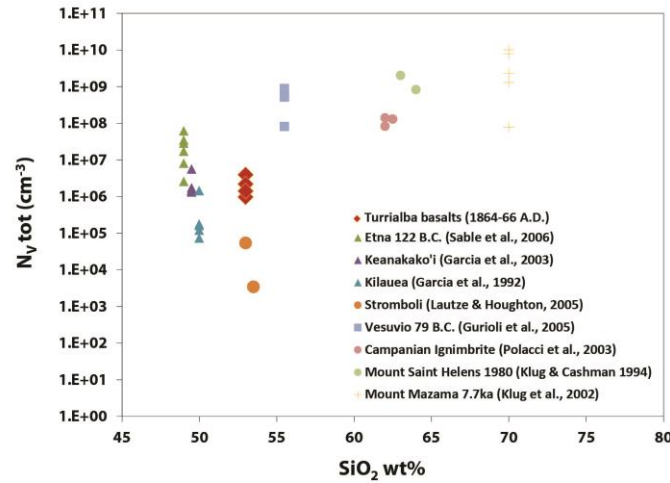
Fig. 5.21 ‑ VND (cm^{-3}) against Silica content (wt %) for Turrialba 1864-1866 samples and comparison with data from other eruptions (modified after Sable et al., 2006).

All the textural parameters investigated suggest that this eruption, fed by basaltic-andesite magmas, display similar features to Strombolian-type eruptions, with a final stage made of breadcrust dense bombs. Shallow melt undergoes open-system degassing that induced crystallization and densification of the magma inside the conduit. This cap of degassed magma stops at shallow level into the conduit and favors the increase of pressure of gas flux from below, until a critical pressure is reached, resulting in explosive fragmentation of the magma.

5.6 Volcanological implications

As observed in the previous chapters, geochemical parameters suggest a strong magmatic signature in fumaroles of Turrialba volcano since the year of 2007. This is confirmed also by the He-isotopic signature that display high ^{3}He/^{4}He (> 7.7 Ra), suggesting that fumaroles are fed by a ^{3}He-rich magmatic source. In particular, the study of noble gases trapped in fluid inclusions of crystals from a compositional suite of rock samples (from basaltic-andesites to more evolved products; see Chapter 4), suggest that the magma actually feeding the crater fumaroles is similar in composition to the most recent erupted basaltic-andesites rocks. However, as suggested by the high variability of

eruptive products, Turrialba volcano display a wide spectrum of eruptive intensity, ranging from explosive Plinian eruption to effusive events.

The eruption of a magma similar in composition with the basaltic-andesites emitted between 1864 and 1866, will certainly produce Strombolian to Hawaiian eruptive events, as also confirmed by textural analysis. The eruption of this kind of magma will produce ash and lapilli fall-out, and possible pyroclastic surges, the latter occurring only in the crater area. As observed by stratigraphic and textural investigations, the last eruptive stage was characterized by the emission of breadcrust to dense bombs. The emission of ballistic is essentially limited to the summit zone of the volcano, as indicated by the presence of numerous bombs on the crater terrace and by the observation of numerous bomb sags in the stratigraphic sequence. This could pose a severe hazard in particular for tourists that come to visit the top of the volcano. However, Turrialba volcano experienced more powerful eruption.

The Plinian to Sub-Plinian eruption investigated in this study, is considered as the most explosive event occurred at Turrialba volcano. This eruptive event is dated 1.9ka and emitted 0.2 km^3 of magma (considering only the fall-out deposits; Reagan et al., 2006). Textural characterization and rheological calculations suggest that this magma experienced high disequilibrium condition during its uprising, high strain rates into the conduit and high ascent rates. The high viscosities reached by this magma are high enough to reach brittle fragmentation domain due to high elongational strain rate. This eruption is considered a stratigraphic marker in Costa Rica, suggesting the wide dispersion of the related eruptive products. Respect to the former, this eruption could pose a severe hazard to the entire central Costa Rica, due to the intensity of the event and also to the position of Turrialba volcano, that is downwind respect to the main metropolitan areas of this Country. Ash and pumices will fall several km away from the volcano, while the flank of the volcano, and the summit region, could be interested by pyroclastic flows and surges, related to the collapse of the eruptive column.

In order to better constraint the eruptive behavior of andesitic magmas, and due to the better knowledge of basaltic magmas, we choose to investigate the multiphase rheology of 1.9ka eruption andesite magma of Turrialba volcano. Knowing the rheological properties of these magmas, and considering the effect of both vesicles and crystals on viscosity, could lead us to better characterize the eruptive style of this magmas, and to develop a model of eruptive dynamic.

6. *The multiphase rheology of magmas from Turrialba 1.9ka eruption*

The styles, dynamics and intensity of volcanic eruptions are strongly controlled by the properties and behavior of magmas during transport. Consequently, computational models intended to simulate the behavior and hazards of potential eruptions from specific volcanoes depend on detailed, accurate knowledge of the rheology of magmas under volcanic conditions. Silicate melts are Newtonian liquids over a wide range of stresses and strain rates, and they behave as a non-Newtonian fluids only when the shear rate approaches the structural relaxation rate (Webb and Dingwell, 1990a). The viscosity of pure liquids can be calculated to a good approximation as a function of temperature and composition, and may vary by several orders of magnitude for geologically relevant conditions (Hui and Zhang, 2007; Giordano et al., 2008).

Natural magmas, however, are commonly transported and erupted at temperatures below their *liquidus* and, consequently, they contain suspended crystals and, in the case of near-surface magmas, and lavas, bubbles. The presence of suspended solids and bubbles strongly affects the viscosity of magmas and can transform their behavior from simple Newtonian fluids to more complex rheological materials (e.g. Krieger, 1972; Lejeune and Richet, 1995; Bruckner and Deubener, 1997; Manga et al., 1998; Lejeune et al., 1999; Llewellin et al., 2002; Stein and Spera, 2002; Sato, 2005; Caricchi et al., 2007; Lavallée et al., 2007; Cordonnier et al., 2009; Vona et al., 2011; Avard and Whittington, 2012; Vona et al., 2013). Factors influencing multiphase magma rheology and eventually the onset of non-Newtonian behavior are the chemical and thermal evolution of the host melt during crystallization and/or bubble segregation, the concentration, shapes, size distributions and maximum packing fraction of suspended particles, as well as the pore fluid pressure and the shear strain rate undergone by magmas. Most rheological studies of natural multiphase suspensions, with few exceptions (e.g. Lavallée et al., 2007; Harris and Allen, 2008; Lavallée et al., 2009; Avard and Whittington, 2012; Vona et al., 2013), have focused on the separate effects of crystals and bubbles on magma rheology. These studies have independently modeled crystal-bearing (e.g. Pinkerton and Stevenson, 1992; Pinkerton and Norton, 1995; Sato, 2005; Ishibashi and Sato, 2007; Caricchi et al., 2008; Ishibashi, 2009; Picard et al., 2011; Vona et al., 2011) or bubbles-bearing suspensions (e.g. Bagdassarov and Dingwell, 1992; Lejeune et al., 1999; Llewellin et al., 2002; Rust and Manga, 2002; Robert et al., 2008a,b).

In this study, we use high-temperature deformation experiments to investigate the multiphase rheology (crystals+bubbles+liquid) of natural samples from the Turrialba 1.9ka subplinian andesitic eruption. In order to characterize the rheology of partially crystallized andesitic magma, we

performed a series of experiments at both constant strain rate and variable strain rate conditions (from 10^{-5} to 10^{-3} s^{-1}), in a range of temperature between 790°C and 870°C. Our experimental data aim to estimate the effects of crystals and vesicles on the rheology of these multiphase suspensions. In the case of a reactivation of volcanic activity, what kind of eruptive style and magma composition is to be expected?

We suggest that the next Turrialba eruption will likely be fed by a basalt-andesitic magma, as inferred by the high ^{3}He/^{4}He ratio measured in olivines of the most mafic products, and in the fumarolic field (*Chapters 3 – 4*). However, the more explosive eruption of andesitic magmas, as the one erupted in 1.9 ka (*Chapter 5*), is not to be excluded a priori. For the hazard standpoint, the evaluation of the maximum explosive event attended in case of renewal of activity is of primary importance. For this reason, and because the basaltic endmember has been already investigated in much more details, we decided to explore the rheological behavior and the effect of crystal and bubbles on the dynamic such silicic magmas.

6.1 The rheology of magmatic suspensions

Viscosity is defined as the resistance to flow under specific applied stress (σ) conditions and it is expressed by complex functions of applied stress and resulting strain (γ) and strain-rates. For a Newtonian liquid,

$$\sigma = \eta \dot{\gamma} \tag{1.1}$$

where η is the Newtonian viscosity. The presence of a solid or a gaseous phase to form a solid or bubble suspension can yield non-Newtonian behavior, expressed by the more general equation (e.g., Herschel and Bulkley, 1926):

$$\sigma = \sigma_0 + K\dot{\gamma}^n \tag{1.2}$$

where σ_0 is a stress threshold to be overcome in order to have flow, namely the yield stress; K is the flow consistency (which corresponds to shear viscosity at $\dot{\gamma} = 1$ s^{-1}) and *n* is the flow index which describes the degree of non-Newtonian behavior, being equal to 1 for Newtonian fluids, $n > 1$ for shear-thickening and $n < 1$ for shear-thinning fluids. For non-Newtonian fluid, $\sigma/\dot{\gamma}$ changes as a function of the deformation rate and if $\sigma_0 = 0$, is equal to Kε^{n-1}. In this case, it is convenient to use an apparent viscosity defined as $\eta_{app} = \sigma/\dot{\gamma}$ measured at a particular stress or strain rate.

From eq. (1.1), assuming zero yield stress (e.g. Lavallée et al., 2007; Avard and Whittington, 2012), the relative viscosity (ratio between stress and strain rate divided by the viscosity of the suspending liquid, η_l) can be written as:

$$\eta_r = \frac{K}{\eta_l} \dot{\gamma}^{n-1} \qquad (1.3)$$

where $K_r = K/\eta_l$ represents the relative consistency.

6.1.1 Crystal bearing magma rheology

A number of experimental and modeling studies have investigated the rheological properties of different crystal-bearing natural magmas at *subliquidus* temperatures (e.g Gay et al., 1969; Shaw, 1969; Spera et al., 1988; Pinkerton and Stevenson, 1992; Pinkerton and Norton, 1995; Sato, 2005; Ishibashi and Sato, 2007; Caricchi et al., 2008; Cordonnier et al., 2009; Ishibashi, 2009; Picard et al., 2011; Vona et al., 2011) or of synthetic silicate suspensions (e.g. Costa, 2005; Caricchi et al., 2007; Costa et al., 2009, Mueller et al., 2010; Cimarelli et al., 2011).

In crystal-melt suspensions, the dispersed phase acts as a "hard" or non-deformable inclusion which increases the viscosity of the suspension through both hydrodynamic and mechanical interaction among crystals. In general, an increasing crystal content of suspensions generate a sigmoidal increase in viscosity as a function of crystal content (Lejeune and Richet, 1995). For low solid fractions, the viscosity increases slowly with the particle volume fraction (ϕ), close to the geometrical mean (Reuss bond; Reuss, 1929), and the suspension maintains a Newtonian rheological behavior (strain-rate independence). When ϕ exceeds a critical value (ϕ_c), particles start to interact with each other and a solid network of particles begins to form, causing a more rapid increase in viscosity and the onset of non-Newtonian flow, characterized by Bingham-like rheology and/or shear thinning effects. As the solid fraction is further increased another rheological threshold, corresponding to the maximum packing density of solid particles (ϕ_m), causes the viscosity to approach the Voigh bound (Voigt, 1928). At this point the system behaves essentially as a single phase solid material and flow ceases, eventually culminating in brittle failure if additional stress is applied to the material (*Fig. 6.1*).
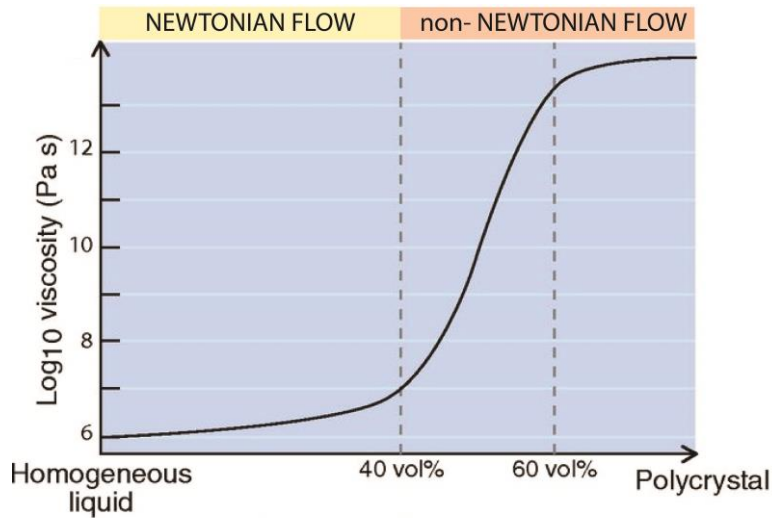
Fig. 6.1 – Crystal fraction against viscosity for solid suspensions (modified after Lejeune and Richet, 1995)

It is thus useful to distinguish the three following concentration regimes (e.g. Rutgers, 1962a, b; Thomas, 1965; Pabst et al., 2006; Mueller et al., 2010): 1) a dilute flow regime, where the viscosity increase is nearly linear and rheology is Newtonian; 2) a semi-dilute regime, where the viscosity exhibits a higher order dependence on crystal content, but rheology remains Newtonian and 3) a concentrated regime, where the suspension shows a rapid increase in viscosity and the onset of Non-Newtonian behavior.

Some studies have established that the transition between the semi-dilute and concentrated flow region occurs when ϕ reaches the critical ϕ_c value (Rutgers, 1962a,b; Thomas 1965; Saar et al., 2001; Pabst et al.,2006; Mueller et al. 2010). For suspensions of spherical particles, Rutgers (1962a,b) and Thomas (1965) found the upper limit for the dilute regime at $\phi \leq 0.02$ and $\phi \leq 0.01$, respectively, and that of the semi-dilute regime at $\phi_c \leq 0.25$. For mono-disperse suspensions of elongated particles, Doi and Edwards (1978) defined these regimes as functions of particle aspect ratios (R = long axis/short axis) (*Fig. 6.2*).

To predict viscosity of liquids containing solid suspended particles in the dilute and semi-dilute concentration regimes, different derivations of the equations of Einstein (1906) and Roscoe (1952) are commonly used.
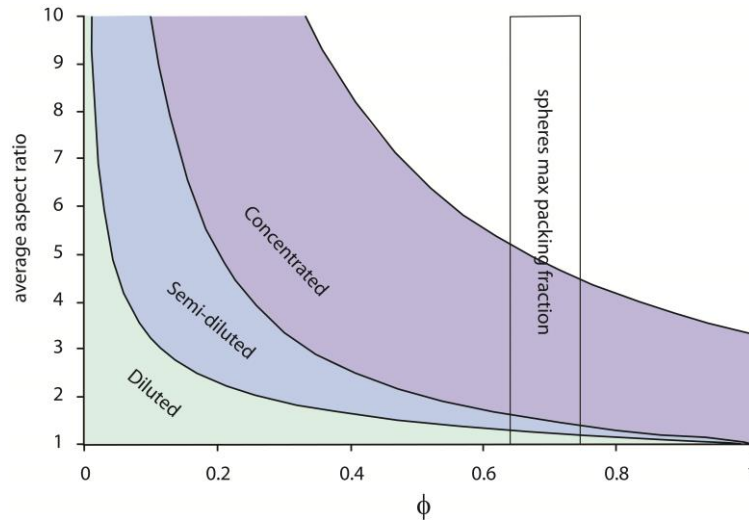
Fig. 6.2 – Concentration regimes for mono-disperse supsensions as a function of aspect ratio and crystal content after Doi and Edwards (1978). Fields are separated by the conditions: diluted $\phi < 1/R^2$; semi-diluted $1/R2 < \phi < 1/R$; concentrated $\phi < 3.3/R$.

For the simplest system of a very dilute suspension of solid spherical monodisperse particles ($\phi < 0.03$), Einstein (1906) calculated that the viscosity follows the equation:

$$\eta_r = (1 + B\phi) \tag{1.4}$$

where η_r is the relative viscosity, defined as the ratio of the effective suspension viscosity over that of the homogeneous suspending fluid (η_s / η_m) and *B* is the Einstein coefficient or intrinsic viscosity, an adjustable parameter which is commonly assumed to be equal to 2.5, although, more recently, some authors give alternative values ranging from 1.5 to 5.5 (e.g. Jeffrey and Acrivos, 1976; Pabst et al., 2006).

To expand the range of applicability to higher crystal fractions, incorporating the effects of hydrodynamically interacting particles (in the semi-dilute regime), Roscoe (1952) introduced an equation known as the Einstein-Roscoe (ER) equation, which considers the maximum packing density of solid particles (ϕ_m):

$$\eta_r = \left(1 - \frac{\phi}{\phi_m}\right)^{-2.5} \tag{1.5}$$

For monodisperse spherical particles, ϕ_m ranges from a maximum of 0.74 when the particles show the most compact ordered hexagonal arrangement (Shaw, 1965) to 0.60 for less compact, disordered arrangements (Marsh, 1981).

The ER equation set with the value of ϕ_m=0.60 (determined empirically by Marsh (1981) using Shaw's (1969) viscosity data), is appropriate to describe relative viscosity increase for particle fraction $\phi <$ ca. 0.3-0.4 (below the onset of non-Newtonian behaviour) for a suspension containing uniform spherical or equantly shaped particles, and has been used extensively in the simulation of natural magmas (e.g. Ryerson et al., 1988; Pinkerton and Stevenson, 1992; Lejeune and Richet, 1995). However, as demonstrated by Sato (2005), it is not applicable to natural magmas containing elongated crystals (i.e. tabular plagioclase), as both ϕ_m and the exponent in the ER equation vary as functions of the textural attributes of the particles (such as shape, size distribution and orientation) as well as the total applied stress, ϕ.

It should be clear that a knowledge of the values of ϕ_m as a function of the textural attributes of the solid particles is critical for the accurate modeling of the rheological behaviour of magmas. It is therefore evident that, in addition to the main factors of the viscosity of the suspending melt and the concentration of crystals, any parameterization must take into account the textural attributes of the suspension and the different deformation regimes (stress - strain rate) applied.

A semi-empirical modification of the ER equation was proposed by Krieger and Dougherty (1959) to be applied to non-spherical particles (KD equation):

$$\eta_r = \left(1 - \frac{\phi}{\phi_m}\right)^{-B\phi_m} \tag{1.6}$$

For values of $B\phi_m$=2.5, Eq. 2.3 yields the ER equation, where B and ϕ_m are fitting parameters. At constant ϕ_m, an increase in B anticipate the deviation from the ER, yielding a higher relative viscosity already at low crystal fraction. On the contrary, increasing the packing fraction at constant B shifts the curves towards higher ϕ.

It has been observed that the intrinsic viscosity, B, is very sensitive to the axial ratio (R) of spheroids, as it increases when the particles shape deviates from an istropic form (Jeffery et al., 1922).

Maron and Pierce (1956) provided a similar relation for $\eta_r(\phi)$ where $B\phi_m = 2$:

$$\eta_r = \left(1 - \frac{\phi}{\phi_m}\right)^{-2} \tag{1.7}$$

which has been extensively used in fiber suspensions (Pabst et al., 2006), requiring only one fitting parameter.

Kitano et al. (1981) and Pabst et al. (2006) fitted the viscosity data on polymer melts with different volume fraction of monodisperse fibers of different aspect ratios with the Maron-Pierce equation. They proposed an inverse linear dependence of ϕ_m on the average aspect ratio using:

$$\phi_m = c - m\bar{R} \tag{1.8}$$

where, $\bar{R}$ is the average aspect ratio (long/short axis ratio) and m and c are empirical constants. Recently Mueller et al. (2010) derived a non-linear dependence for $\phi_m (\bar{R})$ from their experimental data on monodisperse suspensions:

$$\phi_m = \frac{2}{0.321\bar{R}+0.302} \tag{1.9}$$

The effect of the particle size distribution on ϕ_m has been studied by Kansal et al. (2002) on the basis of numerical simulations. The value of ϕ_m increases for spheres with a wide size distribution ($\phi_m=0.87$ for a polydisperse random sphere packing), approaching unity for elongated particles, if the smaller particles completely fill the space between the larger ones.

The dependence of bimodal particle sizes on ϕ_m was found empirically by Chong et al. (1971) on the basis of their viscosity measurements on bi-dispersed sphere systems as:

$$\phi_m = \phi_{m(md)} \cdot \left(\frac{d}{D}\right)^{-0.1041} \tag{1.10}$$

where $\phi_{m(md)}$ represent the maximum packing fraction for a monodispersed system, and d and D are the diameters of the smaller and the bigger particles, respectively. Anisotropic particles with a preferred orientation have a higher $_m$, providing a more ordered packing structure as shown by Donev et al. (2004) with ϕ_m increasing from 0.64 to 0.74 with decreasing of particle orientations dispersion.

For concentrated suspensions, any parameterization of the rheological properties must take into account, (in addition to textural factors) the deformation regime, which may involve the development of yield stress and/or shear thinning effects (Non-Newtonian behaviour). With increasing strain rate, the suspensions can successively show Newtonian, non-Newtonian and

Bingham behaviour (*Fig. 6.3*; Krieger, 1972; Van der Werff and de Kruif, 1989; Brückner and Deubener, 1997; Deubener and Brückner, 1997; Caricchi et al., 2007).
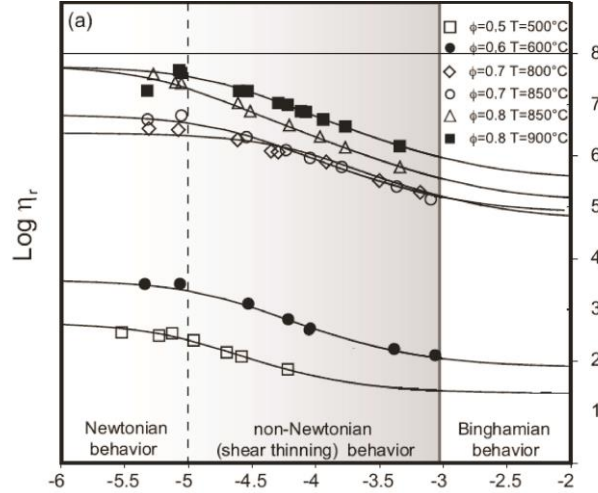
Fig. 6.3 – Evolution of different rheological behaviors as a consequence of increasing strain rate (from Caricchi et al., 2007).

At low strain rates ($\dot{\gamma} < 10^{-5}$ s^{-1}; Brückner and Deubener, 1997; Scott and Kohlstedt, 2006; Caricchi et al., 2007) the relative viscosity increase depends only on the crystal fraction (Newtonian behaviour). Increasing the strain rate above this threshold results in a decrease of the apparent viscosity, a non-Newtonian behavior known as shear thinning (e.g. Webb and Dingwell, 1990) until a minimum value is reached. This minimum represents the onset of pseudo-Bingham behavior in which the relative viscosity is lower than in the Newtonian field but is no longer dependent on the strain rate (*Fig. 6.4*).

A semi-empirical parameterization of the relative viscosity, valid for low to medium-high concentrated suspensions of spherical particles was proposed by Costa (2005) and then modified by Caricchi et al. (2007) and Costa et al. (2009) to take into account the shear rate ($\dot{\gamma}$) dependence of the suspension rheology.
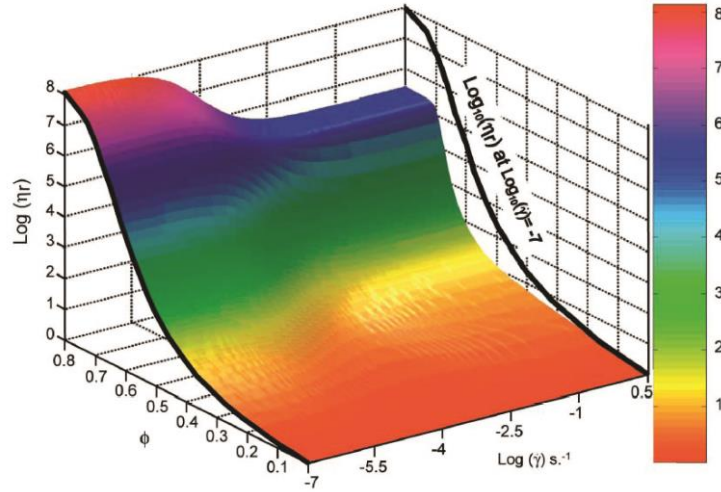
Fig. 6.4 – 3D plot of the prediction model by Caricchi et al. (2007). Increasing strain rate results in a decrease in relative viscosity (shear thinning) and the shift of ϕ_c (here ϕ_{max}) towards higher crystal content (from Caricchi et al., 2007).

The relation between relative viscosity and the solid fraction is given by:

$$\eta(\phi) = \frac{1 + \varphi^\delta}{[1 - F(\varphi, \varepsilon, \gamma)]^{B\phi^*}}$$ (1.11)

where

$$F = (1 - \xi) erf\left[\frac{\sqrt{\pi}}{2(1-\xi)} \varphi(1 + \varphi^\gamma)\right]$$ (1.12)

with $\varphi = \phi/\phi^*$ where ϕ^*, ξ, γ and δ are empirical parameters that depend on the deformation rate and B is the Einstein coefficient. Although this model can successfully predict the multiphase rheology of suspensions containing ϕ = 0.1-0.8 isotropic particles for a wide range of strain rates, it fails when the aspect ratio of the solids increases. Moreover, Vona et al., (2011) took into account not only the crystal content, but also the crystal shape and, with it, the strain-rate dependence of the rheological properties that appear to play primary roles in influencing the transport properties of magmas. In particular, the relative viscosity (η_r) is expressed as:

$$\eta_r = \left(1 - \frac{\phi}{\phi_m}\right)^{-2[1 - \alpha \log(\dot{\gamma})]}$$ (1.13)

where $\dot{\gamma}$ is the applied strain rate and α is a constant equal to 0.06.

6.1.2 – Bubble-bearing magma rheology

In bubble-melt mixtures, the bubbles can either increase or decrease the shear viscosity of a suspension depending on the dynamic regime (Manga et al. 1998; Spera and Stein 2000; Llewellin et al. 2002a; Stein and Spera 2002; Llewellin et al. 2002b; Rust and Manga 2002; Llewellin and Manga 2005; Mader et al. 2013). The relative viscosity is:

$$\eta_r = \eta_s(\phi)/\eta_l \tag{1.14}$$

where η_s is the suspension viscosity and η_l is the viscosity of the liquid phase is a function of the gas volume-fraction ϕ, that may increase or decrease with increasing ϕ depending on the conditions of shear and the bubble-relaxation time λ. The quantity λ is a measure of the timescale over which a bubble can respond to changes in its shear environment. For a single bubble in an infinite medium:

$$\lambda = \frac{\eta_0 R}{\Gamma} \tag{1.15}$$

where R is the undeformed bubble radius and Γ is the bubble–liquid interfacial tension. There is some evidence that λ is an increasing function of ϕ (Oldroyd 1953; Oosterbroek and Mellema 1981; Loewenberg and Hinch 1996; Llewellin et al. 2002b), however, Rust et al. (2003) show that the dependence of λ on ϕ is rather weak so, for simplicity, the previous equation is used for all ϕ.

The effect of bubbles on the magma rheology depends on the type of magma flow, that can be simplified as "steady" or "unsteady" (Llewellin and Manga, 2005). A flow is decribed as "steady" when the condition of shear have remained constant for a time before present t≫ λ (Llewellin et al., 2002; Rust and Manga, 2002). Manga and Loewenberg (2001), Llewellin et al. (2002), Rust and Manga (2002) and Stein and Spera (2002) show that, for a steady flow, the viscous regime is controlled by the capillary number *Ca*, given by:

$$Ca = \lambda\dot{\gamma} = \frac{\lambda\eta_0 R}{\Gamma} \tag{1.16}$$

where $\dot{\gamma}$ is the shear strain-rate. *Ca* describes the relative importance of viscous stresses, which tend to deform the bubbles, and interfacial stresses, which tend to restore them to sphericity. Since the flow is steady, *Ca* refers to the equilibrium between these forces, hence, the bubble shape is also stable (bubbles are described as relaxed) and is referred to as the equilibrium deformation. The magnitude of equilibrium bubble-deformation, therefore, depends on *Ca*. If *Ca*≪1, interfacial tension forces dominate and bubbles are approximately spherical (e.g., Taylor 1934). If *Ca*≫1, viscous forces dominate and bubbles will be elongate (e.g. Hinch and Acrivos 1980). The effect of

bubble shape on viscosity can be explained as follows: Bubbles deform flow lines within the suspending medium, which tends to increase viscosity; bubbles provide free-slip surfaces within the suspending medium, which tends to decrease viscosity. For small *Ca* (bubbles are almost spherical) flow-line distortion is great and free-slip surface area is small, hence, $\eta_r > 1$; for large *Ca* (bubbles are elongate) flow-line distortion is small and free-slip surface area is great, hence, $\eta_r < 1$.

In principle, if the shape of bubbles can be determined as a function of Ca and ϕ then the rheology of the suspension can predicted (e.g., Batchelor 1970). The problem, however, lies in determining bubble shape. For dilute suspensions, analytical results are available for small deformations (e.g., Taylor, 1934) and highly elongate bubbles (e.g., Hinch and Acrivos, 1980). Models are also derived for intermediate deformation (e.g., Wu et al. 2002). In general theoretical results for bubble shape agree well with experimental measurements (e.g., Rust and Manga 2002; Hu and Lips 2003; Yu and Bousmina 2003). When the suspension is no longer dilute, however, the interactions between bubbles affect their shapes and consequently the rheology. Unfortunately, the rheology can be predicted accurately only if the bubble shape is accurately known (Cristini et al. 2002). However, if the shear strain-rate is changing, the flow is unsteady. In fact, Llewellin et al. (2002a,b) have shown that there are degrees of steadiness of flow which can be described using the dynamic capillary number Cd, given by:

$$Cd = \lambda \frac{\ddot{\gamma}}{\dot{\gamma}} \tag{1.17}$$

where $\dot{\gamma}$ is the rate of change of shear strain-rate. *Cd* compares the timescale over which the bubbles can respond to changes in their shear environment (the bubble-relaxation time λ) with the timescale over which the shear environment changes (of order $\ddot{\gamma}/\dot{\gamma}$). If *Cd*≪1, the bubbles are able to respond continuously to the changes in shear environment. Consequently, the bubbles are always approximately in their equilibrium deformation and the flow is approximately steady. Since the flow is approximately steady, the dynamic regime is controlled by the capillary number *Ca*. If, however, *Cd*≫1, the shear environment is changing too rapidly for the bubbles to respond, therefore the bubbles are unrelaxed. Since the bubbles never reach their equilibrium deformation, *Ca* is undefined and the flow is described as unsteady. In an unsteady flow, the bubbles do not have time to respond elastically to changes in shear, hence, they behave as if they have no bubble–liquid interfacial tension. Since there is, effectively, no elastic force affecting the shape of the bubbles their response to the local shearing of the suspending liquid is purely viscous and, since they have negligible viscosity, they deform passively with the suspending liquid. This decreases the distortion of flow-lines around the bubbles leading to a decrease in the viscosity of the suspension as ϕ

increases (Llewellin et al., 2002a). In summary: if $Cd \ll 1$, flow is approximately steady so regime is determined by considering Ca; $Cd \gg 1$ denotes unsteady flow and viscosity decreases with increasing gas volume-fraction.

Llewellin and Manga (2005) parameterized the effect of bubbles on the relative viscosity of a bubbly suspension, considering a single equation for the positive dependence of η_r on ϕ and a single equation for the negative dependence of ηr on ϕ, regardless of whether the decrease in viscosity in the latter case is related to steady ($Ca>1$) or un- steady ($Cd>1$) flow.

6.1.3 – Three phase mixtures

Only very few studies have explored the rheology of crystal and bubble-bearing magmas. Lavallée et al. (2008), Lavalléè et al. (2012), Avard and Whittington (2012) and Vona et al. (2013) have investigated natural samples by uniaxial deformation experiments. The authors have observed pseudo-plastic behavior with a strong shear thinning component for all the investigated magmas and provided equations describing the apparent viscosity as a function of temperature and strain rate for the multiphase magmas. The individual effect of crystal and bubbles was theoretically parameterized by Phan-Thien and Pham (1997) and later applied by Harris and Allen (2008) for the study of basaltic magmas from Mauna Loa and Mount Etna. Phan-Thien and considered three cases as a function of relative size of crystals and bubbles and express the relative viscosity as a function of variable crystal and bubble fraction.

In case 1, crystals are smaller than bubbles:

$$\eta_r(\phi_{xls}, \phi_{bub}) = [1 - \phi_{xls}/(1 - \phi_{bub})]^{-\frac{5}{2}}(1 - \phi_{bub})^{-1} \tag{1.18}$$

In case 2, crystals and bubbles are of the same size range

$$\eta_r(\phi_{xls}, \phi_{bub}) = [1 - \phi_{xls} - \phi_{bub}]^{-(5\phi_{xls} + 2\phi_{bub})/2(\phi_{xls} + \phi_{bub})} \tag{1.19}$$

In case 3, crystals are larger than bubbles

$$\eta_r(\phi_{xls}, \phi_{bub}) = [1 - \phi_{bub}/(1 - \phi_{xls})]^{-1}(1 - \phi_{xls})^{-\frac{5}{2}} \tag{1.20}$$

This treatment does not take into account the effect of textural variability, being applicable to spherical particles only, and strain rate dependency on the rheology.

In this study, we investigated the rheology of a natural sample derived from the Turrialba 1.9ka Subplinian eruption, containing between 39 and 51 % open porosity and crystal content of ca. 0.30 % with respect to the solid fraction. The experiments were performed at temperatures ranging from

790°C to 870°C. These measurements allow to address the relative importance of the combined presence of crystals and vesicles and vesicles alone on the viscosity variation of natural andesitic magmas. We choose this sample as representative of the erupted magma, on the basis of its crystal and bubble content, and due to a sufficient presence of glass matrix.

6.2 - Methods

6.2.1 - Sample selection and preparation

The samples used for viscosity determination in this study are scoriaceous volcanic bombs (sample TU37/6), emitted by the 1.9ka Subplinian eruption of Turrialba volcano. Rocks were collected during the 2012 field trip from a proximal outcrop (*Fig. 6.5*), described in *Chapter 5*. The 1.9ka Suplinian eruption of Turrialba is one of the most powerful eruption of this volcano, and is constituted by the emission of ~ 0.2 km^3 of andesitic magma (Reagan et al.,2006).
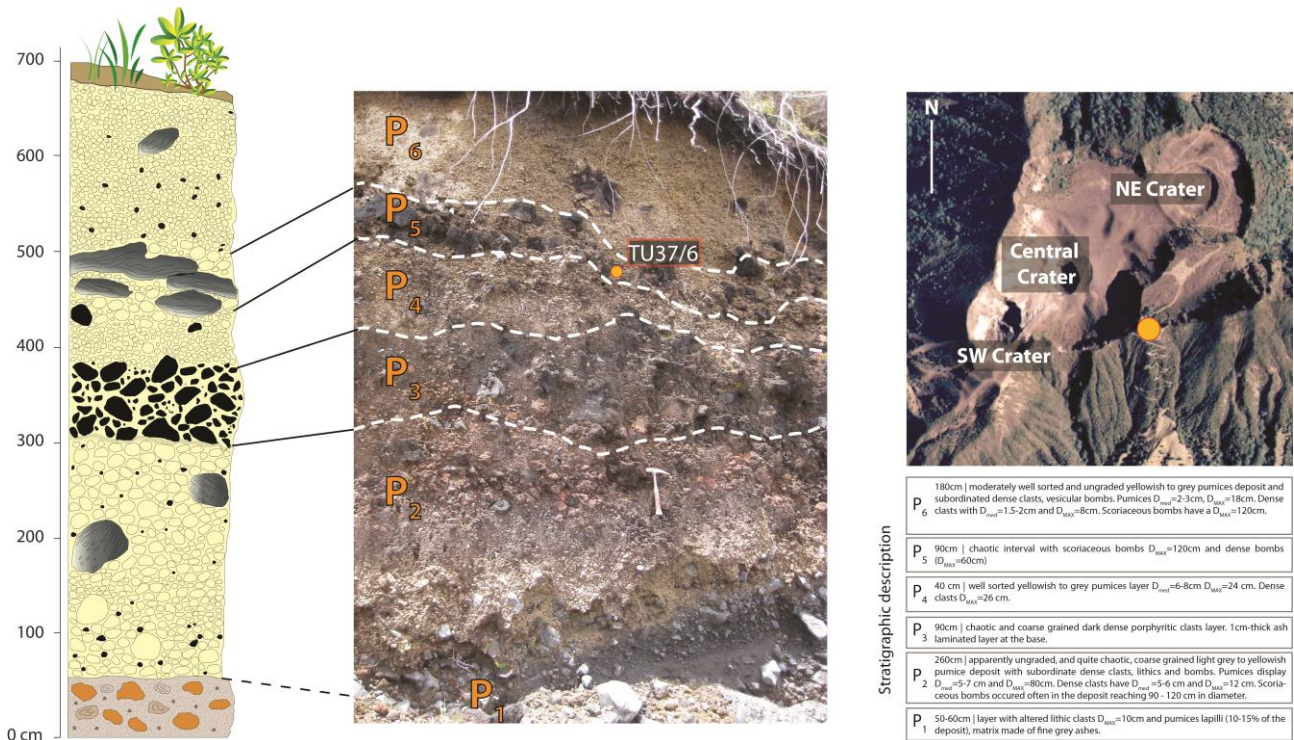
Fig. 6.5 – Sample location and stratigraphic description of the proximal outcrop of the 1.9ka eruption.

6.2.2. – Textural characterization

Samples TU37/6 are volcanic bombs and present vesicles with regular outlines, highly rounded, varying in shapes from sub-circular to ovoidal. Bubble coalescence mainly affect the largest bubbles which exhibit cuspidate re-entrant outlines, that are related to wall ruptures or septa retraction. The mineralogy consists of plagioclase (18.2 vol. %, value melt referenced), clino- and orthopyroxene (9.5 vol. %, value melt referenced) and oxides. All crystals are euhedral, and sometimes polycrystalline clusters are observed. Plagioclase has an elongated shape with aspect ratio 1.00 – 2.80 – 4.00 (*Fig. 6.6*), while pyroxenes display a more rounded shape (*Fig. 6.6*).
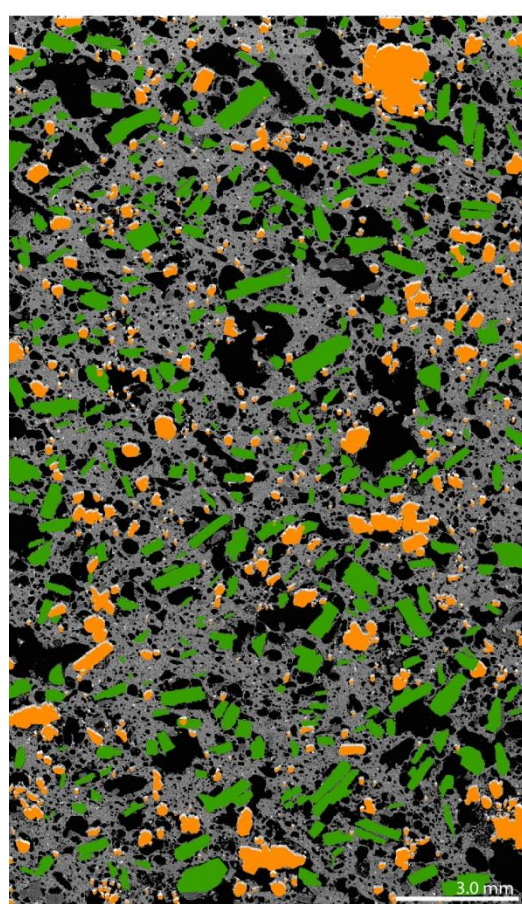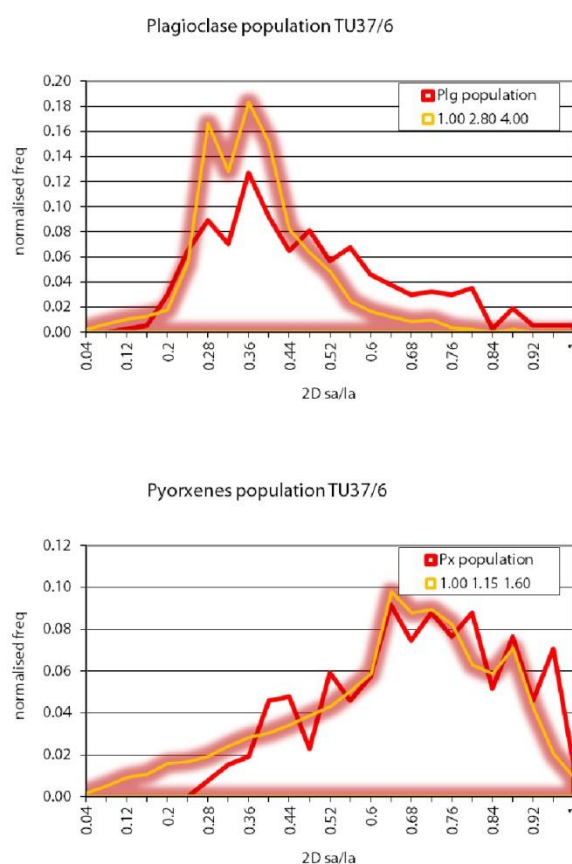
Fig. 6.6 – On the left, SEM image of the selected TU37/6 thin section, representative of the entire sample. Textural characterization were performed using Image J software. On the right, plagioclase and pyroxenes aspect ratio characterization with CSDSlice software (Morgan and Jerram, 2006).

6.2.3 - Density and porosity measurements

In order to perform uniaxial deformation experiments, 32 cylindrical cores of 14.5 – 15.0 mm in diameter and 25.8 – 34.3 mm in length were drilled from the scoria samples. Cores were cleaned and dried at T ~ 70°C for 24h to perform matrix density and volume measurements using an He-pycnometer at Istituto Nazionale di Geofisica e Vulcanologia, ROMA-1.

Eruptive products contain two types of porosity: connected and isolated. Connected porosity is defined as the volume fraction of pores that are connected to each other and can be physically accessed by gas or fluid. Isolated porosity is defined as the volume fraction of porosity that is isolated by the skeletal framework. The total porosity of a rock (ϕ_r) is given by the sum of connected and isolated porosities and is:

$$\phi_T = \left(\frac{V_{\phi T}}{V_{DRE} + V_{\phi T}}\right) \tag{1.21}$$

where V_{DRE} is volume of the dense rock equivalent (e.g. rock powder) and $V_{\Phi T}$ is the volume of the total pore space in the sample. Connected (ϕ_C) and isolated (ϕ_I) porosities are given by:

$$\phi_C = \left(\frac{V_{\phi C}}{V_{DRE} + V_{\phi C} + V_{\phi I}}\right) \tag{1.22}$$

$$\phi_I = \left(\frac{V_{\phi I}}{V_{DRE} + V_{\phi I}}\right) \tag{1.23}$$

The corresponding densities are defined on the basis of how they are measured. The dense rock equivalent (DRE) density of the sample (ρ_{DRE}) is the density of the rock framework of the sample alone (e.g. without porosity) and was measured on samples of rock powder by He-pycnometry. Powdering the sample ensures that there are no pores and that the He-pycnometry experiment measures the true volume (V_{DRE}) of a fixed mass of rock powder (M_R).

$$\rho_{DRE} = \frac{M_R}{V_{DRE}} \tag{1.24}$$

The skeletal density (ρ_{sk}) is the density of the rock and the isolated porosity. Using He-pycnometry, the gas infiltrates the samples connected pores but cannot access the isolated pores. Therefore, the He-pycnometry experiment measures the volume of the rock/solid framework and the isolated (inaccessible) pores (e.g. the skeletal volume: $V_{DRE} + V_{\Phi I}$).

$$\rho_{sk} = \left(\frac{M_R}{V_{DRE} + V_{\phi I}} \right) \tag{1.25}$$

The bulk density (ρ_B) of pre- and post-run samples was first determined geometrically, using the mass (M_R) and the bulk volume of the rock cylinder. In order to perform the most precise bulk volume measurements, especially for the highly deformed post-run samples, we developed a methodology based on using two free software available online: 123D© AUTODESK© and WINGS 3D© . We captured a maximum of 50 photographs per sample, performing at least two 360° views around the rock sample with different perspectives (*Fig. 6.6A*). The photographs, taken always at the same focal distance from the sample, were then uploaded to the 123D© Catch application to realized a 3D model of the sample (*Fig. 6.6B*). 3D models were then scaled and processed with WINGS3D© software, in order to calculate the volume of the sample. With this methodology the volume calculation has an uncertainty of ∼ 1 %.
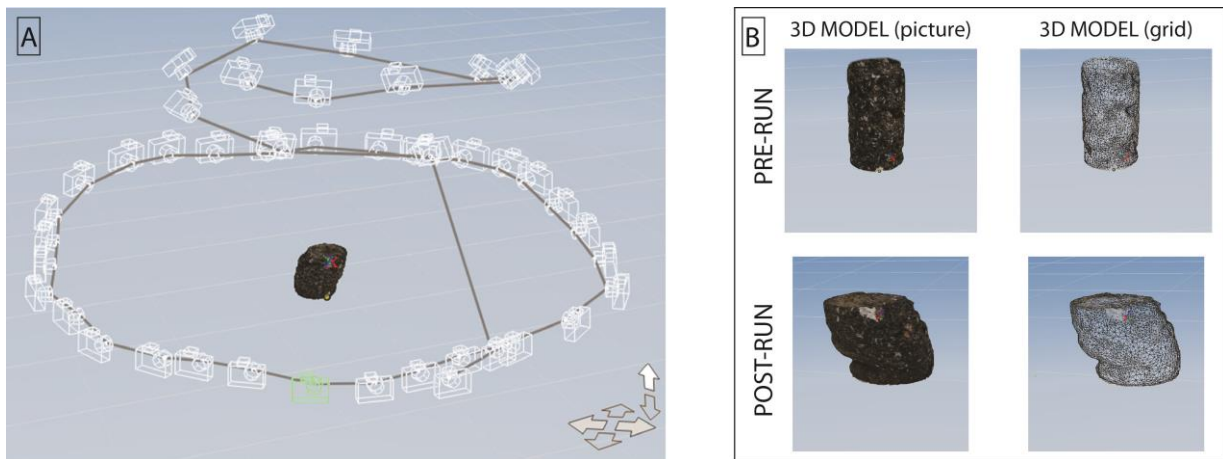
Fig. 6.6 – A) The path followed by the camera during the acquisition of photographs around the rock sample. B) 3D models of pre-run and post-run samples, with textured (left) and grid (right) models. The latter was used for the volume calculations.

The bulk volume incorporates the volume of the rock (V_{DRE}), as well as the volume of connected ($V_{\Phi C}$) and isolated ($V_{\Phi I}$) porosity.

$$\rho_B = \left(\frac{M_R}{V_{DRE} + V_{\phi C} + V_{\phi I}} \right) \qquad (1.26)$$

The values of bulk density (ρ_B), skeletal density (ρ_{sk}) and dense rock equivalent density (ρ_{DRE}) of the samples were finally used to extract the values of connected (ϕ_C), total (ϕ_T) and isolated (ϕ_I) porosities according to the following relationships:

$$\phi_C = 1 - \frac{\rho_B}{\rho_{sk}} \qquad (1.27)$$

$$\phi_r = 1 - \frac{\rho_B}{\rho_{DRE}} \qquad (1.28)$$

$$\phi_I = \frac{\rho_S}{\rho_{sk}} - \frac{\rho_B}{\rho_{DRE}} \qquad (1.29)$$

Core samples belonging to TU37/6 display a bulk density ranging between 1.28 and 1.60 g/cm^3. The matrix density ranges between 2.50 and 2.62 g/cm^3. The dense rock equivalent is 2.80 ($\pm$0.003) g/cm^3. Average porosity is of 44 %, with a maximum value of 51% and a minimum of 39%. Closed porosity ranges between 0 and 3 %. In *Fig. 6.7* the density distribution of 1.9ka andesitic eruption of Turrialba volcano is plotted. Other samples from the same eruptive unit (TU37/8) are also reported for comparison purposes.
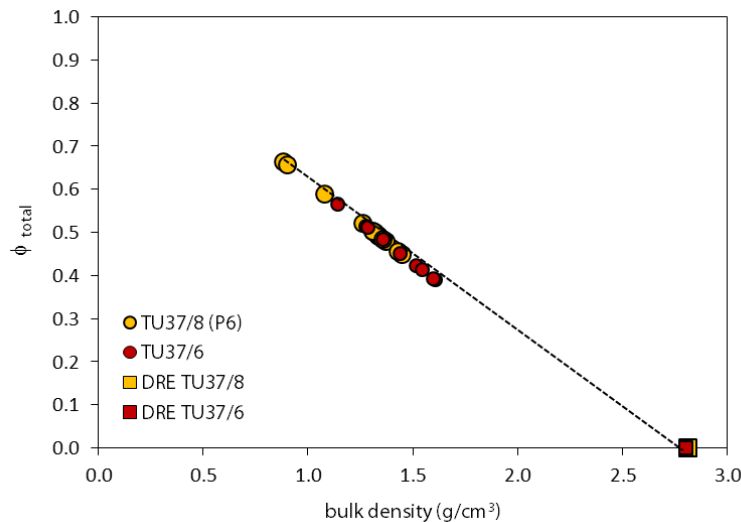
Fig. 6.7 – Density measurements of TU37/8 (orange circles) from Turrialba 1.9ka eruption. Bulk density is the ratio between the sample weight and the volume of the core. Values of the Dense Rock Equivalent (DRE) measured by pycnometry on sample powder is reported.

6.2.4 The Volcanology Deformation Rig (VDR)

Uniaxial deformation experiments were performed at Experimental Volcanology and Petrology Laboratory (EVPLab) of Roma Tre University (Rome, Italy) using the Volcanology Deformation Rig (VDR), a low-load high-temperature apparatus previously described by Quane et al. (2004). The base of the VDR is a LoadTrac II loadframe manufactured by Geocomp Corporation. The unit performs both constant displacement rate and constant load tests. Displacement is achieved by controlling the position of the bottom platen using an electronic stepper motor with a displacement speed range from 5 x 10^{-6} to 2.5 x 10^{-2} cm/s and measured using a built-in linear variable differential transformer (LVDT) displacement transducer with a 7.6 cm travel range and 0.00013 resolution. Load is measured using a S-type load cell attached to a fixed crossarm. Samples can be loaded at rates from zero to 1.9 kg/s, and the maximum attainable load is 1136 kg with 0.086 kg resolution. The unit is factory calibrated for apparatus distortion during loading. An internal processor applies calibration factors for displacement (determined using a gauge block) and load (determined using a proving ring), thereby converting raw data into corrected output. Experimental output (e.g. measurements) can be collected every 0.01 s throughout the experiment. This stand-alone base unit has been modified to perform high temperature measurements, through the addition of a FIH fiber insulated heater tube furnace. The furnace has helically wound, Fe-Cr-Al alloy resistance wire elements embedded in a rigid body of high-temperature refractory fiber. It is 30.5 cm long, and has inner and outer diameters of 7.6 and 15.25 cm, respectively. It is seated on the steel base and surrounds the lower piston, the sample and most of the upper piston. The furnace generates temperatures up to 1100°C. A K-type thermocouple is used to monitor and control temperature during the experiments.

Temperature calibration

In order to constrain the temperature gradient inside the experimental cell, following the calibration method by Quane et al. (2004), we prepared a set of cores from Turrialba sample, with center holes drilled throughout their length. In addition to the regular VDR thermocouple (positioned at the base of the core inside the lower piston), a calibration thermocouple attached to an external temperature-monitoring device was inserted into the center hole and fixed to load cell. Then the lower piston was moved downward with respect to the additional thermocouple, to map the temperature profile from the bottom to the top of the core. This procedure was used to sample temperatures at ~ 0.2 cm intervals for different experimental configurations (*Fig. 6.8*). Without insulation (SETUP 1) and only with a refractory at the base of the furnace, the gradient inside the cell was of 17°C. Adding a refractory at the top of the furnace, the gradient increased to 22°C (SETUP 2). Filling completely

the space between pistons and the furnace walls with Cotronics Rescor blanket insulation, the gradient remained around 22°C (SETUP 3). Finally, wrapping the insulation only around the upper piston, we produced a symmetric temperature profile that reaches steady-state after 1 hour dwell time, and showed a total variation of ~ 11°C (SETUP 4 and SETUP 5).
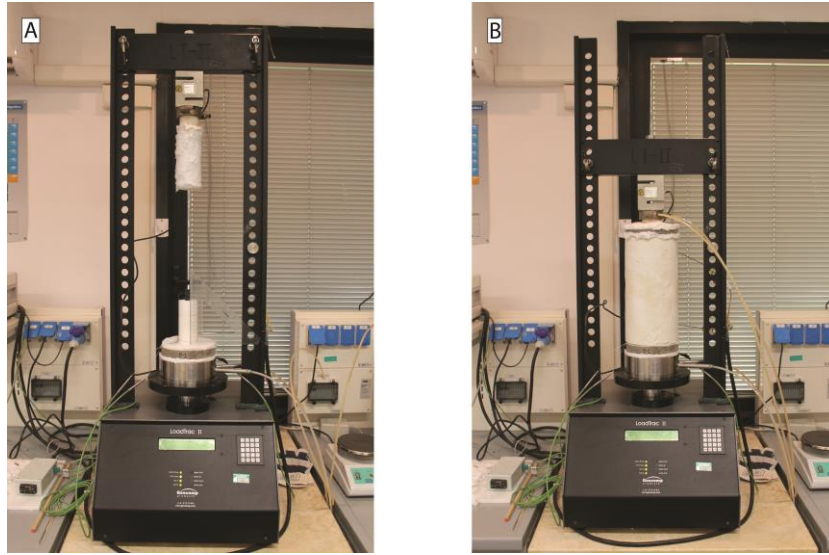
Fig. 6.7 – The experimental apparatus adopted in this study before (A) and during an experiment (B; with the furnace equipped).
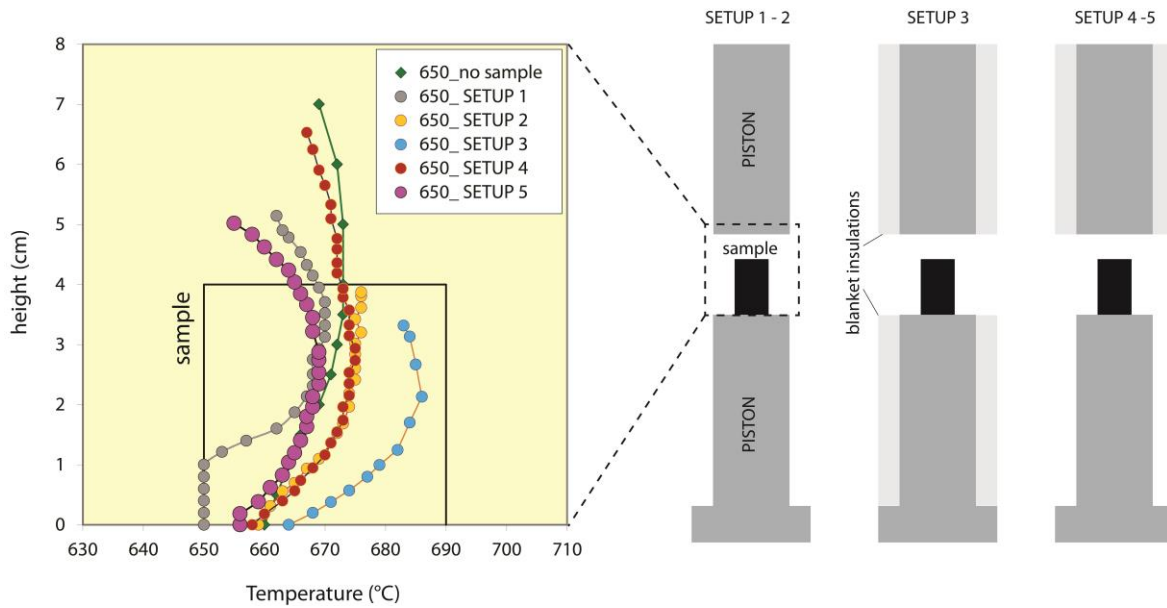
Fig. 6.8 – Temperature profiles (in °C) in experimental cell as a function of sample height and different insulation strategies (SETUP 1 – 5). On the left, schematic of furnace and pistons assembly to show range of insulation strategies adopted.

A constant shift of temperature reading (of about 5 °C) was observed between the controlling thermocouple placed inside the lower piston and the additional one placed inside the sample at zero position (Fig. 6.8), likely due to the different thermal conductivity of rock sample and the piston.

Controlling and evaluating the actual experimental temperature is fundamental especially for measurements close to glass transition, where the activation energy for viscous flow is greater and the viscosity-temperature relationship is steeper (e.g. Hess et al., 2008). For this reason all the viscosity measurements were conducted with the addition of two external thermocouple, one at the base of the sample (in the furnace chamber, not inside the piston) and the other one close to the middle part of the sample where the maximum temperature is measured (*Fig. 6.9*).The integration of the two temperature readings allowed a better constrain of the temperature gradient affecting the sample and represent an improvement with respect to the VDR experimental set-up of previous studies (i.e. Quane et al., 2004; Robert et al., 2008; Vona et al., 2013).

Fig. 6.9 – Photographic sketch of thermocouple positions respect to the sample.

Viscosity calibration

Each experiment generates a nearly continuous set of raw measurements including: time (s), load (kg) and displacement (mm) from which we compute uniaxial stress (MPa), strain and strain rate (s^{-1}). Uniaxial stress (σ) is calculated from:

$$\sigma = \frac{load}{\pi r^2} \qquad (1.30)$$

where r is the radius of the sample core. This relationship between core geometry and stress can be exploited to extend the upper and lower ranges of the VDR even though the load cell has an upper limit of 1136 kg.

Strain is calculated as:

$$\varepsilon = \frac{\Delta l}{l} \qquad (1.31)$$

where Δl is the experimental displacement and l is the original length of the sample. Cumulative (or incremental) strain rates are calculated from values of time and displacement:

$$\varepsilon^0 = \frac{\left(\frac{\Delta l}{l}\right)}{\Delta t} \qquad (1.32)$$

where Δt is the measurement time interval.

The viscosity was calculated according to the calculation by Gent (1960) as follows:

$$\eta = \frac{2\pi m g h^3}{3V\frac{dh}{dt}(2\pi h^3 + V)} \qquad (1.33)$$

where m is the applied load, g is the gravity acceleration, h is the sample height, V is the sample volume and dh/dt is the displacement rate.

The press was calibrated on solid glass cores ($\sim$ 10 x 25 mm) of NIST (NBS) standard reference material (SRM) 717a (borosilicate glass) under constant displacement and dry conditions at temperatures between 570 °C and 610 °C, corresponding to certified viscosity ranging from $10^{10.04}$ and $10^{11.05}$ Pa s. The resulting experimental accuracy corresponds to 0.1 log units (*Fig. 6.10*).
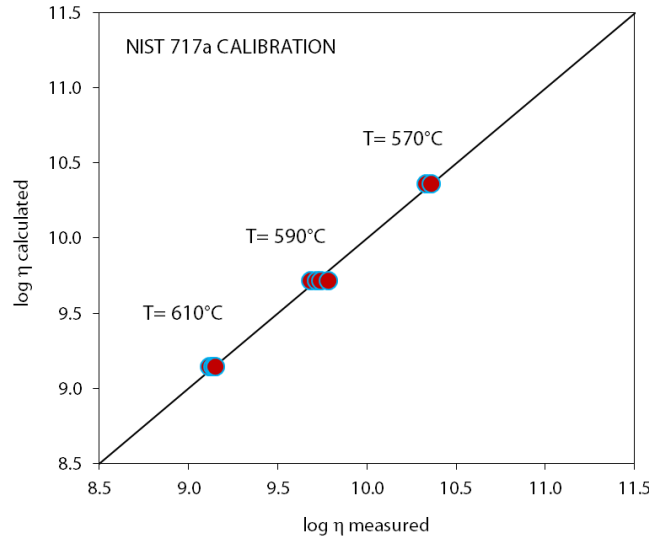
Fig. 6.10 – Measured against calculated viscosity for the standard NIST717a adopted for the calibration of the uniaxial press.

6.3 Experimental Results

Uniaxial deformation experiments were performed isothermally, under unconfined conditions (i.e. $\sigma_2 = \sigma_3 = 0$) by deforming crystal- and pore- bearing cylindrical specimen at constant displacement rate (CDR). Full details are listed in *Table 6.1*. On specimens of sample TU37/6, five experiments were run at temperatures between 790 and 870°C, and at variable strain rate (VSR), with a progressive strain rate stepping from a minimum of 1.0×10^{-5} s^{-1} to a maximum of 7×10^{-4} s^{-1}. These experiments, whose duration was comprised between ~1h and ~8h, were performed to investigate strain- (or time-) dependent effects on the rheological response due to the textural change of natural samples.

Measurement segments started only after the elastic response to any change of stress or temperature was complete, and the viscous relaxation time of the sample had been exceeded (Dingwell and Webb, 1989). To evaluate the relaxation timescale at the experimental conditions, we first calculated the viscosity (η) of the residual liquid matrix using the viscosity model by Giordano et al. (2008). The obtained values of viscosity were used to estimate the characteristic structural relaxation timescale (τ) as the ratio of the interstitial liquid's Newtonian viscosity to the bulk shear modulus of silicate melts ($G_\infty = 10^{10.5}$ Pa; Whittington, 2012), following Maxwell (1867) relationship (Dingwell and Webb, 1990). *Figure 6.11* shows the relaxation time (τ) and the characteristic relaxation strain rate ($\dot{\varepsilon}_{relax} = \tau^{-1}$) for the anhydrous Turrialba 1.9ka eruption liquid matrix as a

function of the inverse of temperature. In order to be in the viscous regime at a given temperature, the experimental deformation rate must be slower than the characteristic structural relaxation time. According to Dingwell and Webb (1990), brittle failure occurs when the applied strain rate ($\dot{\varepsilon}$) is higher than $\dot{\varepsilon} > 0.01\,\dot{\varepsilon}_{relax}$ and non-Newtonian behavior occurs when it is higher than $\dot{\varepsilon} > 0.001\,\dot{\varepsilon}_{relax}$ (Dingwell and Webb, 1990; Papale, 1999). Most of the experimental conditions pertain to the Newtonian behavior viscous regime for the liquid matrix (T between 790°C and 870°C for sample TU37/6). Only for one experiment conducted at T = 715°C, the liquid approaches the brittle field.
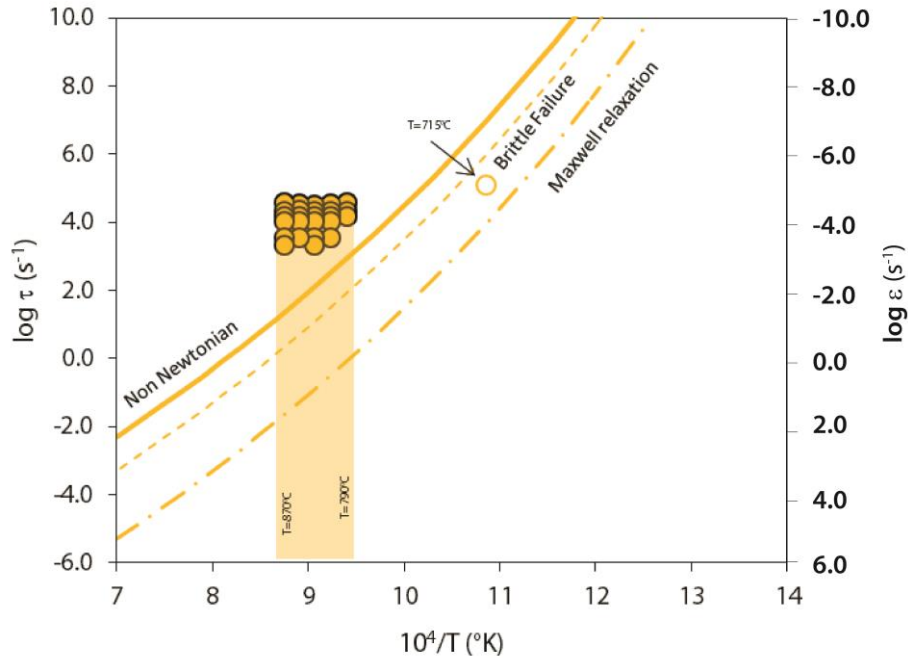
Fig. 6.11 – Characteristic relaxation time (τ)- characteristic relaxation rate ($\dot{\varepsilon}_{relax} = \tau^{-1}$)-temperature relationship for Turrialba 1.9ka anhydrous andesitic liquid. (τ)-T curve is determined using the Maxwell relationship (Dingwell and Webb, 1990), Turrialba 1.9ka liquid viscosity was calculated with Giordano et al. (2008). Brittle failure (dashed line) and Non-Newtonian behavior (light grey line) fields are calculated according to Dingwell and Webb (1990) as 2 and 3 $\log_{10}$ units above the relaxation time respectively. The vertical orange area represent the temperature interval at which experiments were run.

Tab. 6.1 – Summary informations for all the experiments on natural rocks in the uniaxial deformation press

Exp. Typ.	Sample	Temp. (°C)	Duration (s)	Density (g/cm^3)		Total porosity (%)		Open porosity (%)		Closed porosity (%)		ε (%)
				before	after	before	after	before	after	before	after	
VSR	B22	770	6750	1.59	1.68	43.30	40.23	38.63	35.84	4.67	0.04	0.16
VSR	B7	790	2655	1.61	1.71	42.72	38.89	38.34	34.81	4.37	0.04	0.16
VSR	B5	810	2274	1.54	1.63	44.91	41.86	40.96	37.93	3.95	0.04	0.12
VSR	B4	830	1387	1.28	1.45	54.38	48.31	48.79	43.64	5.60	0.05	0.21
VSR	B8	850	893	1.29	1.43	54.11	48.96	49.01	44.65	5.10	0.04	0.14
VSR	B9	870	934	1.60	1.70	42.92	39.49	38.60	35.59	4.32	0.04	0.13

6.3.1 Variable Strain Rate (VSR) measurements

Variable Strain Rate (VSR) measurements were first performed to investigate the quasi-instantaneous response of the apparent viscosity to applied stress and to evaluate possible onsets of Non-Newtonian rheological response of Turrialba magmas. Each deformation step reached a strain lower than about 0.10, to preserve as much as possible the original textural features of natural samples, limiting the processes of fabric evolution due to deformation (e.g. porosity loss, orientation of crystals, strain localization, etc.).

On each measured core of the TU37/6 subsets, from four to eight consecutive segments of deformation were performed at different strain rates. All samples were subjected to different deformation histories, with steps of increasing or decreasing strain rates. The results of the measurements are reported in *Table 6.2 and Table 6.3*. As a typical behavior, regardless of deformation paths, stress reached a stable value at constant strain rate indicative of flow conditions, but some exceptions were observed. In the following all the measurement results are described in detail as a function of the increasing temperature (*Figs. 6.12-6.13*).

In experiment run at T = 715°C (the lowest investigated temperature) flow conditions were not achieved as brittle failure was observed at a strain rate of about 1×10^{-5} s^{-1} under an applied stress of 13.53 MPa (*Fig. 6.12*), resulting in the failure of the sample.

Specimens of sample TU37/6 display a similar stress pattern (*Fig. 6.13a*), at lower strain rates (1 – 7 x 10^{-5} s^{-1}), flow condition were achieved, with constant stress values. At higher strain rates (1-7 x 10^{-4} s^{-1}) an increase of stress value with time was observed. This could be related to the quick geometrical changes occurring in the rock cylinder during the deformation. As expected, increasing temperature, flow conditions were reached at lower stress values. Viscosity patterns are presented in *Fig. 6.14b*. At constant temperature, with increasing strain rate, a slight decrease in viscosity with increasing strain rate is observed (maximum difference of -0.06 Pa s), very close to the accuracy

limit of this method. The effect of temperature on viscosity is shown in *Fig. 6.15*. As can be seen, increasing temperature from 790°C to 870°C, yields a decrease of viscosity of ~2 orders of magnitude (*Fig. 6.15*), varying from $10^{10.9}$ Pa s to $10^{9.0}$ Pa s.
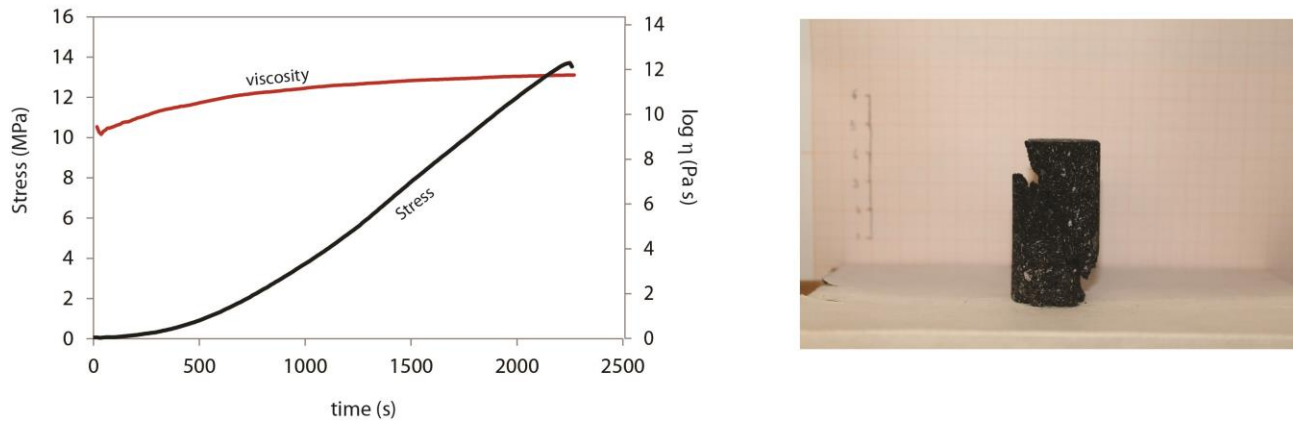
Fig. 6.12 – On the left, the evolution of applied stress and viscosity with increasing time at T =715°C. On the right an image of the sample TU37/6 after brittle failure occurred.
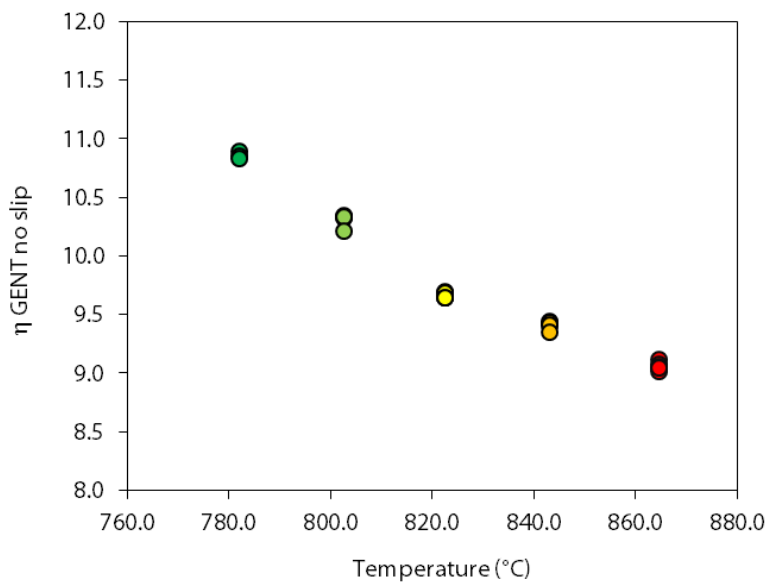
Fig. 6.14 – Viscosity as a function of temperature at the considered strain rates for variable strain rate measurements of Turrialba andesites 1.9ka.

Tab. 6.2 – Summary of the performed experiments on specimens of sample TU37/6

Sample	Initial porosity (Φ_T)	Deformation step	$T_{furnace}$	T_{base}	T_{av}	Instrumental strain (ε_m)	Strain rate (s^{-1})	Stress (Mpa)	Log η meas.	Log η app.
B7	0.39	I	790	774	782.0	-	-	-	-	-
		II	790	774	782.0	0.070	2.74E-05	6.96	10.89	11.40
		III	790	774	782.0	0.108	4.69E-05	11.23	10.85	11.38
		IV	790	774	782.0	0.151	6.62E-05	15.35	10.83	11.36
B5	0.41	I	810	795	802.5	-	-	-	-	-
		II	810	795	802.5	0.024	2.82E-05	1.94	10.33	10.84
		III	810	795	802.5	0.045	4.84E-05	3.31	10.33	10.84
		IV	810	795	802.5	0.069	6.62E-05	4.67	10.34	10.85
		V	810	795	802.5	0.087	9.35E-05	6.49	10.33	10.84
		VI	810	795	802.5	0.123	2.82E-04	15.28	10.21	10.73
B4	0.51	I	830	815	822.5	0.011	3.08E-05	0.43	9.64	10.14
		II	830	815	822.5	0.025	4.80E-05	0.75	9.69	10.20
		III	830	815	822.5	0.040	6.69E-05	1.03	9.69	10.19
		IV	830	815	822.5	0.054	9.62E-05	1.49	9.69	10.19
		V	830	815	822.5	0.084	2.89E-04	4.18	9.64	10.16
		VI	830	815	822.5	0.134	4.67E-04	6.99	9.64	10.18
B8	0.51	I	850	836	843.0	0.005	2.87E-05	0.23	9.41	9.90
		II	850	836	843.0	0.012	4.47E-05	0.39	9.44	9.94
		III	850	836	843.0	0.024	6.52E-05	0.55	9.43	9.93
		IV	850	836	843.0	0.040	9.81E-05	0.79	9.41	9.91
		V	850	836	843.0	0.063	2.95E-04	2.11	9.35	9.85
B9	0.39	I	870	859	864.5	0.010	2.75E-05	0.11	9.12	9.61
		II	870	859	864.5	0.016	4.85E-05	0.18	9.08	9.57
		III	870	859	864.5	0.022	6.66E-05	0.23	9.05	9.54
		IV	870	859	864.5	0.035	9.58E-05	0.34	9.05	9.55
		V	870	859	864.5	0.060	2.95E-04	0.98	9.01	9.52
		VI	870	859	864.5	0.103	4.61E-04	1.62	9.04	9.55

$T_{furnace}$ (°C) is the temperature measured with the thermocouple positioned in the middle of the sample. T_{base} (°C), is the temperature measured at the base of the sample.
T_{av} is an average temperature calculed between the two.
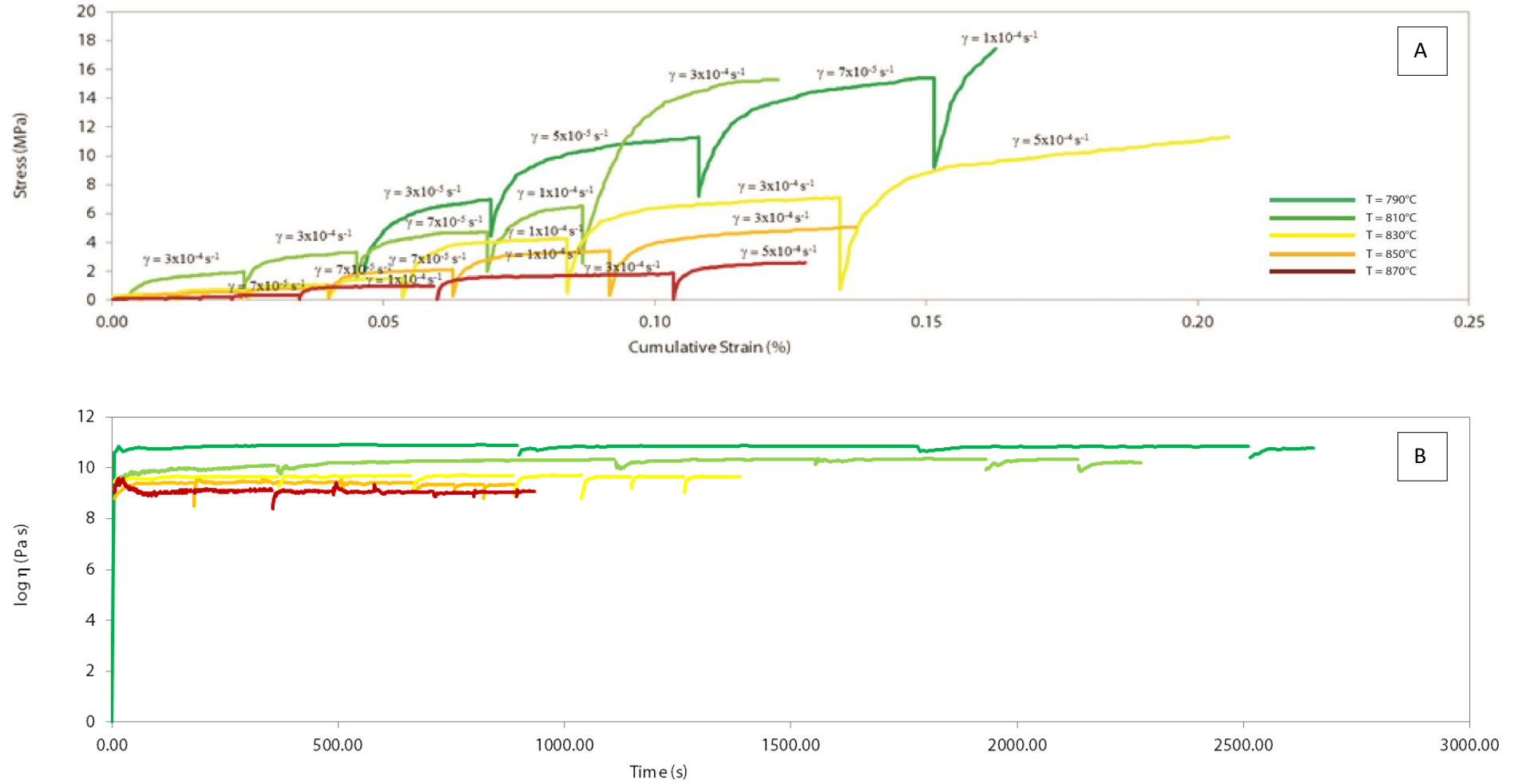
Fig. 6.13 – A) Stress (MPa) vs. cumulative strain (%) patterns of the performed experiments on TU37/6 specimens.

6.4 Discussion

6.4.1 Textural and structural observations

At the end of each measurement, the experimental cores were analyzed to determine the change in core geometry and porosity due to deformation. The results are reported in *Table 6.1*.

During uniaxial deformation experiments on porous rocks, strain is manifested by a reduction of sample length (i.e. shortening). The shortening can be accommodated by both a change of core geometry (e.g. barreling), and a reduction of primary porosity (i.e. volume loss), therefore the total strain, can be described by two components (Quane and Russell, 2005): 1) axial strain (ε_a), accommodated by the reduction of sample length, that is given by:

$$\varepsilon_a = \frac{\phi_i - \phi_f}{1 - \phi_i} \tag{1.36}$$

where ϕ_I is the initial sample porosity and ϕ_f is the porosity of the run product; 2) radial strain (ε_r) is accommodated by change of core geometry (e.g. bulging), and is given by:

$$\varepsilon_r = 1 - \frac{r_i^2}{r_f^2} \tag{1.37}$$

where r_i is the pre-run core radius and r_f is the mean radius of the post-run core. For low amount of total strain, the volume change can be considered to be accommodated by axial strain mainly due to a decrease in porosity, while the radial strain causes no appreciable volume variation. For these conditions, these components can be calculated independently (Quane et al., 2004; Quane and Russell, 2005, 2006). *Fig. 6.16a* shows the total sample strain versus the sum of the two independent components (axial and radial). The linear relationship shows that *Eqs. 1.36* and *1.37* can be used to describe the volume changes related to compression for runs between T=790°C and T=870°C. In *Fig. 6.16b* the individual contribution of axial and radial strain are compared. The strain become dominantly axial (ε_a) in the most experiments performed, this means that compaction is the main type of deformation.
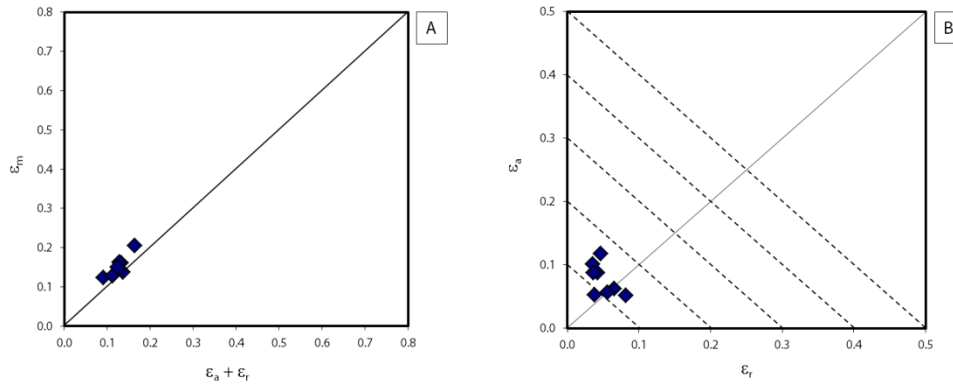
Fig. 6.14 – A) Instrumental strain (ε_m) compared to the sum of axial and radial strain ($\varepsilon_a+\varepsilon_r$). B) Comparison of axial strain (ε_a) and radial strain (ε_r) components. Dashed lines are iso-strain lines.

During experiments a reduction of porosity were observed. According to Avard and Whittington (2012), a detailed observation of the porosity change can provide information on how the deformation is accommodated (*Fig. 6.17*). In particular, simple compaction would lead to a decrease in total porosity and isolated porosity, whereas closure of pore connections may lead to an increase of isolated porosity even as total porosity decreases. Conversely, bubble growth increases both isolated and total porosity, while cracking or tearing will increase connected porosity. In all the VSR experiments total porosity variations ranged between -6.8 % and -11.7 %.. All the analyzed samples were characterized by a significant (almost complete) reduction of isolated porosity (-99%), that confirms, both with the reduction in open porosity, a compaction of the sample during the deformation (*Fig. 6.17*).
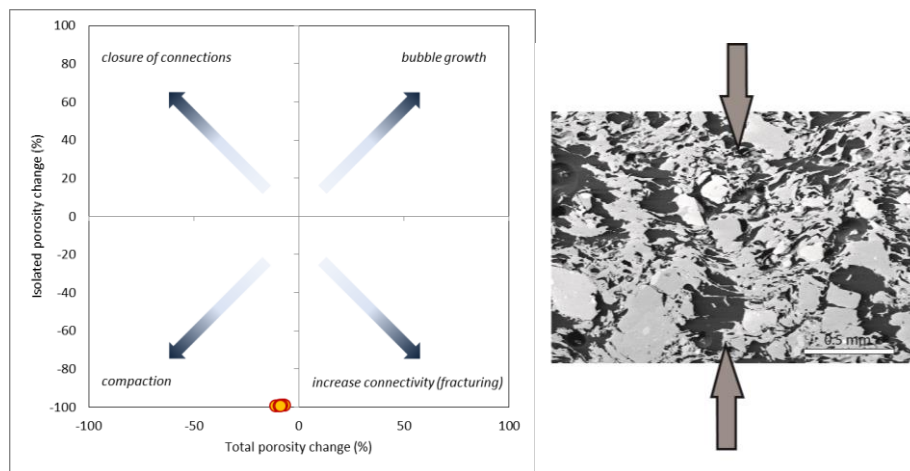
Fig. 6.15– On the left, variation of the isolated porosity as a function of total porosity change. Experimental samples are the orange circles. On the right, SEM image of an analyzed sample, showing the effect of deformation and compaction (magnification 40x).

6.4.2 Fitting of experimental data

In order to parameterize the flow behavior of these complex natural materials, measurements were used to derive stress-strain rate relationships under flow conditions. We observed a linear trend between the applied stress and strain rate (on logarithmic basis) in the temperature interval investigated, so that at higher applied stresses correspond higher strain rate values (*Fig 6.16a*).

Assuming $\sigma_0 = 0$, data were fitted to the following simplified power law expression (e.g. Lavallée et al., 2007; Avard and Whittington, 2012; Vona et al., 2013):

$$\sigma = K\dot{\varepsilon}^n$$

Fitting can be expressed in log terms for stress (*Fig. 6.16a*) or for apparent viscosity (*Fig. 6.16b*):

$$log\sigma = logK + nlog\dot{\varepsilon} \tag{1.34}$$

$$log\eta_{app} = logK + (n-1)log\dot{\varepsilon} \tag{1.35}$$

The fitting is good across the whole dataset, displaying R^2 values between 0.98 and 1. The results of the fitting are reported in *Table 6.3*. Flow consistencies varies from log K = 9.34 to log K = 10.93 decreasing K value with increasing temperature. Flow index n varies from 0.90 to 1.01 in the temperature interval considered, and similarly to the log K consistency.

Data in *Fig. 6.16* display one trend as function of temperature. All the samples display a steep linear trend, typical of Newtonian behavior, testified by n values close to 1. A very small shear thinning behavior is observed, yielding a decrease of apparent viscosity between 0.06 log_{10} and 0.12 log_{10} units with increasing strain rates from $\dot{\varepsilon} = 1 \times 10^{-4}$ s^{-1} and $\dot{\varepsilon} = 7 \times 10^{-4}$ s^{-1}.
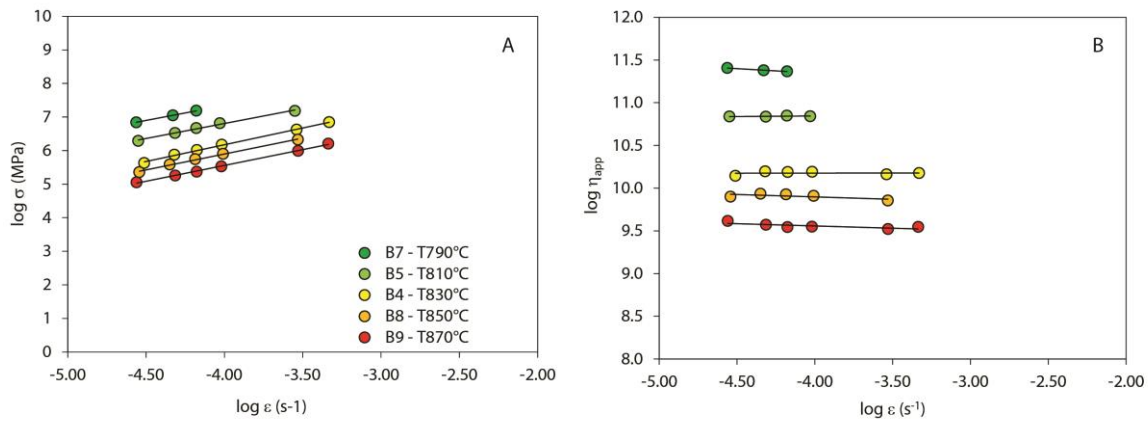
Fig. 6.16 – A) Stress vs. strain rate plot for TU37/6 at different temperatures and B) variation of apparent viscosity as a function of applied strain rate. Black lines represent the fitting results using *Eq. 1.33*.

Tab. 6.3 – Fitting parameters of experimental data.

Sample	Temp. (°C)	Power law-fit parameters		R^2
		n	logK (Pa s)	
B7	782.0	0.90	10.93	1.000
B5	802.5	1.01	10.90	0.992
B4	822.5	1.00	10.18	0.996
B8	843.0	0.94	9.66	0.998
B9	864.5	0.95	9.34	0.998

Over the limited experimental temperature range, we assume an Arrhenian temperature dependence of the viscosity (Avard and Whittington, 2012). Expressing the apparent viscosity as a function of strain rate, following the general equation 1.35, and fitting the resulting equation for temperatures between 1063°K and 1143°K, and strain rates between 3 x 10⁻⁵ s⁻¹ and 7 x 10⁻⁴ s⁻¹, the obtained best fit is:

$$log\eta_{app} = -13.5613 + \frac{25139.4}{T(°K)} - 0.1108\ log\dot\gamma \qquad (1.36)$$

This *Eq. 1.36* fits our database with a root-mean-squared-deviation (RMSD) of 0.010 log unit Pa for the apparent viscosity. The values calculated vs measured viscosity are shown in *Fig. 6.17*.
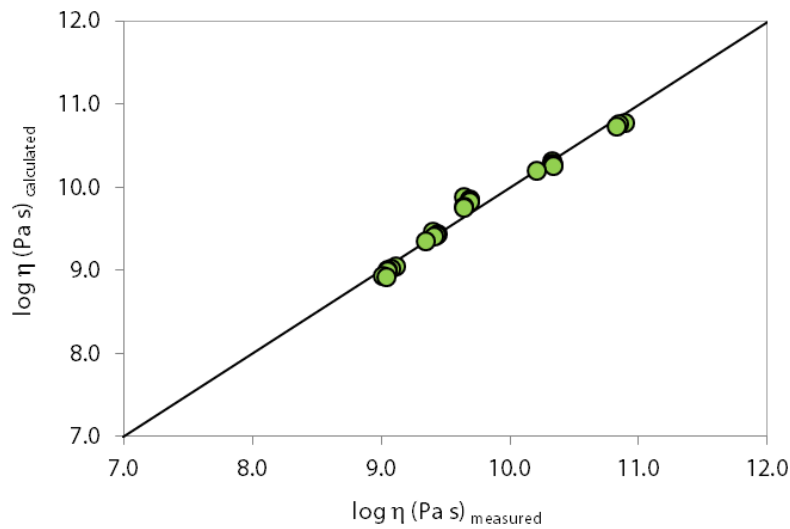
Fig. 6.17 – Calculated vs. measured viscosity for Turrialba 1.9ka andesites. Black line represents 1:1 ratio.

6.4.3 Combined effects of crystals and pores on the rheology of Turrialba 1.9ka andesites

The formulation we presented in equation 1.36 can be only applied to the specific case of our samples. Only very few studies have explored the rheology of crystal and bubble-bearing magmas. Lavallée et al. (2007), Lavalléè et al. (2012), Avard and Whittington (2012) and Vona et al. (2013) have investigated the combined effects of crystals and pores on natural samples without defining the singular contribution of each phase (crystals or pores or liquid) to the multiphase rheological response. In this section we try to calculate separately each component, using the rheological predictive models available in literature.

We first calculate the liquid viscosity as a function of the chemical composition of the glass matrix, using Giordano et al. (2008) model. Then we follow two procedures (A and B) to calculate the multiphase apparent viscosity.

A) We calculate separately the effect of crystals on the two phase (liquid + crystals) viscosity using Vona et al. (2011) (Eq. 1.13); and then following Llewellin and Manga (2005) we add the contribution of bubbles using the formulations by (A_1) Pal (2003) and (A_2) Bagdassarov and Dingwell (1992), to consider a minimum and a maximum effect, respectively.

In *Fig. 6.18* the simple effect of crystals on viscosity (A) and the addition of the effect of bubbles (A_1 and A_2) are presented. The addition of crystals to the liquid phase (A) increases the viscosity of the mixture by a factor comprised between 7 and 8 (relative viscosity), causing a net increase in apparent viscosity between 0.8 and 0.9 log Pa s. The slight difference in apparent viscosity observed as a function of strain rate , is due to the strain rate effects on melt (shear thinning), as modeled by the equation of Vona et al. (2011). The maximum increase is indeed calculated for the lower deformation rates at which the experiments were performed.

The initial different in total porosity of pre-run samples ($\Phi = 0.39 - 0.51$), translates in slight differences in the calculated effect of bubbles on viscosity both using the formulations by Pal (2003) (A_1) and Bagdassarov and Dingwell (1992) (A_2).
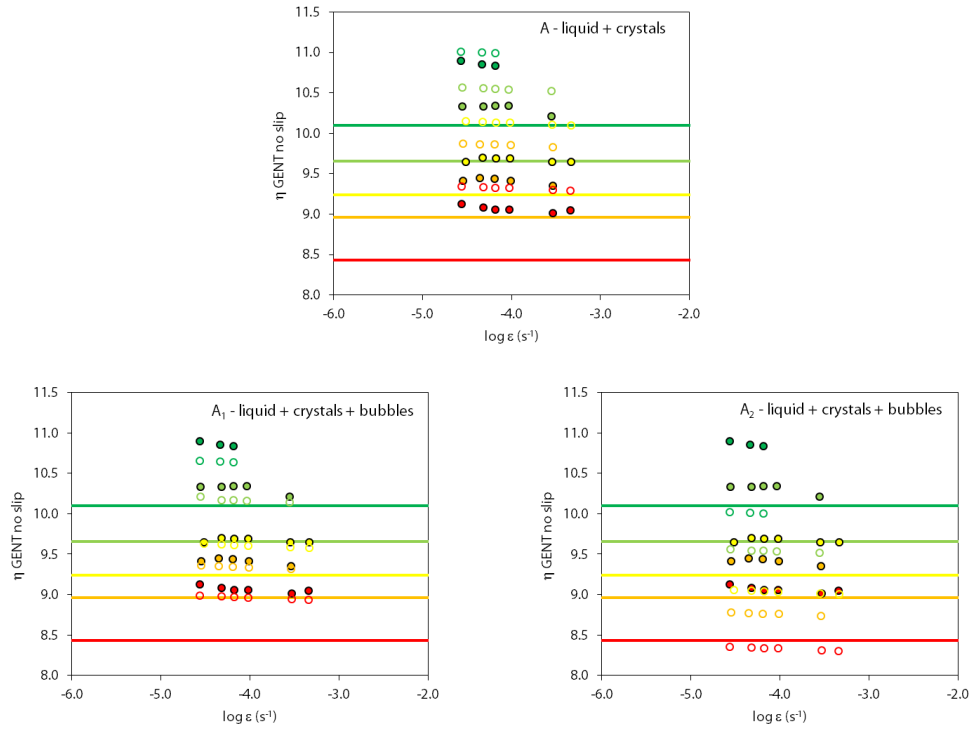
Fig. 6.18 – Viscosity vs. strain rate for the measured samples: colored dots are viscosity measurements performed at variable strain rate and described in *par. 6.3.1* (for the legend see *Fig. 6.16*). Lines represent the viscosity of the residual glass at the range of temperature at which experiments were performed (Giordano et al., 2008). Empty dots are calculated viscosities with the three different forumaltions of A) Vona et al. (2011); A_1) Vona et al. (2011) + Pal (2003); A_2) Vona et al. (2011) + Bagdassarov and Dingwell (1992).

Adding the contribution of bubbles, using the model for viscosity calculation by Pal (2003) (A_1; *Fig. 6.18*), on the relative viscosity (liquid + crystals) obtained with model by Vona et al. (2011), the relative viscosity displays values very similar to those measured during our experiments. Depending on the initial porosity, Pal equation leads to a decrease of relative viscosity of $0.3 - 0.5$ log units, with the highest values pertaining to the sample with the highest initial porosity ($\Phi = 0.51$). The difference between calculated multiphase viscosity (liquid + crystals + bubbles) and measured viscosity ranges between 0.02 Pa s and 0.2 Pa s. A very good match can be observed for the high temperature experiments (T interval $= 830 - 870°C$), whereas the maximum discrepancy is observed for the two experiments run at the lowermost temperatures (T $= 790 - 810°C$).

Calculating the effect of bubble using the model of Bagdassarov and Dingwell (1992) (A_2; *Fig. 6.18*), a decrease in viscosity between 0.9 - 1 log units is predicted. This yields to a significant difference ($0.6 - 0.9$ log units) in the calculated apparent viscosity for the three phase melt (liquid + crystals + bubbles) with respect to the measured values.

160

B) In this case we calculate directly the three phase apparent viscosities, using the formulation of Phan-Thien and Pham (1997). Different equations can be used considering the following three cases identified by these authors: if crystals are smaller than bubbles (Eq. 1.18; not the case of this study); B_1, if crystals and bubbles are of the same size range (Eq. 1.19); B_2, if crystals are larger than bubbles (Eq. 1.20).

In *Fig. 6.19* the viscosity calculated using B_1 and B_2 is reported. Using the formulation B_1 a discrepancy with measured viscosity between 0.2 and 0.5 log units is observed. A better reproducibility is achieved using the equation B_2, that displays a difference comprised between 0.1 and 0.3 log units. In both cases the highest deviation occurred at the lower temperatures.
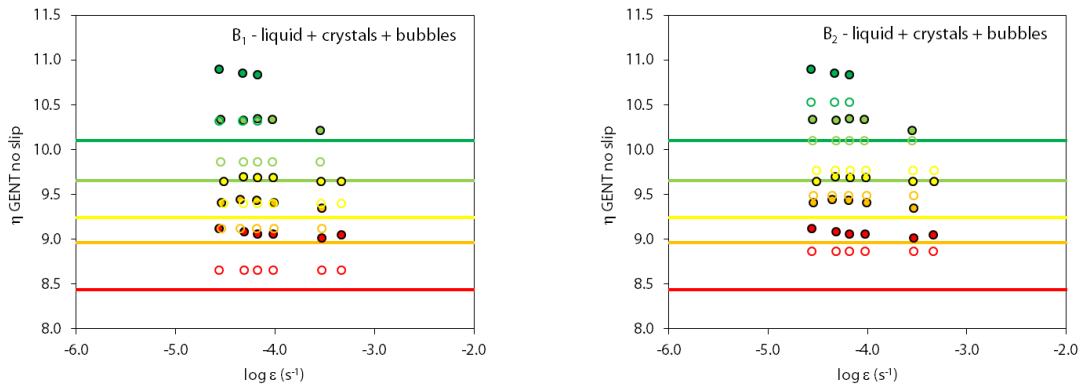
Fig. 6.19 - Viscosity vs. strain rate for the measured samples (fill circles) and calculated three phase viscosity (empty circles) using models B_1 (left) and B_2 (right).

The results of calculations using models A and B, and the best fit obtained in Eq. 1.36 are reported in *Tab. 6.4* together with the values of the root mean squared error (RMSE) and in *Fig. 6.20* against the measured values of viscosity. As expected the best reproducibility is obtained using the best fitting model calibrated exactly on andesites of Turrialba volcano samples (RMSE= 0.0096). However, a very good reproducibility can be also achieved using the models available in literature, and in particular: model A_1 (RMSE= 0.0155), in which the effect of crystals is calculated with Vona et al. (2011) and that of bubbles is calculated with model by Pal (2003); model B_2 (RMSE= 0.0365), where the equation considers crystals larger than bubbles (as in the case of this study; *Fig. 6.6*).
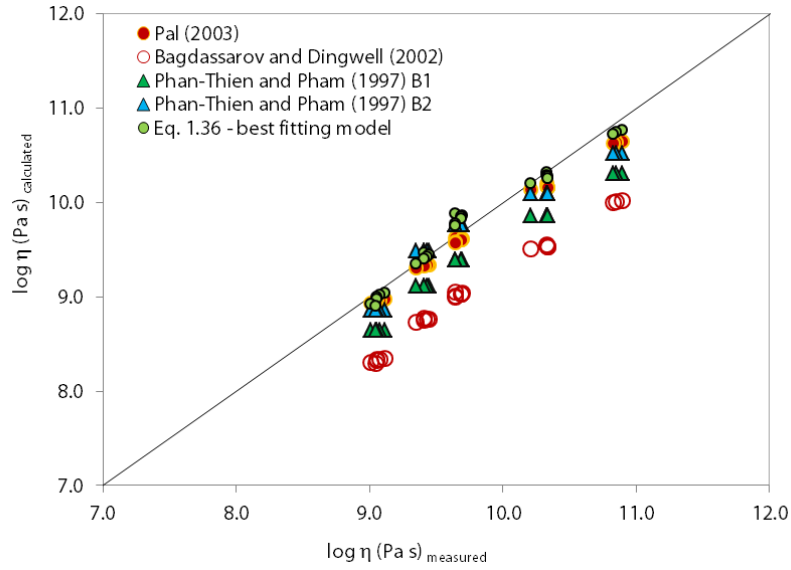
Fig. 6.20 – Calculated vs. measured multiphase viscosity at the considered strain rates, for sample TU37/6.

Despite the good reproducibility, as indicated by the low RMSE, Phan-Thien and Pham (1997) model consider an increase in viscosity due to the increase of bubble content. However at our experimental conditions (unconfined uniaxial deformation), the general effect of pores on the melt viscosity is to determine a decrease (Avard and Whittington, 2012; Lavallée et al., 2013; Vona et al., 2013). In addition in model B_2, the effect of crystals is calculated using the Einstein-Roscoe viscosity model, that does not take into account the effect of crystals shape and deformation rates on the viscosity, known to play a crucial role on the rheology of magma suspensions (Sato 2005; Ishibashi and Sato, 2007; Vona et al., 2011). For these reasons we believe that the most satisfying model is given by the combination of formulation used in Vona et al. (2011), for the effect of crystals, and in Pal (2003) for the effect of bubbles.

Tab. 6.4 – Data and details of viscosity models utilized in this study.

Sample	Initial porosity (ΦT)	Strain rate (s⁻¹)	Log η meas.	Log η$_{calc}$ best fit (Eq. 1.36)	Log η liq. (Giordano et al. 2008)	Log η$_r$ liq.+cryst (Vona et al., 2011)	Log η$_r$ liq.+cryst+ bl (Pal, 2003)	Log η$_r$ liq.+cryst+bl (Bagdassarov and Dingwell, 1992)	Log η$_r$ liq.+cryst+bl (B$_2$) (Phan-Thien and Pham, 1997)	Log η$_r$ liq.+cryst+bl (B$_3$) (Phan-Thien and Pham, 1997)
B7	0.39	2.74E-05	10.89	10.78	10.10	8.07	10.65	10.02	10.31	10.52
		4.69E-05	10.85	10.75	10.10	7.89	10.64	10.01	10.31	10.52
		6.62E-05	10.83	10.74	10.10	7.77	10.63	10.00	10.31	10.52
B5	0.41	2.82E-05	10.33	10.31	9.66	8.06	10.18	9.55	9.86	10.10
		4.84E-05	10.33	10.29	9.66	7.88	10.17	9.54	9.86	10.10
		6.62E-05	10.34	10.27	9.66	7.78	10.16	9.54	9.86	10.10
		9.35E-05	10.33	10.26	9.66	7.66	10.15	9.53	9.86	10.10
		2.82E-04	10.21	10.20	9.66	7.31	10.13	9.51	9.86	10.10
B4	0.51	3.08E-05	9.64	9.88	9.24	8.03	9.62	9.05	9.39	9.76
		4.80E-05	9.69	9.86	9.24	7.88	9.61	9.04	9.39	9.76
		6.69E-05	9.69	9.84	9.24	7.77	9.61	9.03	9.39	9.76
		9.62E-05	9.69	9.82	9.24	7.65	9.60	9.03	9.39	9.76
		2.89E-04	9.64	9.77	9.24	7.30	9.58	9.01	9.39	9.76
		4.67E-04	9.64	9.75	9.24	7.15	9.57	9.00	9.39	9.76
B8	0.51	2.87E-05	9.41	9.46	8.96	8.06	9.35	8.77	9.12	9.49
		4.47E-05	9.44	9.44	8.96	7.91	9.34	8.77	9.12	9.49
		6.52E-05	9.43	9.42	8.96	7.78	9.34	8.76	9.12	9.49
		9.81E-05	9.41	9.40	8.96	7.65	9.33	8.75	9.12	9.49
		2.95E-04	9.35	9.35	8.96	7.29	9.31	8.73	9.12	9.49
B9	0.39	2.75E-05	9.12	9.04	8.43	8.07	8.98	8.35	8.65	8.86
		4.85E-05	9.08	9.02	8.43	7.88	8.97	8.34	8.65	8.86
		6.66E-05	9.05	9.00	8.43	7.77	8.96	8.33	8.65	8.86
		9.58E-05	9.05	8.99	8.43	7.65	8.96	8.33	8.65	8.86
		2.95E-04	9.01	8.93	8.43	7.29	8.94	8.31	8.65	8.86
		4.61E-04	9.04	8.91	8.43	7.16	8.93	8.30	8.65	8.86
RMSE				0.0096			0.0155	0.5188	0.1509	0.0365

All viscosity values are expressed in Pa s

6.5 Volcanological implications on the 1.9ka andesitic eruption

As stated above, Eq. 1.36 is the best way to evaluate a multiphase rheology of our samples, but it can be applied only to the specific crystal and bubbles content of sample TU37/6. The good reproducibility of viscosity, using the model A_1, could suggest that this is the most suitable model to evaluate the multiphase rheology of Turrialba andesitic magmas, covering the observed range of porosity and crystallinity of samples related to the 1.9ka eruption (Chapter 5). In particular, choosing three representative samples of the entire density distribution of this eruptive products (low density, $\Phi= 0.72$, crystallinity= 0.09; mode density, $\Phi= 0.67$, crystallinity= 0.12; high density, $\Phi= 0.45$, crystallinity= 0.27; see Chapter 5 for details) it is possible to predict their multiphase rheology (liquid + bubbles + crystals) using the model A_1. Results are plotted in *Fig. 6.21*, where calculated three phases viscosity is expressed as a function of the strain rate (values are calculated at the constant temperature of 1000°C). Low and mode density samples display a variation of ~0.10 log units, with the relative viscosity ranging between 5.68 and 5.70 Pa s. High density samples are characterized by a significant increase in viscosity by more than 1 order of magnitude with respect to the formers (7.23 – 7.32 Pa s). In *Fig. 6.21* also the three phase viscosity of high density sample, calculated with Eq. 1.36, is plotted. The discrepancy between this model and that of Pal (2003) is comprised between -0.15 and -0.28 log units (see paragraph 6.4.3), and this can be regarded as the minimum error for this kind of simulation.
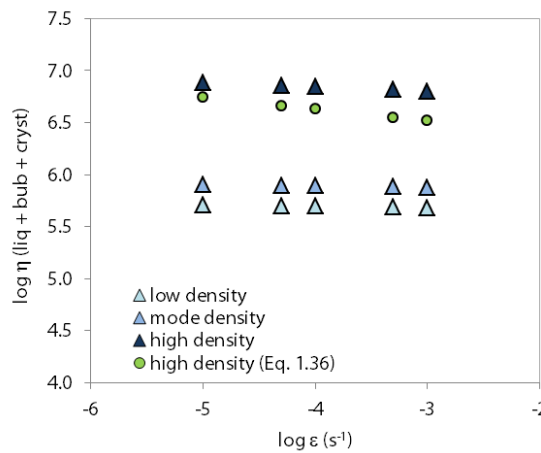
Fig. 6.21 – Three phase viscosity vs. strain rate for the selected samples of Turrialba 1.9ka eruption.

We suggest that the three samples, showing differences in textural characteristics, represent a orizontal zonation of the magma column characterized by a decrease in temperature from the axis of the conduit to its wall. In particular the low and modal density samples can be interpreted as magma portions located in the axial and hotter zone of the magma column, where a high vesicularity and a low crystal content are expected, while the high density samples would represent its outer colder margin. In the outer margin, complex behavior is expected. A decrease in temperature due to diffusional loss of heat, accompanied by a frictional terms , both resulting in an increase in viscosity.

This produces a decrease in magma rising velocity, that, together with the decrease in temperature, favors the crystallization of magma at the conduit walls and the development of a permeable flow, thus decreasing porosity (outgassing; e.g. Cashman and Blundy, 2000).
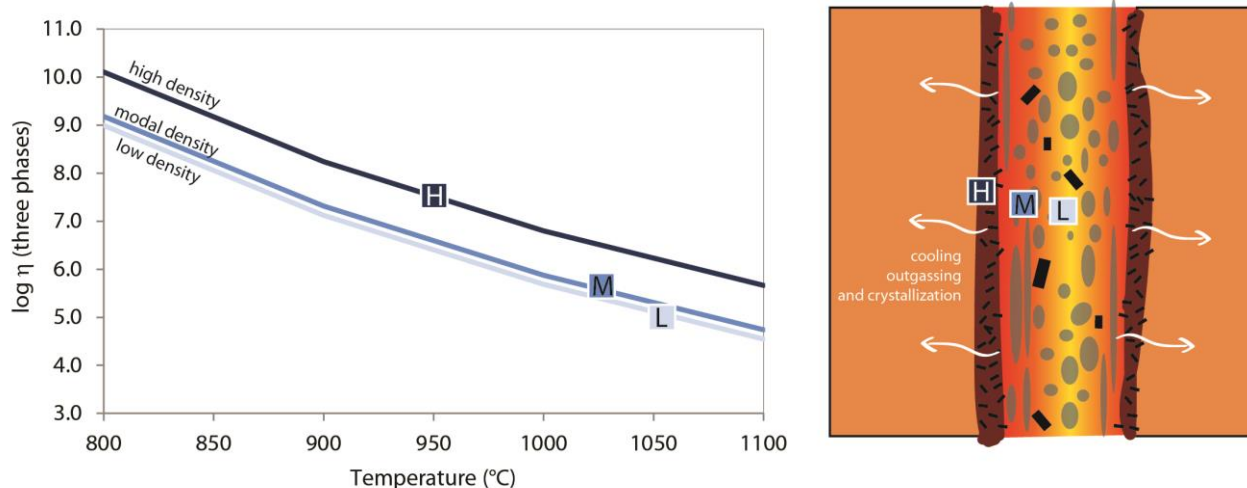
Fig. 6.22 – On the left, three phases mixture viscosity, calculated at different temperatures for high, modal and low density clasts of 1.9ka Turrialba eruption. On the right, sketch of the magma conduit.

Both these effects would concur to further increase magma viscosity in the chilled margins, developing a strong velocity gradient between the hot axial and the cold margin zones. This would also translate in well-developed shear zones, characterized by very high strain rates, as testified by a preferential elongation of vesicles observed in natural samples (see Chapter 5 for details; e.g. Martí et al., 1999). We tried to reconstruct the expected three phase viscosity of magma mixture at different temperatures. As shown above, at a given temperature, the textural features of the three samples, can lead to a difference of more than ~1 order of magnitude in viscosity. However,

considering a lateral gradient of temperature in the order of e.g. 150°C , from a conduit axis temperature of ~1050°C (expected eruptive temperature for an andesitic magma), this effect could further increase up to 3 orders of magnitude the viscosity, as presented in *Fig. 6.22*. This huge difference in viscosity could be responsible to significant rheological contrasts possibly resulting in high strain rates and brittle fragmentation of magma.

7. Conclusions

This study represents a step toward the comprehension and the characterization of the feeding system of Turrialba, a volcano of central Costa Rica, whose reactivation could severely hamper the economy of Costa Rica. A geochemical survey of the degassing system and sampling the eruptive products of the last 10ka of activity was performed. Geochemical analyses and experimental volcanology investigations were carried out in laboratories of Roma Tre University, INGV Roma-1 and INGV-Palermo.

In order to understand the composition of the magmatic source and of the degassing magma involved in the ongoing unrest phase, the noble gas geochemistry composition of gases and fluid inclusions hosted in olivine and pyroxenes of volcanic rock was analyzed. The suite of rock samples analyzed displayed a calc-alkaline affinity, ranging in composition from basaltic-andesite to dacite, and were characterized by a trace element geochemistry compatible with a subduction zone with OIB-like signature. Sr and Nd analyses were performed, confirming that the crustal contamination is negligible. The ^{3}He/^{4}He ratio of fluid inclusions from the most mafic eruptive products (SiO_2=52.5wt% and MgO=6wt%) varied from 7.86 to 8.07 Ra, while that from andesite lavas varied from 7.03 to 7.18 Ra. The He isotope values of the most mafic products are in the range of typical arc volcanoes (7-8 Ra), suggesting that contamination of the mantle wedge below the volcano by crustal He is negligible. The fumaroles collected in 2011-survey showed an helium isotope composition of 7.50-7.96 Ra, well in the range of that measured in fluid inclusions from more mafic and recently erupted rocks. For this reasons, we can assumed that magma involved in the ongoing unrest phase and feeding the crater fumarolic field had petrological and geochemical features comparable to the basaltic-andesitic rocks analyzed in this study. In addition, long-term monitoring of He isotope composition carried out in the last years at Turrialba displayed a progressive increase of ^{3}He/^{4}He ratios, which could be related to the simultaneous unrest testified by the increased seismic activity. We inferred that this variation could be related to a refill of the plumbing system by ^{3}He-rich magmas, which should be very primitive and rising directly from the mantle.

The fluid geochemistry investigation performed during the March 2011 campaign, allowed us to constraint the state of activity of the volcano. 973 measurements of CO_2 soil degassing were performed, covering the entire summit region of the volcano. The total flux of CO_2 degassing from the soil, estimated for the investigated area, is of 3.43 t/ha per day, well in the range of the values

reported in previous 2008 survey (3.96 t/ha per day), confirming that a wide CO_2 flux anomaly affected the area comprised between West and Central Crater. Simultaneously, soil temperature prospection was carried out; temperature ranges between 5°C and 85°C, with the highest values concentrated between West and Central Crater. The slight difference in the total flux of CO_2 from the soil and the sensible decrease in temperature, occurred between 2008 and 2011 at West Crater, could be related to the opening of a phreatic vent, which would act as a drain for the fluids rising inside the shallower feeding system. A total of 5 profiles of CO_2 soil flux and temperature were performed at "Falla Ariete", is a tectonic structure where in 2007 the appearance of fumaroles was observed. Data of CO_2 soil degassing in this sector, collected during the 2011 campaign, were compared with those performed in 2008 in the same area. Anomalies were observed in both surveys but they appear increase substantially in 2011. A maximum flux value of 5375 $gm^{-2}d^{-1}$ was measured during the 2011-survey, compared to the maximum flux of 1994 $gm^{-2}d^{-1}$ collected in the 2008-survey. An expansion of the fractured zone near the fault was observed. The chemical composition of fumaroles analyzed during this study, characterized by CO_2-dominated emissions, has not shown remarkable compositional variations with respect to the gas samples collected by Vaselli et al. (2008). This would suggest that during our 2011-survey, Turrialba was still in the "magmatic-dominated" stage identified by these authors. In addition, the He-isotope composition of free gases measured during this investigation was extremely high at both West and Central Crater (respectively between 7.93 – 7.96 Ra and 7.78 – 7.88 Ra), also confirming the magmatic origin of these gases . All these data suggest that the degassing system was still very active during March 2011, and that this was fed by [3]He-rich fluids both in central and peripheral position respect to the main degassing area.

Noble gas geochemistry investigation of fluid inclusions hosted in crystals of mafic samples and in gases of the fumarolic field of Turrialba volcano, highlighted the possibility that the composition of the magma feeding the crater fumaroles, and stored in the plumbing system, could be similar to those that fed the most recent eruption of 1864-1866. For this reason we performed a textural parameterization of the basaltic-andesites rocks emitted in the most recent eruption, and, to cover the entire spectra of potential eruptive events, of a more explosive magmatic end member dated ~1.9ka (Reagan et al., 2006). The eruption fed by basaltic-andesites, is characterized by an alternation of ash and lapilli stratigraphic sequence, with a final stage made of scoriae and bombs. These product were analyzed for textural analysis. Vesicles are rounded and essentially underformed; at the same time the coalescence structures observed in scoria samples, probably suggest the residing of 1864-1866 magma in a medium-shallow reservoir. Vesicle size and volume

distributions, and vesicle number density (10^4 – 10^6 cm^{-3}) are in the range of Strombolian eruptions, similar to the same events of Stromboli, Villarica or Hawaiian volcanoes.

The study of the andesitic eruptive products of 1.9ka Turrialba eruption, provided interesting insights into the eruption dynamics. Detailed composition and textural analysis were performed on all different pumices types. Interestingly, all the examined products display a rather homogeneous andesitic bulk rock composition, accompanied by the same mineralogic assemblage of stable mineral phases. However, according to their bulk density and porosity, pumice clasts may be subdivided in three groups: low, intermediate and high density clasts. All the textural features investigated: the elevated VND (10^7 – 10^8 cm^{-3}), the porosity distribution (75.8 % – 43.0 %), the polymodal volume distribution, the minimum and maximum size of bubbles (0.009 – 1.18 mm), the high D numbers (2.81 – 2.92) and lastly the highly elongated and deformed bubbles all concur to classify this eruption as a very high energy Sub-plinian eruption. The observed heterogeneity in density/porosity clasts, is consistent with a magma experiencing rapid ascent under a marked lateral velocity gradient. The viscosity that such andesitic magma can experience are high enough to reach brittle fragmentation due to high elongational strain rate (Papale et al., 1999).

Geochemical and geological features of Turrialba volcano, suggest that that the next eruption will likely be fed by a basalt-andesitic magma, as inferred by the high ^{3}He/^{4}He ratio measured in olivines of the most mafic products, and in the fumarolic field (*Chapters 3 – 4*). However, the more explosive eruption of andesitic magmas, as the one erupted in 1.9 ka (*Chapter 5*), is not to be excluded a priori. For the hazard standpoint, the evaluation of the maximum explosive event attended in case of renewal of activity is of primary importance. For this reason, and because the basaltic endmember has been already investigated in much more details, we decided to explore the rheological behavior and the effect of crystal and bubbles on the dynamic such silicic magmas.

In order to better constrain the viscosity of the highly explosive andesitic magma, a multiphase rheology investigation of eruptive products from the 1.9ka subplinian eruption was performed. Experiments were carried out at variable strain rates ($\sim 10^{-5}$ s^{-1} to $\sim 10^{-3}$ s^{-1}) and temperatures (770 – 870°C). We observed a wide range of apparent viscosities, varying with temperature, crystallinity and vesicularity, and varying between ~9 and ~11 Pa s in the range of considered experimental temperatures. We obtained a best-fit equation that could predict the multiphase rheological behavior of the studied samples. Then, choosing three representative samples of the entire density distribution of this eruptive products (low density, Φ= 0.72, crystallinity= 0.09; mode density, Φ= 0.67, crystallinity= 0.12; high density, Φ= 0.45, crystallinity= 0.27; see *Chapter 5* for details) we

try to predict the multiphase rheology (liquid + bubbles + crystals) of this andesitic magma using the model by Pal (2003). We calculate a difference of ~1 Pa s in magma viscosity (liquid+bubbles+crystals) between high and low density samples, that coupled with a lateral temperature gradient inside the conduit of the volcano, could increase up to ~3 Pa s. This huge difference in viscosity could be responsible to significant rheological contrasts possibly resulting in high strain rates and brittle fragmentation of magma. It is clear that in case of a reactivation of the volcanic magmatic activity, the eruption of an andesitic magma could produce very high energy explosive eruptions, that could pose a serious hazard to the metropolitan area downwind of Turrialba volcano.

References

Abers, G.A., Plank, T., Hacker, B.R., 2003. The wet Nicaraguan slab. Geophys. Res. Lett., 30(2). doi:10.1029/2002GL015649.

Abratis, M., Woerner G., 2001. Ridge collision, slab-window formation, and the flux of Pacific asthenosphere into the Caribbean realm. Geology, 29, pp. 127-130.

Adamek, S., Frohlich, C., Pennington, W.D., 1988. Seismicity of the Caribbean-Nazca Plate Boundary: Constraints on microplate tectonics of the Panama region. J. Geophys. Res., 93(B3), pp. 2053-2075.

Alvarado, G.E., 1984. Aspectos petrologicos-geologicos de los volcanes y unidades lavicas del Cenozoico Superior de Costa Rica.-183 pags Univ. Costa Rica (Tésis de Lic.).

Alvarado Vilalón, F., 1984. Geología estructural y tectónica al sur del Valle Central, Costa Rica (Tarbaca)., Tésis Lic, Escuela Centroamericana de Geología, UCR.

Alvarado, G.E., Kussmaul, S., Chiesa, S., Gillot, P.Y., Appel, H., Worner, G., Rundle, c., 1992. Resumen cronoestratigráfico de las rocas igneas de Costa Rica basado en dataciónes radiométrica. J. South. Am. Sci., 6 : 151-168.

Alvarado, G.E., 2002. Geologia de Turrialba: una historia de 60 millones de anos. Colleccion Patrimonio y Futuro n°17, serie Angostura n°1. Instituto Costarricense de Electricidad Sugerencia Gestion Administrativa, Patrimonio Historico y Tecnologico (Museo).

Andrews, J.N., 1985. The isotopic composition of radiogenic helium and its use to study groundwater movement in confined aquifers. Chem. Geol., 49, 339-351.

Arculus, R.J., Powell, R., 1986. Source component mixing in the regions of magma generation. J. Geophys. Res., 91, 5913-5926.

Avanzinelli, R., Boari, E., Conticelli, S., Francalanci, L., Guarneri, L., Perini, G., Petrone, C.M., Tommasini, S., Ulivi, M., 2005. High precision Sr, Nd and Pb isotopic analyses using the new generation Thermal Ionisation Mass Spectrometer ThermoFinnigan Triton-Ti®. Per. Mineral., 74, 3, pp. 147-166.

Avard, G., Whittington, A.G., 2012. Rheology of arc dacite lavas: experimental determination at low strain rates. Bull Volcanol, 74, 1039-1056.

Avard, G., Pacheco, J., Martinez, M., Miranda, S., Conde, V., Galle, B., 2013. The opening vents like decompression valves of the hydrothermal system at Turrialba volcano, Costa Rica. IAVCEI, 2013, Scientific Assembly, July 20-24, Kagoshima, Japan. *Abstract*

Bagdassarov, N.S., Dingwell, D.B., 1992. A rheological investigation of vesicular rhyolite. J. Volcanol Geotherm Res, 50, 307-322.

Ballentine, C.J., Mazurek., M., Gautschi, A., 1994. Thermal constraints on crustal rare gas release and migration: evidence from Alpine fluid inclusions. Geochim. Cosmochim. Acta, 58, 4333-4348.

Barberi, F., Neri, G., Valenza, M., Villari, L., 1991. 1987-1990 unrest at Vulcano. Acta Vulcanol., 1, 95-106.

Barberi, F., Bertagnini, A., Landi, P., Principe, C., 1992. A review on phreatic eruptions and their precursors. J Volcanol Geotherm Res, 128:273-285.

Barberi, F., Carapezza, M.L., 1994. Helium and CO_2 soil gas emissions from Santorini (Greece). Bull. Volcanol., 56, 335-342.

Barboza, V., Fernandez, E., Duarte, E., J., Sàenz, Martinez, M., Moreno, N., Marino, T., Van der Laat, R., Hernández, E., Malavassi, E., Valdes, J., 2003. Changes in the activity of Turrialba volcano: seismicity, geochemistry and deformation. In 8th Gas Workshop, IAVCEI, March-April, Nicaragua-Costa Rica.

Barckhausen, U., Ranero, C.R., von Huene, S., Cande, C., Roeser, H.A., 2001. Revised tectonic boundaries in the Cocos Plate off Costa Rica: Implications for the segmentation of the convergent margin and for plate tectonic models. J. Geophys. Res., 106(B9), 19,207-19,220.

Barquero, R., Krinitzsky, E., Climent, A., 1993. P.H. Angostura. Estudio Sismologico y de Amenanza sismica. Inf. Interno ICE, 12pp.

Batchelor, G.K., 1970. The stress system in a suspension of force-free particles. *J. Fluid Mech.* **41**, 470–545.

Beauducel, F., Besson, P., 2008. The review of the 1975-77 eruption of La Soufrière de Guadeloupe (FW1). EOS Trans AGU 89(53): Abstract V44A-03

Benjamin, E.R., Plank, T., Wade, J.A., Kelley, K.A., Hauri, E.H., Alvarado, G.E., 2007. High water contents in basaltic magmas from Irazú volcano, Costa Rica. J. of Volcanol. and Geoth. Res., 168, pp.68-92.

Bently, L.R., 1974. Crustal structure of the Carnegie ridge, Panama basin and Cocos ridge. MS Thesis, University of Hawaii, Honolulu, 49 pp.

Bonaccorso, A., 2002. Ground deformation of the southern sector of the Aeolian islands volcanic arc from geodetic data. Tectonophys 3151:181-192.

Boschini, I. 1989: Incidencia de las fuentes sísmicas en la región Caribe de Costa Rica. San José, Costa Rica. Universidad de Costa Rica, Escuela Centroamericana de Geología. Tesis de Licenciatura, 97 pp.

Bruckner, R. and Deubener, J., 1997. Description and interpretation of the two phase flow behaviour of melts with suspended crystals. *Journal of Non-Crystalline Solids* **209**, 283-291.

Calmus, T., Aguillon-Robles, A., Maury, R.C., Bellon, H., Benoit, M., Cotten, J., Bourgois, J., Michaud, F., 2003. Spatial and temporal evolution of basalts and magnesian andesites (bajaites) from Baja California, Mexico: the role of slab melts. Lithos 66, 77–105.

Calvo, C., Bolz, A., 1994. The oldest calc-alkaline island arc volcanism in Costa Rica. Marine tephra from the Loma Chumico Formation (Albian to Campanian). Profil, 7, pp. 235-264.

Campion, R., Martinez-Cruz, M., Lecoq, T., Caudron, C., Pacheco, J., Pinardi, G., Hermans, C., Carn, S., Bernard, A., 2012. Space- and ground-based measurements of sulphur dioxide emissions from Turrialba volcano (Costa Rica). Bull. Volcanol., 74, pp. 1757-1770.

Capasso, G., Favara, R., Inguaggiato, S., 1997. Chemical features and isotopic gaseous manifestation on Vulcano island (Aeolian Island): an interpretative model of fluid circulation. Geochim. Cosmochim. Acta, 61, 3425-3442.

Capasso, G., Favara, R., Francofonte, S., Inguaggiato, S., 1999. Chemical and isotopic variations in fumarolic discharge and thermal waters at Vulcano Island (Aeolian Islands, Italy) during 1996: evidence of resumed volcanic activity. J. of Volcanol Geotherm Res, 88, 3, p. 167-175.

Carapezza, M.L., Granieri, D., 2004. CO_2 soil flux at Vulcano (Italy): comparison of active and passive methods and application to the identification of actively degassing structure. Appl. Geochem., 19, 73-88.

Caricchi, L., Burlini, L., Ulmer, P., Gerya, T., Vassalli, M., and Papale, P., 2007. Non-Newtonian rheology of crystal-bearing magmas and implications for magma ascent dynamics. *Earth and Planetary Science Letters* **264**, 402-419.

Caricchi, L., Giordano, D., Burlini, L., Ulmer, P., and Romano, C., 2008. Rheological properties of magma from the 1538 eruption of Monte Nuovo (Phlegrean Fields, Italy): An experimental study. *Chemical Geology* **256**, 158-171.

Carr, M.J., 1984. Symmetrical and segmented variation of physical and geochemical characteristics of the Central American volcanic front. J. of Volc. and Geoth. Res., v.20, p. 231-252.

Carr., M.J., 2007. CentAm Database: A Geochemical Database of Volcanic Rocks from Central America. http://www-rci.rutgers.edu/~carr/index.html .

Carr, M.J., Stoiber, R., 1990. Volcanism. In: Dengo G., Case, J.E., (eds). The Caribbean region. The geology of North America. Vol H., Geol. Soc. Am. Boulder., CO, pp. 375.391.

Carr, M.J., Feigenson, M.D., Bennett, E.A., 1990. Incompatible element and isotopic evidence for tectonic control of source mixing and melt extraction along the Central American arc. Contributions to Mineralogy and Petrologi, v. 105, pp. 369-380.

Carr, M.J., Feigenson, M.D., Patino, L.C., Walker, J.A., 2003. Volcanismo and geochemistry in Central America: progress and problems, inside the subduction factory. Geophys. Monogr., pp. 153-179.

Casadevall, T.J., 1981. The 1980 eruptions of Mount St. Helens from March 29 through December 1980. US Geol Surv Prof Pap 1250:193-200.

Cashman, K.V., Blundy, J., 2000. Degassing and crystallization of ascending andesite and dacite. Phil Trans Royal Soc London (A) 358:1487-1513.

Castillo, P. 2012. Adakite petrogenesis. Lithos 134-135, 304-316.

Chiodini, G., Cioni, R., Guidi, M., Marini, L., 1991. Geochemical variations at Fossa Grande crater fumaroles (Vulcano Island, Italy) in summer 1988. Acta Vulcanol, 1:179-192.

Chiodini, G., Cioni, R., Marini, L., Panichi, C., 1995. Origin of the fumarolic fluids of Vulcano Island, Italy, and implications for the vulcanic surveillance. Bull. Volcanol., 57, 99-110.

Chiodini, G., Cioni, R., Guidi, M., Marini, L., Raco, B., 1998. Soil CO_2 flux measurements in volcanic and geothermal areas. Appl. Geochem, 13, 543-552.

Chiodini, G., Caliro, S., Cardellini, C., Granieri, D., Avino, R., Baldini, A., Donnini, M., Minopoli, C., 2010. Long term variations of the Campi Flegrei (Italy) volcanic system as revealed by the monitoring of hydrothermal activity. J. Geophys. Res., 115, B03205, doi:10.1029/2008JB006258.

Chong, J. S., Christiansen, E. B., and Baer, A. D., 1971. Rheology of concentrated suspensions. *Journal of Applied Polymer Science* **15**, 2007-2021.

Cimarelli, C., Costa, A., Mueller, S., Mader, H., 2011. Rheology of magmas with bimodal crystal size and shape distributions: Insights from analog experiments. Geochem Geophys Geosys, DOI:10.129 /2011GC003606

Clocchiatti, R., Gioncada, A., Mosbah, M., Sbrana, A., 1994. Possible deep origin of sulfur output at Vulcano (Southern Italy) in the light of melt inclusions studies. Acta vulcanol, 5, 49-54.

Conde, V., Bredemeyer, S., Duarte, E., Pacheco, J.F., Miranda, S., Galle, B., Hansteen, T.H., 2013. SO_2 degassing from Turrialba Volcano linked to seismic signatures during the period 2008-2012. Int. J. Earth Sci., doi:10.1007/s00531-013-0958-5.

Condomines, M., Gronvold, K., Hooker, P.J., Muehlenbachs, K., O'Nions, R.K., 1983. Helium, oxygen, strontium and neodymium isotopic relationships in Icelandic volcanics. Earth Planet. Sci. Lett., 66:125-136.

Cordonnier, B., Hess, K.-U., Lavallée, Y., Dingwell, D.B., 2009. Rheological properties of dome lavas: Case study of Unzen volcano. Earth Planet. Sci. Lett. 279, 263–272.

Correale, A., Martelli, M., Paonita, A., Rizzo, A., Brusca, L., Scribano, V., 2012. New evidences of mantle heterogeneity beneath the Hyblean Plateau (southeast Sicily, Italy) as inferred from noble gases and geochemistry of ultramafic xenoliths. Lithos, 132-133, 70-81.

Correale, A., Paonita, A., Martelli, M., Rizzo, A., Rotolo, S.G., Corsaro, R.A., Di Renzo, V., 2014. A two-component mantle source feeding Mt. Etna magmatism: Insights from the geochemistry of primitive magmas. Lithos, 184-187, 243-258.

Costa, A., 2005. Viscosity of high crystal content melts: dependence on solid fraction. *Geophysical Research Letters* **32**, 5 pp.

Costa, A., Caricchi, L., and Bagdassarov, N., 2009. A model for the rheology of particle-bearing suspensions and partially molten rocks. *Geochemistry Geophysics Geosystems* **10**.

Crawford, A.J., Falloon, T.J., Eggins, S., 1987. The origin of island arc high-alumina basalts. Contrib. Mineral. Petrol., 97, 417-430.

Crider, J.G., Frank, D., Malone, S.D., Poland, M.P., Werner, C., Caplan-Auerbach, J., 2011. Magma at depth: A retrospective analysis of the 1975 unrest at Mount Baker, Washington, USA. Bull Volcanol. doi:10.1007/s00445-010-0441-0.

Cristini, V., Macosko, C.W., Jansseune, T., 2002. A note on the transient stress calculation via numerical simulations. *J. Non- Newton. Fluid Mech.* **105**, 177– 187.

de Boer, J.Z., Drummond, M.S., Bordelon, M.J., Defant, M.J., Bellon, H., Maury, R.C., 1995. Cenozoic magmatic phases of the Costa Rican island arc (Cordillera de Talamanca), in Geologic and Tectonic Development of the Caribbean Plate Boundary in Southern Central America, edited by P. Mann, Spec. Pap. Geol. Soc. Am., 295, 35-56.

Defant, M.J., Drummond, M.S., 1990. Derivation of some modern arc magmas by melting of young subducted lithosphere. Nature, 346, 662-665.

Defant, M.J., Jackson, T.E., Drummond, M.S., 1992. The geochemistry of young volcanism throughout western Panama and southeastern Costa Rica: an overview. J. Geol. Soc., 149, 569-579.

deMets, C., Gordon, R.G., Argus, D.F., Stein, S., 1994. Effects of recent revisions to the geomagnetic reversal time scale on estimates of current plate motions. Geophys. Res. Lett., 31(20), pp. 2191-2194.

deMets, C., 2001. A new estimate for present-day Cocos-Caribbean Plate motion: implications for slip along the central American volcanic arc. Geophys. Res. Lett., 28, pp. 4043-4046.

Dinc, A.N., Koulakov, I., Thorwart, M., Rabbel, W., Flueh, E.R., Arroyo I., Taylor, W., Alvarado, G., 2010. Local earthquake tomography of central Costa Rica: transition from seamount to ridge subduction. Geophys. J. Int., 183, pp. 286-302.

Dingwell, D.B., 1986. Viscosity-temperature relationships in the system Na2Si2O5-Na4Al2O5. Geochim. Cosmochim. Acta 50, 1261-1265.

Dingwell, D.B., 1989a. Shear viscosities of ferrosilicate liquids. Am. Mineral. 74, 1038-1044.

Dingwell, D.B., 1989b. Effect of fluorine on the viscosity of dipside liquid. Am. Mineral. 74, 333-338.

Dingwell, D.B., 1991. Redox viscometry of some Fe-bearing silicate liquids. Am. Mineral. 76, 1560-1562.

Dingwell, D. B., 1996. Volcanic dilemma: Flow or blow? Science 273, 1054-1055.

Dingwell, D.B., 2006. Transport properties of magmas: diffusion and rheology. Elements 2, 281-286.

Dingwell, D. B. and Virgo, D., 1987. The effect of oxidation state on the viscosity of melts in the system Na2O-FeO-Fe2O3-SiO2. Geochimica et Cosmochimica Acta, 195-205.

Dingwell, D.B., and Virgo, D., 1988. Viscosity-oxidation state relationship for hedenbergitic melt. Carnegie Institution of Washinglon Year Book, 87, 48-53.

Dingwell, D. B., Knoche, R., Webb, S. L., and Pichavant, M., 1992. The effect of B2O3 on the viscosity of haplogranitic liquids. American Mineralogist 77, 457-461.

Dingwell, D.B., Bagdassarov, N.S., Bussod, G.Y., and Webb, S.L., 1993. Magma rheology. In R.W. Luth, Ed., Experiments at high pressure and applications to the Earth's mantle.

Mineralogical Association of Canada, Short Course Handbook, 21, 131–196.

Doi, M. and Edwards, S. F., 1978. Dynamics of rod-like macromolecules in concentrated-solution .1. *Journal of the Chemical Society-Faraday Transactions Ii* **74**, 560-570.

Donnelly, T.W., Horne, G.S., Finch, R.C., Lopez-Ramos, E., 1990. Northern Central America: The Maya and Chortis blocks. In The Caribbean Region, pp. 37-76, eds Dengo, G. & Case, J.E.. The Geology of North America, H, The Geological Society of America, Boulder, CO.

Dorel, J., Feuillard, M., 1980. Note sur le crise sismo-volcanique à la Soufrière de La Guadeloupe, 1975-1977. Bull Volcanologique 43:419-430.

Doukas, M.P., Gerlach, T.M., 1995. Sulfur dioxide scrubbing during the 1992 eruptions of Crater Peak, Mount Spurr volcano, Alaska. In: Keith TEC (ed) The 1992 eruptions of Crater Peak vent, Mount Spurr volcano, Alaska. US Geol Surv Bull B-2139:47–57.

Drummond, M.S., Bordelon, M., de Boer, J.Z., Defant, M.J., Bellon, H., Feigenson, M.D., 1995. Igneous petrogenesis and tectonic setting of plutonic and volcanic rocks of the Cordillera de Talamanca, Costa Rica-Panama, Central American arc. American Journal of Science, 295, 875–919.

Dzierma, Y., Thorwart, M.M., Rabbel, W., Fluch, E.R., Alvarado, G.E., Mora, M.M., 2010. Imaging crustal structure in south central Costa Rica with receiver functions. Geoch. Geoph. Geosys. doi:10.1029/2009GC002936.

Eiler, J.M., Carr, M.J., Reagan, M., Stolper, E., 2005. Oxygen isotope constraints on the sources of Central American arc lavas. Geoch. Geoph. Geosys., 6 (Q07007). Doi:10.1029/2004GC000804.

Einstein, A., 1906. Eine neue Bestimmung der Molekul-dimensionen. *Ann. Phys.* **19**, 289-306.

Elliott, T.R., 2003. Tracers of the slab. In: Eiler, J. (Eds.), Inside the Subduction factory. American Geophysical Union Monograph, vol. 138. American Geophysical Union, Washington, D.C., pp. 23-45.

Escalante, G., 1990. The geology of southern Central America and western Colombia, in The Geology of North America, vol. H, The Caribbean Region, edited by G. Dnego and J.E. Case, chap. 8, pp. 201-228, Geol. Soc. Of Am., Boulder, Colo.

Eyre, T.S., Christopher, J.B., De Barros, L., O'Brien, G.S., Martini, F., Lokmer, I., Mora, M.M., Pacheco, J.F., Soto, G.J., 2013. Moment tensor inversion for the source location and mechanism of long period (LP) seismic events from 2009 at Turrialba volcano, Costa Rica. J. of Volcanol. and Geoth. Res., 258, pp. 215-223.

Fan, G, Beck, S, & Wallace, T. The Seismic Source Parameters of the 1991 Costa Rica Aftershock Sequence: Evidence for a Transcurrent Plate Boundary. J. Geoph Res. 98, B9: 15,759-15,778, (1993).

Feigenson, M.D., Carr, M.J., 1986. Positively correlated Nd and Sr isotope ratios of lavas from the Central American volcanic front. Geology, 14, 79-82.

Feigenson, M.D., Carr, M.J., 1993. The source of Central American lavas: inferences from geochemical inverse modeling. Contrib. Mineral. Petrol., 113, pp. 226-235.

Feigenson, M.D., Carr, M.J., Maharaj, S.V., Juliano, S., Bolge L.L., 2004. Lead isotope composition of Central American volcanoes: influences of the Galapagos plume. Geochem. Geophys. Geosyst., 5, Q06001, doi:10.1029/2003GC000621.

Fernandez, M. Seismicity of the Pejibaye-Matina, Costa Rica, region: a strike-slip tectonic boundary?, Geofisica Internacional, 48(4), 351-364, (2009).

Feuillard, M., Allegre, C.J., Brandeis, G., Gaulon, R., Le Mouel, J.L., Mercier, J.C., Pozzi, J.P., Semet, M.P., 1983. The 1975-1977 crisis of La Soufrière de Guadeloupe (F.W.I.): a still-born magmatic eruption. J of Volcanol and Geotherm Res, 16, 317-334.

Fischer, T.P., Hilton, D.R., Zimmer, M.M., Shaw, A.M., Sharp, Z.D., Walker, J.A., 2002 – Subduction and recycling of Nitrogen along the Central American Margin. Science, 297, 1154.

Fischer, T.P., Takahata, N., Sano, Y., Sumino, H., Hilton, D.R., 2005. Nitrogen isotopes of the mantle: insights from mineral separates. Geophys. Res. Lett., 32, L11305, doi:10.1029/2005GL022792.

Francalanci, L., Taylor, S.R., McCulloch, M.T., Woodhead, J.D., 1993. Geochemical and isotopic variations in the calc-alkaline rocks of Aeolian arc, southern Tyrrhenian Sea, Italy: constraints on magma genesis. Contrib. to Mineral. And Petrol., 113, 3, pp. 300-313.

Furukawa, Y., Tatsumi, Y., 1999. Melting of a subducting slab and production of high-Mg andesite magmas: unusual magmatism in SW Japan at 13–15 Ma. Geophysical Research Letters 26, 2271–2274.

Gao, Y., Hou, Z., Kamber, B.S., Wei, R., Meng, X., Zhao, R., 2007. Adakite-like porphyries from the southern Tibetan continental collision zones: evidence for slab melt metasomatism. Contributions to Mineralogy and Petrology 153, 105–120.

Gardine, M., West, M., Cox, T., 2011. Dike emplacement near Paricutin volcano, Mexico, in 2006. Bull Volcanol. doi:10.1007/s00445-010-0437-9.

Garofalo, K., Tassi, F., Vaselli, O., Delgado-Huertas, A., Tedesco D., Frische, M., Hanstein, T.H., Poreda, R.J., Strauch, W., 2006. Fumarolic gases at Mombacho Volcano (Nicaragua): presence of magmatic gas species and implications for volcanic surveillance. Bull. Volcanol. doi:10.1007/s00445-006-0108-z.

Gasparon, M., Hilton, D.R., Varne, R., 1994. Crustal contamination processes traced by helium isotopes-examples from the Sunda Arc, Indonesia. Earth Planet. Sci. Lett., 126, 15-22.

Gay, E., P. Nelson, and W. Armstrong, 1969. Flow properties of suspensions with high solids concentration, AIChE J. **15**, 815–822.

Gazel, E., Alvarado, G.E., Obando, J., Alfaro, A., 2005. Evolución magmática del arco de Sarapiquí, Costa Rica. Rev. Geol. Am. Cent., 32, 13-31.

Gazel, E., Carr, M.J., Hoernle, K., Feigenson, M.D., Szymanski, D., Hauff, F., van den Bogaard, P., 2009. Galapagos-OIB signature in southern Central America: Mantle refertilization by arc-hot spot interaction. Geoch. Geophys. Geosys., 10(2), Q02S11, doi:10.1029/2008GC002246.

Giammanco, S., Gurrieri, S., Valenza, M., 1998. Anomalous soil CO_2 degassing in relation to faults and eruptive fissures on Mount Etna (Sicily, Italy). Bull. Volcanol., 60, 252-259.

Gill, J.B., 1981. Orogenic Andesites and Plate Tectonics. Springer, Berlin. 390 pp.

Giordano, D., Russel, J.K., Dingwell, D.B., 2008. Viscosity of magmatic liquids: A model. Earth and Planet Sci Lett, 271, 123-134.

González-Viquez, C., 1910. Temblores, terremotos, inundaciones, y erupciones volcánicas en Costa Rica 1608-1910. Tipografia de Avelino Alsina, San José de Costa Rica, pp. 1-200.

Goss, A.R., Kay, S.M., 2006. Steep REE patterns and enriched Pb isotopes in southern Cnetral American arc magmas: evidence for forearc subduction erosion?. Geochem. Geophys. Geosys., 7, Q05016, doi:10.1029/2005GC001163.

Granieri, D., Carapezza M.L., Chiodini G., Avino R., Caliro S., Ranaldi M., Ricci T. & Tarchini L., 2006. Correlated increase in CO_2 fumarolic content and diffuse emission from La Fossa crater (Vulcano, Italy): Evidence of volcanic unrest or increasing gas release from a stationary deep magma body? . Geophys. Res. Lett., 33, L13316, doi:10.1029/2006GL026460.

Graham, D., Lupton, J., Albarede, F., Condomines, M., 1990. Extreme temporal homogeneity of helium isotopes at Piton de la Fournaise, Reunion Island. Nature 347:545-548.

Gudmundsson, A., Brenner, S.L., 2004. How mechanical layering affects local stresses, unrests, and eruptions of volcanoes. Geophys Res Lett, 31(16):L16606.

1. Güendel, F. and Protti, M.: 1998, Sismicidad y sismotectónica de América Central, Física de la Tierra 10, 19–51.

Guivel, C., Lagabrielle, Y., Bourgois, J., Martin, H., Arnaud, N., Fourcade, S., Cotten, J., Maury, R.C., 2003. Very shallow melting of oceanic crust during spreading ridge subduction: origin of near-trench Quaternary volcanism at the Chile Triple Junction. Journal of Geophysical Research 108, 2345. doi:10.1029/2002JB002119.

Harris, A.J.L., Allen, J.S., 2008. One-, two- and three-phase viscosity treatments for basaltic lava flows. J of Geoph Res (Solid Earth) 113 (b2), B09212.

Harrison, D., Barry, T., Turner, G., 2004. Possible diffusive fractionation of helium isotopes in olivine and clinopyroxene phenocrysts. Eur. J. Mineral., 16, 213-220.

Hauff, F., Hoernle, K., and Schmidt, A., 2003. Sr-Nd-Pb composition of Mesozoic Pacific oceanic crust (Site 1149 and 801, ODP Leg 185): implications for alteration of ocean crust and the input into the Izu-Bonin-Mariana subduction system. Geochem. Geophys. Geosyst., 4. doi:10.1029/2002GC000421

Herrstrom, E.A., Reagan, M.K., Morris, J.D., 1995. Variations in lava composition associated with flow of asthenosphere beneath southern Central America. Geology, 23, pp. 617-620.

Herschel, W.H., and Bulkley, R., 1928. Measurement of consistency as applied to Rubber-Benzene solutions. *Proc. ASTM Kolloid Z.* **26**, 621.

Hess, K.-U., Cordonnier, B., Lavallée, Y., Dingwell, D.B., 2008. Viscous heating in rhyolite: An in situ experimental determination. Earth Planet. Sci. Lett. 275, 121–126.

Hey, R.N., 1977. A new class of pseudo-faults and their bearing on plate tectonics: a propagating rift model. Earth and Planetary Science Letters, 37, pp. 321-325.

Hinch, E.J., Acrivos, A., 1980. Long slender drops in a simple shear flow. *J. Fluid Mech.* **98**, 305–328.

Hilton, D.R., Hammerschmidt, K., Teufel, S., Friedrichsen, H., 1993. Helium isotope characteristics of Andean geothermal fluids and lavas. Earth Planet. Sci. Lett., 120, 265-282.

Hilton, D.R., Barling, J., Wheller, G.E., 1995. Effect of shallow-level contamination on the helium isotope systematics of ocean-island lavas. Nature, 373, pp. 330-333.

Hilton, D.R., Fischer, T.P., Marty, B., 2002. Noble gases and volatile recycling at subduction zones. In: Porcelli, D., Ballentine, C.J., Wieler, R., (Eds.), Noble Gases in Cosmochemistry and Geochemistry. Mineralogical Society of America, Washington, pp. 319-370.

Hilton, D.R., Ramirez, C.J., Mora-Amador, R., Fischer, T.P., Furi., E., Barry, P.H., Shaw, A.M., 2010. Monitoring of temporal and spatial variations in fumarolic helium and carbon dioxide characteristics at Poas and Turrialba volcanoes, Costa Rica (2001-2009). Geochemical Journal, 44, 431-440.

Hirn, A., Michel, B., 1979. Evidence of migration of mainshocks during seismo-volcanic crises of La Soufrière (Guadeloupe, Lesser Antilles) in 1976. J. Volcanol Geotherm Res 6:295-304.

Hoernle, K., van den Bogaard, P., Werner, R., Lissinna, B., Hauff, F., Alvarado, G., Garbe-Schonberg, C.D., 2002. Missing history (16-71 Ma) of the Galapagos hotspot: implications for the tectonic and biological evolution of the Americas. Geology, 30, 795-798.

Hoernle, K., Abt, D.L., Fischer, K.M., Nichols, H., Hauff, F., Abers, G.A., van den Bogaard, P., Heydolph, K., Alvarado, G., Protti, M., Strauch, W., 2008. Arc-parallel flow in the mantle wedge beneath Costa Rica and Nicaragua. Nature, vol. 451, pp.1094-1098.doi:10.1038/nature06550.

Hu, Y.T., Lips, A., 2003. Transient and steady state three-dimensional drop shapes and dimensions under planar extensional flow. *J. Rheol.* **47**, 349–369.

Hui, H.J., Zhang, Y., 2007. Toward a general viscosity equation for natural anhydrous and hydrous silicate melts. Geochim. Cosmochim. Acta 71, 403–416.

Husen, S., Quintero, R., Kissling, E., Hacker, B., 2003. Subduction-zone structure and magmatic processes beneath Costa Rica constrained by local earthquake tomography and petrological modelling. Geophys. J. Int., 155, pp. 11-32.

Iacono-Marziano, G., Paonita, A., Rizzo, A., Scaillet, B., Gaillard, F., 2010. Noble gas solubilities in silicate melts: new experimental results and a comprehensive model of the effect of liquid composition, temperature and pressure. Chem. Geol., 279, 145-157.

Irvine, T.N., Baragar, W.R.A., 1971. A guide to the chemical classification of the common volcanic rocks. Canadian Journal of Earth Sciences, 8(5): 523-548, 10.1139/e71-055.

Ishibashi, H., 2009. Non-Newtonian behavior of plagioclase-bearing basaltic magma: Subliquidus viscosity measurement of the 1707 basalt of Fuji volcano, Japan. *Journal of Volcanology and Geothermal Research* **181**, 78-88.

Ishibashi, H. and Sato, H., 2007. Viscosity measurements of subliquidus magmas: Alkali olivine basalt from the Higashi-Matsuura district, Southwest Japan. *Journal of Volcanology and Geothermal Research* **160**, 223-238.

Kansal, A. R., Torquato, S., and Stillinger, F. H., 2002. Computer generation of dense polydisperse sphere packings. *Journal of Chemical Physics* **117**, 8212-8218.

Kay, R.W., 1978. Aleutian magnesian andesites: melts from subducted Pacific Ocean crust. Journal of Volcanology and Geothermal Research 4, 117–132.

Kay, S.M., Ramos, V.A., Marquez, M., 1993. Evidence in Cerro Pampa volcanic rocks of slab melting prior to ridge trench collision in southern South America. Journal of Geology 101, 703–714.

Kim, H.K., Nagao, K., Sumino, H., Tanaka, T., Hayashi, T., Nakamura, T., Lee, J.I., 2008. He–Ar and Nd–Sr isotopic compositions of late Pleistocene felsic plutonic back arc basin rocks from Ulleungdo volcanic island, South Korea: Implications for the genesis of young plutonic rocks in a back arc basin. Chem. Geol., 253, 180-195.

Krawinkel, H., Seyfred, H., Calvo, C., Astorga, A., 2000. Origin and inversion of sedimentary basins in Southern Central America: Zeitschrift für Angenwandle Geologie: Sonderheft. v.1, p. 71-77.

Krieger, I.M., 1972. Rheology of monodisperse lattices. Advances in Colloid and Interface Science, 3, 111-136.

Krieger, I. M. and Dougherty, T. J., 1959. A Mechanism for Non-Newtonian Flow in Suspensions of Rigid Spheres. *Journal of Rheology* **3**, 137-152.

Kucera, C.L., Kirkham, D.R., 1971. Soil respiration studies in tallgrass praire in Missouri. Ecology, 52, 912-915.

Kumagai, H., Chouet, B., Nakano, M., 2002. Waveform inversion of oscillatory signatures in long-period events beneath volcanoes. Journal of Geophysical Research, 107 (B11).

Kumagai, H., Chouet, B.A., Dawson, P.B., 2005. Source process of a long-period event at Kilaueea volcano, Hawaii. Geophysical Journal International, 161 (1), 243-254.

Kuno, H., 1960. High-alumina basalts. J. Petrol., 1, pp. 121.145.

Lavallée, Y., Hess, K.-U., Cordonnier, B., Dingwell, D.B., 2007. Non-Newtonian rheological law for highly crystalline dome lavas. Geology, 35, p.843

Lavallée, Y., Meredith, P. G., Dingwell, D. B., Hess, K. U., Wassermann, J., Cordonnier, B., Gerik, A., and Kruhl, J. H., 2008. Seismogenic lavas and explosive eruption forecasting. *Nature* **453**, 507-510.

Lavallée, Y., Varley, N.R., Alatorre-Ibargüengoitia, M.A., Hess, K.-U., Kueppers, U., Mueller, S., Richard, D., Scheu, B., Spieler, O., Dingwell, D.B., 2012. Magmatic architecture of dome-building eruptions at Volcán de Colima, Mexico. Bull. Volcanol. 74, 249–260.

Leeman, W.P., Carr, M.J., Morris, J.D., 1994. Boron geochemistry of the Central American Volcanic Arc: constraints on the genesis of subduction related magmas. Geoch. Et Cosmoch. Acta, 58, pp. 149-168.

Lejeune, A. M. and Richet, P., 1995. Rheology of crystal-bearing silicate melts - An experimental study at high viscosities. Journal of Geophysical Research-Solid Earth 100, 4215-4229.

Lewis, J.C., Boozer, A.C., Lopez, A., Montero, W., 2008. Collision versus silver transport in the hanging wall at the Middle America subduction zone: Constraints from background seismicity in central Costa Rica. Geochem. Geophys. Geosyst., 9, Q07S06, doi:10.129/2007GC001711.

Linkimer, L., Beck, S.L., Schwartz, S.Y., Zandt, G., Levin, V., 2010. Nature of crustal terranes and the Moho in northern Costa Rica from receiver function analysis. Geochem. Geophys. Geosyst., 11, Q01S19, doi:10.1029/2009GC002795.

Liotta, M., Paonita, A., Caracausi, A., Martelli, M., Rizzo, A., Favara, R., 2010. Hydrothermal processes governing the geochemistry of the crater fumaroles at Mount Etna volcano (Italy). Chem. Geol., 278, 92-104.

Llewellin, E. W., Mader, H. M., and Wilson, S. D. R., 2002a. The rheology of a bubbly liquid. Proceedings of the Royal Society of London Series a-Mathematical Physical and Engineering Sciences 458, 987-1016.

Llewellin, E.W., Mader, H.M., Wilson, S.D.R., 2002b. The constitutive equation and flow dynamics of bubbly magmas. Geophys. Res. Lett. 29 (Art. No. 2170).

Llewellin, E. W. and Manga, A., 2005. Bubble suspension rheology and implications for conduit flow. *Journal of Volcanology and Geothermal Research* **143**, 205-217.

Loewenberg, M., Hinch, E.J., 1996. Numerical simulation of a concentrated emulsion in shear flow. *J. Fluid Mech.* **321**, 395–419.

Lücke, O.H., Götze, H.J., Alvarado, G., 2008. A constrained 3D density model of the upper crust from gravity data interpretation for Central Costa Rica. Int. J. Geophys., 860902, doi:10.1155/2010/860902.

Lustrino, M., Dallai, L., 2003. On the origin of EM–I end-member. – N. Jb. Mi- ner. Abh. (179): 085 –100; Stuttgart.

Mader, H.M., Llewellin, E.W., Mueller, S.P., 2013. The rheology of two-phase magmas: A review and analysis. J. of Volc. and Geoth Res, 257, 135-158.

Manga, M., Castro, J., Cashman, K., Loewenberg, M., 1998. Rheology of bubble-bearing magmas. J. Volcanol. Geotherm. Res. 87, 15– 28.

Manga, M., Loewenberg, M., 2001. Viscosity of magmas containing highly deformable bubbles. *J. Volcanol. Geotherm. Res.* **105**, 19–24.

Maron, S. H. and Pierce, P. E., 1956. Application of ree-eyring generalized flow theory to suspensions of spherical particles. *Journal of Colloid Science* **11**, 80-95.

Marsh, B. D., 1981. On the crystallinity, probability of occurrence, and rheology of lava and magma. *Contributions to Mineralogy and Petrology* **78**, 85-98.

Marshall, J.S., Fisher, D.M., Gardner, T.W., 2000. Central Costa Rica deformed belt: Kinematics of diffuse faulting across the western Panama block. Tectonics, 19(3), 468-492.

Martelli, M., Nuccio, P.M., Stuart, F.M., Burgess, R., Ellam, R.M., Italiano, F., 2004. Helium-strontium isotope constraints on mantle evolution beneath the Roman Comagmatic Province, Italy. Earth Planet. Sci. Lett., 224, 295-308.

Martini, F., Tassi, F., Vaselli, O., Del Potro, R., Martinez, M., Van del Laat, R., Fernandez, E., 2010. Geophysical, geochemical and geodetical signals of reawakening at Turrialba volcano (Costa Rica) after almost 150 years of quiescence. J. of Volc. Geoth. Res., 198, 416-432.

Martini, M., 1983. Variation in the surface manifestations at Vulcano Island (Aeolian Islands, Italy). Bull. Volcanol., 46, 264-265.

Marty, B., 2012. The origins and concentrations of water, carbon, nitrogen and noble gases on Earth. Earth and Planet. Sci. Lett., 313-314, 56-66.

Marty, B., Jambon, A., 1987. C/^{3}He in volatile fluxes from the solid earth: implications for carbon geodynamics. Earth Planet. Sci. Lett., 83, 16-26.

Marty, B., Trull, T., Lussiez, P., Basile, I., Tanguy, J.C., 1994. He, Ar, O, Sr and Nd isotope constraints on the origin and evolution of Mount Etna magmatism. Earth Planet. Sci. Lett., 126, 23-26.

McCulloch, M.T., Kyser, T.H., Woodhead, J.D., Kinsley, L., 1994. Pb-Sr-Nd-O isotopic constraints on the origin of rhyolites from the Taupo Volcanic Zone of New Zealand: Evidence for assimilation followed by fractionation from basalt. Contrib. Mineral. Petrol., 115, 303-312.

Meschede, U. Barckhausen, H.-U. Worm, 1998. Extinct spreading on the Cocos Ridge. Terra Nova, 10, pp. 211–216

Montero, W., 2003. El sistema de falla Atirro-Río Sucio y la cuenca de tracción de Turrialba-Irazú: indentación tectónica relacionada con la colisión del levantamiento del Coco. Rev. Geol. De Am. Cent., 28: 05-29.

Moran, S.C., Newhall, C., Roman, D.C., 2011. Failed magmatic eruptions: late-stage cessation of magma ascent. Bull Volcanol. 73:115-122. doi:10.1007/s00445-010-0444-x

Morgan, D.J., Jerram, D.A., 2006. On estimating crystal shape for crystal size distribution analysis. J Volc Geoth Res, 154, 1-7.

Morris, J., Leeman, W.P., Tera, F., 1990. The subducted component in island arc lavas: constraints from Be isotopes and B-Be systematics. Nature, 344, 31-36.

Morris, J., Valentine, R., Harrison, T., 2002. [10]Be imaging of sediment accretion and subduction along the northeast Japan and Costa Rica convergent margins. Geology, 30, 59-62.

Mueller, S., Llewellin, E. W., and Mader, H. M., 2010. The rheology of suspensions of solid particles. *Proceedings of the Royal Society a-Mathematical Physical and Engineering Sciences* **466**, 1201-1228.

Newman, A.V., Stiros, S., Feng, L., Psimoulis, P., Moschas, F., Saltogianni, V., Jiang, Y., Papazachos, C., Panagiotopoulos, D., Karagianni, E., Vamvakaris, D., 2012. Recent geodetic unrest at Santorini Caldera, Greece. Geoph. Res. Lett., v. 39, L051286.

Nuccio, P.M., Paonita, A., Sortino, F., 1999. Geochemical modeling of mixing between magmatic and hydrothermal gases: the case of Vulcano Island, Italy. Earth Planet Sci Lett, 167, 3-4, p. 321-333.

Nuccio, P.M., Paonita, A., 2001. Magmatic degassing of multicomponent vapours and assessment of magma depth: Application on Vulcano Island (Italy). Earth Planet Sci Lett, 193, 467-481.

Nuccio, P.M., Paonita, A., Rizzo, A., Rosciglione A., 2008. Elemental and isotope covariation of noble gas in mineral phases from Etnean volcanics erupted during 2001-2005, and genetic relation with peripheral gas discharges. Earth Planet. Sci. Lett., 272, 683-690.

Oldroyd, J.G., 1953. The elastic and viscous properties of emulsions and suspensions. *Proc. R. Soc. A* **218**, 122– 132.

Oosterbroek, M., Mellema, J., 1981. Linear viscoelasticity in emulsions: I. The effect of an interfacial film on the dynamic viscosity of nondilute emulsions. *J. Colloid Interface Sci.* **8**,

14– 26.

OVSICORI-UNA, 2005. Report of the Turrialba Volcanic Activity. Smithsonian Institution.

OVSICORI-UNA, 2007. Report of the Turrialba Volcanic Activity. Smithsonian Institution.

OVSICORI-UNA, 2008. Report of the Turrialba Volcanic Activity. Smithsonian Institution.

OVSICORI-UNA, 2010. Report of the Turrialba Volcanic Activity. Smithsonian Institution.

OVSICORI-UNA, 2011. Report of the Turrialba Volcanic Activity. Smithsonian Institution.

OVSICORI-UNA, 2012. Report of the Turrialba Volcanic Activity. Smithsonian Institution.

OVSICORI-UNA, 2013. Report of the Turrialba Volcanic Activity. Smithsonian Institution.

Ozima, M., Podosek, F.A., 1983. Noble Gas Geochemistry. Cambridge University Press. 340 pp.

Pabst, W., Gregorova, E., and Berthold, C., 2006. Particle shape and suspension rheology of short-fiber systems. *Journal of the European Ceramic Society* **26**, 149-160.

Padron, E., Perez, N. M., Hernandez, P. A., Sumino, H., Melian, G. V., Barrancos, J., Nolasco, D., Padilla, G., Dionis, S., Rodriguez, F., Hernandez, I., Calvo, D., Peraza, M.D., Nagao, K., 2013. Diffusive helium emissions as a precursory sign of volcanic unrest. Geology, 41(5), 539–542. doi:10.1130/G34027.1.

Pal, R., 2003. Rheological behavior of bubble-bearing magmas. Earth and Planet Sci Lett, 207, 165-179.

Paniagua, S., 1984. Contribución al conocimento de la geología y petrología del vulcanismo plioceno-Cuaternario de la Cordillera de Costa Rica, 255 pp., Tesis de Maestria, Universidad de Chile.

Paonita, A., Caracausi, A., Iacono-Marziano, G., Martelli, M., Rizzo, A., 2012. Geochemical evidence for mixing between fluids exsolved at different depths in the magmatic system of Mt Etna (Italy). Geoch. Et Cosmoch. Acta, 84, 380-394.

Paonita, A., Federico, C., Bonfanti, P., Capasso, G., Inguaggiato, S., Italiano, F., Madonia, P., Pecoraino, G., Sortino, F., 2013. The episodic and abrupt geochemical changes at La Fossa fumaroles (Vulcano Island, Italy) and related constraints on the dynamics, structure and compositions of the magmatic system. Geochem Cosmochim Acta, 120, 158-178.

Papale, P., 1999. Strain-induced magma fragmentation in explosive eruptions. *Nature* **397**, 425-428.

Parks, M.M., Biggs, J., England, P., Mather, T.A., Nomikou, P., Palamartchouk, K., Papanikolaou, X., Paradissis, D., Parsons, B., Pyle, D.M., Raptakis, C., Zacharis, V., 2012. Evolution of Santorini Volcano dominated by episodic and rapid fluxes of melt from depth. Nature Geosci., v. ngeo1562, p- 749-754.

Parks, M. M. et al., 2013. Distinguishing contributions to diffuse CO_2 emissions in volcanic areas from magmatic degassing and thermal decarbonation using soil gas ^{222}Rn–δ^{13}C systematics: Application to Santorini volcano, Greece. Earth Planet. Sci. Lett., 377-378, 180-190.

Patino, L.C., Carr, M.J., Feigenson, M.D., 2000. Local and regional variations in Central American arc lavas controlled by variations in subducted sediment input. Contrib. Mineral. Petrol., 138:265-283.

Peacock, S.M., Rushmer, T., Thompson, A.B., 1994. Partial melting of subducting oceanic crust. Earth and Planetary Science Letters 121, 227–244.

Phan-Thien, N., Pham, D.C., 1997. Differential multiphase models for polydispersed suspensions and particulate solids. J Non Newt Fluid Mech. , 72:305–318. doi: 10.1016/S0377-

Picard, D., Arbaret, L., Pichavant, M., Champallier, R., Launeau, P., 2011. Rheology and microstructure of experimentally deformed plagioclase suspensions. Geology, 39, 747-750.

Pinkerton, H. and Stevenson, R. J., 1992. Methods of determining the rheological properties of magmas at sub-liquidus temperatures. *Journal of Volcanology and Geothermal Research,* **53**, 47-66.

Pinkerton, H. and Norton, G., 1995. Rheological properties of basaltic lavas at sub-liquidus temperatures: laboratory and field measurements on lavas from Mount Etna. *Journal of Volcanology and Geothermal Research* **68**, 307-323.

Plank, T., Langmuir, C.H., 1993. Tracing trace element from sediment input to volcanic output at subduction zones. Nature 362, 739–742.

Poreda, R., Craig, H., 1989. Helium isotope ratios in circum-Pacific volcanic arcs. Nature, 338, 473-478.

Protti, M., McNally, K., Pacheco, J., González, V., Montero, C., Segura, J., Brenes, J., Barboza, V., Malavassi, E., Güendel, F., Simila, G., Rojas, D., Velasco, A., Mata, A., Schillinger, W., 1995. The March 25, 1990 (Mw=7.0, ML=6.8), earthquake at the entrance of the Nicoya Gulf, Costa Rica: its prior activity, foreshocks, aftershocks, and triggered seismicity. J. Geoph. Res., 100 (B10), 20345-20358.

Quane, S.L., Russell, J.K., Kennedy, L.A., 2004. A low-load, high-temperature deformation apparatus for volcanological studies. Am. Mineral. 89, 873–877.

Quane, S.L., Russell, J.K., 2005. Welding: insights from high-temperature analogue experiments. J. Volcanol. Geotherm. Res. 142, 67–87.

Quane, S.L., Russell, J.K., 2006. Bulk and particle strain analysis in high-temperature deformation experiments. J of Volc and Geoth Res, 142, 67-87.

Reagan, M.K., Gill, J.B., 1989. Coexisting calcalkaline and high-niobium basalts from Turrialba volcano, Costa Rica: implications for residual titanates in arc magma sources. J. of Geophys. Res., v.B94, pp. 4619-4633.

Reagan, M.K., Duarte, E., Soto, G.J., Fernández, E., 2006. The eruptive history of Turrialba volcano, Costa Rica, and potential hazards from future eruptions. Geol. Soc. Am. Spec. Pap., 412, pp. 235-258.

Reuss, A., 1929. Berechnung der Fließgrenze von Mischkristallen auf Grund der Plastizitätsbedingung für Einkristalle. *Z. Angew. Math. Mech.* **9**, 49-58.

Rizzo, A., Caracausi, A., Favara, R., Martelli, M., Paonita, A., Paternoster, M., Nuccio, P.M., Rosciglione, A., 2006. New insights into magma dynamics during last two eruptions of Mount Etna as inferred by geochemical monitoring from 2002 to 2005. Geochem. Geophys. Geosyst., 7, doi:10.1029/2005GC001175.

Rizzo, A., Grassa, F., Inguaggiato, S., Liotta, M., Longo, M., Madonia, P., Brusca, L., Capasso, G., Morici, S., Rouwet, D., Vita, F., 2009. Geochemical evaluation of observed changes in volcanic activity during the 2007 eruption at Stromboli (Italy). J. Volcanol. Geotherm. Res., 182, 246-254.

Robert, G., Russell, J.K., Giordano, D., 2008a. Rheology of porous volcanic materials: High-temperature experimentation under controlled water pressure. Chem. Geol. 256, 216–230.

Robert, G., Russell, J. K., Giordano, D., and Romano, C., 2008b. High-temperature deformation of volcanic materials in the presence of water. *American Mineralogist* **93**, 74-80.

Roscoe, R., 1952. The viscosity of suspensions of rigid spheres. British Journal of Applied Physics 3, 269-367.

Ruiz Cubillo, P., Turrin, B. D., Soto, G. J., Del Potro, R., Gagnevin, D., Gazel, E., Mora Fernandez, M., Carr, M. J., Swisher, C. C., 2010. Unveiling Turrialba (Costa Rica) volcano's latest geological evolution through new ^{40}Ar/^{39}Ar ages. Abstract - American Geophysical Union, AGU Fall Meeting 2010.

Rust, A.C., Manga, M., 2002a. Effects of bubble deformation on the viscosity of diluite suspensions. J. Non-Newtonian Fluid Mech, 104, 53-63.

Rutgers, I. R., 1962a. Relative viscosity and concentration. *Rheologica Acta* **2**, 305-348.

Rutgers, I. R., 1962b. Relative viscosity of suspensions of rigid spheres in Newtonian liquids. *Rheologica Acta* **2**.

Saar, M.O., Manga, M., Cashman, K. V, Fremouw, S., 2001. Numerical models of the onset of yield strength in crystal-melt suspensions. Earth Planet. Sci. Lett. 187, 367–379.

Saginor, I., Gazel, E., Condie, C., Carr, M.J., 2013. Evolution of geochemical variations along the Central American volcanic front. Geochemistry, Geophysics, Geosystems 14: 4504–4522, doi:10.1002/ggge.20259

Sajona, F.G., Maury, R.C., Bellon, H., Cotten, J., Defant, M.J., Pubellier, M., Rangin, C., 1993. Initiation of subduction and the generation of slab melts in western and eastern Mindanao, Philippines. Geology 21, 1007–1010.

Sajona, F.G., Maury, R.C., Bellon, H., Cotten, J., Defant, M., 1996. High field strength element enrichment of Pliocene–Pleistocene island arc basalts, Zamboanga Peninsula, western Mindanao (Philippines). Journal of Petrology 37, 693–726.

Sano, Y., Marty, B., 1995. Origin of fumarolic gas from island arcs. Chem. Geol., 119, pp. 265-274.

Sano, Y., Wakita, H., 1985. Geographical distribution of 3He/4He in Japan: Implications for arc tectonics and incipient magmatism. J. Geophys., Res., 90, pp. 8729-8741.

Sano, Y., Williams, S.N., 1996. Fluxes of mantle and subducted carbon along convergent plate boundaries. Geophys. Res. Lett., 23, 2749-2752.

Sano, Y., Nakamura, Y., Wakita, H., Urabe, A., Tominaga, T., 1984. Helium-3 emission related to volcanic activity. Science, 224, 150-151.

Sato, H., 2005. Viscosity measurement of subliquidus magmas: 1707 basalt of Fuji volcano. *Journal of Mineralogical and Petrological Sciences* **100**, 133-142.

Semet, M., Vatin-Pèrignon, N., 1979. The 16th century activity of La Soufrière de Guadeloupe (F.W.I.): a model for explosive andesitic volcanism in the Lesser Antilles. EOS, Trans. Am. Geophys. Union, 60: 833. (*abstr.*)

Shaw, A.M., Hilton, D.R., Fisher, T.P., Walker J.A., Alvarado, G.E., 2003. Contrasting He-C relationships in Nicaragua and Costa Rica: insights into C cycling through subduction zones. Earth Planet. Sci. Lett., 214, pp. 419-513.

Shaw, A.M., Hilton, D.R., Fisher, T.P., Walker J.A., de Leew G.A.M., 2006. Helium isotope variations in mineral separates from Costa Rica and Nicaragua: Assessing crustal contributions, timescale variations and diffusion-related mechanism. Chem. Geol., 230, pp. 124-139.

Shaw, H. R., 1969. Rheology of Basalt in the Melting Range. *J. Petrology* **10**, 510-535.

Shaw, H.R., 1980. Fracture mechanism of magma transport from the mantle to the surface. In: Hargraves RB (ed) Physics of magmatic processes. Princeton University Press, Princeton, pp. 201-264.

Shimizu, A., Sumino, H., Nagao, K., Notsu, K., Mitropoulos, P., 2005. Variation in noble gas isotopic composition of gas samples from the Aegean arc, Greece. J. of Volcan. And Geoth. Res., 140, 321-339, doi:10.1016/j.volgeores.2004.08.016.

Sicardi, L., 1941. Il recente ciclo dell'attività fumarolica dell'isola di Vulcano. Bull. Volcanol., 7, p.85-140.

Sinton, C.W., Duncan, R.A., Storey, M., Lewis, J., and Estrada, J.J., 1998. An oceanic flood basalt province within the Caribbean plate. Earth Planet. Sci. Lett., 155(3–4):221–235. doi:10.1016/S0012-821X(97)00214-8

Snyder, G., Poreda, R.J., Hunt, A., Fehn, U., 2001. Regional variations in volatile composition: isotopic evidences for carbonate recycling in the Central American volcanic arc. Geochem. Geophys. Geosyst. 2:1057. doi:10.129/2001GC000163

Snyder, G., Poreda, R.J., Fehn, U., Hunt, A., 2003. Sources of nitrogen and methane in Central American geothermal settings: noble gas and 129I evidence for crustal and magmatic volatile components. Geochem. Geophys. Geosyst. 4:9001. doi:10.10129/2002GC000363

Sortino, F., Nonell, A., Toutain, J.P., Munoz, M., Valladon, M., Volpicelli, G., 2006. A new method for sampling fumarolic gases: analysis of major, minor and metallic trace elements with ammonia solutions. J. of Volcanol. and Geoth. Res., 158, 244-256.

Soto, G.J., 1988. Estructuras volcano-tectónicas del Volcán Turrialba, Costa Rica, América Central. 5th Chilean Geological Congress, 8-12 August, Santiago, pp. 163-175.

Spera, F.J., Stein,

Spera F.J., Borgia A., Strimple J., 1988. Rheology of melts and magmatic suspensions 1. Design and calibration of concentric cylinder viscometer with application to rhyolite magma, *Journal of Geophysical Research* **93**, 273–10,294.

Spera, F.J., Stein, D.J., 2000. Comment on "Rheology of bubble bearing magmas" by Lejeune et al.. *Earth Planet. Sci. Lett.* 175, 327–331.

Stein, D.J., Spera, F.J., 1992. Rheology and microstructure of magmatic emulsions: theory and experiments. *J. Volcanol. Geotherm. Res.* **49**, 157–174.

Stern, C.R., Kilian, R., 1996. Role of the subducted slab, mantle wedge and continental crust in the generation of adakites from the Andean Austral Volcanic Zone. Contributions to Mineralogy and Petrology, 123, 263-281.

Stoiber, R.E., Carr, M.J., 1974. Quaternary volcanic and tectonic segmentation of Central America. Bull. Volcanol., 37:304-325, doi:10.1007/BF02597631.

Sun, S.S., McDonough, W.F., 1989. Chemical and isotopic systematics of oceanic basalts: implications for mantle composition and processes. In: Saunders, A.D., Norry, M.J. (Eds.), Magmatism in Ocean Basins. Geol. Soc. London Spec. Pub., vol. 42, pp. 313-345.

Taisne, B., Tait, S., Jaupart, C., 2011. Conditions for the Arrest of a Vertical Propagating Dyke. Bull Volcanol, doi:10.1007/s00445-010-0440-1

Tassi, F., Vaselli, O., Barboza, V., Fernandez, E., Duarte, E., 2004. Fluid geochemistry in the period 1998-2002 at Turrialba Volcano (Costa Rica). Ann. Geophys. 47:1501-1511.

Tassi, F., Vaselli, O., Papazachos, C.B., Giannini, L., Chiodini, G., Vougioukalakis, G.E., Karagianni, E., Vamvakaris, V., Panagiotopoulos, D., 2013. Geochemical and isotopic changes in the fumarolic and submerged gas discharges during the 2011–2012 unrest at Santorini caldera (Greece). Bull. Volcanol., v. 75, p. 1-15.

Taylor, G.I., 1934. The formation of emulsions in definable fields of flow. *Proc. R. Soc. A* **146**, 501–523.

Tazieff, H., 1977. La Soufrière, volcanology and forecasting. Nature, 269:96-97.

Thomas, D. G., 1965. Transport characteristics of suspension: VIII. A note on the viscosity of Newtonian suspensions of uniform spherical particles. *Journal of Colloid Science* **20**, 267-277.

Thorkelson, D.J., Breitsprecher, K., 2005. Partial melting of slab window margins: genesis of adakitic and non-adakitic magmas. Lithos 79, 25–41.

Van Andel, T.H., Heath, G.R., Malfait, B.T., Heinrichs, D.F., Ewing, J.I., 1971. Tectonics of the Panama Basin, eastern equatorial Pacific. Geological Society of America Bulletin, 82, 1489-1508.

van Soest, M.C., Hilton, D.R., Macpherson, C.J., Mattey, D.P., 2002. Resolving sediment subduction and crustal contamination in the Lesser Antilles island Arc: a combined He-O-Sr isotope approach. J. Petrol., 43, 143-170.

Vaselli, O., Tassi, F., Duarte, E., Fernandez, E., Poreda R.J., Delgado Huertas, A., 2010. Evolution of fluid geochimistry at the Turrialba volcano (Costa Rica) from 1998 to 2008. Bull. Volc., 72, pp. 397-410.

Vasseur, J., Wadsworth, F.B., Lavallée, Y., Hess, K.-U., Dingwell, D.B., 2013. Volcanic sintering: Timescales of viscous densification and strength recovery. Geophys. Res. Lett. 40, 5658–5664.

Vincent, P.M., Vatin-Pèrignon, N., Semet, M. and Chemin~e, J.L., 1979. Le DSme de la Soufrière (Guadeloupe): son age et son mode de raise en place. C.R. Acad. Sci. Paris, Sur. D, 288: 51--54.

Von Huene, R., Ranero, C.R., Weinrebe, 2000. Quaternary convergent margin tectonics of Costa Rica, segmentation of the Cocos Plate and Central American volcanism. Tectonics, 19(2), pp. 314-334.

Von Seebach, K., 1865, Besteigung des Vulkans Turrialba in Costa Rica: Petermann's Mitteil, v. 9, p. 321–324.

Vona, A., Romano, C., Dingwell, D.B., Giordano, D., 2011. The rheology of crystal-bearing basaltic magmas from Stromboli and Etna. Geochem et Cosmochem Acta, 75, 3214-3236.

Vona, A., Romano, C., Giordano, D., Russell, J.K., 2013. The multiphase rheology of magmas from Monte Nuovo (Campi Flegrei, Italy). Chem Geol, 346, 213-227.

Voigt, W., 1928. *Lehrbuch der Kristallphysik*, Leipzig, Germany.

Webb, S.L., Dingwell, D.B., 1990. The onset of Non-Newtonian rheology of silicate melts – A fiber elongation study. Phys Chem Minerals, 17, 125-132.

White, R.S., Dupré, B., Vidal, P., 1985. Isotope and trace element geochemistry of sediments from the Barbados Ridge-Demarara Plain region. Geochem. Cosmochim. Acta, 49, 1857-1886.

Wilson, M. (1989). Igneous Petrogenesis: A Global Tectonic Approach, Unwin Hyman, London.

Wu, Y., Zinchenko, A.Z., Davis, R.H., 2002. Ellipsoidal model for deformable drops and application to nonNewtonian emulsion flow. *J. Non-Newton. Fluid Mech.* **102**, 281–298.

Yogodzinski, G.M., Kelemen, P.B., 1998. Slab melting in the Aleutians: implication of anion probe study of clinopyroxene in primitive adakite and basalt. Earth and Planetary Science Letters 158, 53–65.

Yogodzinski, G.M., Kay, R.W., Volynets, O.N., Koloskov, A.V., Kay, S.M., 1995. Magnesian andesite in the western Aleutian Komandorsky region: implications for slab melting and processes in the mantle wedge. Geological Society of America Bulletin 107, 505–519

Yogodzinski, G.M., Lees, J.M., Churikova, T.G., Dorendorf, F., Woerner, G., Volynets, O.N., 2001. Geochemical evidence for the melting of subducting oceanic lithosphere at plates edges. Nature 409, 500–504.

Yu, W., Bousmina, M., 2003. Ellipsoidal model for droplet deformation in emulsions. *J. Rheol.* **47**, 1011 –1039.

Acknowledgements

APPENDIX 1: *Electron microprobe analyses*

PLAGIOCLASE

Sample	TU 4										TU5							
Rock	DACITE lava flow										BASALT-ANDESITE lava flow							
notes	mf1	mf2	ph1	ph2 core	ph2 rim	ph3 core	ph3 int	ph3 rim	ph4 core	ph4 rim	Line 1 plgf1	Line 2 plgf1	Line 3 plgf1	Line 4 plgf1	Line 5 plgf1	Line 6 plgf1	Line 7 plgf1	Line 8 plgf1
SiO_2	51.44	50.85	55.45	53.16	51.97	54.27	54.96	54.56	55.28	56.26	49.51	51.90	51.44	52.21	51.67	53.08	51.95	50.54
Al_2O_3	26.56	26.06	27.52	25.45	27.01	28.62	29.24	29.83	30.42	29.48	30.32	27.86	28.39	28.81	28.91	28.42	29.22	29.47
Fe_2O_3	0.59	0.70	0.61	0.50	0.78	0.78	0.77	0.70	0.65	0.82	0.66	0.70	0.68	0.72	0.68	0.71	0.80	0.88
CaO	12.15	10.80	9.41	8.96	10.17	11.35	11.52	12.10	12.19	11.33	13.67	11.56	11.54	11.42	12.03	11.80	13.15	12.90
Na_2O	4.14	4.20	5.57	5.32	4.79	4.63	4.71	4.68	4.74	5.26	3.16	4.19	4.33	4.34	4.22	4.41	3.69	3.53
K_2O	0.29	0.44	0.49	0.47	0.47	0.39	0.36	0.39	0.38	0.48	0.18	0.31	0.33	0.31	0.29	0.31	0.24	0.26
Tot.	95.17	93.05	99.05	93.86	95.19	100.05	101.57	102.26	103.65	103.63	97.49	96.52	96.72	97.81	97.81	98.72	99.05	97.58
Formula su 8 ossigeni																		
Si	2.453	2.473	2.520	2.547	2.468	2.454	2.448	2.419	2.417	2.458	2.314	2.435	2.412	2.417	2.398	2.436	2.384	2.356
Al	1.494	1.494	1.474	1.438	1.513	1.525	1.535	1.560	1.568	1.518	1.670	1.541	1.569	1.572	1.581	1.538	1.581	1.620
Fe	0.021	0.026	0.021	0.018	0.028	0.027	0.026	0.023	0.021	0.027	0.023	0.025	0.024	0.025	0.024	0.024	0.028	0.031
Ca	0.621	0.563	0.458	0.460	0.518	0.550	0.550	0.575	0.571	0.530	0.684	0.581	0.580	0.566	0.598	0.580	0.647	0.644
Na	0.383	0.396	0.491	0.495	0.441	0.406	0.407	0.402	0.401	0.446	0.287	0.381	0.394	0.390	0.380	0.392	0.329	0.319
K	0.018	0.027	0.028	0.029	0.028	0.023	0.021	0.022	0.021	0.027	0.010	0.018	0.019	0.018	0.017	0.018	0.014	0.016
Σ CATIONI (%)	4.99	4.98	4.99	4.99	5.00	4.98	4.99	5.00	5.00	5.01	4.99	4.98	5.00	4.99	5.00	4.99	4.98	4.99
An	60.79	57.08	46.86	46.79	52.44	56.16	56.25	57.53	57.45	52.89	69.73	59.25	58.38	58.14	60.10	58.59	65.36	65.83
Ab	37.47	40.18	50.25	50.28	44.69	41.51	41.63	40.26	40.39	44.44	29.21	38.87	39.67	39.99	38.17	39.59	33.20	32.59
Or	1.74	2.74	2.88	2.93	2.87	2.32	2.12	2.21	2.16	2.66	1.06	1.89	1.96	1.87	1.73	1.83	1.43	1.59
Tot.	100	100	100	100	100	100	100	100	100	100	100	100	100	100	100	100	100	100
Ca+Na+K	1.02	0.99	0.98	0.98	0.99	0.98	0.98	1.00	0.99	1.00	0.98	0.98	0.99	0.97	1.00	0.99	0.99	0.98
Si+Al	3.95	3.97	3.99	3.99	3.98	3.98	3.98	3.98	3.98	3.98	3.98	3.98	3.98	3.99	3.98	3.97	3.97	3.98

Sample	TU5													
Rock	BASALT-ANDESITE bomb													
notes	Line 1 plgf2	Line 2 plgf2	Line 3 plgf2	Line 4 plgf2	Line 5 plgf2	Line 7 plgf2	Line 8 plgf2	Line 1 plgmf1	Line 2 plgmf1	Line 3 plgmf1	Line 4 plgmf1	Line 5 plgmf1	Line 6 plgmf1	Line 7 plgmf1	Line 1 plgf3
SiO_2	50.60	51.36	50.69	49.95	50.03	47.97	49.91	48.86	49.33	49.07	49.53	49.59	50.82	49.80	51.15
Al_2O_3	29.09	29.13	29.48	29.43	29.25	30.54	29.08	29.52	28.78	29.17	29.35	28.36	27.93	28.68	26.86
Fe_2O_3	0.59	0.62	0.90	0.86	0.81	0.76	0.97	0.71	0.79	0.84	0.87	0.94	0.85	0.87	0.80
CaO	12.22	11.94	12.37	13.32	12.88	14.00	12.68	13.10	12.55	12.84	12.92	12.30	11.41	12.09	11.13
Na_2O	3.68	4.00	3.84	3.47	3.50	2.83	3.60	3.16	3.73	3.44	3.32	3.77	4.11	3.75	4.41
K_2O	0.26	0.27	0.26	0.22	0.23	0.16	0.35	0.18	0.25	0.23	0.22	0.27	0.32	0.26	0.31
Tot.	96.45	97.32	97.53	97.26	96.70	96.26	96.59	95.54	95.42	95.58	96.20	95.24	95.43	95.45	94.65
Formula su 8 ossigeni															
Si	2.379	2.392	2.362	2.341	2.354	2.276	2.354	2.327	2.354	2.338	2.343	2.370	2.414	2.371	2.449
Al	1.613	1.600	1.620	1.626	1.622	1.708	1.617	1.658	1.619	1.638	1.637	1.598	1.564	1.610	1.516
Fe	0.021	0.022	0.032	0.030	0.029	0.027	0.034	0.025	0.028	0.030	0.031	0.034	0.030	0.031	0.029
Ca	0.616	0.596	0.617	0.669	0.649	0.712	0.641	0.669	0.642	0.656	0.655	0.630	0.581	0.616	0.571
Na	0.336	0.361	0.347	0.316	0.319	0.261	0.329	0.292	0.345	0.317	0.304	0.349	0.379	0.346	0.409
K	0.016	0.016	0.015	0.013	0.014	0.009	0.021	0.011	0.015	0.014	0.013	0.017	0.019	0.016	0.019
Σ CATIONI (%)	4.98	4.99	4.99	5.00	4.99	4.99	5.00	4.98	5.00	4.99	4.98	5.00	4.99	4.99	4.99
An	63.69	61.26	63.04	67.02	66.08	72.48	64.65	68.83	64.06	66.45	67.35	63.27	59.34	63.02	57.18
Ab	34.70	37.09	35.39	31.63	32.51	26.55	33.24	30.02	34.45	32.16	31.29	35.06	38.69	35.38	40.95
Or	1.61	1.64	1.57	1.34	1.41	0.96	2.11	1.15	1.49	1.39	1.35	1.68	1.96	1.60	1.87
Tot.	100	100	100	100	100	100	100	100	100	100	100	100	100	100	100
Ca+Na+K	0.97	0.97	0.98	1.00	0.98	0.98	0.99	0.97	1.00	0.99	0.97	1.00	0.98	0.98	1.00
Si+Al	3.99	3.99	3.98	3.97	3.98	3.98	3.97	3.99	3.97	3.98	3.98	3.97	3.98	3.98	3.97

PLAGIOCLASE

Sample	TU5															
Rock	BASALT-ANDESITE bomb															
notes	Line 2 plgf3	Line 4 plgf3	Line 5 plgf3	Line 6 plgf3	Line 7 plgf3	Line 8 plgf3	plgmf2	Line 1 plgf4	Line 2 plgf4	Line 3 plgf4	Line 4 plgf4	Line 5 plgf4	Line 6 plgf4	Line 7 plgf4	Line 8 plgf4	Line 10 plgf4
SiO_2	50.42	48.22	48.71	48.77	48.61	47.82	48.85	44.40	44.89	44.42	44.98	43.83	44.09	44.73	44.93	50.18
Al_2O_3	27.21	28.82	28.40	28.97	29.17	28.27	29.23	31.04	30.88	31.35	30.61	31.10	31.03	30.77	30.73	26.98
Fe_2O_3	0.73	0.74	0.79	0.82	0.87	0.73	0.82	0.88	0.75	0.73	0.67	0.83	0.73	0.76	0.80	0.78
CaO	11.67	13.21	12.63	13.02	13.18	13.07	13.07	16.00	15.87	16.24	15.74	15.95	16.01	15.83	15.47	11.15
Na_2O	4.12	3.05	3.39	3.39	3.12	3.09	3.19	1.92	1.69	1.57	2.12	1.66	1.69	1.68	1.96	3.96
K_2O	0.30	0.19	0.21	0.22	0.21	0.21	0.16	0.06	0.07	0.06	0.08	0.04	0.05	0.06	0.05	0.20
Tot.	94.44	94.23	94.12	95.18	95.14	93.19	95.31	94.28	94.15	94.37	94.20	93.42	93.59	93.82	93.94	93.25
Formula su 8 ossigeni																
Si	2.423	2.331	2.355	2.335	2.328	2.339	2.333	2.170	2.191	2.166	2.197	2.160	2.168	2.191	2.197	2.435
Al	1.542	1.643	1.619	1.635	1.647	1.630	1.646	1.788	1.777	1.802	1.762	1.807	1.799	1.777	1.772	1.543
Fe	0.026	0.027	0.029	0.029	0.031	0.027	0.029	0.032	0.028	0.027	0.025	0.031	0.027	0.028	0.030	0.028
Ca	0.601	0.684	0.654	0.668	0.676	0.685	0.669	0.838	0.830	0.848	0.824	0.842	0.843	0.831	0.811	0.580
Na	0.384	0.286	0.318	0.315	0.289	0.293	0.295	0.181	0.160	0.149	0.200	0.159	0.161	0.159	0.186	0.373
K	0.018	0.012	0.013	0.014	0.013	0.013	0.010	0.004	0.004	0.004	0.005	0.003	0.003	0.004	0.003	0.012
Σ CATIONI (%)	4.99	4.98	4.99	5.00	4.98	4.99	4.98	5.01	4.99	5.00	5.01	5.00	5.00	4.99	5.00	4.97
An	59.92	69.69	66.43	67.03	69.11	69.12	68.68	81.91	83.45	84.76	80.06	83.92	83.67	83.57	81.13	60.09
Ab	38.27	29.13	32.29	31.61	29.58	29.58	30.32	17.74	16.12	14.85	19.47	15.82	16.00	16.02	18.58	38.65
Or	1.81	1.17	1.28	1.35	1.31	1.30	1.01	0.35	0.43	0.39	0.47	0.26	0.33	0.40	0.29	1.26
Tot.	100	100	100	100	100	100	100	100	100	100	100	100	100	100	100	100
Ca+Na+K	1.00	0.98	0.99	1.00	0.98	0.99	0.97	1.02	0.99	1.00	1.03	1.00	1.01	0.99	1.00	0.97
Si+Al	3.96	3.97	3.97	3.97	3.97	3.97	3.98	3.96	3.97	3.97	3.96	3.97	3.97	3.97	3.97	3.98

Sample	TU5								TU7									
Rock	BASALT-ANDESITE bomb								ANDESITE lava flow									
notes	Line 12 plgf4	plgf5c	plgf5r	plgf6c	plgf6r	plgf7c	plgmf3	plgmf4	Line 1 plgf1	Line 2 plgf1	Line 3 plgf1	Line 4 plgf1	Line 5 plgf1	Line 6 plgf1	Line 7 plgf1	Line 8 plgf1	Line 9 plgf1	Line 10 plgf1
SiO_2	50.46	51.46	49.03	47.76	48.00	48.96	50.43	48.55	49.65	49.83	49.28	49.48	52.30	51.72	51.46	51.47	56.84	58.30
Al_2O_3	27.26	26.44	27.72	28.89	27.85	27.13	26.93	27.73	30.16	30.33	30.51	30.62	28.82	28.45	27.88	28.97	25.90	24.38
Fe_2O_3	0.84	0.69	1.06	0.61	0.83	0.80	0.98	0.74	0.69	0.80	0.80	0.73	0.64	0.81	0.67	0.87	0.62	0.48
CaO	11.52	9.89	11.62	12.30	12.12	11.60	10.79	12.14	14.48	14.90	14.79	14.77	12.15	12.30	11.80	12.71	8.91	7.33
Na_2O	3.85	4.91	3.80	3.57	3.51	3.89	4.08	3.56	3.15	3.01	3.03	2.92	4.09	4.08	4.21	3.93	5.63	6.43
K_2O	0.37	0.44	0.32	0.20	0.22	0.26	0.38	0.23	0.17	0.14	0.12	0.16	0.27	0.26	0.25	0.24	0.52	0.60
Tot.	94.31	93.84	93.54	93.33	92.53	92.63	93.59	92.95	98.31	99.01	98.53	98.67	98.25	97.61	96.28	98.19	98.42	97.52
Formula su 8 ossigeni																		
Si	2.426	2.479	2.383	2.329	2.360	2.401	2.440	2.375	2.31	2.30	2.29	2.29	2.41	2.41	2.42	2.38	2.59	2.67
Al	1.545	1.501	1.588	1.661	1.614	1.568	1.536	1.599	1.65	1.65	1.67	1.67	1.57	1.56	1.55	1.58	1.39	1.32
Fe	0.031	0.025	0.039	0.022	0.031	0.029	0.036	0.027	0.02	0.03	0.03	0.03	0.02	0.03	0.02	0.03	0.02	0.02
Ca	0.594	0.510	0.605	0.643	0.638	0.609	0.559	0.636	0.72	0.74	0.74	0.73	0.60	0.61	0.60	0.63	0.44	0.36
Na	0.359	0.459	0.358	0.337	0.335	0.370	0.383	0.338	0.28	0.27	0.27	0.26	0.37	0.37	0.38	0.35	0.50	0.57
K	0.022	0.027	0.020	0.012	0.014	0.016	0.023	0.014	0.01	0.01	0.01	0.01	0.02	0.02	0.02	0.01	0.03	0.03
Σ CATIONI (%)	4.98	5.00	4.99	5.00	4.99	4.99	4.98	4.99	5.00	5.00	5.00	4.99	4.98	4.99	4.99	4.99	4.97	4.97
An	60.88	51.21	61.58	64.77	64.66	61.21	57.92	64.37	71.02	72.62	72.41	72.99	61.17	61.56	59.83	63.20	45.20	37.24
Ab	36.82	46.05	36.42	33.99	33.93	37.15	39.67	34.17	27.98	26.55	26.88	26.09	37.24	36.92	38.65	35.37	51.66	59.14
Or	2.30	2.73	2.01	1.24	1.40	1.64	2.42	1.46	1.00	0.84	0.72	0.92	1.59	1.53	1.52	1.43	3.14	3.63
Tot.	100	100	100	100	100	100	100	100	100	100	100	100	100	100	100	100	100	100
Ca+Na+K	0.98	1.00	0.98	0.99	0.99	1.00	0.97	0.99	1.02	1.02	1.02	1.00	0.98	1.00	1.00	1.00	0.96	0.97
Si+Al	3.97	3.98	3.97	3.99	3.97	3.97	3.98	3.97	3.96	3.95	3.96	3.96	3.98	3.97	3.97	3.97	3.98	3.99

PLAGIOCLASE

Sample	TU7																					
Rock	ANDESITE lava flow																					
notes	plgml1	plgml2	plgml3	plgf2c	plgf2r	plgml4	plgmf1	Line 1 3	Line 2 3	Line 3 3	Line 4 3	Line 5 3	Line 6 3	Line 7 3	Line 8 3	Line 9 3	Line 10 3	Line 11 3	Line 12 3	plgmf2	plgmf3	plgmf2
SiO$_2$	50.93	53.13	52.97	52.42	54.73	51.96	51.72	47.12	47.16	50.13	49.87	50.29	50.04	50.78	49.69	51.74	51.27	51.93	51.83	49.86	51.02	49.60
Al$_2$O$_3$	28.63	27.98	28.17	28.74	26.31	28.49	28.97	30.49	30.85	29.36	29.61	29.30	28.68	28.44	29.19	27.95	28.30	27.66	26.81	28.86	28.82	29.56
Fe$_2$O$_3$	0.83	0.78	1.04	0.80	1.09	1.00	0.78	0.89	0.90	0.69	0.75	0.75	0.70	0.72	0.79	0.94	1.02	0.98	1.04	0.80	0.94	0.73
CaO	12.61	11.78	11.91	12.18	10.75	12.40	12.54	15.51	15.87	13.72	13.90	13.58	13.46	13.00	13.98	13.34	12.52	12.50	11.62	14.12	13.15	14.56
Na$_2$O	3.99	4.41	4.27	4.31	4.92	4.11	4.01	2.28	2.22	3.24	3.34	3.36	3.58	3.81	3.26	3.81	3.87	4.06	4.63	3.26	3.71	3.14
K$_2$O	0.14	0.21	0.27	0.14	0.29	0.17	0.16	0.08	0.05	0.09	0.10	0.12	0.09	0.12	0.08	0.13	0.15	0.20	0.17	0.11	0.15	0.09
Tot.	97.14	98.29	98.62	98.59	98.10	98.13	98.19	96.37	97.05	97.23	97.56	97.41	96.54	96.86	96.98	97.91	97.13	97.33	96.09	97.01	97.79	97.68
Formula su 8 ossigeni																						
Si	2.38	2.45	2.44	2.41	2.52	2.41	2.39	2.24	2.23	2.35	2.33	2.35	2.36	2.38	2.34	2.41	2.40	2.42	2.45	2.35	2.38	2.32
Al	1.58	1.52	1.53	1.56	1.43	1.55	1.58	1.71	1.72	1.62	1.63	1.61	1.60	1.57	1.62	1.53	1.56	1.52	1.49	1.60	1.58	1.63
Fe	0.03	0.03	0.04	0.03	0.04	0.03	0.03	0.03	0.03	0.02	0.03	0.03	0.02	0.03	0.03	0.03	0.04	0.03	0.04	0.03	0.03	0.03
Ca	0.63	0.58	0.59	0.60	0.53	0.62	0.62	0.79	0.80	0.69	0.70	0.68	0.68	0.65	0.70	0.66	0.63	0.63	0.59	0.71	0.66	0.73
Na	0.36	0.39	0.38	0.38	0.44	0.37	0.36	0.21	0.20	0.29	0.30	0.30	0.33	0.35	0.30	0.34	0.35	0.37	0.42	0.30	0.33	0.28
K	0.01	0.01	0.02	0.01	0.02	0.01	0.01	0.00	0.00	0.01	0.01	0.01	0.01	0.01	0.00	0.01	0.01	0.01	0.01	0.01	0.01	0.01
Σ CATIONI (%)	5.00	4.98	4.98	4.99	4.97	4.99	4.99	4.99	5.00	4.98	4.99	4.98	5.00	4.99	4.99	4.99	4.98	4.99	5.00	4.99	4.99	5.00
An	**63.04**	**58.87**	**59.70**	**60.46**	**53.76**	**61.89**	**62.78**	**78.62**	**79.56**	**69.71**	**69.30**	**68.55**	**67.13**	**64.92**	**70.00**	**65.43**	**63.56**	**62.21**	**57.49**	**70.09**	**65.61**	**71.57**
Ab	**36.12**	**39.86**	**38.72**	**38.70**	**44.54**	**37.13**	**36.28**	**20.92**	**20.15**	**29.76**	**30.12**	**30.71**	**32.32**	**34.39**	**29.55**	**33.84**	**35.57**	**36.60**	**41.49**	**29.29**	**33.49**	**27.90**
Or	**0.84**	**1.27**	**1.58**	**0.84**	**1.70**	**0.98**	**0.94**	**0.45**	**0.29**	**0.53**	**0.58**	**0.73**	**0.55**	**0.69**	**0.45**	**0.73**	**0.88**	**1.19**	**1.02**	**0.62**	**0.91**	**0.54**
Tot.	100	100	100	100	100	100	100	100	100	100	100	100	100	100	100	100	100	100	100	100	100	100
Ca+Na+K	1.00	0.99	0.98	0.99	0.99	0.99	0.99	1.01	1.01	0.99	1.00	0.99	1.01	1.01	1.01	1.02	0.99	1.01	1.02	1.02	1.00	1.02
Si+Al	3.96	3.97	3.96	3.97	3.95	3.96	3.97	3.95	3.95	3.97	3.96	3.97	3.96	3.96	3.96	3.94	3.96	3.95	3.94	3.95	3.96	3.95

PLAGIOCLASE

Sample	TU7															TU8	
Rock	ANDESITE lava flow															ANDESITE lava flow	
notes	plgf4c	plgf4r	plgmf3	plgmf4	plgml5	plgf5c	plgf5r	Line 1 plgmf6	Line 2 plgmf6	Line 3 plgmf6	Line 4 plgmf6	Line 5 plgmf6	Line 6 plgmf6	Line 7 plgmf6	Line 8 plgmf6	Line 1 plgf1	Line 2 plgf1
SiO$_2$	53.66	51.06	51.34	51.33	50.83	52.68	49.25	44.63	45.05	43.96	48.49	50.46	52.33	52.70	53.54	51.54	52.27
Al$_2$O$_3$	26.96	28.09	28.63	28.22	28.45	28.04	30.13	32.27	32.46	32.70	29.44	28.38	27.68	27.22	26.72	28.61	27.39
Fe$_2$O$_3$	0.91	0.96	0.88	0.96	0.95	0.86	0.77	0.72	0.75	0.78	0.65	0.75	0.93	0.91	1.00	0.89	0.78
CaO	11.24	12.29	12.82	12.87	12.93	12.02	14.39	17.91	18.06	18.16	14.54	13.03	12.46	11.63	11.10	12.93	12.06
Na$_2$O	4.65	3.97	3.76	3.77	3.80	4.17	3.22	1.06	1.08	1.15	2.99	3.42	3.84	4.47	4.80	3.88	4.37
K$_2$O	0.23	0.18	0.16	0.14	0.15	0.15	0.14	0.05	0.04	0.03	0.11	0.11	0.16	0.20	0.26	0.20	0.21
Tot.	97.65	96.55	97.58	97.29	97.12	97.93	97.89	96.65	97.43	96.77	96.23	96.14	97.40	97.14	97.41	98.05	97.09
Formula su 8 ossigeni																	
Si	2.49	2.40	2.39	2.40	2.38	2.44	2.30	2.13	2.14	2.10	2.30	2.38	2.44	2.46	2.49	2.391	2.443
Al	1.47	1.56	1.57	1.55	1.57	1.53	1.66	1.82	1.81	1.84	1.65	1.58	1.52	1.50	1.46	1.565	1.509
Fe	0.03	0.03	0.03	0.03	0.03	0.03	0.03	0.03	0.03	0.03	0.02	0.03	0.03	0.03	0.03	0.031	0.027
Ca	0.56	0.62	0.64	0.64	0.65	0.60	0.72	0.92	0.92	0.93	0.74	0.66	0.62	0.58	0.55	0.643	0.604
Na	0.42	0.36	0.34	0.34	0.35	0.37	0.29	0.10	0.10	0.11	0.28	0.31	0.35	0.40	0.43	0.349	0.396
K	0.01	0.01	0.01	0.01	0.01	0.01	0.01	0.00	0.00	0.00	0.01	0.01	0.01	0.01	0.02	0.012	0.013
Σ CATIONI (%)	4.98	4.99	4.98	4.98	4.99	4.97	5.01	5.00	5.00	5.01	5.00	4.97	4.97	4.99	4.99	4.99	4.99
An	56.41	62.42	64.73	64.80	64.65	60.86	70.57	90.04	90.00	89.57	72.35	67.39	63.57	58.27	55.24	64.04	59.65
Ab	42.20	36.47	34.31	34.34	34.43	38.26	28.61	9.67	9.74	10.27	26.97	31.96	35.47	40.52	43.25	34.76	39.11
Or	1.39	1.11	0.96	0.86	0.92	0.88	0.82	0.29	0.26	0.16	0.68	0.65	0.96	1.21	1.51	1.20	1.24
Tot.	100	100	100	100	100	100	100	100	100	100	100	100	100	100	100	100	100
Ca+Na+K	0.99	0.99	0.99	0.99	1.00	0.98	1.02	1.02	1.02	1.04	1.02	0.98	0.98	1.00	1.00	1.00	1.01
Si+Al	3.96	3.96	3.96	3.95	3.95	3.97	3.96	3.95	3.95	3.95	3.95	3.97	3.96	3.96	3.95	3.96	3.95

Sample	TU8															
Rock	ANDESITE lava flow															
notes	Line 3 plgf1	Line 4 plgf1	Line 5 plgf1	Line 6 plgf1	Line 7 plgf1	Line 8 plgf1	Line 9 plgf1	Line 1 plgf2	Line 2 plgf2	Line 3 plgf2	Line 4 plgf2	Line 5 plgf2	Line 6 plgf2	Line 7 plgf2	Line 8 plgf2	Line 9 plgf2
SiO_2	52.98	51.66	52.27	49.24	49.00	48.41	48.96	53.28	53.36	54.23	54.13	53.63	53.41	52.96	56.36	50.55
Al_2O_3	28.48	28.12	27.84	30.35	30.61	29.92	30.16	26.94	26.83	26.97	26.45	26.26	27.09	26.88	23.03	28.97
Fe_2O_3	0.94	0.84	0.74	0.62	0.73	0.64	0.58	0.65	0.73	0.70	0.77	0.58	0.81	0.75	1.66	0.73
CaO	11.65	12.36	11.94	14.95	15.03	14.80	14.69	11.01	11.14	10.73	10.59	10.43	11.24	10.91	9.19	13.90
Na_2O	4.61	4.10	4.39	2.99	2.95	2.96	2.82	4.73	4.69	4.84	5.09	4.79	4.85	4.50	4.61	3.34
K_2O	0.25	0.19	0.23	0.10	0.06	0.08	0.07	0.46	0.41	0.42	0.43	0.46	0.39	0.37	1.24	0.11
Tot.	98.92	97.27	97.41	98.25	98.38	96.81	97.27	97.06	97.16	97.89	97.45	96.15	97.78	96.37	96.09	97.61
Formula su 8 ossigeni																
Si	2.429	2.412	2.434	2.293	2.280	2.289	2.298	2.484	2.486	2.502	2.511	2.517	2.475	2.484	2.646	2.360
Al	1.539	1.548	1.528	1.666	1.679	1.667	1.669	1.481	1.473	1.467	1.447	1.453	1.480	1.486	1.275	1.595
Fe	0.033	0.029	0.026	0.022	0.026	0.023	0.021	0.023	0.026	0.024	0.027	0.020	0.028	0.027	0.058	0.026
Ca	0.572	0.619	0.596	0.746	0.749	0.750	0.739	0.550	0.556	0.531	0.526	0.525	0.558	0.548	0.462	0.695
Na	0.410	0.371	0.396	0.270	0.266	0.272	0.256	0.428	0.424	0.433	0.458	0.435	0.436	0.409	0.420	0.303
K	0.015	0.011	0.013	0.006	0.003	0.005	0.004	0.027	0.024	0.025	0.026	0.027	0.023	0.022	0.074	0.007
Σ CATIONI (%)	5.00	4.99	4.99	5.00	5.00	5.00	4.99	4.99	4.99	4.98	4.99	4.98	5.00	4.98	4.93	4.98
An	57.40	61.82	59.26	72.97	73.54	73.04	73.93	54.72	55.37	53.67	52.15	53.13	54.86	55.98	48.33	69.22
Ab	41.13	37.05	39.41	26.43	26.13	26.47	25.66	42.58	42.21	43.80	45.33	44.09	42.85	41.79	43.92	30.11
Or	1.47	1.13	1.33	0.60	0.33	0.49	0.40	2.70	2.42	2.52	2.53	2.78	2.29	2.24	7.76	0.68
Tot.	100	100	100	100	100	100	100	100	100	100	100	100	100	100	100	100
Ca+Na+K	1.00	1.00	1.01	1.02	1.02	1.03	1.00	1.00	1.00	0.99	1.01	0.99	1.02	0.98	0.96	1.00
Si+Al	3.97	3.96	3.96	3.96	3.96	3.96	3.97	3.96	3.96	3.97	3.96	3.97	3.96	3.97	3.92	3.95

PLAGIOCLASE

Sample	TU8											TU9								
Rock	ANDESITE lava flow											ANDESITE lava flow								
notes	Line 10 plgf2	plgf3c	plgf3r	plgf4c	plgf4r	plg5	plgmf1	plgmf2	plgmf3	plgml1	plgml2	plgf1c	plgf1r	plgmf1	plgf2c	plgf2r	Line 1 plgf3	Line 2 plgf3	Line 3 plgf3	Line 4 plgf3
SiO_2	50.10	50.63	49.84	47.05	50.17	51.06	48.73	49.27	50.14	49.10	50.93	53.59	54.29	46.42	49.61	56.65	54.21	53.63	53.43	54.09
Al_2O_3	29.50	29.19	29.59	31.83	29.93	28.20	30.77	30.19	29.32	30.09	29.82	29.03	27.62	33.79	31.34	25.69	27.93	28.15	27.98	28.07
Fe_2O_3	0.75	0.71	0.73	0.67	0.89	0.90	0.66	0.82	0.82	0.78	0.85	0.65	0.61	0.57	0.55	0.44	0.77	0.67	0.76	0.64
CaO	13.69	12.91	13.83	16.48	13.70	12.91	15.10	14.44	13.61	14.45	13.81	11.74	10.38	16.99	14.74	7.93	10.56	10.87	10.96	10.90
Na_2O	3.53	3.51	3.18	2.29	3.34	3.92	2.82	2.89	3.44	3.22	3.49	4.61	5.13	1.65	3.04	6.32	4.93	4.78	4.82	4.98
K_2O	0.10	0.14	0.11	0.11	0.17	0.13	0.09	0.13	0.11	0.12	0.18	0.43	0.54	0.04	0.15	0.76	0.43	0.46	0.40	0.44
Tot.	97.68	97.09	97.27	98.43	98.20	97.12	98.17	97.73	97.43	97.77	99.07	100.05	98.56	99.45	99.43	97.79	98.83	98.55	98.34	99.12
Formula su 8 ossigeni																				
Si	2.339	2.369	2.334	2.200	2.329	2.393	2.272	2.302	2.345	2.297	2.344	2.428	2.488	2.146	2.280	2.600	2.478	2.461	2.458	2.468
Al	1.624	1.610	1.634	1.755	1.638	1.558	1.691	1.663	1.617	1.660	1.618	1.551	1.492	1.842	1.698	1.390	1.505	1.522	1.518	1.510
Fe	0.027	0.025	0.026	0.024	0.031	0.032	0.023	0.029	0.029	0.028	0.029	0.022	0.021	0.020	0.019	0.015	0.027	0.023	0.026	0.022
Ca	0.685	0.647	0.694	0.826	0.682	0.648	0.754	0.723	0.682	0.724	0.681	0.570	0.510	0.841	0.725	0.390	0.517	0.534	0.540	0.533
Na	0.320	0.319	0.289	0.207	0.301	0.356	0.255	0.262	0.312	0.292	0.311	0.405	0.456	0.148	0.271	0.562	0.437	0.425	0.430	0.440
K	0.006	0.008	0.006	0.006	0.010	0.008	0.005	0.008	0.007	0.007	0.011	0.025	0.031	0.003	0.009	0.045	0.025	0.027	0.024	0.026
Σ CATION	5.00	4.98	4.98	5.02	4.99	4.99	5.00	4.99	4.99	5.01	4.99									
An	67.75	66.42	70.14	79.45	68.69	64.06	74.33	72.87	68.17	70.73	67.91	57.01	51.12	84.84	72.17	39.13	52.83	54.16	54.36	53.36
Ab	31.65	32.73	29.20	19.93	30.32	35.16	25.14	26.37	31.16	28.55	31.03	40.49	45.73	14.91	26.97	56.39	44.60	43.13	43.27	44.09
Or	0.60	0.85	0.65	0.62	0.99	0.78	0.53	0.76	0.67	0.72	1.06	2.50	3.14	0.26	0.86	4.48	2.57	2.71	2.37	2.56
Tot.	100	100	100	100	100	100	100	100	100	100	100	100	100	100	100	100	100	100	100	100
Ca+Na+K	1.01	0.97	0.99	1.04	0.99	1.01	1.01	0.99	1.00	1.02	1.00	1.00	1.00	0.99	1.01	1.00	0.98	0.99	0.99	1.00
Si+Al	3.96	3.98	3.97	3.95	3.97	3.95	3.96	3.97	3.96	3.96	3.96	3.98	3.98	3.99	3.98	3.99	3.98	3.98	3.98	3.98

Sample	TU9																
Rock	ANDESITE lava flow																
notes	Line 5 plgf3	Line 6 plgf3	Line 7 plgf3	Line 8 plgf3	Line 9 plgf3	Line 10 plgf3	Line 11 plgf3	Line 12 plgf3	Line 13 plgf3	Line 14 plgf3	plgf4c	plgf4r	plgf5cinch	plgf5rinch	plgmf1inch	plgf6c	plgf6r
SiO_2	53.60	55.35	54.36	54.52	55.27	53.86	53.30	53.86	51.54	54.33	50.81	56.13	56.63	59.10	53.76	47.40	47.34
Al_2O_3	27.77	27.63	27.54	27.40	27.60	28.12	28.13	28.25	25.61	27.80	30.11	26.45	26.01	24.31	28.00	33.30	32.80
Fe_2O_3	0.67	0.76	0.63	0.80	0.66	0.65	0.63	0.60	0.42	0.53	0.84	0.70	0.50	0.52	0.49	0.62	0.81
CaO	10.83	10.21	9.98	10.38	10.32	10.61	11.14	10.60	9.10	10.08	13.61	9.07	8.18	6.29	11.00	16.63	16.15
Na_2O	4.83	5.19	5.17	5.08	4.91	4.93	4.86	4.92	4.93	5.25	3.12	5.78	5.90	6.70	4.85	2.04	2.13
K_2O	0.45	0.50	0.46	0.52	0.42	0.46	0.38	0.38	0.45	0.44	0.46	0.67	0.67	1.03	0.40	0.07	0.11
Tot.	98.15	99.64	98.13	98.69	99.17	98.63	98.43	98.61	92.05	98.43	98.95	98.80	97.89	97.96	98.49	100.07	99.32
Formula su 8 ossigeni																	
Si	2.469	2.506	2.497	2.496	2.510	2.468	2.451	2.466	2.520	2.490	2.340	2.558	2.593	2.691	2.467	2.176	2.189
Al	1.508	1.475	1.492	1.478	1.477	1.519	1.525	1.525	1.476	1.502	1.635	1.421	1.404	1.305	1.515	1.802	1.788
Fe	0.023	0.026	0.022	0.027	0.023	0.022	0.022	0.021	0.015	0.018	0.029	0.024	0.017	0.018	0.017	0.022	0.028
Ca	0.534	0.495	0.491	0.509	0.502	0.521	0.549	0.520	0.477	0.495	0.671	0.443	0.401	0.307	0.541	0.818	0.800
Na	0.431	0.456	0.460	0.451	0.432	0.438	0.433	0.437	0.467	0.467	0.279	0.511	0.523	0.591	0.432	0.182	0.191
K	0.027	0.029	0.027	0.031	0.024	0.027	0.022	0.022	0.028	0.026	0.027	0.039	0.039	0.060	0.023	0.004	0.006
Σ CATIONI (%)																	
An	53.87	50.55	50.22	51.39	52.40	52.84	54.66	53.10	49.03	50.13	68.68	44.62	41.63	32.06	54.32	81.49	80.26
Ab	43.45	46.53	47.04	45.53	45.09	44.42	43.15	44.61	48.07	47.27	28.53	51.49	54.30	61.71	43.34	18.11	19.12
Or	2.68	2.92	2.73	3.08	2.51	2.74	2.19	2.29	2.89	2.60	2.79	3.90	4.07	6.23	2.34	0.40	0.62
Tot.	100	100	100	100	100	100	100	100	100	100	100	100	100	100	100	100	100
Ca+Na+K	0.99	0.98	0.98	0.99	0.96	0.99	1.00	0.98	0.97	0.99	0.98	0.99	0.96	0.96	1.00	1.00	1.00
Si+Al	3.98	3.98	3.99	3.97	3.99	3.99	3.98	3.99	4.00	3.99	3.97	3.98	4.00	4.00	3.98	3.98	3.98

Sample								TU10a								
Rock								ANDESITE lava flow								
notes	Line 1 plgf1	Line 2 plgf1	Line 3 plgf1	Line 4 plgf1	Line 5 plgf1	Line 6 plgf1	Line 7 plgf1	Line 8 plgf1	Line 1 plgf2	Line 2 plgf2	Line 3 plgf2	Line 4 plgf2	Line 5 plgf2	Line 6 plgf2	Line 7 plgf2	Line 8 plgf2
SiO_2	51.28	54.44	55.30	53.96	54.12	54.23	54.58	49.68	45.91	46.47	45.58	45.65	45.43	49.45	52.57	52.95
Al_2O_3	30.13	27.90	27.61	28.43	28.01	28.39	27.29	31.15	33.76	34.11	34.10	33.17	33.55	30.52	28.78	28.40
Fe_2O_3	0.47	0.50	0.47	0.48	0.58	0.52	0.68	0.79	0.61	0.59	0.67	0.70	0.78	0.72	0.68	0.79
CaO	13.19	10.54	10.51	11.40	10.69	10.79	10.10	14.20	17.28	17.33	17.59	17.30	17.77	14.25	11.48	11.26
Na_2O	3.59	4.85	5.06	4.51	4.95	4.88	5.09	3.00	1.47	1.43	1.44	1.46	1.28	3.21	4.47	4.53
K_2O	0.24	0.50	0.47	0.42	0.45	0.43	0.51	0.23	0.04	0.05	0.08	0.05	0.06	0.22	0.39	0.42
Tot.	98.87	98.73	99.42	99.21	98.79	99.26	98.24	99.04	99.06	99.98	99.47	98.32	98.88	98.37	98.37	98.34
Formula su 8 ossigeni																
Si	2.356	2.487	2.508	2.458	2.475	2.467	2.506	2.289	2.133	2.138	2.114	2.139	2.120	2.297	2.421	2.438
Al	1.632	1.503	1.476	1.527	1.510	1.523	1.477	1.692	1.850	1.850	1.864	1.832	1.846	1.672	1.563	1.542
Fe	0.016	0.017	0.016	0.017	0.020	0.018	0.023	0.027	0.021	0.020	0.024	0.025	0.028	0.025	0.024	0.027
Ca	0.649	0.516	0.511	0.557	0.524	0.526	0.497	0.701	0.860	0.854	0.874	0.868	0.889	0.709	0.567	0.556
Na	0.319	0.430	0.445	0.398	0.439	0.431	0.453	0.268	0.132	0.127	0.129	0.132	0.116	0.289	0.400	0.404
K	0.014	0.029	0.027	0.024	0.026	0.025	0.030	0.013	0.002	0.003	0.005	0.003	0.004	0.013	0.023	0.025
Σ CATIONI (%)																
An	66.09	52.93	52.00	56.84	52.99	53.57	50.71	71.37	86.49	86.76	86.71	86.52	88.16	70.12	57.29	56.44
Ab	32.51	44.09	45.26	40.66	44.37	43.87	46.27	27.26	13.29	12.92	12.81	13.17	11.47	28.60	40.40	41.06
Or	1.40	2.98	2.74	2.50	2.63	2.56	3.02	1.37	0.22	0.32	0.49	0.30	0.37	1.28	2.31	2.50
Tot.	100	100	100	100	100	100	100	100	100	100	100	100	100	100	100	100
Ca+Na+K	0.98	0.97	0.98	0.98	0.99	0.98	0.98	0.98	0.99	0.98	1.01	1.00	1.01	1.01	0.99	0.98
Si+Al	3.99	3.99	3.98	3.99	3.98	3.99	3.98	3.98	3.98	3.99	3.98	3.97	3.97	3.97	3.98	3.98

PLAGIOCLASE

Sample								TU10a									
Rock								ANDESITE lava flow									
notes	plgml1	Line 1 plgf3	Line 2 plgf3	Line 3 plgf3	Line 4 plgf3	Line 5 plgf3	Line 6 plgf3	Line 7 plgf3	Line 8 plgf3	Line 9 plgf3	Line 10 plgf3	plgmf1	Line 1 plgf4	Line 2 plgf4	Line 3 plgf4	Line 4 plgf4	Line 5 plgf4
SiO_2	49.43	51.99	48.77	45.41	54.24	54.84	53.28	53.39	53.44	52.90	53.41	45.59	54.81	53.73	54.48	55.39	53.24
Al_2O_3	30.97	29.64	31.74	33.62	27.95	27.40	29.07	28.31	28.18	27.68	29.01	34.47	27.90	29.03	27.05	27.41	28.79
Fe_2O_3	0.87	0.70	0.59	0.71	0.62	0.55	0.67	0.69	0.65	0.60	0.71	0.55	0.63	0.60	0.53	0.50	0.63
CaO	14.10	12.68	15.29	17.04	11.20	9.60	12.01	11.33	10.89	10.80	11.53	17.94	10.39	11.72	10.45	10.19	11.58
Na_2O	3.20	4.10	2.67	1.29	4.57	5.54	4.30	4.62	4.43	4.74	4.28	1.25	5.17	4.33	5.13	5.01	4.49
K_2O	0.24	0.38	0.21	0.06	0.38	0.49	0.34	0.42	0.43	0.36	0.38	0.05	0.45	0.37	0.49	0.55	0.36
Tot.	98.80	99.49	99.26	98.14	98.96	98.43	99.66	98.75	98.01	97.08	99.31	99.85	99.36	99.77	98.14	99.05	99.08
Formula su 8 ossigeni																	
Si	2.286	2.377	2.249	2.129	2.476	2.511	2.422	2.448	2.462	2.463	2.432	2.105	2.490	2.436	2.507	2.519	2.433
Al	1.689	1.597	1.726	1.859	1.504	1.479	1.558	1.530	1.530	1.520	1.557	1.877	1.494	1.552	1.467	1.469	1.551
Fe	0.030	0.024	0.020	0.025	0.021	0.019	0.023	0.024	0.022	0.021	0.024	0.019	0.022	0.021	0.018	0.017	0.022
Ca	0.699	0.621	0.756	0.856	0.548	0.471	0.585	0.557	0.537	0.539	0.563	0.888	0.506	0.569	0.515	0.497	0.567
Na	0.287	0.364	0.239	0.117	0.404	0.492	0.379	0.410	0.396	0.428	0.378	0.112	0.456	0.380	0.457	0.442	0.398
K	0.014	0.022	0.012	0.004	0.022	0.029	0.019	0.024	0.025	0.021	0.022	0.003	0.026	0.022	0.029	0.032	0.021
Σ CATIONI (%)																	
An	69.88	61.68	75.04	87.63	56.21	47.48	59.47	56.14	56.06	54.52	58.48	88.54	51.21	58.61	51.44	51.18	57.50
Ab	28.70	36.13	23.72	11.99	41.49	49.61	38.55	41.40	41.31	43.32	39.24	11.15	46.13	39.17	45.67	45.56	40.37
Or	1.42	2.19	1.24	0.38	2.29	2.90	1.98	2.47	2.63	2.16	2.28	0.31	2.66	2.22	2.88	3.26	2.13
Tot.	100	100	100	100	100	100	100	100	100	100	100	100	100	100	100	100	100
Ca+Na+K	1.00	1.01	1.01	0.98	0.97	0.99	0.98	0.99	0.96	0.99	0.96	1.00	0.99	0.97	1.00	0.97	0.99
Si+Al	3.97	3.97	3.98	3.99	3.98	3.99	3.98	3.98	3.99	3.98	3.99	3.98	3.98	3.99	3.97	3.99	3.98

PLAGIOCLASE

Sample	TU10a							TU15							
Rock	ANDESITE lava flow							DACITE lava flow							
notes	Line 6 plgf4	Line 7 plgf4	Line 8 plgf4	Line 9 plgf4	Line 10 plgf4	plgmf2	plgmf3	Pl1c	Pl1r	Pl2c	Pl2r	Pl3c	Pl3r	Pl4c	Pl4r
SiO_2	53.77	54.66	53.45	51.62	48.92	49.46	52.99	54.80	55.52	54.29	56.64	57.47	56.85	53.56	54.06
Al_2O_3	27.82	27.34	28.30	30.31	31.52	31.22	28.82	28.38	27.96	28.16	26.85	26.04	26.80	27.30	29.28
Fe_2O_3	0.58	0.58	0.63	0.69	0.78	0.91	0.84	0.65	0.57	0.57	0.66	0.57	0.59	0.71	0.54
CaO	10.15	10.35	11.04	12.62	14.39	14.22	11.28	10.72	10.41	10.27	9.02	8.17	9.07	10.67	11.30
Na_2O	4.95	5.15	4.72	3.96	2.91	3.01	4.56	4.92	5.10	4.88	5.71	5.87	5.70	5.05	4.57
K_2O	0.47	0.55	0.40	0.36	0.21	0.22	0.41	0.61	0.41	0.45	0.58	0.59	0.57	0.43	0.37
Tot.	97.74	98.63	98.53	99.56	98.74	99.03	98.88	100.08	99.95	98.61	99.46	98.72	99.58	97.72	100.11
Formula su 8 ossigeni															
Si	2.481	2.502	2.453	2.357	2.264	2.281	2.427	2.475	2.503	2.481	2.559	2.605	2.564	2.480	2.439
Al	1.513	1.476	1.531	1.632	1.720	1.698	1.556	1.511	1.486	1.518	1.430	1.392	1.425	1.490	1.558
Fe	0.020	0.020	0.022	0.024	0.027	0.031	0.029	0.022	0.019	0.020	0.022	0.020	0.020	0.025	0.018
Ca	0.502	0.508	0.543	0.618	0.714	0.703	0.554	0.519	0.503	0.503	0.437	0.397	0.438	0.529	0.546
Na	0.443	0.457	0.420	0.351	0.261	0.269	0.405	0.431	0.445	0.433	0.501	0.516	0.499	0.453	0.400
K	0.028	0.032	0.024	0.021	0.012	0.013	0.024	0.035	0.023	0.026	0.033	0.034	0.033	0.025	0.021
Σ CATIONI (%)															
An	51.57	50.92	55.05	62.44	72.30	71.38	56.35	52.66	51.74	52.29	45.00	41.90	45.20	52.52	56.46
Ab	45.57	45.89	42.55	35.44	26.47	27.32	41.19	43.77	45.85	45.01	51.58	54.49	51.42	44.97	41.36
Or	2.85	3.19	2.40	2.12	1.23	1.30	2.46	3.57	2.40	2.70	3.42	3.61	3.38	2.51	2.18
Tot.	100	100	100	100	100	100	100	100	100	100	100	100	100	100	100
Ca+Na+K	0.97	1.00	0.99	0.99	0.99	0.98	0.98	0.98	0.97	0.96	0.97	0.95	0.97	1.01	0.97
Si+Al	3.99	3.98	3.98	3.99	3.98	3.98	3.98	3.99	3.99	4.00	3.99	4.00	3.99	3.97	4.00

Sample													TU3/1							
Rock													ANDESITE lava flow							
notes	pxf1c	pxf1r	pxmf1	pxmf2	pxmf3	pxmf4	pxml1	pxml2	pxml3	pxf2c	pxf2r	pxmf5	pxmf6c	pxmf6int	pxmf6r	pxml4	pxml5	pxml6	pxml7	Line 1 pxf3
SiO_2	52.50	50.60	53.96	49.38	53.84	49.91	50.98	53.44	53.98	52.02	50.21	53.50	53.10	51.63	50.33	52.92	50.34	53.25	53.83	50.63
TiO_2	0.33	0.66	0.26	0.61	0.36	0.59	0.67	0.34	0.37	0.21	0.67	0.32	0.32	0.35	0.75	0.33	0.73	0.29	0.22	0.62
Al_2O_3	2.10	2.47	2.04	3.85	1.37	3.11	3.40	1.57	1.59	1.98	3.20	2.04	1.98	2.00	2.25	2.23	2.46	1.34	1.25	2.75
FeOt	6.82	10.83	13.94	6.82	13.38	8.27	8.36	13.51	13.80	5.78	8.78	12.75	14.24	7.40	9.46	13.79	9.09	15.72	14.73	7.14
MnO	0.26	0.31	0.33	0.22	0.31	0.21	0.25	0.36	0.32	0.16	0.23	0.36	0.33	0.28	0.28	0.36	0.29	0.34	0.39	0.27
MgO	17.90	15.78	28.22	15.36	29.10	16.42	15.85	28.09	28.50	17.44	16.00	29.06	28.53	17.02	15.57	28.02	15.52	27.07	28.59	15.77
CaO	19.94	18.13	2.31	21.33	1.60	19.69	19.94	2.30	1.96	21.27	20.41	1.61	1.76	20.22	19.88	1.84	19.64	1.79	1.84	21.51
Na_2O	0.20	0.33	0.06	0.28	0.03	0.29	0.40	0.03	0.04	0.29	0.34	0.02	0.05	0.22	0.43	0.04	0.30	0.03	0.05	0.29
K_2O	0.00	0.03	0.01	0.00	0.02	0.00	0.02	0.02	0.00	0.00	0.02	0.00	0.01	0.02	0.00	0.00	0.02	0.02	0.02	0.00
Cr_2O_3	0.16	0.02	0.05	0.22	0.02	0.00	0.01	0.07	0.03	0.21	0.00	0.00	0.00	0.02	0.00	0.04	0.02	0.00	0.00	0.11
TOTAL	100.21	99.16	101.17	98.06	100.02	98.49	99.88	99.74	100.58	99.36	99.86	99.67	100.32	99.14	98.95	99.58	98.41	99.85	100.91	99.07

Formula: 4 cationi, 6 Ox

Si	1.914	1.892	1.907	1.851	1.917	1.861	1.880	1.915	1.917	1.909	1.852	1.907	1.890	1.909	1.881	1.898	1.892	1.921	1.908	1.880
Ti	0.009	0.018	0.007	0.017	0.010	0.017	0.019	0.009	0.010	0.006	0.019	0.009	0.009	0.010	0.021	0.009	0.021	0.008	0.006	0.017
Al IV	0.086	0.108	0.093	0.149	0.083	0.139	0.120	0.085	0.083	0.091	0.148	0.093	0.110	0.091	0.119	0.102	0.108	0.079	0.092	0.120
Al VI	0.004	0.001	-0.008	0.021	-0.026	-0.002	0.028	-0.019	-0.016	-0.005	-0.008	-0.007	-0.027	-0.003	-0.020	-0.007	0.001	-0.021	-0.040	0.000
Fe3+	0.073	0.095	0.092	0.109	0.092	0.128	0.084	0.087	0.082	0.100	0.145	0.084	0.124	0.090	0.128	0.093	0.088	0.087	0.124	0.103
Fe2+	0.135	0.244	0.320	0.105	0.306	0.129	0.173	0.318	0.328	0.078	0.126	0.296	0.300	0.139	0.168	0.321	0.198	0.387	0.313	0.119
Mn	0.008	0.010	0.010	0.007	0.009	0.007	0.008	0.011	0.010	0.005	0.007	0.011	0.010	0.009	0.009	0.011	0.009	0.010	0.012	0.008
Mg	0.973	0.880	1.487	0.858	1.545	0.913	0.871	1.500	1.509	0.954	0.880	1.545	1.514	0.938	0.868	1.499	0.870	1.457	1.511	0.873
Ca	0.779	0.726	0.087	0.856	0.061	0.787	0.788	0.088	0.074	0.836	0.807	0.062	0.067	0.801	0.796	0.071	0.791	0.069	0.070	0.856
Na	0.014	0.024	0.004	0.021	0.002	0.021	0.028	0.002	0.003	0.021	0.024	0.001	0.003	0.015	0.031	0.003	0.021	0.002	0.004	0.021
K	0.000	0.001	0.000	0.000	0.001	0.000	0.001	0.001	0.000	0.000	0.001	0.000	0.000	0.001	0.000	0.000	0.001	0.001	0.001	0.000
Cr	0.005	0.001	0.001	0.006	0.000	0.000	0.000	0.002	0.001	0.006	0.000	0.000	0.000	0.001	0.000	0.001	0.001	0.000	0.000	0.003
Tot. Extra Quad.	4.00	4.00	4.00	4.00	4.00	4.00	4.00	4.00	4.00	4.00	4.00	4.00	4.00	4.00	4.00	4.00	4.00	4.00	4.00	4.00
Wo%	39.75	37.34	4.40	44.41	3.05	40.19	41.09	4.43	3.73	42.51	41.22	3.10	3.35	40.71	40.62	3.57	40.63	3.46	3.46	43.88
En%	49.64	45.25	74.86	44.50	77.07	46.65	45.46	75.27	75.71	48.48	44.95	77.77	75.52	47.66	44.29	75.57	44.69	72.82	74.90	44.76
Fs%	10.61	17.41	20.74	11.09	19.88	13.17	13.45	20.30	20.56	9.01	13.83	19.13	21.14	11.63	15.09	20.86	14.68	23.72	21.64	11.36
Tot. Quad.	100.00	100.00	100.00	100.00	100.00	100.00	100.00	100.00	100.00	100.00	100.00	100.00	100.00	100.00	100.00	100.00	100.00	100.00	100.00	100.00

PYROXENES

Sample							TU3/1										
Rock							ANDESITE lava flow										
notes	Line 2 pxf3	Line 3 pxf3	Line 4 pxf3	Line 5 pxf3	Line 6 pxf3	Line 7 pxf3	Line 8 pxf3	Line 9 pxf3	Line 10 pxf3	pxmf7c	pxmf7r	pxmf8	pxf4c	pxf4r	pxf5	Line 1 pxf5	Line 2 pxf5
SiO_2	50.86	50.23	50.83	51.20	51.49	50.99	50.99	52.10	51.97	52.40	52.19	54.21	51.33	50.90	49.96	52.26	51.27
TiO_2	0.40	0.48	0.73	0.29	0.36	0.35	0.38	0.31	0.37	0.28	0.58	0.31	0.60	0.44	0.73	0.29	0.27
Al_2O_3	2.44	3.24	4.15	2.52	2.45	2.69	2.45	2.33	2.11	1.75	1.85	1.21	2.76	1.45	4.34	2.06	2.68
FeOt	6.79	6.73	7.08	6.55	6.34	6.32	6.53	7.12	7.77	7.25	9.88	13.05	8.07	9.04	6.80	5.71	5.53
MnO	0.22	0.10	0.16	0.17	0.17	0.20	0.19	0.21	0.30	0.27	0.39	0.41	0.20	0.31	0.21	0.25	0.27
MgO	16.20	16.85	15.79	17.32	17.45	17.07	17.36	17.69	17.74	18.30	15.80	28.22	16.02	16.90	15.88	17.54	17.00
CaO	21.14	20.89	20.96	20.14	20.14	20.33	19.90	19.26	19.34	18.32	19.54	1.78	20.55	18.95	21.13	21.67	20.81
Na_2O	0.25	0.25	0.22	0.19	0.26	0.25	0.30	0.28	0.28	0.21	0.34	0.06	0.37	0.30	0.28	0.23	0.20
K_2O	0.01	0.01	0.02	0.00	0.00	0.00	0.01	0.03	0.01	0.02	0.05	0.01	0.01	0.00	0.00	0.00	0.00
Cr_2O_3	0.13	0.23	0.30	0.18	0.18	0.18	0.18	0.06	0.00	0.10	0.00	0.00	0.16	0.03	0.33	0.27	0.21
TOTAL	98.44	99.01	100.22	98.56	98.85	98.38	98.30	99.40	99.89	98.90	100.62	99.25	100.05	98.32	99.66	100.28	98.24
Formula: 4 cationi, 6 Ox																	
Si	1.896	1.855	1.865	1.898	1.901	1.893	1.893	1.914	1.903	1.934	1.922	1.949	1.889	1.905	1.840	1.902	1.904
Ti	0.011	0.013	0.020	0.008	0.010	0.010	0.011	0.008	0.010	0.008	0.016	0.008	0.016	0.012	0.020	0.008	0.008
Al IV	0.104	0.145	0.135	0.102	0.099	0.107	0.107	0.086	0.097	0.066	0.078	0.051	0.111	0.095	0.160	0.098	0.096
Al VI	0.003	-0.004	0.045	0.007	0.008	0.011	0.001	0.015	-0.006	0.010	0.002	0.001	0.009	-0.031	0.028	-0.010	0.022
Fe3+	0.094	0.133	0.057	0.087	0.085	0.089	0.102	0.074	0.102	0.054	0.071	0.038	0.091	0.122	0.101	0.101	0.067
Fe2+	0.118	0.075	0.160	0.116	0.111	0.107	0.101	0.145	0.136	0.170	0.233	0.354	0.157	0.160	0.108	0.072	0.105
Mn	0.007	0.003	0.005	0.005	0.005	0.006	0.006	0.007	0.009	0.009	0.012	0.012	0.006	0.010	0.007	0.008	0.008
Mg	0.900	0.928	0.864	0.957	0.961	0.945	0.961	0.969	0.969	1.007	0.868	1.513	0.879	0.943	0.872	0.952	0.941
Ca	0.844	0.827	0.824	0.800	0.797	0.809	0.792	0.758	0.759	0.724	0.771	0.068	0.810	0.760	0.834	0.845	0.828
Na	0.018	0.018	0.016	0.013	0.019	0.018	0.021	0.020	0.020	0.015	0.024	0.004	0.026	0.022	0.020	0.016	0.015
K	0.000	0.000	0.001	0.000	0.000	0.000	0.001	0.001	0.000	0.001	0.002	0.001	0.000	0.000	0.000	0.000	0.000
Cr	0.004	0.007	0.009	0.005	0.005	0.005	0.005	0.002	0.000	0.003	0.000	0.000	0.005	0.001	0.010	0.008	0.006
Tot. Extra Quad.	4.00	4.00	4.00	4.00	4.00	4.00	4.00	4.00	4.00	4.00	4.00	4.00	4.00	4.00	4.00	4.00	4.00
Wo%	43.16	42.12	43.25	40.81	40.79	41.47	40.48	38.96	38.60	37.04	39.69	3.47	41.83	38.27	43.54	42.89	42.66
En%	46.02	47.28	45.35	48.83	49.19	48.46	49.15	49.80	49.29	51.51	44.66	76.66	45.36	47.49	45.52	48.30	48.48
Fs%	10.81	10.60	11.40	10.36	10.03	10.07	10.37	11.24	12.11	11.45	15.65	19.88	12.82	14.24	10.94	8.81	8.85
Tot. Quad.	100.00	100.00	100.00	100.00	100.00	100.00	100.00	100.00	100.00	100.00	100.00	100.00	100.00	100.00	100.00	100.00	100.00

Sample	TU3/1											TU4						
Rock	ANDESITE lava flow											DACITE lava flow						
notes	Line 3 pxf5	Line 4 pxf5	Line 5 pxf5	Line 6 pxf5	Line 7 pxf5	Line 8 pxf5	Line 9 pxf5	Line 10 pxf5	pxf6	pxf7	pxf8	mphPx2	mphPx3	mphPx6	px1c	px1r	Px4c	Px4r
SiO$_2$	52.47	52.11	51.77	52.89	52.54	51.53	49.62	49.93	39.01	50.41	39.59	47.38	50.73	51.98	51.78	50.83	54.42	49.57
TiO$_2$	0.24	0.30	0.35	0.23	0.33	0.39	0.63	0.74	0.01	0.53	0.03	1.98	0.74	0.64	0.87	0.68	0.31	0.41
Al$_2$O$_3$	2.02	1.96	2.10	2.14	2.02	2.44	4.51	3.46	0.04	4.19	0.02	5.56	2.72	1.82	2.23	1.94	0.78	1.09
FeOt	5.84	5.76	6.20	6.20	6.08	6.20	7.10	8.54	16.89	6.12	16.58	7.88	6.78	8.07	7.58	8.14	15.99	16.20
MnO	0.20	0.14	0.19	0.16	0.09	0.19	0.17	0.18	0.25	0.18	0.23	0.21	0.22	0.31	0.19	0.19	0.44	0.48
MgO	17.40	17.38	17.56	17.31	17.21	16.67	15.26	15.33	44.26	15.77	44.38	14.05	16.25	16.12	16.93	15.78	26.95	26.61
CaO	21.42	20.54	21.21	21.24	20.80	20.85	21.51	20.47	0.12	21.97	0.22	21.33	21.25	20.20	19.75	20.83	1.54	1.43
Na$_2$O	0.26	0.22	0.19	0.27	0.21	0.23	0.33	0.37	0.02	0.29	0.06	0.39	0.23	0.36	0.23	0.30	0.04	0.04
K$_2$O	0.02	0.00	0.00	0.00	0.00	0.00	0.02	0.00	0.00	0.00	0.04	0.02	0.00	0.00	0.01	0.03	0.01	0.03
Cr$_2$O$_3$	0.29	0.20	0.17	0.23	0.21	0.11	0.21	0.00	0.00	0.55	0.00							
TOTAL	100.15	98.62	99.73	100.66	99.49	98.60	99.36	99.02	100.59	100.01	101.15	98.79	98.92	99.50	99.58	98.72	100.47	95.87
Formula: 4 cationi, 6 Ox																		
Si	1.913	1.928	1.895	1.920	1.931	1.913	1.836	1.860	1.305	1.849	1.317	1.775	1.883	1.925	1.910	1.899	1.957	1.863
Ti	0.007	0.008	0.010	0.006	0.009	0.011	0.018	0.021	0.000	0.015	0.001	0.056	0.021	0.018	0.024	0.019	0.008	0.012
Al IV	0.087	0.072	0.105	0.080	0.069	0.087	0.164	0.140	0.695	0.151	0.683	0.225	0.117	0.075	0.090	0.101	0.043	0.137
Al VI	0.000	0.014	-0.014	0.012	0.018	0.020	0.032	0.012	-0.693	0.030	-0.682	0.021	0.002	0.005	0.007	-0.016	-0.010	-0.089
Fe3+	0.085	0.051	0.108	0.068	0.042	0.058	0.115	0.112	1.389	0.097	1.369	0.121	0.091	0.060	0.052	0.102	0.040	0.207
Fe2+	0.093	0.127	0.082	0.120	0.145	0.134	0.104	0.154	-0.917	0.090	-0.908	0.125	0.120	0.190	0.181	0.152	0.441	0.302
Mn	0.006	0.004	0.006	0.005	0.003	0.006	0.005	0.006	0.007	0.006	0.007	0.007	0.007	0.010	0.006	0.006	0.013	0.015
Mg	0.946	0.959	0.959	0.937	0.943	0.923	0.842	0.852	2.208	0.862	2.201	0.785	0.899	0.890	0.931	0.879	1.445	1.491
Ca	0.837	0.815	0.832	0.826	0.819	0.829	0.852	0.817	0.004	0.863	0.008	0.856	0.845	0.802	0.780	0.834	0.059	0.057
Na	0.018	0.016	0.013	0.019	0.015	0.016	0.024	0.026	0.001	0.021	0.004	0.028	0.016	0.026	0.017	0.022	0.003	0.003
K	0.001	0.000	0.000	0.000	0.000	0.000	0.001	0.000	0.000	0.000	0.001	0.001	0.000	0.000	0.001	0.002	0.000	0.002
Cr	0.008	0.006	0.005	0.007	0.006	0.003	0.006	0.000	0.000	0.016	0.000	0.000	0.000	0.000	0.000	0.000	0.000	0.000
Tot. Extra Quad.	4.00	4.00	4.00	4.00	4.00	4.00	4.00	4.00	4.00	4.00	4.00	4.00	4.00	4.00	4.00	4.00	4.00	4.00
Wo%	42.68	41.73	42.01	42.34	42.03	42.65	44.54	42.22	0.15	45.13	0.29	45.35	43.22	41.28	40.11	42.40	2.98	2.79
En%	48.25	49.13	48.41	48.02	48.38	47.45	43.98	44.02	82.25	45.06	82.43	41.57	46.01	45.85	47.86	44.67	72.80	72.46
Fs%	9.07	9.14	9.58	9.64	9.59	9.90	11.48	13.76	17.60	9.80	17.28	13.08	10.77	12.88	12.02	12.93	24.22	24.75
Tot. Quad.	100.00	100.00	100.00	100.00	100.00	100.00	100.00	100.00	100.00	100.00	100.00	100.00	100.00	100.00	100.00	100.00	100.00	100.00

PYROXENES

Sample	TU4															TU5				
Rock	DACITE lava flow															BASALT-ANDESITE bomb				
notes	Px5c	Px5r	Px7c	Px7r	Px8	mphOl8	opx1	opx2	opx3	opx4c	opx4r	opx5	opx6	opx7	opx9	opxf1	pxf2	pxf3	pxf4	pxf5c
SiO_2	52.17	52.19	53.44	50.17	53.10	55.22	54.54	54.75	53.32	54.68	54.25	53.86	54.48	53.78	54.68	50.19	50.24	49.72	49.59	49.15
TiO_2	0.50	0.58	0.42	1.22	0.32	0.36	0.35	0.30	0.43	0.38	0.34	0.28	0.18	0.34	0.35	0.56	0.85	0.76	0.89	0.81
Al_2O_3	1.36	1.29	1.23	2.90	1.12	0.74	1.90	0.62	0.76	0.56	0.97	0.89	0.56	1.00	0.95	2.28	2.44	2.32	2.52	3.23
FeOt	7.67	8.82	8.64	7.42	17.13	16.24	15.81	17.29	16.97	16.83	15.88	17.78	17.12	17.74	16.63	7.27	8.16	8.26	7.76	7.35
MnO	0.22	0.44	0.36	0.25	0.45	0.53	0.52	0.68	0.73	0.58	0.42	0.67	0.66	0.54	0.50	0.18	0.16	0.27	0.27	0.22
MgO	16.09	15.74	15.41	15.84	26.75	27.34	27.50	26.34	26.68	26.24	27.89	25.95	26.84	25.94	26.44	15.22	15.06	14.86	15.09	14.81
CaO	20.84	20.68	20.61	20.89	1.66	1.38	1.45	1.61	1.37	1.30	1.39	1.44	1.24	1.29	1.55	21.04	19.88	20.12	20.07	20.18
Na_2O	0.36	0.42	0.33	0.33	0.01	0.03	0.02	0.00	0.00	0.03	0.01	0.05	0.03	0.02	0.02	0.27	0.36	0.34	0.38	0.34
K_2O	0.03	0.00	0.00	0.01	0.00	0.01	0.01	0.00	0.00	0.01	0.01	0.01	0.00	0.00	0.01	0.01	0.02	0.01	0.01	0.00
Cr_2O_3																0.03	0.01	0.04	0.10	0.02
TOTAL	99.22	100.14	100.44	99.03	100.54	101.85	102.09	101.59	100.25	100.61	101.16	100.91	101.10	100.65	101.13	97.06	97.18	96.70	96.68	96.10
Formula: 4 cationi, 6 Ox																				
Si	1.936	1.927	1.971	1.865	1.913	1.960	1.925	1.960	1.928	1.974	1.931	1.943	1.953	1.945	1.961	1.906	1.910	1.902	1.893	1.885
Ti	0.014	0.016	0.012	0.034	0.009	0.010	0.009	0.008	0.012	0.010	0.009	0.007	0.005	0.009	0.009	0.016	0.024	0.022	0.026	0.023
Al IV	0.064	0.073	0.029	0.135	0.087	0.040	0.075	0.040	0.072	0.026	0.069	0.057	0.047	0.055	0.039	0.094	0.090	0.098	0.107	0.115
Al VI	-0.005	-0.017	0.025	-0.007	-0.040	-0.009	0.004	-0.014	-0.039	-0.002	-0.028	-0.019	-0.023	-0.013	0.001	0.008	0.020	0.006	0.007	0.031
Fe3+	0.068	0.087	0.005	0.097	0.110	0.033	0.054	0.038	0.088	0.009	0.080	0.066	0.062	0.050	0.021	0.073	0.049	0.073	0.075	0.062
Fe2+	0.170	0.185	0.262	0.133	0.406	0.449	0.413	0.480	0.425	0.499	0.392	0.471	0.451	0.486	0.478	0.158	0.211	0.192	0.173	0.174
Mn	0.007	0.014	0.011	0.008	0.014	0.016	0.016	0.021	0.022	0.018	0.013	0.020	0.020	0.016	0.015	0.006	0.005	0.009	0.009	0.007
Mg	0.890	0.867	0.848	0.878	1.436	1.447	1.448	1.406	1.439	1.413	1.480	1.396	1.435	1.399	1.414	0.862	0.854	0.847	0.859	0.847
Ca	0.829	0.818	0.815	0.832	0.064	0.053	0.055	0.062	0.053	0.050	0.053	0.056	0.048	0.050	0.060	0.856	0.810	0.825	0.821	0.829
Na	0.026	0.030	0.024	0.024	0.001	0.002	0.002	0.000	0.000	0.002	0.000	0.003	0.002	0.002	0.001	0.020	0.027	0.025	0.028	0.026
K	0.001	0.000	0.000	0.000	0.000	0.000	0.000	0.000	0.000	0.000	0.001	0.001	0.000	0.000	0.001	0.001	0.001	0.001	0.001	0.000
Cr	0.000	0.000	0.000	0.000	0.000	0.000	0.000	0.000	0.000	0.000	0.000	0.000	0.000	0.000	0.000	0.001	0.000	0.001	0.003	0.000
Tot. Extra Quad.	4.00	4.00	4.00	4.00	4.00	4.00	4.00	4.00	4.00	4.00	4.00	4.00	4.00	4.00	4.00	4.00	4.00	4.00	4.00	4.00
Wo%	42.34	41.81	42.24	42.88	3.17	2.65	2.78	3.11	2.65	2.55	2.64	2.80	2.39	2.52	3.03	43.93	42.12	42.59	42.60	43.38
En%	45.50	44.28	43.94	45.24	71.23	73.02	73.52	70.82	71.75	71.67	73.79	70.22	71.90	70.45	71.68	44.22	44.39	43.76	44.56	44.29
Fs%	12.16	13.91	13.82	11.88	25.60	24.32	23.71	26.07	25.59	25.78	23.57	26.99	25.71	27.03	25.29	11.85	13.49	13.65	12.85	12.33
Tot. Quad.	100.00	100.00	100.00	100.00	100.00	100.00	100.00	100.00	100.00	100.00	100.00	100.00	100.00	100.00	100.00	100.00	100.00	100.00	100.00	100.00

Sample	TU5								TU7										
Rock	BASALT-ANDESITE bomb								ANDESITE lava flow										
notes	pxf5r	pxf6	pxf7c	pxf7r	pxmf1c	pxmf1r	pxmf2c	pxmf2r	pxmf1c	pxmf1r	pxml1	pxml2	pxml1	pkml3	pxmf2c	pxmf2r	pxml4	pxml5	pxf1c
SiO_2	47.85	49.23	45.88	46.38	48.19	48.69	48.13	45.47	51.18	50.47	53.60	53.88	53.02	60.83	52.26	53.68	53.92	53.17	50.10
TiO_2	1.12	0.47	1.15	0.53	0.55	0.80	0.61	1.12	0.68	0.77	0.33	0.37	0.39	0.98	0.37	0.44	0.33	0.28	0.73
Al_2O_3	3.66	2.14	3.75	13.74	3.05	1.86	2.87	5.08	2.39	3.33	1.36	1.78	1.61	8.94	2.44	1.01	1.17	3.30	2.42
FeOt	8.72	8.49	7.85	4.57	4.32	9.25	4.47	8.75	8.61	8.08	14.51	14.40	13.82	7.28	14.13	17.50	15.24	12.76	9.45
MnO	0.22	0.25	0.23	0.13	0.08	0.30	0.10	0.22	0.22	0.17	0.44	0.32	0.38	0.09	0.39	0.43	0.45	0.29	0.39
MgO	14.06	15.17	13.80	9.03	15.15	15.28	15.35	13.52	15.76	15.55	27.28	27.63	27.64	7.62	27.41	25.81	25.57	28.96	15.26
CaO	19.86	18.10	19.68	15.82	21.58	17.02	20.89	18.13	19.85	20.66	1.85	2.20	1.83	4.74	1.84	2.07	1.64	0.39	19.85
Na_2O	0.36	0.26	0.34	1.69	0.23	0.29	0.25	0.42	0.32	0.31	0.00	0.00	0.05	2.86	0.03	0.04	0.09	0.00	0.45
K_2O	0.04	0.00	0.00	0.12	0.00	0.02	0.00	0.05	0.02	0.02	0.01	0.03	0.02	2.42	0.00	0.01	0.13	0.03	0.00
Cr_2O_3	0.11	0.03	0.22	0.02	0.43	0.03	0.48	0.11	0.00	0.02	0.06	0.00	0.02	0.04	0.06	0.04	0.00	0.00	0.00
TOTAL	96.00	94.15	92.91	92.03	93.58	93.52	93.16	92.85	99.03	99.38	99.42	100.63	98.78	95.80	98.91	101.02	98.53	99.18	98.66
Formula: 4 cationi, 6 Ox																			
Si	1.848	1.931	1.827	1.841	1.883	1.926	1.889	1.813	1.908	1.872	1.937	1.921	1.921	2.354	1.892	1.934	1.981	1.902	1.879
Ti	0.033	0.014	0.035	0.016	0.016	0.024	0.018	0.033	0.019	0.021	0.009	0.010	0.011	0.029	0.010	0.012	0.009	0.007	0.021
Al IV	0.152	0.069	0.173	0.159	0.117	0.074	0.111	0.187	0.092	0.128	0.063	0.079	0.079	-0.354	0.108	0.066	0.019	0.098	0.121
Al VI	0.015	0.030	0.003	0.484	0.023	0.013	0.021	0.051	0.013	0.018	-0.005	-0.004	-0.010	0.762	-0.004	-0.023	0.031	0.041	-0.014
Fe3+	0.098	0.029	0.120	-0.222	0.066	0.035	0.058	0.100	0.065	0.090	0.049	0.064	0.071	-0.840	0.093	0.067	-0.018	0.044	0.126
Fe2+	0.184	0.249	0.142	0.373	0.075	0.271	0.089	0.191	0.203	0.161	0.390	0.366	0.348	1.076	0.335	0.460	0.486	0.338	0.171
Mn	0.007	0.008	0.008	0.005	0.003	0.010	0.003	0.007	0.007	0.005	0.013	0.010	0.012	0.003	0.012	0.013	0.014	0.009	0.012
Mg	0.810	0.887	0.820	0.535	0.883	0.901	0.898	0.803	0.876	0.860	1.470	1.469	1.493	0.440	1.480	1.387	1.401	1.545	0.854
Ca	0.822	0.761	0.840	0.673	0.904	0.721	0.878	0.775	0.793	0.821	0.072	0.084	0.071	0.196	0.071	0.080	0.065	0.015	0.798
Na	0.027	0.020	0.027	0.130	0.017	0.023	0.019	0.032	0.023	0.022	0.000	0.000	0.003	0.214	0.002	0.003	0.006	0.000	0.033
K	0.002	0.000	0.000	0.006	0.000	0.001	0.000	0.002	0.001	0.001	0.001	0.001	0.001	0.119	0.000	0.000	0.006	0.001	0.000
Cr	0.003	0.001	0.007	0.000	0.013	0.001	0.015	0.004	0.000	0.000	0.002	0.000	0.001	0.001	0.002	0.001	0.000	0.000	0.000
Tot. Extra Quad.	4.00	4.00	4.00	4.00	4.00	4.00	4.00	4.00	4.00	4.00	4.00	4.00	4.00	4.00	4.00	4.00	4.00	4.00	4.00
Wo%	42.96	39.49	43.73	49.51	46.88	37.41	45.67	41.43	40.93	42.50	3.61	4.24	3.59	22.52	3.60	4.00	3.34	0.77	40.96
En%	42.32	46.04	42.66	39.32	45.80	46.73	46.70	42.98	45.21	44.52	74.24	74.10	75.29	50.44	74.78	69.54	72.45	79.56	43.82
Fs%	14.72	14.46	13.61	11.17	7.32	15.87	7.63	15.60	13.86	12.98	22.15	21.66	21.12	27.04	21.62	26.46	24.22	19.67	15.21
Tot. Quad.	100.00	100.00	100.00	100.00	100.00	100.00	100.00	100.00	100.00	100.00	100.00	100.00	100.00	100.00	100.00	100.00	100.00	100.00	100.00

Sample	TU7													TU8				
Rock	ANDESITE lava flow													ANDESITE lava flow				
notes	pxf1r	pxf2c	pxf2r	pxmf3c	pxmf3r	pxrimolml3	pxf3	pxf4	pxf5c	pxf5r	pxmf4	pxmf5	pxf6	pxf1c	pxf1r	pxf2c	pxf2r	pxf3c
SiO_2	49.97	50.12	49.39	53.97	53.01	53.36	50.49	51.63	50.36	49.68	53.41	53.06	50.54	49.66	51.87	52.26	54.00	50.40
TiO_2	0.73	0.83	0.83	0.36	0.41	0.36	0.64	0.33	0.48	0.71	0.31	0.33	0.71	0.69	0.45	0.35	0.42	0.64
Al_2O_3	3.33	3.40	4.43	1.27	1.21	1.07	3.61	1.79	1.81	3.22	1.42	0.92	2.34	2.71	2.10	1.98	1.55	2.81
FeOt	7.11	7.40	7.14	13.61	16.04	15.83	6.11	5.80	8.12	7.90	13.20	13.53	8.63	8.18	7.55	14.71	13.30	8.43
MnO	0.12	0.34	0.18	0.39	0.44	0.48	0.11	0.17	0.33	0.18	0.39	0.29	0.23	0.32	0.25	0.40	0.30	0.24
MgO	15.60	15.39	15.37	27.74	25.84	25.74	15.56	16.83	15.58	15.58	28.56	27.46	15.44	15.70	17.74	27.43	28.51	15.68
CaO	21.83	20.82	21.76	1.86	1.98	2.39	21.38	21.17	20.07	20.60	1.75	1.73	20.27	20.61	19.63	1.72	1.71	20.69
Na_2O	0.25	0.34	0.31	0.03	0.05	0.07	0.27	0.18	0.27	0.25	0.00	0.01	0.41	0.39	0.24	0.02	0.05	0.35
K_2O	0.01	0.00	0.00	0.02	0.01	0.03	0.00	0.00	0.01	0.03	0.00	0.02	0.01	0.00	0.01	0.00	0.01	0.00
Cr_2O_3	0.06	0.00	0.09	0.04	0.00	0.10	0.36	0.38	0.00	0.00	0.00	0.00	0.10	0.04	0.12	0.00	0.05	0.16
TOTAL	99.00	98.63	99.49	99.28	98.99	99.42	98.55	98.27	97.02	98.14	99.03	97.33	98.67	98.31	99.95	98.88	99.89	99.42
Formula: 4 cationi, 6 Ox																		
Si	1.856	1.871	1.825	1.946	1.940	1.945	1.881	1.923	1.915	1.865	1.922	1.951	1.892	1.861	1.899	1.895	1.929	1.870
Ti	0.020	0.023	0.023	0.010	0.011	0.010	0.018	0.009	0.014	0.020	0.008	0.009	0.020	0.019	0.012	0.010	0.011	0.018
Al IV	0.144	0.129	0.175	0.054	0.060	0.055	0.119	0.077	0.085	0.135	0.078	0.049	0.108	0.139	0.101	0.105	0.071	0.130
Al VI	0.002	0.021	0.018	0.000	-0.008	-0.009	0.040	0.001	-0.004	0.007	-0.018	-0.009	-0.005	-0.020	-0.010	-0.020	-0.006	-0.007
Fe3+	0.118	0.086	0.131	0.035	0.048	0.047	0.052	0.060	0.083	0.108	0.079	0.041	0.100	0.147	0.100	0.107	0.058	0.122
Fe2+	0.103	0.145	0.090	0.375	0.443	0.435	0.138	0.121	0.176	0.140	0.319	0.375	0.170	0.109	0.131	0.339	0.339	0.139
Mn	0.004	0.011	0.006	0.012	0.014	0.015	0.003	0.005	0.011	0.006	0.012	0.009	0.007	0.010	0.008	0.012	0.009	0.008
Mg	0.864	0.857	0.847	1.492	1.410	1.399	0.865	0.934	0.883	0.872	1.533	1.506	0.862	0.877	0.968	1.484	1.518	0.868
Ca	0.869	0.833	0.862	0.072	0.078	0.093	0.854	0.845	0.818	0.828	0.067	0.068	0.813	0.827	0.770	0.067	0.065	0.822
Na	0.018	0.025	0.022	0.002	0.003	0.005	0.020	0.013	0.020	0.018	0.000	0.001	0.029	0.028	0.017	0.001	0.004	0.025
K	0.000	0.000	0.000	0.001	0.000	0.001	0.000	0.000	0.001	0.001	0.000	0.001	0.000	0.000	0.000	0.000	0.001	0.000
Cr	0.002	0.000	0.003	0.001	0.000	0.003	0.011	0.011	0.000	0.000	0.000	0.000	0.003	0.001	0.004	0.000	0.001	0.005
Tot. Extra Quad.	4.00	4.00	4.00	4.00	4.00	4.00	4.00	4.00	4.00	4.00	4.00	4.00	4.00	4.00	4.00	4.00	4.00	4.00
Wo%	44.47	43.37	44.67	3.64	3.92	4.72	44.72	43.11	41.74	42.52	3.38	3.42	41.80	42.19	39.09	3.35	3.30	42.14
En%	44.22	44.61	43.90	75.56	71.27	70.84	45.30	47.68	45.08	44.76	76.73	75.67	44.31	44.74	49.17	74.30	76.65	44.45
Fs%	11.31	12.03	11.43	20.79	24.81	24.44	9.98	9.21	13.18	12.72	19.89	20.91	13.88	13.08	11.74	22.35	20.05	13.40
Tot. Quad.	100.00	100.00	100.00	100.00	100.00	100.00	100.00	100.00	100.00	100.00	100.00	100.00	100.00	100.00	100.00	100.00	100.00	100.00

PYROXENES

Sample	TU8																TU9		
Rock	ANDESITE lava flow																ANDESITE lava flow		
notes	pxf3r	pxf4	pxf5c	pxf5r	pxmf1	pxmf2	pxmf3	pxmf4	pxmf5c	pxmf5r	pxmf5rinter	pxolmf5rim	pxml1	pxml2	pxml3	pxml3	pxmf1	pxml1	pxml2
SiO_2	50.24	51.94	53.48	53.03	50.58	53.93	51.01	52.24	52.01	49.99	48.19	50.98	51.62	54.31	49.99	53.87	52.86	51.57	52.00
TiO_2	0.84	0.47	0.29	0.29	0.76	0.17	0.47	0.38	0.32	0.91	1.13	0.61	0.38	0.21	0.72	0.30	0.11	0.17	0.28
Al_2O_3	3.54	2.19	1.11	1.63	2.36	1.02	2.59	1.76	1.84	2.46	5.64	2.42	2.14	0.75	3.22	0.93	0.63	2.13	1.97
FeOt	7.95	6.25	14.43	13.63	8.95	13.79	6.01	5.89	7.15	8.56	8.23	7.59	6.35	13.44	8.39	13.80	17.90	18.53	14.37
MnO	0.26	0.13	0.39	0.36	0.22	0.41	0.23	0.20	0.19	0.18	0.17	0.18	0.19	0.40	0.17	0.39	0.80	0.75	0.44
MgO	15.86	17.34	27.87	27.71	15.62	27.91	16.28	17.28	17.92	15.82	14.93	16.51	17.27	28.18	15.35	28.28	25.93	24.29	28.06
CaO	20.92	20.94	1.72	1.75	19.86	1.74	22.02	20.52	19.20	20.01	21.02	20.01	20.88	1.73	20.37	1.73	1.23	1.52	1.47
Na_2O	0.25	0.23	0.08	0.00	0.39	0.00	0.33	0.22	0.18	0.28	0.30	0.26	0.24	0.01	0.33	0.03	0.00	0.03	0.00
K_2O	0.00	0.01	0.00	0.01	0.00	0.01	0.00	0.00	0.00	0.01	0.00	0.03	0.01	0.01	0.03	0.03	0.01	0.03	0.04
Cr_2O_3	0.11	0.44	0.01	0.03	0.01	0.00	0.12	0.35	0.05	0.03	0.09	0.15	0.27	0.03	0.00	0.02	0.00	0.00	0.04
TOTAL	99.96	99.94	99.37	98.44	98.74	98.99	99.06	98.84	98.85	98.24	99.69	98.73	99.35	99.06	98.57	99.38			
Formula: 4 cationi, 6 Ox																			
Si	1.851	1.901	1.928	1.926	1.892	1.950	1.885	1.932	1.922	1.878	1.782	1.897	1.899	1.960	1.871	1.938	1.934	1.905	1.884
Ti	0.023	0.013	0.008	0.008	0.021	0.005	0.013	0.011	0.009	0.026	0.031	0.017	0.011	0.006	0.020	0.008	0.003	0.005	0.008
Al IV	0.149	0.099	0.072	0.074	0.108	0.050	0.115	0.068	0.078	0.122	0.218	0.103	0.101	0.040	0.129	0.062	0.066	0.095	0.116
Al VI	0.005	-0.005	-0.025	-0.004	-0.004	-0.007	-0.002	0.009	0.002	-0.014	0.028	0.003	-0.008	-0.008	0.013	-0.023	-0.039	-0.002	-0.032
Fe3+	0.113	0.083	0.086	0.061	0.097	0.049	0.111	0.044	0.069	0.105	0.146	0.082	0.098	0.038	0.101	0.071	0.099	0.091	0.134
Fe2+	0.133	0.108	0.349	0.353	0.183	0.368	0.075	0.138	0.152	0.164	0.109	0.154	0.098	0.368	0.162	0.344	0.449	0.481	0.301
Mn	0.008	0.004	0.012	0.011	0.007	0.013	0.007	0.006	0.006	0.006	0.005	0.006	0.006	0.012	0.005	0.012	0.025	0.023	0.013
Mg	0.872	0.946	1.498	1.501	0.871	1.504	0.897	0.953	0.987	0.886	0.823	0.916	0.947	1.516	0.856	1.517	1.415	1.338	1.516
Ca	0.826	0.821	0.066	0.068	0.796	0.068	0.872	0.813	0.760	0.805	0.833	0.798	0.823	0.067	0.817	0.067	0.048	0.060	0.057
Na	0.018	0.017	0.005	0.000	0.028	0.000	0.023	0.016	0.013	0.021	0.022	0.019	0.017	0.001	0.024	0.002	0.000	0.002	0.000
K	0.000	0.000	0.000	0.000	0.000	0.001	0.000	0.000	0.000	0.001	0.000	0.001	0.001	0.000	0.001	0.001	0.000	0.001	0.002
Cr	0.003	0.013	0.000	0.001	0.000	0.000	0.004	0.010	0.001	0.001	0.003	0.004	0.008	0.001	0.000	0.001	0.000	0.000	0.001
Tot. Extra Quad.	4.00	4.00	4.00	4.00	4.00	4.00	4.00	4.00	4.00	4.00	4.00	4.00	4.00	4.00	4.00	4.00	4.00	4.00	4.00
Wo%	42.51	41.91	3.32	3.44	40.88	3.39	44.61	41.75	38.62	41.09	43.60	40.91	41.87	3.37	42.20	3.33	2.39	3.06	2.85
En%	44.87	48.31	74.92	75.69	44.74	75.64	45.90	48.90	50.15	45.19	43.08	46.98	48.20	76.23	44.23	75.89	70.36	67.90	75.48
Fs%	12.62	9.77	21.76	20.87	14.38	20.97	9.50	9.35	11.23	13.72	13.32	12.11	9.94	20.40	13.57	20.77	27.25	29.05	21.67
Tot. Quad.	100.00	100.00	100.00	100.00	100.00	100.00	100.00	100.00	100.00	100.00	100.00	100.00	100.00	100.00	100.00	100.00	100.00	100.00	100.00

PYROXENES

Sample	TU9														TU10a				
Rock	ANDESITE lava flow														ANDESITE lava flow				
notes	pxml3	pxf1c	pxf1r	pxf2c	pxf2r	pxmf1inch	pxmf2inch	pxml4inch	pxml5inch	pxml6inch	pxf3	pxf4	pxf5	pxf7	pxf1	pxf2	pxf3	pxf4	pxmf1
SiO_2	51.22	51.65	55.04	54.42	53.40	53.69	51.87	52.91	52.51	53.46	51.03	51.03	53.00	51.11	50.90	51.70	50.42	48.80	52.74
TiO_2	0.68	0.38	0.58	0.21	0.24	0.27	0.31	0.16	0.27	0.20	0.59	0.41	0.18	0.76	0.73	0.53	0.80	1.48	0.30
Al_2O_3	3.36	1.32	2.68	0.88	1.05	0.96	2.20	0.81	1.50	0.86	1.57	1.18	0.45	2.44	2.97	1.89	3.24	4.39	0.73
FeOt	7.35	8.92	7.91	16.63	17.02	18.44	19.33	19.24	18.07	19.42	8.77	8.86	17.24	8.50	8.24	7.96	7.65	9.20	15.49
MnO	0.18	0.56	0.29	0.59	0.61	0.76	0.74	0.75	0.77	0.95	0.45	0.48	0.73	0.32	0.26	0.32	0.14	0.45	0.50
MgO	16.29	15.26	13.85	27.48	26.44	25.18	24.35	23.82	24.78	23.84	15.77	15.69	26.10	15.62	15.73	16.44	15.20	14.13	26.74
CaO	19.66	20.80	18.58	1.35	1.40	1.32	1.33	1.46	1.70	1.61	20.42	20.90	1.70	20.04	20.41	20.19	20.50	20.76	1.97
Na_2O	0.24	0.36	0.74	0.01	0.00	0.03	0.01	0.02	0.00	0.04	0.36	0.37	0.04	0.38	0.33	0.35	0.30	0.42	0.01
K_2O	0.11	0.01	0.70	0.03	0.01	0.00	0.00	0.03	0.00	0.00	0.00	0.01	0.02	0.02	0.00	0.00	0.00	0.00	0.00
Cr_2O_3	0.14	0.02	0.05	0.00	0.01	0.03	0.00	0.00	0.02	0.00	0.00	0.04	0.00	0.00	0.00	0.00	0.12	0.01	0.00
TOTAL															99.66	99.40	98.45	99.75	98.91
Formula: 4 cationi, 6 Ox																			
Si	1.896	1.927	2.030	1.935	1.933	1.950	1.899	1.962	1.927	1.961	1.905	1.906	1.936	1.902	1.885	1.914	1.891	1.819	1.932
Ti	0.019	0.011	0.016	0.006	0.006	0.007	0.008	0.004	0.007	0.006	0.017	0.011	0.005	0.021	0.020	0.015	0.023	0.041	0.008
Al IV	0.104	0.073	-0.030	0.065	0.067	0.050	0.101	0.038	0.073	0.039	0.095	0.094	0.064	0.098	0.115	0.086	0.109	0.181	0.068
Al VI	0.043	-0.015	0.147	-0.028	-0.022	-0.009	-0.006	-0.003	-0.008	-0.001	-0.026	-0.042	-0.045	0.009	0.014	-0.004	0.034	0.012	-0.036
Fe3+	0.042	0.092	-0.124	0.083	0.077	0.046	0.091	0.034	0.066	0.032	0.113	0.140	0.103	0.075	0.084	0.086	0.048	0.116	0.089
Fe2+	0.185	0.186	0.368	0.411	0.438	0.514	0.501	0.562	0.488	0.564	0.161	0.137	0.424	0.190	0.172	0.160	0.192	0.170	0.386
Mn	0.006	0.018	0.009	0.018	0.019	0.023	0.023	0.024	0.024	0.030	0.014	0.015	0.023	0.010	0.008	0.010	0.005	0.014	0.016
Mg	0.899	0.849	0.762	1.457	1.427	1.364	1.329	1.317	1.355	1.304	0.878	0.874	1.421	0.867	0.869	0.907	0.850	0.786	1.460
Ca	0.780	0.832	0.734	0.051	0.054	0.051	0.052	0.058	0.067	0.063	0.817	0.836	0.067	0.799	0.810	0.801	0.824	0.829	0.077
Na	0.017	0.026	0.053	0.000	0.000	0.002	0.001	0.001	0.000	0.003	0.026	0.027	0.002	0.028	0.023	0.025	0.022	0.031	0.000
K	0.005	0.001	0.033	0.001	0.001	0.000	0.000	0.001	0.000	0.000	0.000	0.000	0.001	0.001	0.000	0.000	0.000	0.000	0.000
Cr	0.004	0.000	0.002	0.000	0.000	0.001	0.000	0.000	0.001	0.000	0.000	0.001	0.000	0.000	0.000	0.000	0.003	0.000	0.000
Tot. Extra Quad.	4.00	4.00	4.00	4.00	4.00	4.00	4.00	4.00	4.00	4.00	4.00	4.00	4.00	4.00	4.00	4.00	4.00	4.00	4.00
Wo%	40.90	42.45	42.20	2.56	2.72	2.60	2.64	2.95	3.38	3.23	41.50	42.09	3.30	41.40	41.88	40.96	43.05	43.61	3.84
En%	47.17	43.34	43.78	72.75	71.48	69.04	67.36	66.80	68.57	66.42	44.59	43.97	70.56	44.90	44.92	46.43	44.42	41.31	72.57
Fs%	11.93	14.21	14.02	24.69	25.80	28.36	29.99	30.25	28.05	30.35	13.91	13.93	26.14	13.71	13.20	12.60	12.53	15.08	23.58
Tot. Quad.	100.00	100.00	100.00	100.00	100.00	100.00	100.00	100.00	100.00	100.00	100.00	100.00	100.00	100.00	100.00	100.00	100.00	100.00	100.00

PYROXENES

Sample	TU10a								TU15							
Rock	ANDESITE lava flow								DACITE lava flow							
notes	pxf5c	pxf5r	pxf6c	pxf6r	pxmf2	pxmf3	pxmf4	pxmf5	mphOpx1	mphOpx2	mphOpx6	mphOpx7	mphPx1	mphPx2	Opx3	mlOpx4
SiO_2	53.81	53.45	54.41	53.53	52.64	53.15	54.82	53.49	53.45	53.27	54.00	54.43	53.94	53.64	53.37	53.79
TiO_2	0.40	0.39	0.31	0.33	0.45	0.32	0.07	0.30	0.33	0.14	0.24	0.22	0.33	0.47	0.35	0.19
Al_2O_3	0.94	2.30	0.70	2.51	1.55	0.94	1.06	1.20	0.89	0.76	0.79	0.77	1.22	1.31	0.89	0.69
FeOt	15.35	13.59	15.89	13.53	16.36	16.09	12.42	16.11	18.89	18.30	18.91	19.16	17.58	18.32	18.31	17.91
MnO	0.51	0.38	0.47	0.34	0.62	0.49	0.41	0.57	0.79	0.76	0.95	0.91	0.52	0.52	0.68	0.71
MgO	27.42	27.77	27.43	29.28	26.31	26.77	29.96	26.32	25.24	25.85	24.76	24.86	25.93	25.23	25.38	25.19
CaO	1.50	2.09	1.37	1.68	1.78	1.59	1.40	1.66	1.20	1.48	1.50	1.27	1.82	1.86	1.69	1.68
Na_2O	0.03	0.02	0.03	0.00	0.06	0.01	0.00	0.03	0.01	0.00	0.03	0.00	0.02	0.03	0.06	0.05
K_2O	0.00	0.02	0.00	0.00	0.03	0.00	0.00	0.01	0.00	0.00	0.00	0.01	0.02	0.01	0.00	0.02
Cr_2O_3	0.00	0.00	0.00	0.01	0.00	0.00	0.02	0.00								
TOTAL	99.97	100.06	100.66	101.30	99.96	99.35	100.26	99.88	100.79	100.57	101.17	101.63	101.38	101.39	100.72	100.23
Formula: 4 cationi, 6 Ox																
Si	1.939	1.912	1.950	1.882	1.909	1.933	1.940	1.942	1.941	1.931	1.958	1.966	1.936	1.933	1.935	1.959
Ti	0.011	0.010	0.008	0.009	0.012	0.009	0.002	0.008	0.009	0.004	0.007	0.006	0.009	0.013	0.009	0.005
Al IV	0.061	0.088	0.050	0.118	0.091	0.067	0.060	0.058	0.059	0.069	0.042	0.034	0.064	0.067	0.065	0.041
Al VI	-0.021	0.008	-0.020	-0.015	-0.025	-0.027	-0.016	-0.007	-0.021	-0.037	-0.008	-0.001	-0.013	-0.011	-0.027	-0.011
Fe3+	0.063	0.061	0.056	0.115	0.097	0.078	0.072	0.052	0.062	0.098	0.038	0.024	0.062	0.054	0.077	0.045
Fe2+	0.400	0.345	0.421	0.282	0.399	0.412	0.295	0.437	0.511	0.457	0.535	0.555	0.466	0.498	0.478	0.501
Mn	0.015	0.011	0.014	0.010	0.019	0.015	0.012	0.018	0.024	0.023	0.029	0.028	0.016	0.016	0.021	0.022
Mg	1.473	1.481	1.466	1.535	1.423	1.451	1.581	1.425	1.367	1.397	1.339	1.339	1.388	1.356	1.372	1.368
Ca	0.058	0.080	0.053	0.063	0.069	0.062	0.053	0.065	0.047	0.057	0.058	0.049	0.070	0.072	0.065	0.066
Na	0.002	0.001	0.002	0.000	0.004	0.001	0.000	0.002	0.001	0.000	0.002	0.000	0.002	0.002	0.004	0.003
K	0.000	0.001	0.000	0.000	0.001	0.000	0.000	0.000	0.000	0.000	0.000	0.001	0.001	0.000	0.000	0.001
Cr	0.000	0.000	0.000	0.000	0.000	0.000	0.000	0.000	0.000	0.000	0.000	0.000	0.000	0.000	0.000	0.000
Tot. Extra Quad.	4.00	4.00	4.00	4.00	4.00	4.00	4.00	4.00	4.00	4.00	4.00	4.00	4.00	4.00	4.00	4.00
Wo%	2.90	4.07	2.63	3.17	3.48	3.09	2.66	3.27	2.35	2.86	2.96	2.50	3.52	3.64	3.29	3.32
En%	73.90	75.27	73.48	76.90	71.56	72.47	78.98	72.01	68.78	69.53	67.94	68.07	69.90	68.48	68.85	69.13
Fs%	23.20	20.66	23.88	19.93	24.96	24.44	18.36	24.72	28.87	27.61	29.10	29.43	26.58	27.89	27.86	27.55
Tot. Quad.	100.00	100.00	100.00	100.00	100.00	100.00	100.00	100.00	100.00	100.00	100.00	100.00	100.00	100.00	100.00	100.00

OLIVINES

Sample	TU3/1a	TU4																	
Rock	ANDESITE lava flow	DACITE lava flow																	
notes	olf1c	f1	f2	f3	f4	f5	f6	f7	f8	f9	f10	f11	f12	f13	f14	f15	f16	f17	f18
SiO_2	38.63	40.81	37.43	39.56	39.70	39.02	39.27	38.57	38.66	38.95	39.58	38.76	40.16	40.17	39.95	40.08	39.46	39.91	40.96
FeO	19.27	9.20	22.14	16.81	14.98	19.32	7.43	18.87	7.26	20.95	15.20	18.39	12.57	10.44	11.65	10.35	14.37	12.48	9.27
MnO	0.29	0.12	0.30	0.34	0.19	0.27	0.10	0.38	0.07	0.27	0.23	0.34	0.22	0.16	0.19	0.19	0.23	0.12	0.19
MgO	42.80	50.20	39.93	43.78	46.17	42.80	42.22	42.93	40.22	41.15	45.29	43.11	47.80	48.94	48.65	48.00	45.67	47.17	49.76
CaO	0.08	0.14	0.20	0.16	0.23	0.23	0.17	0.10	0.17	0.15	0.17	0.16	0.23	0.03	0.16	0.24	0.16	0.16	0.11
Cr_2O_3	0.00	0.04	0.00	0.02	0.04	0.00	0.03	0.00	0.02	0.00	0.00	0.03	0.03	0.05	0.02	0.29	0.15	0.06	0.09
NiO	0.00																		
Tot.	101.06	100.52	100.00	100.67	101.31	101.63	89.22	100.85	86.39	101.47	100.46	100.79	101.01	99.79	100.61	99.15	100.04	99.89	100.38
Formula su 4 Ox																			
Si	0.981	0.993	0.976	0.996	0.985	0.985	1.061	0.980	1.077	0.991	0.991	0.983	0.988	0.990	0.983	0.996	0.990	0.992	0.998
Fe	0.409	0.187	0.483	0.354	0.311	0.408	0.168	0.401	0.169	0.446	0.318	0.390	0.259	0.215	0.240	0.215	0.301	0.259	0.189
Mn	0.006	0.002	0.007	0.007	0.004	0.006	0.002	0.008	0.002	0.006	0.005	0.007	0.005	0.003	0.004	0.004	0.005	0.002	0.004
Mg	1.620	1.821	1.553	1.643	1.708	1.611	1.701	1.627	1.670	1.562	1.691	1.631	1.754	1.799	1.785	1.778	1.708	1.749	1.807
Ca	0.002	0.004	0.005	0.004	0.006	0.006	0.005	0.003	0.005	0.004	0.005	0.004	0.006	0.001	0.004	0.006	0.004	0.004	0.003
Cr	0.000	0.001	0.000	0.000	0.001	0.000	0.000	0.000	0.000	0.000	0.000	0.000	0.000	0.001	0.000	0.004	0.002	0.001	0.001
Ni	0.000	0.000	0.000	0.000	0.000	0.000	0.000	0.000	0.000	0.000	0.000	0.000	0.000	0.000	0.000	0.000	0.000	0.000	0.000
Somma M1	2.038	2.015	2.048	2.009	2.030	2.030	1.877	2.039	1.846	2.017	2.018	2.033	2.024	2.019	2.034	2.008	2.021	2.016	2.004
Fo % =	79.60	90.57	76.03	81.98	84.43	79.57	90.91	79.90	90.73	77.56	83.95	80.40	86.95	89.17	87.99	89.03	84.79	86.97	90.36
Fa	20.10	9.31	23.64	17.65	15.37	20.15	8.97	19.70	9.18	22.15	15.80	19.24	12.82	10.67	11.82	10.77	14.96	12.91	9.44
Tefr	0.30	0.12	0.33	0.37	0.20	0.29	0.12	0.40	0.09	0.29	0.25	0.36	0.23	0.16	0.20	0.20	0.24	0.12	0.20

Sample		TU4																	
Rock		DACITE lava flow																	
notes	f19	f20	f21	f22	f23	f24	f25	f26	f27	f28	f29	f30	f31	f32	f33	f34	f35	f36	f37
SiO_2	40.97	39.56	38.65	40.50	38.66	40.00	39.03	39.44	38.44	39.06	38.68	40.44	39.34	38.76	38.77	39.46	40.00	37.51	40.00
FeO	17.70	16.77	19.06	9.07	20.62	12.55	14.17	15.61	20.29	14.45	19.99	11.25	17.26	18.22	19.38	14.76	11.20	22.06	10.46
MnO	0.35	0.28	0.42	0.07	0.41	0.21	0.22	0.28	0.37	0.22	0.29	0.19	0.29	0.31	0.30	0.23	0.17	0.47	0.10
MgO	44.07	43.91	38.78	49.28	40.79	47.18	44.26	44.56	41.05	45.04	40.72	48.17	42.78	42.08	40.99	44.51	47.58	38.53	48.54
CaO	0.10	0.16	0.13	0.15	0.18	0.12	0.13	0.10	0.22	0.14	0.14	0.13	0.16	0.19	0.19	0.15	0.15	0.17	0.15
Cr_2O_3	0.02	0.00	0.02	0.00	0.00	0.01	0.04	0.00	0.04	0.00	0.06	0.06	0.07	0.02	0.00	0.02	0.01	0.00	0.00
NiO																			
Tot.	103.21	100.68	97.05	99.06	100.67	100.07	97.85	99.97	100.40	98.90	99.87	100.23	99.89	99.58	99.63	99.13	99.10	98.74	99.24
Formula su 4 Ox																			
Si	1.006	0.995	1.020	0.998	0.992	0.993	0.999	0.994	0.988	0.991	0.997	0.996	1.000	0.994	0.998	0.999	0.996	0.990	0.992
Fe	0.364	0.353	0.421	0.187	0.442	0.261	0.303	0.329	0.436	0.307	0.431	0.232	0.367	0.391	0.417	0.312	0.233	0.487	0.217
Mn	0.007	0.006	0.009	0.002	0.009	0.004	0.005	0.006	0.008	0.005	0.006	0.004	0.006	0.007	0.007	0.005	0.003	0.011	0.002
Mg	1.614	1.647	1.526	1.811	1.560	1.746	1.689	1.674	1.573	1.703	1.565	1.769	1.621	1.609	1.574	1.680	1.767	1.517	1.794
Ca	0.003	0.004	0.004	0.004	0.005	0.003	0.004	0.003	0.006	0.004	0.004	0.003	0.004	0.005	0.005	0.004	0.004	0.005	0.004
Cr	0.000	0.000	0.000	0.000	0.000	0.000	0.001	0.000	0.001	0.000	0.001	0.001	0.001	0.000	0.000	0.000	0.000	0.000	0.000
Ni	0.000	0.000	0.000	0.000	0.000	0.000	0.000	0.000	0.000	0.000	0.000	0.000	0.000	0.000	0.000	0.000	0.000	0.000	0.000
Somma M1	1.988	2.010	1.960	2.003	2.017	2.014	2.002	2.012	2.024	2.018	2.007	2.008	2.000	2.012	2.003	2.002	2.008	2.019	2.017
Fo % =	81.31	82.12	78.02	90.58	77.56	86.82	84.58	83.34	77.99	84.55	78.17	88.25	81.29	80.19	78.78	84.11	88.18	75.30	89.13
Fa	18.32	17.59	21.50	9.35	21.99	12.96	15.19	16.37	21.62	15.22	21.52	11.56	18.39	19.47	20.89	15.64	11.64	24.18	10.77
Tefr	0.36	0.30	0.48	0.08	0.45	0.22	0.24	0.29	0.39	0.23	0.31	0.20	0.31	0.34	0.33	0.25	0.17	0.52	0.11

OLIVINES

Sample	TU4		TU5																					
Rock	DACITE lava flow		BASALT-ANDESITE bomb																					
notes	f38	f39	olf1c	olf2c	olf3c	olf3r	olf4c	olf4r	ine 1 olf5	ine 2 olf5	ine 3 olf5	ine 4 olf5	ine 5 olf5	ine 6 olf5	ine 7 olf5	ine 8 olf5	olf6c	olf7c	olf7r	olf8c	olf8r	olmf1	olmf2c	olmf3c
SiO_2	39.51	40.12	37.31	36.97	36.77	36.45	37.09	36.17	38.79	39.03	38.50	38.67	38.28	37.56	37.61	36.66	37.29	35.60	35.75	37.41	38.25	38.02	37.27	36.59
FeO	18.84	7.41	21.25	22.49	21.25	24.53	20.84	23.08	10.86	11.02	10.88	11.12	11.27	12.35	15.92	23.51	16.85	18.30	21.98	11.83	20.52	21.22	20.29	20.82
MnO	0.38	0.12	0.37	0.47	0.31	0.47	0.42	0.41	0.21	0.16	0.03	0.18	0.11	0.16	0.22	0.43	0.31	0.34	0.47	0.18	0.45	0.31	0.34	0.35
MgO	42.01	50.16	37.50	35.56	37.11	33.93	37.17	35.39	44.82	44.88	44.80	44.55	44.38	43.51	41.38	32.55	40.60	38.81	35.19	43.95	34.37	37.55	37.73	37.37
CaO	0.18	0.16	0.18	0.17	0.24	0.22	0.19	0.30	0.20	0.17	0.21	0.25	0.23	0.24	0.21	0.63	0.18	0.23	0.30	0.37	0.69	0.24	0.22	0.20
Cr_2O_3	0.00	0.02	0.05	0.00	0.00	0.00	0.01	0.00	0.00	0.06	0.06	0.00	0.05	0.07	0.00	0.09	0.02	0.00	0.00	0.04	0.02	0.05	0.03	0.00
NiO																								
Tot.	100.91	97.98	96.65	95.66	95.67	95.60	95.71	95.34	94.88	95.32	94.48	94.76	94.32	93.89	95.35	93.86	95.24	93.28	93.69	93.78	94.30	97.38	95.88	95.33
Formula su 4 Ox																								
Si	1.001	0.994	1.003	1.010	0.999	1.008	1.005	0.997	1.008	1.010	1.005	1.008	1.004	0.997	0.999	1.028	0.997	0.983	1.000	0.992	1.048	1.012	1.005	0.997
Fe	0.399	0.153	0.478	0.514	0.483	0.567	0.472	0.532	0.236	0.239	0.238	0.242	0.247	0.274	0.354	0.551	0.377	0.422	0.514	0.262	0.470	0.472	0.458	0.474
Mn	0.008	0.002	0.008	0.011	0.007	0.011	0.010	0.010	0.005	0.004	0.001	0.004	0.003	0.004	0.005	0.010	0.007	0.008	0.011	0.004	0.010	0.007	0.008	0.008
Mg	1.586	1.852	1.503	1.449	1.504	1.399	1.502	1.455	1.737	1.732	1.744	1.731	1.735	1.721	1.638	1.361	1.618	1.597	1.467	1.738	1.404	1.490	1.517	1.518
Ca	0.005	0.004	0.005	0.005	0.007	0.007	0.005	0.009	0.006	0.005	0.006	0.007	0.006	0.007	0.006	0.019	0.005	0.007	0.009	0.011	0.020	0.007	0.006	0.006
Cr	0.000	0.000	0.001	0.000	0.000	0.000	0.000	0.000	0.000	0.001	0.001	0.000	0.001	0.001	0.000	0.001	0.000	0.000	0.000	0.001	0.000	0.001	0.000	0.000
Ni	0.000	0.000	0.000	0.000	0.000	0.000	0.000	0.000	0.000	0.000	0.000	0.000	0.000	0.000	0.000	0.000	0.000	0.000	0.000	0.000	0.000	0.000	0.000	0.000
Somma M1	1.999	2.013	1.995	1.979	2.001	1.984	1.989	2.005	1.983	1.980	1.989	1.985	1.992	2.007	2.003	1.943	2.007	2.035	2.001	2.016	1.905	1.977	1.990	2.006
Fo % =	79.58	92.23	75.57	73.41	75.42	70.75	75.71	72.87	87.83	87.74	87.98	87.55	87.42	86.11	82.04	70.79	80.83	78.77	73.64	86.70	74.50	75.66	76.53	75.88
Fa	20.02	7.64	24.01	26.04	24.22	28.70	23.81	26.65	11.94	12.08	11.98	12.25	12.45	13.71	17.71	28.68	18.82	20.83	25.80	13.09	24.95	23.98	23.08	23.71
Tefr	0.41	0.12	0.42	0.55	0.36	0.55	0.48	0.48	0.24	0.18	0.03	0.20	0.13	0.18	0.25	0.53	0.35	0.40	0.55	0.20	0.55	0.35	0.39	0.40

OLIVINES

Sample	TU5						TU7																	
Rock	BASALT-ANDESITE bomb						ANDESITE lava flow																	
notes	olmf4	olml1	olml2	olml3	olml4	olml5c	olf1c	olf1r	olf2c	olf2r	olf3c	olf3r	olf4c	olf4r	ol5c	ol5r	olivine 1	olivine 2	olivine 3	olivine 4	olivine 5	olivine 6	olivine 7	olivine 8
SiO_2	36.49	37.89	37.65	37.11	36.34	36.94	37.59	38.10	38.47	38.48	38.55	37.68	38.67	38.54	37.29	38.36	38.76	38.96	38.14	38.70	38.77	38.29	37.91	38.50
FeO	23.98	19.88	21.01	21.58	22.77	20.42	20.27	19.94	20.43	23.08	17.35	23.12	17.89	19.97	21.23	23.85	16.67	16.79	16.88	16.41	16.65	16.67	17.47	18.95
MnO	0.47	0.35	0.33	0.41	0.42	0.55	0.30	0.35	0.37	0.40	0.21	0.47	0.29	0.34	0.37	0.48	0.28	0.19	0.23	0.23	0.26	0.21	0.19	0.19
MgO	34.12	37.59	37.38	36.79	35.82	37.46	40.73	41.01	41.18	35.73	44.02	35.02	43.45	40.58	40.13	39.07	43.10	43.25	43.28	43.69	43.71	43.44	42.58	41.61
CaO	0.26	0.29	0.28	0.28	0.29	0.25	0.08	0.14	0.13	0.71	0.15	0.26	0.07	0.14	0.12	0.21	0.14	0.12	0.09	0.04	0.11	0.14	0.09	0.11
Cr_2O_3	0.03	0.00	0.05	0.00	0.03	0.04	0.03	0.05	0.03	0.00	0.01	0.04	0.01	0.02	0.00	0.00	0.07	0.07	0.00	0.00	0.00	0.05	0.01	0.01
NiO							0.00	0.00	0.00	0.00	0.00	0.00	0.00	0.00	0.00	0.00	0.00	0.00	0.00	0.00	0.00	0.00	0.00	0.00
Tot.	95.34	95.99	96.69	96.16	95.67	95.65	99.00	99.57	100.59	98.39	100.30	96.58	100.38	99.58	99.15	101.97	99.01	99.37	98.61	99.07	99.50	98.81	98.24	99.36
Formula su 4 Ox																								
Si	1.009	1.017	1.009	1.005	0.997	1.001	0.981	0.986	0.987	1.022	0.979	1.021	0.983	0.996	0.977	0.986	0.993	0.994	0.983	0.989	0.988	0.984	0.984	0.992
Fe	0.555	0.446	0.471	0.489	0.522	0.463	0.443	0.432	0.438	0.513	0.368	0.524	0.380	0.432	0.465	0.513	0.357	0.358	0.364	0.351	0.355	0.358	0.379	0.408
Mn	0.011	0.008	0.007	0.009	0.010	0.013	0.007	0.008	0.008	0.009	0.004	0.011	0.006	0.007	0.008	0.010	0.006	0.004	0.005	0.005	0.006	0.005	0.004	0.004
Mg	1.407	1.504	1.494	1.485	1.465	1.514	1.585	1.583	1.576	1.415	1.666	1.415	1.646	1.564	1.568	1.498	1.646	1.645	1.663	1.665	1.661	1.664	1.647	1.599
Ca	0.008	0.008	0.008	0.008	0.008	0.007	0.002	0.004	0.004	0.020	0.004	0.007	0.002	0.004	0.003	0.006	0.004	0.003	0.002	0.001	0.003	0.004	0.002	0.003
Cr	0.000	0.000	0.001	0.000	0.000	0.001	0.000	0.001	0.000	0.000	0.000	0.001	0.000	0.000	0.000	0.000	0.001	0.001	0.000	0.000	0.000	0.001	0.000	0.000
Ni	0.000	0.000	0.000	0.000	0.000	0.000	0.000	0.000	0.000	0.000	0.000	0.000	0.000	0.000	0.000	0.000	0.000	0.000	0.000	0.000	0.000	0.000	0.000	0.000
Somma M1	1.981	1.966	1.982	1.991	2.006	1.997	2.037	2.027	2.026	1.957	2.043	1.958	2.035	2.008	2.045	2.027	2.014	2.012	2.034	2.022	2.024	2.032	2.033	2.015
Fo % =	71.32	76.81	75.75	74.89	73.36	76.10	77.92	78.28	77.93	73.07	81.71	72.58	80.99	78.08	76.80	74.11	81.93	81.96	81.85	82.39	82.17	82.10	81.13	79.49
Fa	28.12	22.78	23.87	24.64	26.16	23.26	21.76	21.35	21.68	26.47	18.07	26.87	18.70	21.55	22.79	25.38	17.77	17.84	17.91	17.36	17.55	17.67	18.67	20.30
Tefr	0.56	0.41	0.37	0.47	0.49	0.63	0.32	0.38	0.39	0.46	0.22	0.55	0.31	0.37	0.41	0.52	0.30	0.20	0.24	0.25	0.28	0.23	0.20	0.21

OLIVINES

Sample	TU7															TU8								
Rock	ANDESITE lava flow															ANDESITE lava flow								
notes	ine 9 olf	ine 10 olf	olmf1c	olmf1r	olmf2c	olmf2r	olmf3c	olmf3r	olmf4c	olmf4r	olmf5	olml2	olml3	olml4	olml5	olf1c	olf1r	olf2c	olf2r	olf3	olf4c	olf4r	olf5c	olf5r
SiO_2	37.66	37.09	38.40	37.04	38.19	48.39	38.60	36.54	38.07	39.97	36.90	37.89	37.52	36.88	37.23	38.01	37.48	38.70	35.95	38.55	38.47	37.16	39.00	37.27
FeO	20.44	22.75	20.20	21.51	18.68	13.05	18.03	23.30	20.91	21.15	24.91	21.38	24.07	27.74	27.47	17.87	20.64	17.06	25.76	17.45	17.11	23.93	16.82	24.13
MnO	0.28	0.44	0.33	0.43	0.23	0.31	0.28	0.41	0.49	0.44	0.40	0.43	0.43	0.49	0.64	0.30	0.31	0.23	0.49	0.33	0.27	0.50	0.21	0.38
MgO	40.55	38.41	40.97	38.78	42.08	19.02	42.51	37.06	40.02	30.34	37.10	40.25	37.51	35.16	33.99	43.87	41.16	43.92	36.61	43.83	43.94	38.36	43.68	37.99
CaO	0.11	0.24	0.16	0.18	0.13	3.13	0.14	0.25	0.17	0.83	0.18	0.24	0.20	0.17	0.21	0.05	0.14	0.16	0.22	0.18	0.07	0.21	0.12	0.16
Cr_2O_3	0.00	0.03	0.00	0.03	0.03	0.00	0.00	0.01	0.00	0.01	0.03	0.00	0.05	0.00	0.05	0.05	0.02	0.09	0.00	0.00	0.00	0.03	0.00	0.00
NiO	0.00	0.00	0.00	0.00	0.00	0.00	0.00	0.00	0.00	0.00	0.00	0.00	0.00	0.00	0.00	0.00	0.00	0.00	0.00	0.00	0.00	0.00	0.00	0.00
Tot.	99.04	98.96	100.06	97.98	99.33	83.90	99.55	97.57	99.65	92.73	99.52	100.18	99.78	100.43	99.59	100.16	99.75	100.15	99.03	100.34	99.86	100.19	99.83	99.93
Formula su 4 Ox																								
Si	0.983	0.982	0.989	0.985	0.985	1.386	0.989	0.985	0.990	1.109	0.981	0.982	0.989	0.984	1.000	0.970	0.973	0.982	0.967	0.979	0.980	0.977	0.990	0.982
Fe	0.446	0.504	0.435	0.478	0.403	0.313	0.386	0.525	0.454	0.491	0.554	0.463	0.531	0.619	0.617	0.382	0.448	0.362	0.580	0.371	0.364	0.526	0.357	0.532
Mn	0.006	0.010	0.007	0.010	0.005	0.008	0.006	0.009	0.011	0.010	0.009	0.009	0.010	0.011	0.015	0.006	0.007	0.005	0.011	0.007	0.006	0.011	0.004	0.008
Mg	1.578	1.516	1.574	1.537	1.618	0.812	1.625	1.489	1.551	1.256	1.470	1.556	1.475	1.398	1.361	1.670	1.594	1.662	1.469	1.660	1.669	1.503	1.654	1.492
Ca	0.003	0.007	0.005	0.005	0.003	0.096	0.004	0.007	0.005	0.025	0.005	0.007	0.006	0.005	0.006	0.001	0.004	0.004	0.006	0.005	0.002	0.006	0.003	0.004
Cr	0.000	0.000	0.000	0.000	0.000	0.000	0.000	0.000	0.000	0.000	0.000	0.000	0.001	0.000	0.001	0.001	0.000	0.001	0.000	0.000	0.000	0.000	0.000	0.000
Ni	0.000	0.000	0.000	0.000	0.000	0.000	0.000	0.000	0.000	0.000	0.000	0.000	0.000	0.000	0.000	0.000	0.000	0.000	0.000	0.000	0.000	0.000	0.000	0.000
Somma M1	2.034	2.037	2.021	2.031	2.030	1.228	2.021	2.031	2.021	1.782	2.039	2.035	2.022	2.033	2.000	2.060	2.053	2.035	2.066	2.042	2.041	2.047	2.019	2.037
Fo %=	77.72	74.69	78.05	75.90	79.87	71.73	80.55	73.59	76.92	71.47	72.32	76.69	73.18	68.94	68.31	81.14	77.79	81.91	71.31	81.47	81.85	73.67	82.06	73.42
Fa	21.98	24.82	21.59	23.62	19.88	27.61	19.16	25.95	22.54	27.94	27.23	22.84	26.34	30.51	30.96	18.54	21.88	17.85	28.14	18.19	17.87	25.78	17.72	26.16
Tefr	0.30	0.49	0.35	0.48	0.25	0.67	0.30	0.46	0.53	0.59	0.44	0.46	0.48	0.54	0.73	0.32	0.33	0.24	0.54	0.34	0.28	0.55	0.22	0.42

OLIVINES

Sample	TU8								TU15																
Rock	ANDESITE lava flow								DACITE lava flow																
notes	olf6c	olf6r	olmf2	olmf3	olmf4	olmf5	olmf6	olml1	f1	f2	f3	f4	f5	f6	f7	f8	f9	f10	f11	f12	f13	f14	f15	f16	f17
SiO_2	37.44	36.92	38.27	37.83	38.21	38.00	37.36	37.86	38.60	39.02	39.21	38.81	39.51	38.94	39.62	38.84	38.74	39.11	38.71	39.52	39.09	39.00	39.29	38.75	39.18
FeO	17.40	22.86	20.99	19.47	17.78	22.92	21.66	19.29	13.15	12.40	12.40	12.74	12.61	12.41	12.43	13.26	12.34	12.96	14.06	11.33	13.23	12.52	12.31	12.29	12.68
MnO	0.29	0.35	0.37	0.34	0.23	0.38	0.37	0.52	0.23	0.20	0.13	0.15	0.20	0.16	0.13	0.17	0.16	0.15	0.22	0.14	0.17	0.22	0.17	0.20	0.24
MgO	43.06	39.18	40.60	41.67	43.11	39.58	39.87	42.11	46.99	48.06	47.75	46.97	47.11	47.81	47.20	47.04	47.04	47.12	46.29	47.72	46.30	47.15	46.78	46.57	46.66
CaO	0.08	0.13	0.15	0.19	0.11	0.11	0.15	0.14	0.11	0.11	0.12	0.13	0.10	0.10	0.12	0.14	0.13	0.11	0.12	0.15	0.14	0.08	0.08	0.14	0.13
Cr_2O_3	0.05	0.00	0.00	0.00	0.00	0.00	0.05	0.00	0.03	0.02	0.06	0.03	0.06	0.04	0.01	0.03	0.00	0.01	0.00	0.05	0.00	0.02	0.03	0.04	0.03
NiO	0.00	0.00	0.00	0.00	0.00	0.00	0.00	0.00	0.00	0.00	0.00	0.00	0.00	0.00	0.00	0.00	0.00	0.00	0.00	0.00	0.00	0.00	0.00	0.00	0.00
Tot.	98.31	99.43	100.38	99.50	99.44	101.00	99.46	99.92																	
Formula su 4 Ox																									
Si	0.973	0.973	0.987	0.979	0.981	0.983	0.978	0.976	0.973	0.973	0.979	0.979	0.987	0.975	0.989	0.976	0.979	0.980	0.977	0.988	0.986	0.981	0.989	0.984	0.986
Fe	0.378	0.504	0.453	0.421	0.381	0.496	0.474	0.416	0.277	0.259	0.259	0.269	0.263	0.260	0.259	0.279	0.261	0.272	0.297	0.237	0.279	0.263	0.259	0.261	0.267
Mn	0.006	0.008	0.008	0.008	0.005	0.008	0.008	0.011	0.005	0.004	0.003	0.003	0.004	0.003	0.003	0.004	0.003	0.003	0.005	0.003	0.004	0.005	0.004	0.004	0.005
Mg	1.668	1.539	1.561	1.608	1.649	1.527	1.556	1.618	1.767	1.788	1.777	1.766	1.755	1.784	1.757	1.762	1.773	1.761	1.742	1.779	1.741	1.768	1.756	1.763	1.751
Ca	0.002	0.004	0.004	0.005	0.003	0.003	0.004	0.004	0.003	0.003	0.003	0.004	0.003	0.003	0.003	0.004	0.003	0.003	0.003	0.004	0.004	0.002	0.002	0.004	0.003
Cr	0.001	0.000	0.000	0.000	0.000	0.000	0.001	0.000	0.000	0.000	0.001	0.000	0.001	0.001	0.000	0.000	0.000	0.000	0.000	0.001	0.000	0.000	0.000	0.001	0.000
Ni	0.000	0.000	0.000	0.000	0.000	0.000	0.000	0.000	0.000	0.000	0.000	0.000	0.000	0.000	0.000	0.000	0.000	0.000	0.000	0.000	0.000	0.000	0.000	0.000	0.000
Somma M1	2.055	2.055	2.026	2.042	2.039	2.034	2.044	2.049	2.053	2.054	2.043	2.042	2.026	2.051	2.022	2.049	2.041	2.039	2.046	2.024	2.028	2.038	2.022	2.033	2.027
Fo % =	81.28	75.06	77.21	78.94	81.02	75.17	76.33	79.12	86.23	87.18	87.17	86.65	86.77	87.15	87.02	86.20	87.03	86.49	85.25	88.12	86.03	86.84	86.99	86.93	86.55
Fa	18.42	24.57	22.39	20.69	18.74	24.42	23.26	20.32	13.54	12.62	12.69	13.19	13.02	12.69	12.85	13.62	12.80	13.35	14.52	11.73	13.79	12.93	12.83	12.87	13.19
Tefr	0.31	0.38	0.40	0.37	0.24	0.41	0.41	0.56	0.23	0.21	0.13	0.16	0.21	0.16	0.13	0.18	0.16	0.16	0.23	0.15	0.18	0.23	0.18	0.21	0.25

OLIVINES

Sample	TU15													
Rock	DACITE lava flow													
notes	f18	f19	f20	f21	f22	f23	f24	f25	f26	f27	f28	f29	f30	f31
SiO$_2$	38.28	39.64	39.25	38.48	38.41	38.96	38.89	38.87	39.07	39.18	38.98	39.16	39.24	39.14
FeO	15.16	10.98	12.58	12.28	12.02	11.46	12.61	12.88	11.94	13.10	12.81	12.27	12.11	11.78
MnO	0.18	0.12	0.18	0.13	0.17	0.17	0.19	0.20	0.11	0.24	0.19	0.17	0.14	0.17
MgO	44.66	47.71	46.75	47.07	46.88	47.60	46.95	46.26	47.59	46.44	46.48	46.85	47.20	47.25
CaO	0.14	0.14	0.12	0.14	0.14	0.15	0.12	0.08	0.16	0.15	0.16	0.09	0.17	0.04
Cr$_2$O$_3$	0.02	0.04	0.04	0.01	0.00	0.07	0.02	0.00	0.01	0.07	0.02	0.05	0.00	0.00
NiO	0.00	0.00	0.00	0.00	0.00	0.00	0.00	0.00	0.00	0.00	0.00	0.00	0.00	0.00
Tot.														
Formula su 4 Ox														
Si	0.981	0.992	0.987	0.976	0.978	0.981	0.981	0.986	0.981	0.986	0.985	0.987	0.985	0.986
Fe	0.325	0.230	0.265	0.260	0.256	0.241	0.266	0.273	0.251	0.276	0.271	0.259	0.254	0.248
Mn	0.004	0.003	0.004	0.003	0.004	0.004	0.004	0.004	0.002	0.005	0.004	0.004	0.003	0.004
Mg	1.706	1.780	1.753	1.781	1.780	1.787	1.765	1.749	1.781	1.742	1.751	1.761	1.767	1.775
Ca	0.004	0.004	0.003	0.004	0.004	0.004	0.003	0.002	0.004	0.004	0.004	0.002	0.004	0.001
Cr	0.000	0.001	0.001	0.000	0.000	0.001	0.000	0.000	0.000	0.001	0.000	0.001	0.000	0.000
Ni	0.000	0.000	0.000	0.000	0.000	0.000	0.000	0.000	0.000	0.000	0.000	0.000	0.000	0.000
Somma M1	2.039	2.016	2.026	2.048	2.044	2.038	2.039	2.029	2.039	2.028	2.030	2.026	2.029	2.028
Fo % =	83.85	88.45	86.72	87.12	87.27	87.94	86.73	86.31	87.56	86.12	86.45	87.04	87.29	87.57
Fa	15.96	11.42	13.09	12.74	12.55	11.88	13.07	13.48	12.32	13.63	13.36	12.78	12.56	12.25
Tefr	0.19	0.13	0.19	0.13	0.18	0.18	0.20	0.21	0.11	0.25	0.20	0.18	0.15	0.18